



University of Kentucky
UKnowledge

University of Kentucky Doctoral Dissertations

Graduate School

2010

EFFECT OF FLUORINATION ON PARTITIONING BEHAVIOR AND BILAYER SELF ASSEMBLY

Vivian Aramide Ojogun
University of Kentucky, vaojog2@uky.edu

[Right click to open a feedback form in a new tab to let us know how this document benefits you.](#)

Recommended Citation

Ojogun, Vivian Aramide, "EFFECT OF FLUORINATION ON PARTITIONING BEHAVIOR AND BILAYER SELF ASSEMBLY" (2010). *University of Kentucky Doctoral Dissertations*. 791.
https://uknowledge.uky.edu/gradschool_diss/791

This Dissertation is brought to you for free and open access by the Graduate School at UKnowledge. It has been accepted for inclusion in University of Kentucky Doctoral Dissertations by an authorized administrator of UKnowledge. For more information, please contact UKnowledge@lsv.uky.edu.

ABSTRACT OF DISSERTATION

Vivian Aramide Ojogun

The Graduate School
University of Kentucky

2010

EFFECT OF FLUORINATION ON PARTITIONING BEHAVIOR AND BILAYER
SELF ASSEMBLY

ABSTRACT OF DISSERTATION

A dissertation submitted in partial fulfillment of the
requirements for the degree of Doctor of Philosophy in the
College of Engineering
at the University of Kentucky

By
Vivian Aramide Ojogun

Lexington, Kentucky

Director: Dr. Barbara L. Knutson, Professor of Chemical Engineering

Lexington, Kentucky

2010

Copyright © Vivian Aramide Ojogun 2010

ABSTRACT OF DISSERTATION

EFFECT OF FLUORINATION ON PARTITIONING BEHAVIOR AND BILAYER SELF ASSEMBLY

Fluorinated systems are defined by unique properties that offer advantages in drug delivery, material synthesis and industrial applications. In comparison to their hydrocarbon counterparts, the design of fluorinated solutes for tailored applications is limited by the inability to predict the effect of fluorination on phase behavior. This work examines and interprets the influence of fluorination on the phase behavior of fluorinated solutes and surfactants, with emphasis on their impact on vesicle bilayers.

Thermodynamic partitioning of functionalized series of fluorinated and hydrocarbon nicotinate prodrugs fashioned to promote solubility in a fluorocarbon solvent (perfluorooctyl bromide; PFOB) is measured. Predictive approaches are also employed to describe partitioning of these nicotinates between immiscible phases relevant to drug delivery. The findings reveal no strong correlation of the partitioning trends with biological markers of cytotoxicity and prodrug uptake for PFOB mediated delivery. However, partitioning in model membranes (liposomes), which, increases with the hydrophobicity of the perhydrocarbon nicotinates, suggests incorporation in a cellular matrix is chain length dependent.

The impact of incorporating fluorinated surfactants in catanionic vesicles, which form spontaneously in dilute aqueous solutions and serve as potential substitutes to conventional meta-stable liposome-based vesicles, is studied. Much larger isotropic vesicle regions are observed in the phase map of the partially fluorinated catanionic surfactant pair, cetylpyridinium bromide/ sodium perfluorooctanoate (CPB/SPFO) than in fully fluorinated HFDPC (1,1,2,2,-tetrahydroperfluorododecyl pyridinium chloride)/SPFO. Fluorescence probing of the vesicle bilayers suggest more fluid bilayers in CPB/SPFO than in HFDPC/SPFO due to better chain packing in the fully fluorinated bilayer. However, the vesicle region is expanded in more asymmetric fluorinated bilayers of HFDPC/SPFH (sodium perfluorohexanoate). The increased chain asymmetry in HFDPC/SPFH results in reduced packing density and more fluid bilayers than in HFDPC/SPFO.

The robustness of CPB/SPFO and HFDPC/SPFO vesicles is demonstrated in the synthesis of silica hollow spheres by templating and the retention of encapsulated solutes. Higher colloidal stability of the silica spheres is achieved in HFDPC/SPFO relative to CPB/SPFO due to the barrier effect of the fluorinated bilayer. Similarly, higher solute retention in HFDPC/SPFO is observed. The modulation of phase behavior with fluorination offers opportunities in tunable applications of fluorinated bilayers.

KEYWORDS: fluorinated surfactants, catanionic vesicles, nicotinate prodrugs, partition coefficients, silica

Vivian Aramide Ojogun

January 2010

EFFECT OF FLUORINATION ON PARTITIONING BEHAVIOR AND BILAYER
SELF ASSEMBLY

By

Vivian Aramide Ojogun

Dr Barbara L. Knutson

Director of Dissertation

Dr Barbara L. Knutson

Director of Graduate Studies

January 2010

RULES FOR THE USE OF DISSERTATIONS

Unpublished dissertations submitted for the Doctor's degree and deposited in the University of Kentucky Library are as a rule open for inspection, but are to be used only with due regard to the rights of the authors. Bibliographical references may be noted, but quotations or summaries of parts may be published only with the permission of the author, and with the usual scholarly acknowledgments.

Extensive copying or publication of the dissertation in whole or in part also requires the consent of the Dean of the Graduate School of the University of Kentucky.

A library that borrows this dissertation for use by its patrons is expected to secure the signature of each user.

Name

Date

DISSERTATION

Vivian Aramide Ojogun

The Graduate School

University of Kentucky

2010

EFFECT OF FLUORINATION ON PARTITIONING BEHAVIOR AND BILAYER
SELF ASSEMBLY

DISSERTATION

A dissertation submitted in partial fulfillment of the
requirements for the degree of Doctor of Philosophy in the
College of Engineering
at the University of Kentucky

By
Vivian Aramide Ojogun

Lexington, Kentucky

Director: Dr. Barbara L. Knutson, Professor of Chemical Engineering

Lexington, Kentucky

2010

Copyright ©Vivian Aramide Ojogun 2010

ACKNOWLEDGEMENTS

I am immensely grateful to my mentor, Dr. Barbara Knutson for her guidance and genuine support throughout the course of this research. She truly embodies all the professional and personal attributes that I aspire to in my career. Working in her laboratory has been a wonderful experience and I appreciate her insight and approach in developing my research skills.

I am deeply grateful to all members of my PhD committee, who in various capacities have contributed to the completion of this work. I especially thank Dr. Lehmler for his invaluable technical advice and critique with respect to the membrane and partitioning experiments. I feel fortunate to have been part of his novel and interesting research project, with all the research avenues it provided. I am extremely grateful to Dr. Brion for providing the opportunity to expand my technical skills with the ERTL assistantship. I appreciate and value the sincere interest she has shown in my development and the sound advice she has provided on both professional and personal levels. I am very grateful to Dr. Bummer for support in using the DSC equipment and particularly for his insightful suggestions and questions, which encouraged critical thinking. I am grateful to Dr. Rankin for patiently addressing all my technical questions and the insight he has provided through the years. I thank Dr. Hilt for allowing me to use his laboratory equipment during the initial stages of my research and viewing me as a pseudo-member of his laboratory. I thank Dr. Dziubla for access to his DLS equipment and the useful suggestions with respect to the light scattering analysis.

I thank John May and Trish Coakley of the UK's ERTL facility. Working with these two scientists has made for a truly wonderful experience, here at UK. I thank my laboratory partners, Helen, Kaustav, Brant, Satya and especially Gifty for her consistent and valuable assistance. I thank my wonderful network of friends who provided encouragement and support throughout these five years.

I would like to express my deepest gratitude to my parents, Osagie Ojogun and Laureate Samson and to my sister, Nora, whose love, patience and encouragement made this possible. To my best friend, UGu, whose friendship and support cannot be expressed in words. This dissertation is dedicated to my brother, Richard to encourage him to focus on his goals, in spite of the challenges.

TABLE OF CONTENTS

Acknowledgements.....	iii
List of Tables	ix
List of Figures.....	x
Chapter One: Introduction	1
1.1 Research Goals and Dissertation Organization.....	3
Chapter Two: Background.....	6
2.1 Properties of Fluorinated Surfactants, Applications and Phase Behavior.....	6
2.1.1 Physicochemical Properties of Fluorinated Compounds	6
2.1.2 Effect of fluorinated chains on surfactant self-assembly and thermodynamics of phase behavior	7
2.2 Delivery of Nicotinic Acid Ester Prodrugs in Fluorocarbon	12
2.2.1 Thermodynamics and modeling of solute partitioning between immiscible liquid phases	16
2.2.2 Liposome membrane partitioning	20
2.2.3 Fluorinated Surfactants in Liposomes and Vesicles	28
2.3 Catanionic Surfactant Systems	31
2.3.1 Thermodynamics of Aggregation, Phase Behavior, Stability.....	34
2.3.2 Applications of Catanionic Vesicles	46
2.4 Templating of silica hollow spheres	47
Chapter Three: Partitioning of hydrocarbon and fluorinated nicotinic acid esters (Nicotinates).....	52
3.1 Summary.....	52
3.2 Introduction.....	53

3.3 Experimental Section	54
3.3.1 Materials	54
3.3.2 Apparatus and Procedure	56
3.3.3 Prediction of Prodrug Partitioning in Liquid-Liquid Systems	57
3.4 Calculational	58
3.4.1 Group Contribution Methods for the Estimation of the Nicotinate Solubility Parameters Materials	58
3.4.2 Molecular Dynamics Simulations for the Estimation of the Nicotinate Solubility Parameters	59
3.5 Results and Discussion	61
3.5.1 Partitioning behavior of nicotinate prodrugs (PFMCH/Toluene)	61
3.5.2 Prediction of Nicotinate Fluorophilicity from Molecular Structure	64
3.5.3 PFOB/Water partition coefficients of Nicotinates	67
3.6 Conclusion	68
Chapter Four: Partitioning of homologous nicotinic acid ester prodrugs (nicotinates) into dipalmitoylphosphatidyl choline (DPPC) membrane bilayers	
4.1 Summary	71
4.2 Introduction	72
4.3 Experimental Section	74
4.3.1 Materials	74
4.3.2 Differential Scanning Calorimetry (DSC)	75
4.3.3 Fluorescence Anisotropy Measurements	76
4.3.4 Partition Coefficient Calculations	77
4.4 Results	77
4.4.1 Differential Scanning Calorimetric Measurements	77
4.4.2 Fluorescence Anisotropy Measurements	83
4.4.3 Partition Coefficients of Nicotinates	86

4.5 Discussion.....	88
4.5.1 Differential Scanning Calorimetry.....	88
4.5.2 Fluorescence Anisotropy and Partition Coefficients	92
4.6 Conclusion	94
Chapter Five: Cationic-Anionic vesicle templating from fluorocarbon/fluorocarbon and hydrocarbon/fluorocarbon surfactants	96
5.1 Summary.....	96
5.2 Introduction.....	97
5.3 Experimental Section.....	100
5.3.1 Materials	100
5.3.2 Cationic/Anionic Surfactant Solution Preparation.....	101
5.3.3 Dynamic Light Scattering (DLS).....	102
5.3.4 Transmission Electron Microscopy (TEM)	102
5.3.5 Hollow Silica Particles Synthesis	103
5.4 Results and Discussion	103
5.4.1 Vesicle Formation.....	103
5.4.2 CPB/SPFO Vesicles.....	104
5.4.3 HFDPC/SPFO Vesicles	107
5.4.4 Synthesis of Silica Hollow Spheres	110
5.4.5 CPB/SPFO Vesicle Templated Silica Hollow Particles	112
5.4.6 Stable Silica Hollow Spheres in CPB/SPFO	115
5.4.7 HFDPC/SPFO Vesicle Templated Silica Hollow Particles	117
5.5 Conclusion	119

Chapter Six: Phase Investigations of cationic-anionic vesicle formation in mixtures of hydrocarbon/fluorocarbon and fluorocarbon/fluorocarbon surfactants	121
6.1 Summary	121
6.2 Introduction.....	122
6.3 Experimental Section.....	125
6.3.1 Materials	125
6.3.2 Sample Preparation.....	128
6.3.3 Phase Assignment	128
6.3.4 Probing Surfactant Aggregates using Fluorescence Spectroscopy	129
6.4 Results and Discussion – Phase Behavior	129
6.4.1 CPB/SPFO Aggregates	133
6.4.2 HFDPC/SPFO Aggregates.....	136
6.4.3 CPB/SPFH Aggregates	138
6.4.4 HFDPC/SPFH Aggregates.....	139
6.4.5 Summary of Phase Behavior	140
6.5 Results and Discussion – Fluorescence Study	142
6.5.1 Probing CPB/SPFO Aggregates with pyrene, Py-C4, Py-C10 and Py-C16	145
6.5.2 Probing CTAB/SPFO Aggregates with pyrene, Py-C4, Py-C10 and Py-C16	153
6.5.3 Probing HFDPC/SPFO Aggregates with pyrene, Py-C4 and Py-C16	156
6.6 Conclusion	159

Chapter Seven: Encapsulation of fluorescent dyes in hydrocarbon/fluorinated and fully fluorinated cationic vesicles	161
7.1 Summary	161
7.2 Introduction.....	162
7.3 Experimental Section	165
7.3.1 Materials	165
7.3.2 Vesicle/Solute Preparation.....	166
7.3.3 Dynamic Light Scattering.....	167
7.3.4 Dye Encapsulation and Retention in Vesicles	167
7.3.5 Fluorescence Spectroscopy of R6G /vesicles dispersions	169
7.4 Results and Discussion	170
7.4.1 Effect of R6G dye concentration on vesicles.....	171
7.4.2 R6G dye encapsulation and retention in CPB/SPFO vesicles	172
7.4.3 R6G dye encapsulation and retention in HFDPC/SPFO vesicles	179
7.4.4 Encapsulation of Nonionic Riboflavin	182
7.5 Conclusion	183
Chapter Eight: Conclusions and Future Work	184
8.1 Conclusion	184
8.2 Future Work.....	188
References	192
Vita	206

LIST OF TABLES

Table 3.1, Hildebrand solubility parameters of nicotinate acid ester prodrugs	69
Table 3.2, PFOB/Water Partition Coefficients of nicotinate acid ester prodrugs	70
Table 5.1, Characterization of cationic system aggregates (at pH 3) by dynamic light scattering.	105
Table 5.2, Synthesis of silica particles from CPB/SPFO vesicle solutions (2% wt/wt, $\gamma = 0.8$, pH = 3) as a function of TMOS:surfactant ratio (α).....	112
Table 5.3, Synthesis of silica particles from HFDPC/SPFO vesicle solutions (1.18% wt/wt, $\gamma = 0.78$, pH = 3) as a function of TMOS:surfactant ratio (α)	117
Table 7.1, Hydrodynamic sizes for different surfactant to R6G ratios in CPB/SPFO vesicles (47 mM total surfactant, X(SPFO) = 0.835) and HFDPC/SPFO vesicles (21.75 mM, X(SPFO) = 0.9). Sizes reported 14 days after sample preparation.	172
Table 7.2, Vesicle diameters and polydispersities before and immediately after SEC for the initial encapsulation	179

LIST OF FIGURES

Figure 2.1, Packing parameter and micelle structure	8
Figure 2.2, Proposed transport of prodrug through cellular matrix	14
Figure 2.3, Phospholipid (dipalmitoyl phosphatidylcholine; DPPC) self assembly into planar bilayers with spherical vesicles generated by mechanical forces.	21
Figure 2.4, Representative changes in DPH anisotropy with solute partitioning in bilayer	24
Figure 2.5, Model cationic-anionic-water pseudo-ternary phase diagram.....	33
Figure 2.6, Bilayer model for (a) single surfactant film (b) Catanionic surfactant mixed film.	36
Figure 3.1, Chemical Structures of Nicotinic Acid Esters (Nicotines).	55
Figure 3.2, Chemical Structure of PFOB and PFMCH	56
Figure 3.3, Partition coefficients for perhydrocarbon nicotines in PFMCH-Toluene	62
Figure 3.4, Partition coefficients for fully fluorinated functional chain length nicotines in PFMCH-Toluene	63
Figure 3.5, Partition coefficients for partial fluorinated functional chain length nicotines in PFMCH-Toluene	64
Figure 4.1, Chemical structure of the perhydrocarbon nicotinic acid esters (nicotines).....	75
Figure 4.2, Typical calorimetric scans for mixtures of DPPC with (a) Ethyl nicotinate - C ₂ H ₅ , (b) Butyl nicotinate – C ₄ H ₉ , (c) Hexyl nicotinate – C ₆ H ₁₃ and (d) Octyl nicotinate – C ₈ H ₁₇ in excess water.....	80
Figure 4.3, Partial phase diagrams of mixtures of DPPC with (a) C ₂ H ₅ , (b) C ₄ H ₉ , (c) C ₆ H ₁₃ and (d) C ₈ H ₁₇ in excess water.	81
Figure 4.4, Half width of the (a) main phase transition and (b) pretransition of DPPC with nicotines	82
Figure 4.5, Anisotropy of DPH fluorescent probe in DPPC bilayers as a function of temperature and varying nicotinate concentrations. (a) C ₂ H ₅ (b) C ₄ H ₉ (c) C ₆ H ₁₃ and (d) C ₈ H ₁₇	85

Figure 4.6, Changes in melting temperature, T_m and phase transition width, ΔT_r of the DPPC phase transition as function of concentrations of (a) C2H5, (b) C4H9, (c) C6H13 and (d) C8H17 measured by DPH fluorescence anisotropy.....	86
Figure 4.7, Correlation of experimental DPPC bilayer-aqueous partition coefficients with predicted $K_{o/w}$ partitioning values, published octanol-water values . Trend with cytotoxic data.	87
Figure 5.1, Chemical Structures of anionic surfactant (a) sodium perfluorooctanoate (SPFO; $C_7F_{15}COO^-Na^+$) and cationic surfactants (b) cetylpyridinium bromide (CPB; $C_{21}H_{38}N^+Br^-$) and (c) 1,1,2,2-tetrahydroperfluorododecylpyridinium chloride (HFDPC; $C_{10}F_{21}CH_2CH_2NC_5H_5^+Cl^- \cdot H_2O$).	101
Figure 5.2, Images of negatively stained CPB/SPFO (2.2% wt/wt, $\gamma = 0.85$, pH=3) vesicles (a) TEM image at 18.5 K magnification, (b) TEM image at 49 K magnification.....	106
Figure 5.3, Stained images of HFDPC/SPFO vesicles (a) 0.73% wt/wt, $\gamma=0.72$, pH 3, (b) 2% wt/wt, $\gamma = 0.8$, pH 3	109
Figure 5.4, TEM images of silica particles templated in CPB/SPFO vesicle solutions (2% wt/wt, $\gamma = 0.8$, pH 3), and a TMOS/surfactant ratio of (a) $\alpha = 0.5$ and (b) $\alpha = 0.7$. (c) Silica particles templated at 2% wt/wt, $\gamma = 0.85$, $\alpha = 1$ (titration from an initial pH 6 to final pH 8 with NaOH).	115
Figure 5.5, TEM images of silica particles templated from HFDPC/SPFO solutions at pH 3 (a) 1.18% wt/wt and $\gamma = 0.78$ vesicle solution with TMOS:surfactant $\alpha = 1$, and (b) 0.73% wt/wt and $\gamma = 0.72$ vesicle solution with TMOS:surfactant $\alpha = 2$	118
Figure 6.1, Chemical structures of anionic and cationic surfactants.....	126
Figure 6.2, Chemical structures of pyrene and pyrene derivatized probes.	127
Figure 6.3, Partial Phase Diagrams of (a) CPB/SPFO, (b) HFDPC/SPFO, (c) CPB/SPFH and (d) HFDPC/SPFH in acidic solution (pH 3).	130

Figure 6.4, Images of negatively stained aggregates in (a) CPB/SPFO in 1 % wt/wt; $\gamma = 0.85$ and (b) 3% wt/wt; 0.65 (c) HFDPC/SPFO in 0.92 % wt/wt; $\gamma = 0.85$ and (d) 0.7 % wt/wt; $\gamma = 0.7$. (e) CPB/SPFH 1% wt/wt; $\gamma = 0.65$. (f) HFDPC/SPFH 3.7% wt/wt; $\gamma = 0.9$	141
Figure 6.5, (a) Pyrene in SPFO solution; 0 – 1.7% wt/wt (b) Pyrene in aqueous solutions of CPB; 0 – 0.3% wt/wt (c) Increasing amounts of CPB (0 – 0.3% wt/wt) added to aqueous solution of SPFO/pyrene (1.7 % wt/wt).....	149
Figure 6.6, Fluorescence spectra of (a) pyrene (b) PBA/Py-C4 (C) PDA/Py-C10 (D) PHA/Py-C16 fluorescent probes in CPB/SPFO vesicles and mixed micelle systems; destabilization of vesicles to micelles as a result of salt addition, NaCl (2% wt/wt/0.34M).	151
Figure 6.7, Fluorescence spectra of (a) pyrene (b) PBA/Py-C4 (c) PDA/Py-C10 (d) PHA/Py-C16 fluorescent probes in CTAB/SPFO vesicles and mixed micelle systems ; (destabilization of vesicles to micelles as a result of salt addition, NaCl, 2% wt/wt/0.34M)	155
Figure 6.8, (a) Emission spectra of pyrene as a function of increasing HFDPC concentration (0 – 0.264% wt/wt) in aqueous solution. (b) Decrease in monomer intensity or quenching of pyrene with increasing concentration of CPB and HFDPC in aqueous solutions. (c) Fluorescence spectra of pyrene in SPFO micelles and in HFDPC/SPFO vesicles. (d) Fluorescence of PBA/Py-C4 in HFDPC/SPFO vesicles and in HFDPC/SPFO micelles.	159
Figure 7.1, Chemical structures of (a) Rhodamine 6G and (b) Riboflavin	166
Figure 7.2, Elution profile of R6G-CPB/SPFO system at neutral pH. Surfactant composition is 47 mM, $X_{SPFO} = 0.835$ and R6G (1 mM)	173

Figure 7.3, Effective encapsulation profile of R6G (1mM) in CPB/SPFO vesicles at neutral pH	174
Figure 7.4, Fluorescence emission of R6G (0.05 mM) in (a) CPB/SPFO and (b) HFDPC/SPFO vesicle systems in neutral pH medium.....	178
Figure 7.5, Absorbance spectra of R6G in HFDPC/SPFO vesicles pre-SEC (solid line) and post-SEC (broken line)	181

CHAPTER 1

INTRODUCTION

Fluorocarbons and fluorinated surfactants represent a class of compounds whose special properties have generated enormous interest for their potential in biomedical and industrial applications. Fluorinated compounds are prevalent in cosmetic products, cookware, film materials and constitute important components of electronics, adhesives, wetting agents, lubricants, and plastics.¹ The versatility of these applications can be attributed to the strength of the carbon-fluorine covalent bond, which imparts both strong intramolecular forces and weak intermolecular interactions in fluorinated alkane chains, resulting in physicochemical properties that are distinct from traditional hydrocarbon-based systems.¹⁻⁵

The prevalence of fluorinated materials in industrial chemical applications and the uniqueness of their properties as solutes, solvents, and reactants has earned a separate classification; “fluorous chemistry”, a term coined by I. T. Horvath.⁶ Perfluorinated compounds adhere strongly to the ‘like dissolves like’ principle; their immiscibility with hydrocarbons, for example, is exploited in biphasic catalysis. Compounds functionalized with fluorinated chains constitute an important part of tailored organic synthesis reactions, separations and recovery technologies.⁶⁻⁹ In addition, the ability of perfluorocarbon compounds to dissolve high quantities of oxygen initiated the interest in fluorine engineered catalysis, for applications including the conversion of methane to methanol.¹⁰

Since the ground-breaking work of Clark and Gollan,¹¹ perfluorinated fluids and colloidal systems have gained prominence in biomedical applications as suitable alternatives to hemoglobin derivatives for the transport of oxygen and carbon dioxide, that is effectively acting as potential “blood substitutes”¹²⁻¹⁶ for patients in critical care.¹⁷ The combination of biological and chemical inertness, superior gas absorption and transport capabilities, high surface activity, fluidity and density affords fluorocarbons, such as perfluorooctyl bromide (PFOB), an advantage in ventilation therapy¹⁸⁻²¹ and in treatment of respiratory diseases. Acceptable *in vivo* circulatory residence times ($t_{\text{half-life}}$)

≈ 5.5 days) and reduced effect on red blood cell function are achieved in fluorinated solvents relative to standard hydrocarbon solutions.^{22,23} Several formulations of fluorinated colloidal systems (gels, emulsions, microemulsions, micelles, vesicles and tubules) are currently being explored as contrast agents in imaging of diseased tissues and organs,²⁴⁻²⁷ in the delivery and storage of drugs, proteins and genetic material,²⁸⁻³³ in organ preservation and for eye reconstruction procedures.³⁴

Due to the limited solubility of therapeutic agents in fluorocarbon fluids, incorporation of fluorinated surfactants or partially fluorinated surfactants are often prerequisites for effective solubilization. Novel methods are continually being sought to circumvent the solubility issue with fluorinated surfactants playing an integral role.³⁵

The ability to tailor the phase behavior of self-assembled systems comprising fluorinated surfactants also has applications in supramolecular chemistry (organized molecular assembly). Self-aggregation in amphiphilic systems is amplified in fluorinated surfactants, which are both hydrophobic and lipophobic. The rigidity and bulkiness of the fluorocarbon chains promotes self-assembled aggregate structures of lower curvature, such as rod-like micelles, lamellae and vesicles. The morphology of the aggregates is also dependent on concentration, the nature of the headgroups (nonionic, anionic, cationic and zwitterionic), pH, temperature, pressure and surfactant geometry (straight chain, branching). The fluorophilic character of the surfactant can be adjusted by modifying the proportion of hydrocarbon to fluorocarbon chains in partially fluorinated compounds and tailored to specific applications.³⁶

Applications of liposomes as drug delivery vehicles and templating agents, are constrained by their inherent meta-stability and their long, intensive processes required for preparation. Insertion of perfluoroalkyl chains into the bilayer of hydrocarbon phospholipid aggregates (liposomes) has been shown to greatly improve the stability and reduce the permeability of these model cell membranes, which often function as drug transport vehicles and encapsulation devices.^{31,32,37-40} The phase separation of the perfluoroalkyl chains in hydrocarbon bilayer environments,³⁸ similar to demixing of fluorocarbon–hydrocarbon surfactant mixtures, produces a highly ordered, impervious bilayer core with increased liposome stability.⁴¹⁻⁴³

In contrast to meta-stable liposomes, stable vesicles can be formed in dilute aqueous mixtures of oppositely charged single tailed surfactants. These cationic-anionic or catanionic vesicles form spontaneously and are stabilized by excess charge of the solutions.⁴⁴⁻⁴⁶ The catanionic vesicles provide effective routes for the encapsulation and retention of model compounds,^{47,48} synthesis in nano-reactors,⁴⁹ and transcriptive templating (e.g., the synthesis of stable silica hollow spheres).⁵⁰ The morphology of aggregates in catanionic surfactant mixtures include micelles, lamellar structures and is affected by the tail and headgroup structure of the ionic surfactants⁴⁴, pH, counter ions and ionic strength.^{51,52} The exchange of a hydrogenated surfactant with an analogous fluorinated surfactant can dramatically alter the stabilization mechanism in catanionic surfactant systems,^{53,54} thereby altering the phase behavior, vesicle size, and vesicle size distribution. However, limited literature examines the effect of fully fluorinated surfactant systems on phase behavior.⁴⁴ The corresponding solubilization and permeability in these fluorinated bilayers, critical to applications of catanionic vesicles, is also unexplored.

1.1 Research Goals and Dissertation Organization

Fluorinated surfactants possess unique properties, such as enhanced hydrophobicity (relative to hydrocarbons), lipophobicity, and stiff, bulky chains with a tendency to self assemble into structures with low curvature (rod-like micelles and bilayers). The impact of these unusual characteristics will be manifested in applications where fluorinated surfactants are solubilized in bulk systems or incorporated into organized colloidal assemblies. This work investigates the impact of fluorination on the phase behavior of solutes and surfactants in bulk solvents and in self-assembled bilayers. The modulation of phase behavior with the incorporation of fluorinated moieties will be interpreted from the lipophobic/hydrophobic effects of fluorination on solubilization and changes in the geometric driving forces for bilayer self assembly.

The effect of fluorination on the solubilization of a model prodrug (nicotinic acid esters) for delivery in a fluorocarbon solvent is explored in Chapter 3. The extent of the incorporation of hydrocarbon nicotines in model membrane systems and their interactions with these bilayers is examined in Chapter 4. The hypothesis for the sections

on the prodrug study is that the experimentally determined thermodynamic properties will provide a basis for the interpretation of the uptake of nicotines in fluorocarbon-based drug delivery.

Regions of spontaneous vesicle formation in partially and fully fluorinated surfactant systems are identified and subsequently applied in synthesis of silica hollow spheres in Chapters 5 and 6. Finally, the robustness of these partially and fully fluorinated vesicle bilayers is examined from their ability to encapsulate and retain model solutes (Chapt 7). The research hypothesis for the cationic vesicle studies in this dissertation is that the incorporation of fluorinated surfactants in cationic bilayers will modulate phase behavior which allows for tunable vesicle applications. The specific research goals for each chapter are presented below:

- Determine the physicochemical properties of nicotinic acid prodrugs or nicotinic acid esters derivatized with fluorocarbon and hydrocarbon functional groups to facilitate pulmonary targeted drug delivery in a fluorocarbon medium, (perfluorooctyl bromide/PFOB). In Chapter 3, the thermodynamic parameters of partitioning as they relate to the nicotinic acid ester drug transport by passive diffusion through the pulmonary route are determined experimentally from the relevant, fluorocarbon, hydrocarbon and aqueous biphasic systems. The ability to predict the partitioning behavior as a function of fluorinated and hydrocarbon chain length is further explored using group contribution methods and molecular modeling approach.
- Measure the partitioning of the nicotinic acid prodrugs into on liposomes constituted of the lung-based phospholipid, dipalmitoylphosphocholine/DPPC, which relates to the efficacy as drug delivery agents through the pulmonary route. The mechanisms of incorporation in the liposome bilayers are interpreted as a function of hydrocarbon chain length of the functionalized nicotinate using fluorescence spectroscopic and calorimetric techniques.
- Identify regions of stable vesicle formation and demonstrate the robustness of fully fluorinated cationic vesicle bilayers through the transcriptive templating of silica hollow spheres. In Chapter 5, the relative ability to template hollow spheres from the fully fluorinated cationic surfactant system, sodium

perfluorooctanoate, SPFO/HFDPC (SPFO), 1,1,2,2,-tetrahydroperfluorododecyl pyridinium chloride (HFDPC) and mixed fluorinated/hydrocarbon surfactants, SPFO/CPB (cetylpyridinium bromide) is compared, using complementary methods; transmission electron microscopy (TEM), dynamic light scattering (DLS) and zeta potential measurements .

- Analyze the self-aggregation behavior and characteristics of heterogeneous and homogenous fluorinated, cationic-anionic surfactant aggregates in aqueous solution. In Chapter 6, TEM and DLS are used to establish phase regions of vesicle formation in permutations of the catanionic pairs of fluorinated and hydrocarbon surfactants: sodium perfluorooctanoate (SPFO), 1,1,2,2,-tetrahydroperfluorododecyl pyridinium chloride (HFDPC), sodium pefluorohexanoate (SPFH) and cetylpyridinium bromide (CPB). The nature of intra-vesicle bilayers is studied in the homogenous fluorinated catanionic pair, HFDPC/SPFO and compared with the mixed fluorinated/hydrocarbon pair, CPB/SPFO using pyrene and pyrene carboxylic acids as fluorescent probes.
- Measure the encapsulation efficiency and solute retention of fully fluorinated catanionic systems relative to mixed fluorinated catanionic surfactant vesicles. In Chapter 7, the relative encapsulation and retention of model compound, the ionic dye, rhodamine 6G, and the neutral dye riboflavin in SPFO/HFDPC and SPFO/CPB based vesicles is investigated by combination of size exclusion chromatography (SEC), DLS, UV and fluorescence spectroscopic measurements.
- Conclusions and suggestions for future work based on observations made in the preceding chapters are provided in Chapter 8.

CHAPTER 2

BACKGROUND

This section provides an overview of fluorinated system properties, solution behavior and applications that lays the foundation and motivation for this research study. The physicochemical characteristics of fluorinated surfactants are discussed and examined within the context of phase behavior in colloidal systems, with an emphasis on vesicle bilayers. Thermodynamic properties of fluorinated compounds in bulk systems are also assessed within the framework of drug delivery applications.

2.1 Properties of Fluorinated Surfactants, Applications and Phase Behavior

2.1.1 Physicochemical Properties of Fluorinated Compounds

The position of fluorine as the smallest, electronegative element on the chemical table imparts unique characteristics to fluorinated molecules that have been exploited in diverse applications. With 20% greater bond strength in carbon-fluorine (460 kJ/mol) than the carbon-hydrogen bond and the relatively larger size of the highly electronegative fluorine atom (0.72Å) compared with hydrogen (0.3Å),¹ the carbon-carbon bonds are protected. Thus, perfluorinated compounds are distinguished by high thermal stability and chemical inactivity. Although strong intramolecular forces are ensured by the C-F bond, the weak polarizability of the fluorinated chains results in low intermolecular or van der Waals interactions.⁵⁵ Minimal intermolecular interactions, coupled with the bulkiness and rigidity of the C-F chains, leads to higher density, higher melting points, lower surface tension, low refractive indices, lower boiling points, higher fluidity and surface spreading of fluorocarbon compounds in comparison to hydrocarbons.

These physicochemical properties are also manifested as unfavorable mixing with both aqueous and organic phases. In industrial reactions, the lipophobicity and enhanced hydrophobicity are used to separate and recover organic materials in biphasic catalysis processes.^{6,56} In such processes, heating is used to create a single phase reaction solution of fluorocarbon and hydrocarbons, which is subsequently cooled to the binary phase system, in which fluorophilic and hydrocarbon products are distributed accordingly. Of

specific relevance to clinical applications is the high physisorption of typical gas molecules (O₂, CO₂, Ar, CH₄) in perfluorinated solvents, with superior dissolution abilities, that is 20 times more oxygen and 3 times carbon dioxide than in water.¹³ The high capacity for dissolved gases is attributed to the low cohesive energy density,³ which provides cavities to dissolve the gases without providing for chemical interaction. This, combined with their chemical inertness, affords fluorocarbon liquids such as perfluorooctyl bromide (PFOB) advantages in ventilation therapy and as blood substitutes.^{57,58}

2.1.2 Effect of fluorinated chains on surfactant self-assembly and thermodynamics of phase behavior

Fluorinated surfactants are essential to the application of fluorocarbons in drug delivery, controlled release devices, material synthesis, imaging of damaged tissue (contrast agents), cosmetic agents and fire extinguisher foams.¹

Surfactants or amphiphiles are surface active molecules consisting of two parts, as illustrated in Figure 2.1; the headgroup region, which displays affinity for the aqueous phase (hydrophilic), and tail group, which demonstrates affinity for the organic phase (lyophilic).⁵⁹ The conflicting preferences drive self assembly at surfaces and interfaces, with corresponding reduction of interfacial tensions.

In solution, the unfavorable energetics imposed by dispersed surfactant monomers promotes organized self-assembled aggregates at a specific concentration (critical micelle concentration/CMC), which is typically determined from surface tension measurements. The structural conformation of the micelles (i.e. a closed aggregate form) is dependent on factors that include headgroup type (anionic, cationic, zwitterionic, nonionic), chain length, solution temperature, pH and electrolyte strength. Aggregate shape can be predicted using an equation developed by Israelachvili,⁶⁰ which accounts for the physical structure of the surfactant. The *surfactant packing parameter, P*, is defined as:

$$P = \frac{v}{a_o * l} \quad \text{Equation (2.1)}$$

where v and l are the volume and length of the hydrophobic chain and a_o represents the headgroup area. As depicted in Figure 2.1, spherical micelles, cylindrical micelles,

closed bilayers (vesicles), planar bilayers, inverse micelles are found in the respective fraction ranges: $P \leq 1/3$, $1/3 \leq P \leq 1/2$, $P = 1$ and $P > 1$. However, above a limiting concentration, packing effects induce different micellar aggregates in solution and multiple aggregates are observed. In effect, the morphology of the micelle is a combined result of headgroup interactions, such as electrostatic forces in ionic surfactants or polar in nonionic surfactants, the attractive van der Waals interactions of the hydrocarbon chains.⁶¹






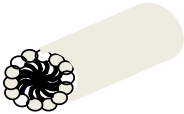


$P = V/(a_0 \cdot l)$	0 - 1/3	1/3 - 1/2	1/2 - 1	> 1
Shape of Surfactant Molecule				
Micelle Structure	 Spherical	 Rod-like	 Lamellar, Vesicle	 Inverted

Figure 2.1: Packing parameter and micelle structure (adapted from Israechavilli⁶⁰)

In the case of fluorinated surfactants, the hydrophobic effect is increased and a lipophobic effect is introduced, which is absent in hydrocarbon surfactants.^{3-5,62-64} As a result, fluorinated surfactants are more surface active and their CMCs are lower than that of their hydrocarbon counterparts.^{65,66} For a fixed concentration (1g/L), sodium perfluorooctanesulfate (PFOS/C₈F₁₇SO₂Na) reduces the surface tension of water by 56%, compared with 11% reduction by sodium octanesulfonate (C₈H₁₇SO₂Na).¹ Due to their lipophobicity, semi-fluorinated alkanes may assume amphiphilic characteristics in fluorocarbon and hydrocarbon media, forming interfacial aggregates.⁶⁷ Although the synthesis routes for typical fluorinated surfactants are more difficult and expensive than for hydrocarbon surfactants,^{1,68} this may be offset by the much smaller amounts required for applications. Akin to other fluorocarbon moieties, fluorosurfactants are chemically and thermally inert with high melting points.¹ The presence of fluorine chains increases

the strength of the corresponding acids, a direct result of the electron-withdrawing strength of fluorine, rendering strong dissociation in solution. Increased surface activity and preference for fluorinated solvent phases has been exploited in the stabilization of fluorocarbon-in water or fluorocarbon-hydrocarbon emulsions and microemulsions. Sadtler and coworkers³³ utilized partially fluorinated surfactants, F-alkyl/alkyl dimorpholinophosphate, in reverse water-in-PFOB emulsions incorporated with anticancer agents and antibiotics. The emulsions were stable for a year with less *in vitro* release (4%) of encapsulated dye, 5, 6 carboxyfluorescein (CF), relative to the hydrocarbon surfactants (37%).

In adherence to Eq. (2.1), the steric hindrance of the rigid, bulky fluorinated chains promotes self-aggregates of lower curvature such as cylindrical micelles, vesicles and lamellar structures. Small angle neutron scattering (SANS) of typical ionic perfluorinated surfactants in aqueous solutions reveals globular micelles, (for lithium perfluorooctanoate (LiPFO;C₇F₁₅COOLi)) and vesicles (for diethylammonium perfluorononanoate (DEAFN;C₈F₁₇COONH₂(C₂H₅)₂),⁶⁹ whereas their hydrocarbon counterparts form more highly curved spherical micelles. SANS analysis demonstrates that the fluorocarbon and hydrocarbon-based micelles are of comparable size, even though the hydrocarbon surfactants possess longer chains. This observation confirms that the fluorinated surfactant tails are in the full extended form (trans-conformation) due to the steric factors inherent in C-F chains, while C-H chains adopt a more flexible gauche conformation. Globular micelles, threadlike micelles and lamellar sheets have also been observed by cryo-TEM in aqueous solutions of homologous series of perfluoroalkylpyridinium cationic surfactants.⁷⁰ X-ray diffraction and polarization microscopy studies reveal the formation of lamellar liquid crystalline structures in families of anionic perfluorinated carboxylic acid surfactants and salts.⁷¹

The interfacial adsorption of fluorinated surfactants cannot always be extrapolated to phase behavior. For example, the surface tension and interfacial properties of sodium perfluorooctanoate (SPFO;C₇H₁₅CO₂Na) and sodium decyl sulfate (SDeS; C₁₀H₂₅SO₄Na) are different, even though the hydrocarbon and fluorocarbon surfactants have comparable CMCs (31 mM and 32 mM respectively).⁶⁶ The hexane-water adsorption energies reflected greater affinity of SDeS than SPFO for the hydrocarbon

phase, which was expected. However, the air-water adsorption energy for SPFO was 24% higher than that for SDeS. Mukerjee and Handa's⁶⁶ interfacial and surface tension measurements also showed that alkane chains (CH₂) had stronger attraction for the hexane than for either water and perfluorohexane, while perfluoroalkane chains (CF₂) had only slightly higher affinity for perfluorohexane relative to the other solvents. This effect was attributed to the weak intermolecular forces in fluorinated chains and highlights the anomalous phase behavior of fluorinated systems. The enhanced micellization effect or hydrophobicity of fluorinated surfactants is driven by the higher energetic penalty in creating water cavities to accommodate the fluorinated chains; that is, the water restructuring effects. Differences in the partial molar heat capacities of CF₄ (98 cal/mol·K) and C₂F₆ (173 cal/mol·K)⁷² compared to CH₄ (50 cal/mol·K) and C₂H₆ (72 cal/mol·K)⁷³ provide evidence for greater water restructuring. Tomasic et al⁷⁴ determined the dissolution enthalpies for fluorinated acids and their sodium salts in comparison with hydrocarbon surfactants. Using low concentrations (< CMC), the heat capacity changes for the respective surfactants were as follows: $\Delta C_p \approx 0.51$ kJ/K mol (perfluorooctanoic acid/HPFO) and 0.55 kJ/K mol (SPFO), which was 25% higher than in the hydrocarbons surfactants. The calorimetric evidence is consistent with the creation of a larger cavity in the presence of a fluorine atom relative to a hydrogen atom. Fluorine creates a bigger water cavity than hydrogen, partially due to the longer bond length: C-F bond = 1.38 Å and C-H = 1.09 Å.⁷⁵ However, the fluorophilic character can be reduced or modulated by having partially fluorinated (insertion of hydrocarbon chains), branched chains⁴ or atomic substituents such as bromide, chlorine, oxygen and hydrogen.⁷⁶ The same study showed much lower ΔC_p for perfluoropolyether carboxylic acid (0.18 kJ/K.mol) and perfluoropolyether carboxylic salt (0.23 kJ/K.mol) due to the presence of branched chains and oxygen atom. Another investigation by Bennett and coworkers⁷⁶ into the surface activity of fluorinated esters in different hydrocarbon solvents (hexadecane, nitromethane, dioxane, ethyl benzene and propylene) revealed that the organic solvent solubility was improved by the presence of branched chains, the presence of a terminal H group, or by decreasing the fluorinated chain length. Eastoe et al⁷⁷ demonstrated with neutron reflectivity data and surface tension measurements that the presence of a terminal H-atom in perfluoroalkyl triethyleneoxide methyl ethers

caused a 75% increase in CMC. Thus, subtle alterations in fluorinated surfactant architecture can elicit strong changes in properties and careful design is critical in achieving the balance of surfactant characteristics for use in drug delivery and other applications.

Fluorinated surfactant micelles have shown promise as drug delivery agents²⁹ and dissolve gases in higher quantities than hydrocarbon surfactant micelles. Micelles of sodium perfluorooctanoate (SPFO), an anionic surfactant, exhibit gas dissolution capabilities greater than sodium-1-heptanesulfonate under similar conditions by the following factors: 4.5 (for O₂), 4.25 (for Ar), 1.9 (for CH₄), 1.36(C₂H₆) and 1.45 (C₃H₈).⁷⁸ The higher propensity of fluorinated surfactants to aggregate is reflected in lower free energies of micellization than with hydrocarbon surfactants⁶⁵ and the hydrophobicity of a fluoroalkyl group, CF₂ is proposed to be equivalent to 1.5 times that of a CH₂ group.⁴ However, this factor is increased when the hydrocarbon chains are components of partially fluorinated surfactants.⁷⁹ In mixtures of fluorocarbon and hydrocarbon surfactants, phase separation is driven by the mutual phobicity of the chains and has been detected by pyrene fluorescence quenching,^{42,43} differential conductance measurements⁸⁰ and small angle neutron scattering.⁸¹ The concentration dependence of demixing has been studied for sodium perfluorononanoate (SPFN) mixed with a hydrocarbon surfactant, sodium n-tetradecyl sulfate (STDS) using pyrene interaction with the quencher, 1-laurylpyridinium chloride (LPC) and conductimetry measurements.⁶² As the concentration of STDS is increased, the micellar system transitioned through segregated micelles to mixed micelles to segregated micelles, with pyrene preferentially solubilized in the hydrocarbon STDS micelles. The CMC of the mixed fluorocarbon and hydrocarbon surfactants is higher than the individual surfactant solutions reflecting their strong deviation from ideal mixing.⁸² Hence, mixtures of fluorocarbons and hydrocarbons are typically classified by this non-ideal phase behavior with positive deviation from ideal mixing. The mutually repulsive interactions means that applications of fluorocarbon solvents require non-traditional surfactants and solutes designed to enhance solubility.

2.2 Delivery of Nicotinic Acid Ester Prodrugs in Fluorocarbon

Thermodynamics and transport topics relevant to the design and interpretation of a novel fluorocarbon mediated prodrug delivery through the pulmonary route are presented in this section. This discussion provides the background for Chapter 3 (fluorinated and hydrocarbon prodrug phase behavior) and Chapter 4 (partitioning of nicotinate prodrugs in model cell bilayers). These thermodynamic measurements and interpretation complement the research collaboration with Dr. H.-J. Lehmler at the University of Iowa, who has investigated the effect of molecular design of nicotinate prodrugs on the uptake and cytotoxicity of the prodrugs delivered in a fluorocarbon solvent.³⁵

Perfluorocarbons (PFCs) have demonstrated biocompatible characteristics (high density, low surface tension, high gas dissolution, biological, chemical and thermal inertness), prompting numerous investigations into their therapeutic applications as drug delivery agents and blood substitutes. Clark and Gollan¹¹ first suggested that PFCs were a viable therapeutic alternative to traditional blood transfusion methods, which suffer from demand/supply imbalance, and possible blood infection challenges. Several PFCs, such as perfluorooctyl bromide (PFOB/C₈H₁₇Br), have gained prominence for potential treatment of acute lung injury or distress in liquid ventilation therapy due particularly to their higher gas dissolution capacities (O₂, CO₂, NO₂) relative to water and blood.¹⁵ Liquid ventilation, a treatment of acute lung impairment, is a short term technique that supplies sufficient levels of required oxygen and opens collapsed airways for gas exchange to effectively oxygenate lungs. Perfluorocarbon fluids (PFCs) provide a balance of properties, such as high density to displace the accumulated fluid or edematous fluid on the diseased lungs, low surface tension and low viscosity to facilitate easy passage through airways and vessels, and appropriate vapor pressures to ensure elimination through exhalation. Partial ventilation therapy allows effective blood flow distribution for target delivery.²¹ Fluosol™ (registered trademark of the Green Cross Corporation, Osaka Japan), an emulsion of perfluorodecalin and perfluorotripropylamine in albumin developed in Japan, which was approved by the food and drug administration (FDA) was used in the USA for a few years but stopped due to storage and stability

problems. This illustrates the limitations posed by most PFC formulations in therapeutic applications.

The potential to extend fluorinated solvent application to drug delivery is also limited by the solubility of typical hydrocarbon-based polar and nonpolar pharmaceuticals. This motivated the study of prodrug delivery system where homologous series of nicotinic acid prodrugs were synthesized with functional groups (hydroalkyl and fluoroalkyl chains) to facilitate solubility in PFOB for administration through the pulmonary route.³⁵ This novel site- targeted drug delivery pathway ensures less body exposure to the drug and even distribution at the intended lung site. The solution of prodrug in fluorocarbon solvent circumvents inherent problems of dispersion formulations (emulsions, micelles etc), which include stability, uniformity and controlled release.

Nicotinic acid ($C_6H_5NO_2$, (NA)), also known as niacin and vitamin B3, is a notable polar pharmaceutical agent characterized by a pyridine structure with carboxyl group at third position (refer to Fig. 3.1 in Chapter 3). Nicotinic acid is recognized for its benefit in the treatment of cardiovascular disease by modifying the lipid lipoprotein constituents of human blood. Addition of nicotinic acid to statin therapy has been shown to reduce levels of low density lipoproteins/LDLs and other bad fats (cholesterol, triglycerides, fatty acids).^{83,84} Conversely, nicotinic acid increases levels of desirable or good fats i.e. high density lipoproteins, HDLs by 21-30%.⁸⁴ It increases the levels of nicotinamide adenine dinucleotide (NAD), which influences cellular response to genomic damage and hence crucial in treatment of carcinogenesis,⁸⁵ with the potential in the treatment of injured lungs.⁸⁶

To facilitate solubility of the polar nicotinic acid drug in the hydrophobic solvent, perfluorooctyl bromide (PFOB), homologous series of the nicotinic acid ester prodrugs were synthesized with perhydrocarbon and perfluorinated functional groups, forming prodrugs. The clinically inactive prodrugs or nicotinic acid esters (nicotinate) are enzymatically converted to the parent nicotinic acid drug at the intended lung site, after passive diffusion through several solvent layers. Efficacy of the PFOB-prodrug delivery is based on design of nicotinic acid esters or nicotinate. Knowledge of physicochemical properties (pKa, solubility) along with transport and cytotoxicity studies as a function of

the homologous series of prodrugs are critical and support the development of a rationale for prodrug design.³⁵

As illustrated in Figure 2.2, the initial hypothesis of prodrug transport in the delivery system, involves the transfer of the prodrug from the PFOB solvent and transport by passive diffusion through the PFOB boundary layer and adjacent aqueous film layer to the intended target cells. Prodrug uptake is described by both paracellular (between cells) and transcellular (across cells) routes. The clinically inactive prodrug is readily converted in vivo to the parent nicotinic acid by enzymatic hydrolysis action. The transport model presented in Figure 2.2 is based on cell monolayer culture studies, which can be utilized for in vitro assessment of the bioavailability and biocompatibility of the prodrugs.

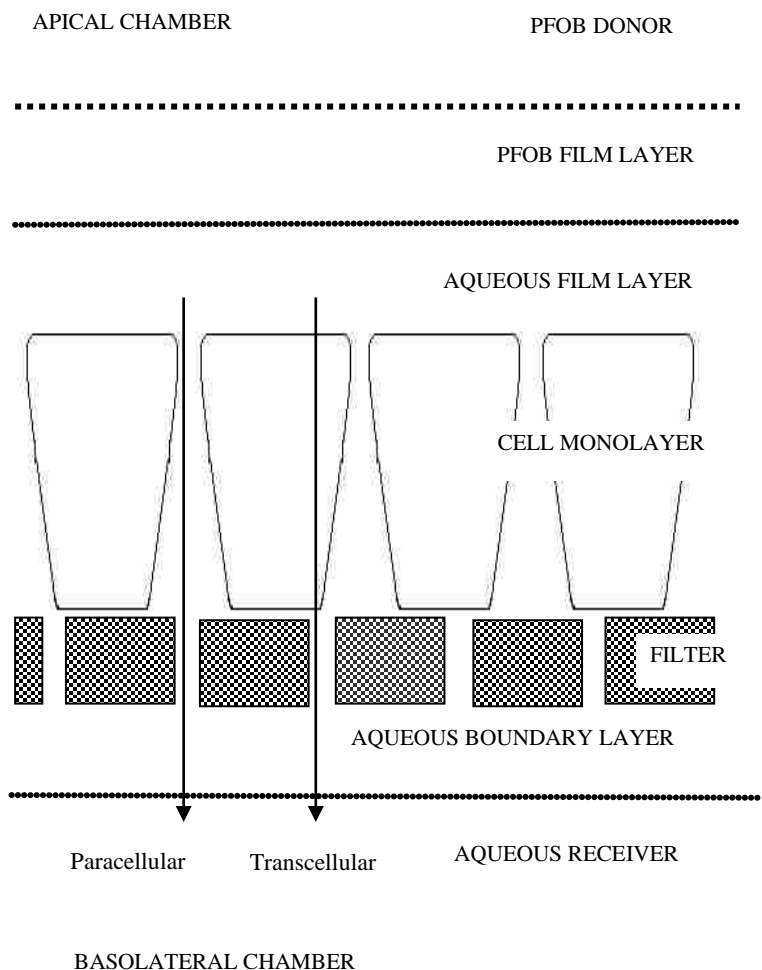


Figure 2.2. Proposed transport of prodrug through cellular matrix (diagram, which has been modified for PFOB transport, adapted from conventional hydrocarbon based delivery.⁸⁷

Applying transport kinetics to the passive diffusion depicted in Figure (2.2), the rate of drug transport can be described using a permeability in series model. The effective permeability coefficient (P_e) is related to the observed experiment mass flux through cell monolayer (J) as follows:

$$J = -V_D \left(\frac{dC_D}{dt} \right) = A * P_e * (C_D - C_R) \quad \text{Equation (2.2)}$$

where A denotes the cross-sectional area, C_D and C_R , the concentration of donor and receiver compartments, V_D , the volume of the donor compartment.

Ignoring convective contributions, intracellular metabolism and protein binding, solute mass transfer resistance will depend on the relative permeability of the solute through individual fluid phases in series. Thus, the effective permeability can also be expressed in terms of the mass transfer resistances (inverse permeability) to prodrug transport:

$$\frac{1}{P_e} = \frac{1}{P_D} + \frac{1}{P_R} + \frac{1}{P_M} + \frac{1}{P_F} + \frac{1}{P_P} \quad \text{Equation (2.3)}$$

where each term in Eq. (2.3) represents a mass transfer resistance or barrier. P_D and P_R are the permeability coefficients of the aqueous diffusion layer on the apical (donor) and basolateral (receiver) chambers and P_P is the PFOB diffusion layer. P_M and P_F are the permeability coefficients of the cell monolayer and filter support used in the drug transport studies.

In the framework of the prodrug transport model, partition coefficients are important thermodynamic tools, as they describe the relative affinity of the prodrugs for the individual phases, hence providing information on the expected mass transfer barriers. They bear a direct relationship to permeability (Eq. 2.4) and are equilibrium-based parameter often applied in quantitative assessment of passive diffusion to cell membranes:⁸⁸

$$P = \frac{K_p * D}{\Delta x} \quad \text{Equation (2.4)}$$

where K_p is the partition coefficient, D the diffusivity and Δx the solvent barrier thickness.

Based on the fluid barriers in Figure 2.2, the relevant partition measurements would be classified as follows: PFOB/water, PFOB/organic and organic/water as they are representative of the different permutations of solvent pairs likely to be encountered by the nicotines in their passage to the target lung cells. The equilibrium partitioning between the fluorocarbon-organic phase and PFOB-water is a measure of the relative affinity of the prodrug nicotines for each phase and the ability to cross the phase barriers described in Figure (2.2). The perfluoro(methylcyclohexane)/(PFMCH)-toluene is used as a standard measure of partitioning between a fluorocarbon and hydrocarbon phase.⁵⁶ The octanol-water partition coefficient ($K_{o/w}$) is used to determine the ability of the nicotines to partition from the aqueous boundary layer to the lipophilic cell membrane, and is a traditional tool for measuring lipophilicity. These thermodynamic parameters elucidate the transport barriers experienced by the prodrug system in the passage to the lung cells and further our aim in designing a model which accurately describes the prodrug transport pathway. In addition to the solvent partitioning, the partition measurements between model membranes (liposomes) and the aqueous phase inform on the solute uptake mechanism or incorporation in a cellular matrix. The design of functionalized prodrugs to minimize the cell cytotoxicity and maximize prodrug uptake requires understanding of drug transport, as interpreted by the partition measurements.

2.2.1 Thermodynamics and modeling of solute partitioning between immiscible liquid phases

A partition coefficient is the equilibrium ratio of a solute in a binary fluid phase system, describing the distribution of a solute between two immiscible phases at a given temperature and pressure.⁸⁹ Partitioning of a solute is described from the free energies of mixing the solute in each phase, which is dependent on the molecular properties of the solute (structure, polarity, size, surface area, molar volume, presence of H-bonds) and its interaction with the solvent. Transfer of solute to a solvent requires two processes; the free energy of cavity formation in the solvent for the solute and favorable interaction energy between the solutes and solvent.

Various techniques exist to quantify solute concentration in each phase at equilibrium with the methods selection based on the molecular properties, binary system, accuracy, costs and expediency. Methods of equilibration have been reviewed by Danielsson and Zhang⁹⁰ and include shake-flask and stir flask methods, which involve mechanical agitation of one or both phases. Subsequent analysis of solute concentration in respective phases is determined by techniques including gas chromatography (GC), high performance liquid chromatography (HPLC), liquid chromatography mass spectrometry (LC-MS) and UV-spectroscopy.⁸⁹ Solute partition coefficients are generally reported for dilute systems (where solute-solute interactions are negligible), and therefore the concentration dependence of the partition coefficient is minimized. For surfactant systems, partition measurements are conducted at concentrations below the CMC to avoid errors as a result of self-assembly.

Liquid-liquid partitioning can also be predicted using classical thermodynamics for non-ideal systems, as applied in Eqs. (2.5) – (2.7). The mass transfer of the solute is driven by the difference in chemical potential, μ , between the two phases and at equilibrium, the chemical potential (Eq. 2.5) is the same in both phases. The preference that the solute demonstrates for a particular phase minimizes the free energy of the whole system.

$$\mu_i = \mu_i^*(T, P) + RT \ln x_i \gamma_i \quad \text{Equation (2.5)}$$

where the excess Gibb's free energy change in non-ideal mixtures is qualified by the activity coefficient, γ , (x is the solute mole fraction) in Eq. 2.5.

$$x_i^\beta \gamma_i^\beta = x_i^\alpha \gamma_i^\alpha \text{ and } K_p = \frac{x_i^\beta}{x_i^\alpha} = \frac{\gamma_i^\alpha}{\gamma_i^\beta} \quad \text{Equation (2.6)}$$

$$\gamma_i^\beta = \exp\left\{\frac{V_i(\delta_i - \delta_\beta)^2}{RT}\right\} \text{ \& } \gamma_i^\alpha = \exp\left\{\frac{V_i(\delta_i - \delta_\alpha)^2}{RT}\right\} \quad \text{Equation (2.7)}$$

α and β denote the respective liquid phases, V_i , the solute's molar volume, K_p is the partition coefficient and δ , the solubility parameter.

The liquid-liquid equilibrium (LLE) partitioning of the solute is quantified by Eq. (2.6). Numerous models exist to describe the non-ideality of liquid mixtures and regular solution theory, RST (Eq. 2.7), allows for description of a wide variety of systems. The theoretical derivation of RST ignores the excess volume of mixing and assumes that excess entropy of mixing is zero at constant temperature and pressure. At equilibrium, the solute partitioning is then described by Eq. (2.7), with molecular interactions expressed by the solubility parameter. The Hildebrand solubility parameter, which is the square root of the cohesive energy density (ratio of energy of vaporization to molar volume at constant temperature) is a measure of the van der Waals forces (London dispersion forces) in a molecule.⁹¹ δ is an important thermodynamic property which is used to index solution properties and is widely used in drug design.⁹² In ideal systems, the enthalpy of mixing is zero as A-B interactions are similar to A-A and B-B, however this is rarely the case and solubility parameter is used to gauge the strength of interaction between solutes and solvents. The closer the solubility parameter values of the solute and the solvent, the more favorable the interactions of the system. Water ($\delta = 48$), is ranked the highest on most scales while perfluoromethylcyclohexane (PFMCH, $\delta = 12.5$) ranks among the lowest, as seen for most fluoruous compounds.⁹³ Solubility parameters increase with polarity, as organic solvents such as toluene ($\delta = 18.2$) and benzene ($\delta = 18.8$) are ranked intermediate between the extremes of water and fluoruous solvents.

The partition coefficient can also be predicted using correlations of molecular properties. The physicochemical properties tested in these correlations include molar volume, the excess molar refraction, H-bond basicity, H-bond acidity, dipolarity/polarizability, molecular surface area⁹⁴⁻⁹⁷ with solubility parameter a recurrent descriptor⁹⁸⁻¹⁰⁰ in these linear free energy relationships (LFER). Hildebrand solubility parameters are often estimated with additivity methods such as Fedors's⁹³ group contribution methods, which divides the molecule into subunits with summation of the vaporization enthalpies and molar volumes. This method has been adapted for various polymer mixtures¹⁰¹ in particular, but is also used for surfactants.⁹⁸ Modification or variations of the Hildebrand solubility parameter (Hansen solubility parameters) which

also account for polar effects and hydrogen bonding are also determined by similar group contribution methods.¹⁰²

Effect of Fluorinated Chain on Partitioning

A standard measure of fluorophilicity of a solute is defined by its partitioning between perfluoro-(methylcyclohexane)/CF₃C₆F₁₁ and toluene.^{7,56} A positive log $K_{(PFMC/Toluene)}$ indicates a preference for the fluorocarbon phase while negative values indicate an affinity of the solute for the organic phase. Several groups have adopted a predictive approach in determining the fluorophilicity of fluorinated compounds. Huque et al.¹⁰³ examined a range of solute descriptors for the development of a linear free energy relationship (LFER) for fluorophilicity. Based on a large selection of 99 fluorinated compounds with wide range of structural features, their parameterization revealed the relative influence on the partitioning was in the order: fluorine content > H-bond acidity > excess molar refraction (index of n and *H*-electrons) > solute polarity/polarisability > McGowan's characteristic molar volume. Kiss et al.⁹⁸ established the fluorine threshold content for fluorophilicity (a positive $K_{(PFMC/Toluene)}$) to be 60%. Using a neural network of descriptors selected from over 50 molecular descriptors, this investigation showed that the Hildebrand solubility parameter was the second most important descriptor (after the solvent extended surface) for a selection of 59 fluorous compounds. Daniels et al.⁹⁷ developed a LFER using modified molecular surface areas descriptors to predict fluorophilicity of both hydrocarbons and fluorinated compounds. They subdivided the molecular surface area into (a) total molecular surface area (b) acidic and (c) basic component surface areas (d) halogen surface area and (e) the exposed surface area of all aromatic carbons; such detail accounted for variations in molecular features with their model yielding reasonable comparison with experimental values (linear regression, $R^2 = 0.94$).

Although significant strides have been made in identifying relevant molecular predictors of the fluorophilicity of solutes, the prediction of the phase behavior of fluorinated molecules is considered to lag that of hydrocarbons.¹⁰³ For example, Arp et al.¹⁰⁴ examined the performance of commonly available software packages (SPARC, ClogP, COSMOtherm and EPI Suite) in predicting the partitioning and absorption behavior of

environmental pollutants, fluorotelomer alcohols and fluorotelomer olefins, and found significant deviations from experimental observations. Some intrinsic properties of fluorinated molecules are not readily captured in standard molecular predictors. For example, fluorinated compound properties are susceptible to peculiarities such as the presence of a hydrogen atom at the tip of the molecule.^{77,105} The placement of a terminal H atom significantly alters the chemical properties of surfactants such as sodium perfluorononanoate ($C_8F_{17}COO^-Na^+/NaPFN$) by introducing a strong permanent dipole moment at the chain tip. Downer et al's¹⁰⁵ studies showed that H-terminated NaPFN (or H-NaPFN) was much more hydrophilic than the fully fluorinated analogue; the CMC increased 4-fold for H-NaPFN. Similar results were observed with sodium salts of bis-(1H, 1H perfluoropentyl)2-sulfosuccinates (DCF4) relative to the H-terminated double chained bis-(1H, 1H, 5H-octafluoropentyl)2-sulfosuccinate (DHCF4), where the CMC of the DHCF4 was 10 times that of the DCF4. In both cases, the interfacial areas per molecule at the CMC increased by 8 – 9 Å and the surface tension increased by 6 – 9 mN/m with the placement of a terminal H-atom.

2.2.2 Liposome membrane partitioning

Liposomes are simplified models of the biological cellular matrix, often used in the study of physiological responses of biomembranes to drugs and solutes. Liposomes are formed from aqueous dispersions of phospholipid (abbreviated to lipid) surfactants, which are hydrophobic fatty acyl chains conjoined to a hydrophilic headgroup, which is usually zwitterionic (neutral) or negatively charged (Figure 2.3).¹⁰⁶ Since Bangham and Horne¹⁰⁷ captured self-assembled bilayer structures in aqueous dispersions of phospholipids by negatively stained TEM 45 years ago, there have been extensive investigations into liposome properties and applications.¹⁰⁸⁻¹¹² Liposomes have been studied extensively for use as model membrane systems,^{113,114} encapsulation agents, drug transport devices¹¹⁵ and synthesis of nano-materials.¹¹⁶

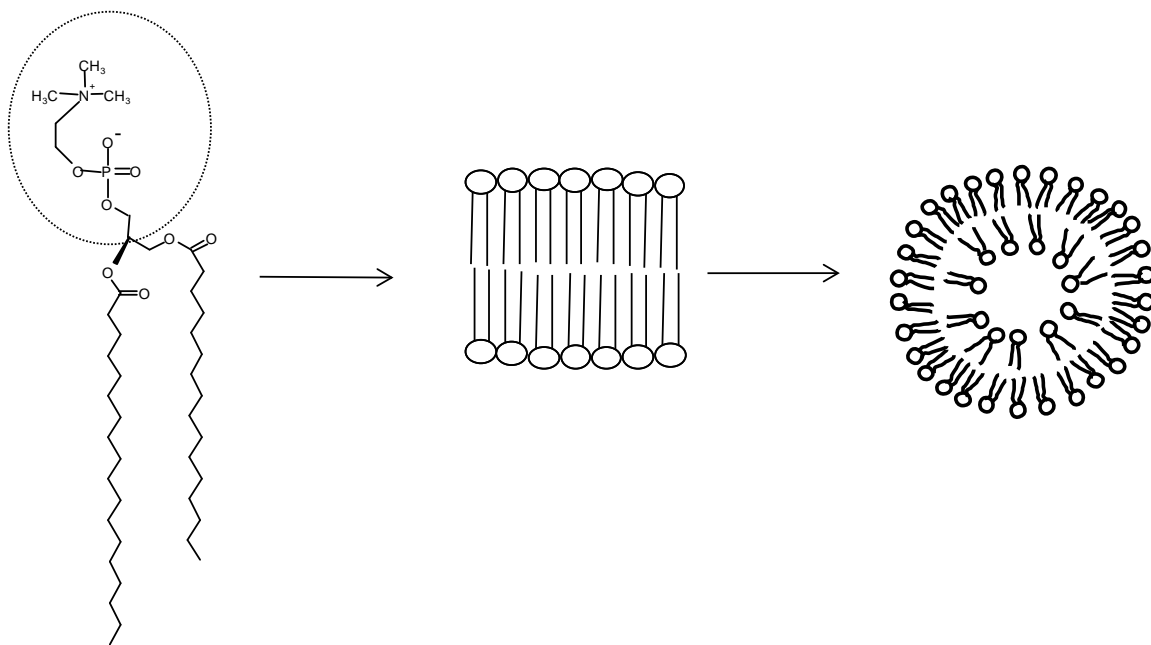


Figure 2.3: Phospholipid (dipalmitoyl phosphatidylcholine; DPPC) self assembly into planar bilayers with spherical vesicles generated by mechanical forces.

As interpreted by the surfactant parameter (Eq. 2.1), planar lamellar structures (Figure 2.3) are the thermodynamically stable aggregates in dilute solution for cylindrically shaped phospholipids (containing bulky fatty acid chains). The spherical vesicle morphology in Figure (2.3) has to be generated by external mechanical forces, making liposomes inherently unstable. Vesicle formation is a result of the compromise between the line energy of a flat bilayer and the bending energy of curvature¹¹⁷ with the latter higher for phospholipid assemblies. Therefore kinetic methods are applied to minimize the bending energy, which determine the final vesicle characteristics. Liposomes are often classed according to size and lamellarity: small unilamellar vesicles/SUVs (≤ 100 nm), large unilamellar vesicles/LUVs, (> 100 nm) and multilamellar vesicles, MLVs, which consist of more than one bilayer in the vesicles.¹⁰⁶ The characteristics of the liposomal colloidal systems are predetermined by the chemical and physical properties of the phospholipid used, solution conditions and the preparation method. As reviewed by Szoka and Papahadjopoulos,¹⁰⁶ the most popular preparative methods include (1) controlled drying and deposition of a uniform dried lipid film from an organic solvent with subsequent rehydration and (2) reverse phase evaporation, where

the organic phase of lipid emulsions is removed by reduced pressure. These methods often produce MLVs that can be reduced to unilamellar vesicles (SUVs) by successive extrusion¹¹⁸ through polycarbonate membranes, sonication, ultra-centrifugation¹¹⁹ and separation by size exclusion chromatography.¹²⁰

A characteristic feature of liposomes is the gel-liquid crystalline (or fluid) phase transition, which occurs at a temperature, T_m (melting temperature) dependent on bilayer properties and solution conditions.¹²¹ In the gel phase ($< T_m$), the lipid chains are tightly packed with strong van der Waals interactions. The chains exist in restricted lateral and rotational motion, with perpendicular alignment to the headgroup plane (trans-conformation) and parallel to each other.¹⁰⁸ Above T_m , in the liquid crystalline phase, the bilayer is marked by less organized arrangement with trans-gauche conformation of the hydrocarbon chains, increased lateral expansion and rotational motion. The phase transition involves the melting of hydrocarbon tails and is similar to an anisotropic - isotropic chain event and the value is dependent on the cohesion of the hydrocarbon chains. The gel phase is rigid with high microviscosity, which decreases with increasing temperature to the more fluid, liquid-crystalline state. Typically, for a well ordered bilayer, the change from gel to fluid phase is a quick transition, occurring over a very narrow temperature range. This is due to conformational restrictions of the ordered chains and excluded volume interactions between the terminal methyl chains in the bilayer.¹⁰⁸ As a result of these packing constraints, the chains in the bilayer have to disorder harmoniously or as a cooperative event.

For a fixed phospholipid headgroup, T_m increases with the length of the fatty acid chains,^{122,123} while branching and unsaturated chains introduce packing irregularities that decrease T_m .¹⁰⁶ The nature of the headgroup interactions, size, nature and position of any charged groups also influence bilayer chain order or bilayer packing and the T_m value.¹²⁴ As semi-permeable membranes encapsulating an aqueous core, the rate of solute diffusion across the liposome bilayer is directly affected by the chain order or bilayer fluidity.

The bilayer or membrane permeability is another key liposome property that affects applicability as model membranes and has consequences for drug delivery applications. A major challenge to liposomal therapy is recognition and interaction with

high density lipoproteins in the plasma¹²⁵ and premature disintegration by the reticuloendothelial system (i.e., the phagocytes or clearance cells of the immune system (liver, spleen, bone marrow and lymph nodes). Reducing the membrane permeability improves the circulation of liposomes and decreases attack by phagocytic cells.⁸⁸ Therefore, permeability of the membrane bilayer is a benchmark of the effectiveness of drug encapsulation and targeted drug delivery by liposomes.

As expressed in Eq. (2.4), permeability or passive diffusion across the membrane can be interpreted in terms of equilibrium partition coefficients, which is a measure of the preferential interaction or solute uptake in the membrane matrix. Hence, measurements of equilibrium partitioning of solutes between the liposome and the bulk aqueous phase constitute a major part liposome research, due to its relevance in drug delivery and solute toxicity.¹²⁶⁻¹³³ Liposome partitioning measurements help elucidate the mechanism of drug interaction with biological membranes and is affected by bilayer chain order or phase state, solute size, shape, charge, hydrophobicity, temperature, pH, electrostatic potential and ionic strength.^{129,130,134}

As model membranes, the choice of constituent phospholipid is important in describing the partitioning in a real biological system. A prominent phospholipid in liposome studies is 1,2 dipalmitoyl-*sn*-glycerol-3-phosphatidylcholine (DPPC) (Figure 2.3) whose phase transition is reported at 41°C.¹³⁴ DPPC is one of the constituents of the pulmonary surfactant found in lung alveoli, so has much relevance for the drug delivery method described in section 2.2.1. As such, DPPC has been utilized in study of solutes which are known to impair respiratory function.¹³⁵

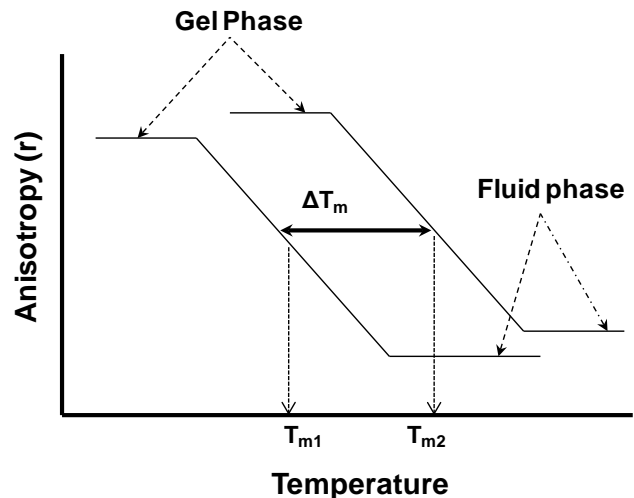


Figure 2.4. Representative changes in DPH anisotropy with solute partitioning in bilayer

The conventional method of quantifying liposome-membrane partitioning ($\log K_{m/w}$) is by correlating changes in the bilayer organization or membrane order with solute uptake or concentration in the bilayer matrix. Several methods used to probe bilayer chain organization and quantify partitioning include, electron spin resonance spectroscopy (ESR),¹²⁷ equilibrium dialysis, isothermal titration calorimetry (ITC),¹⁰⁹ differential scanning calorimetry (DSC),¹³⁶ F NMR,¹³⁷ molecular dynamics simulations¹³⁸ with fluorescence anisotropy¹³⁶ being one of the most fundamental techniques. Fluorescence polarization (anisotropy), which utilizes fluorescent probe such as 1,6-diphenyl-1,3,5-hexatriene (DPH) intercalated in the bilayer, is used to probe changes in membrane fluidity or microviscosity as a function of temperature. DPH is a cylindrical hydrophobic fluorescent probe whose fluorescent intensity is dependent on its rotational diffusion which is dependent on the conformation of the acyl chains or the fluidity of the bilayer. In the gel phase, due to the well packed chains and high microviscosity, the rotational motion is restricted giving high anisotropy when exposed to polarized light (Figure 2.4). In the more fluid, liquid crystalline phase, the reduced chain interaction allows for greater rotational motion of DPH, resulting in low anisotropy (Figure 2.4). Changes in bilayer property such as the melting temperature (T_m), width of the phase transition (temperature range of gel to fluid transition) and onset of transition can then be monitored as a function of solute incorporation.

In lieu of experimental liposome partition measurements ($\text{Log } K_{m/w}$), 1-octanol/water partitioning ($K_{o/w}$) is sometimes used to interpret partitioning of solutes into biological membranes.¹³⁹ The rationale for applying $K_{o/w}$ is based on the transport of drugs through biological systems occurring via transcellular and paracellular routes, with hydrophobic drugs having a propensity for the transcellular route (by way of the membrane bilayer) and hydrophilic drugs for the paracellular route (through the bulk aqueous phase). However, $K_{o/w}$ substitution oversimplifies the bilayer environment and ignores other solute structural effects, steric and binding effects in the headgroup region and temperature induced alterations. Experimental and theoretical studies have shown by experimental and theoretical assessment that this extrapolation is insufficient and sometimes deviates significantly from determined liposome/water partitioning.^{130,131,140,141}

In contrast to the isotropic bulk phases employed in octanol-water measurements, the liposome bilayers are interfacial systems which possess gradations in the environment (polarity and hydrophobicity) from the headgroup region to the centre of the bilayer, where the two monolayers meet.¹³⁴ Molecular dynamic simulations of DPPC bilayers reveal densely packed acyl region with chain order decreasing at the centre of the bilayer¹⁴² (Figure 2.3). Other factors affecting solute incorporation in bilayer include the solute charge and structure¹²⁹ and temperature induced variations in bilayer organization.¹²⁸ The headgroup region possesses charged groups that could act as preferential binding site for charged solutes. Overall, the location or incorporation of solute depends on the bilayer region which presents the best solvent/chemical environment. The permeation is determined by the barrier regions the solute experiences in its diffusion path inter-related to bilayer organization dependent on bilayer organization.

Generally, for a homologous series of compounds, the liposome-water partitioning increases as a function of chain length^{133,143} indicating there is a hydrophobic driving force to partitioning in the bilayer. Ionized compounds often demonstrate higher partitioning than their neutral analogues due to favorable interactions with the ionic groups of the phospholipid.¹²⁹ Typically, solute partitioning into the bilayer disrupts the chain packing and organization, but there are cases where the opposite effect is observed.

An interesting partition phenomenon is the “biphasic effect,” which is a change in partition trend with chain length and concentration for a homologous series of molecules.^{144,145} The partition study of the effects of 1-alkanol with three different liposomal systems, DPMC, distearoylphosphatidylcholine (DSPC) and DPPC,¹⁴⁶ revealed a pivotal concentration or “cut off” point, below which T_m decreased with solute concentration and above which, T_m increased with concentration. The effect was more pronounced with alkanols of chain length $> C12$. Above this chain length, there was greater increase in T_m as a function of the concentration i.e. concentration required for cutoff point decreased with chain length. Matching chain length of the lipid and alkanol increased rigidity of the bilayer through favorable van der Waals interactions and increased packing density, stabilizing the gel phase and increasing T_m .

The ability of partitioning surfactants and solutes to induce drastic phase changes in liposome structure by perturbing the membrane has been widely reported as a function of concentration and chain length^{109,127,132,147} and has physiological relevance for drug interactions with biomembranes.¹⁴⁸ Examples include the gradual disintegration of mixed liposomes (phosphatidic acid/phosphatidylcholine (PA-PC)) by sodium dodecyl sulfate (SDS);¹⁴⁹ the solubilization and transformation of egg-PC LUVs to mixed micelles by zwitterionic surfactant, 3-[(3-Cholamidopropyl)dimethylammonio]-1-propanesulfonate (CHAPS)¹²⁷ and the destabilization action of cetylpyridinium chloride on egg lecithin liposomes.¹⁰⁹ While the exact mechanism varies with the nature of the surfactant and conditions of the liposomal system (pH, ionic strength) liposome disintegration is believed to occur by energetically favorable pore formation in the bilayer due to localized surfactant regions.¹⁵⁰ At low concentrations, surfactant is evenly distributed in the bilayer. As the concentration is increased, the bilayer becomes saturated with surfactant rich regions which lead to solubilization and disintegration of the liposome.¹⁵¹

As permeability is a function of solute partitioning and molecular diffusion, it is sensitive to changes in bilayer organization or barriers in the diffusion path.¹³⁸ Solute permeation through the bilayer is faster at higher temperature, due to increased bilayer irregularities, free volume (void space) creation in the fluid phase, and faster solute diffusion.¹³⁴ Permeability of neutral glucose and alanine was higher for SUVs derived

from dioleoylphosphatidylcholine (DOPC) and soybean phosphatidylcholine (soy-PC) than from dimyristoylphosphatidylcholine (DMPC).¹⁵² This was attributed to the looser membrane packing in the DOPC and soy-PC due to the presence of unsaturated bonds.¹⁵² Similar observations were reported for the thermotropic study of lipid mixtures of DMPC and DPPC.¹⁵³ As the ratio of DMPC:DPPC molar ratio increased from 0.5 to 10:1, the T_m decreased from 40 °C to 25 °C due to the presence of the shorter chain fatty acid of the DMPC lipid. Also, the more fluid bilayers of DMPC had higher encapsulation of thymostimulin (70%) than the DPPC (encapsulation of 55%). However, release of drug was much higher in DMPC (60%) than DPPC (10%) over an hour period. For charged solutes, the permeability is also determined by the headgroup electrostatic potential, system pH¹³³ and ionic strength,¹³² while polar solutes are also influenced by their hydrogen bonding capacity.

The incorporation of cholesterol in bilayers has been demonstrated as an effective means of stabilizing liposomal systems^{109,151,154} and is used extensively in drug delivery. Cholesterol is a steroid-based natural component of mammalian cells, which maintains biomembrane integrity. In liposomes, cholesterol is positioned close to the interface, anchored by its hydroxyl group and with the cyclic rings intercalated between the acyl chains. Cholesterol reorients the lipid acyl chains, reducing trans-gauche conformations. The incorporation of cholesterol reduces the free volume of void space between lipid chains by increasing the chain packing density of the bilayer.¹⁵⁴ De Young and Dill's H NMR studies showed reduced partitioning of hexane¹⁵⁵ and benzene¹²⁸ into dilauroylphosphatidylcholine (DLPC), DMPC and DPPC liposomes with incorporation of 0 - 40 mol% cholesterol. The partitioning of benzene decreased with increasing surface density (headgroup spacing), which is affected by increase in temperature and cholesterol content. The reduction of solute partitioning with addition of cholesterol in bilayers is less effective below the phase transition, suggesting that the ordered gel phase packing effectively reduces permeation. In the fluid phase, the reduction in solute partitioning with addition of cholesterol for DPPC is more significant; this trend corresponds to a significant increase in microviscosity of the bilayer.¹⁵⁶ This is interpreted from the entropic penalty for solute insertion in the bilayer, which increases with the incorporation of cholesterol due to the reduction of free volume. Another

method of improving liposome integrity is via steric stabilization by covalently bonded polymers such as poly(ethylene) glycol derivatives (PEGs) to the bilayer surface. Addition of a 5000 weight PEG to distearoylphosphatidylethanolamine (DSPE) liposomes increased in vivo circulation 10-fold and reduced premature immune disintegration by a factor of 3.¹⁵⁷ However, careful consideration of polymer bulk and hydrophobicity is necessary to obviate adverse effects such as steric perturbation and possible disruption of the membranes.¹⁵⁸

2.2.3. Fluorinated Surfactants in Liposomes and Vesicles

The incorporation of fluorinated surfactants in lipid bilayers greatly influences the chain order and permeability of liposomes. Studies have demonstrated significant improvement in liposome stability with the incorporation of fluorinated chains. Vesicles formed from partially fluorinated DPPC lipids (FC8) displayed 50-fold higher stability than the pure DPPC liposomes, with additional resistance to heat sterilization.³⁰ Improved liposome stability has also been observed for other partially fluorinated lipid systems, is consistent with, as measured using multiple techniques (DSC, optical density, encapsulation measurements)^{31,37,39} and is ascribed to the intrinsic properties of the fluorinated chains.

The impact of the enhanced hydrophobic and lipophobic of fluorinated chains is reflected in permeability and encapsulation studies, in which consistently higher retention of molecules is observed relative to the hydrocarbon vesicles. Retention of encapsulated carboxyfluorescein (CF) was significantly improved (500 %) with insertion of fluorinated chains in di-*O*-alkyl-glycerophosphocholine-based vesicles³² with similar effects determined in phosphatidylserine(PS) vesicles.³⁹ The lower permeability of fluorinated liposomes also reduces the lysis action of bile salts observed with hydrocarbon vesicles³² and limits ion induced vesicle fusion.³⁹ Incorporation of fluorinated chains in lipid bilayers also has implications for biomedical applications. For instance, in vitro studies have shown less disruption of red blood cells (hemolytic effect), reduced adsorption of proteins and reduced premature destruction by the immune system, a process that has often limited applications of traditional hydrocarbon based-liposomes.^{13 37}

Modulation of vesicle characteristics is often a direct function of the amount of fluorinated chains in the bilayer although other factors such as headgroup interactions, position of fluorinated chains also influence these systems.^{159,160} Retention of encapsulated CF increased with the fluorinated chain length in Guillod et al's³¹ study of sugar-based glycerophospholipid vesicles, whereas the fully hydrocarbon vesicles demonstrated no retention. The same study captured a temperature dependent morphological transition of the liposomes from tubules (coiled bilayers) to spherical vesicles, that correlated with the length of the partially fluorinated chains. The transition increased from 15°C in the hydrocarbon bilayers C₁₀H₂₁/C₉H₁₉ to 45 °C in systems with the longest fluorinated chained lipid ((CH₂)₂C₈F₁₇)/((CH₂)₄C₈F₁₇)).

Another interesting effect of the incorporation of fluorinated chains is their impact on liposome gel to fluid phase transition temperatures, T_m. Although incorporation of fluorinated chains in liposome bilayers can increase the characteristic gel to fluid phase transition (T_m), this effect is highly dependent on other structural features which include length, relative proportion and asymmetry of the fluorinated segments in the bilayer.^{31,161} Raviley et al's¹⁶¹ DSC study of partially fluorinated di-*O*-alkylglycerophospholipids liposomes revealed that the impact of fluorinated chains on packing order was affected by interactions with hydrocarbon chains. The transition temperature of the lipid bilayers increased with the degree of fluorination when both lipid chains were uniformly fluorinated. However, chain asymmetry and partially fluorinated lipids where one of the double acyl chains was fully hydrocarbon (similar to jointed F/H chain) resulted in fluid bilayers. Essentially, any structural effects that reduced fluorinated chain interactions resulted in less cohesive packing in the bilayers.

Alternatively, in mixtures of hydrocarbon lipids and fluorinated surfactants, the orientation in the bilayer is different as the chains are not constrained by headgroup attachments. Schmutz et al's³⁸ detailed study of mixtures of dioleoylphosphatidylcholine (DOPC) lipids and semi fluorinated alkanes, C₆H₁₃C₁₀H₂₁ reveal a phase separation of the fluorinated chains in the hydrocarbon bilayers of DOPC liposomes. The exclusion and self aggregation of the fluorinated alkanes towards the center of the bilayer provided a uniform impervious fluorinated nano-compartment. This

conformation, a result of the lipophobicity of the fluorinated chains, also introduced a chain reordering effect in the hydrocarbon sections of the lipid bilayers.

Interestingly, single chain fluorinated surfactants can also form vesicles where the hydrocarbon equivalents form micelles.⁴⁰ Dispersions of single chain phosphocholine surfactants terminated with C_8F_{17} and $C_{10}F_{21}$ chains gave various aggregate forms dependent on temperature, concentration and mixing energy (i.e. sonication). At high surfactant concentration (3% w/v), turbid stable gels or stacked bilayers were observed by TEM while dilution to 0.5% w/v resulted in multilamellar vesicles (MLVs). Further sonication with heat treatment at 40°C led to small unilamellar vesicles, SUVs, (30 – 50 nm), while shaking produced both SUVs (30 nm) and MLVs (300 nm). Sonication at higher temperatures of 70 °C gave globular structures (100 nm) and fibers (1000 nm). The study by Krafft et al⁴⁰ also showed long term stability of these single chained surfactants and the reduced cytotoxicity with red blood cells of fluorinated surfactants in comparison with hydrocarbon surfactants.

The unique ability of single chain perfluoroalkyl surfactants to form stable vesicles was interpreted using geometric arguments based on the packing parameter.¹⁶² The energy of micellization was determined from interfacial tension measurements. Based on energy minimization modeling of C-F bond length and angles in the surfactant, vesicle formation was theoretically possible for single chain fluorinated surfactants (whereas the hydrocarbons form micelles), as observed experimentally, due to greater volume of the C-F chains.

Other interesting phase behaviors have been observed in mixtures of fluorinated surfactants derived from phosphocholine headgroups $C_8F_{17}C_2H_4PC$, with perfluorinated alcohols, $C_8F_{17}C_2H_4-OH$.¹⁶³ With an increase in the fluorinated alcohol concentration in aqueous solution, a transition from vesicles to flexible bilayers to tubules, which are rolled up elongated sheets to rigid sheets/platelets was captured by freeze fracture electron microscopy (FFTEM). The fluorinated alcohol effectively fluidized the bilayers to form the flexible tubules. The rigid platelets suggested bilayer crystallization induced by presence of the alcohol, which was rationalized in terms of the increased packing parameter (due to increase in hydrophobic volume). This crystallization

effectively restricted the spherical vesicle morphology due to reorientation of F-chains that prevented the required spherical curvature.

The potential to effectively tune the properties of vesicle bilayers with fluorination is exemplified in the intrabilayer polymerization work of Krafft et al.¹⁵⁹ Due to the presence of the impervious fluorinated core in the bilayer, the polymerization of lipophilic isodecylacrylate (ISODAC) was restricted to hydrocarbon regions of the bilayer. This confinement resulted in higher localized concentrations of polymer and acceleration of the reaction. In effect, the polymerization reaction was better controlled, which produced more uniform polymers.

These investigations highlight the ability to tune bilayers and aggregate structures by incorporating fluorinated chains. The balance between fluorophilic and lipophilic properties of these bilayers leads to interesting permeability and solubilization in bilayers.

2.3 Catanionic Surfactant Systems

As described in Section 2.2.2, lipid-based vesicles or liposomes have long been established for a variety of applications as drug delivery agents, transport vectors and cosmetic agents. However, they are intrinsically thermodynamic unstable, naturally tending towards a planar lamellar state and thereby releasing any contents captured in their aqueous compartments. This meta-stability or kinetically trapped stability limits their use in various applications.

In contrast, dilute aqueous mixtures of cationic and anionic surfactants spontaneously self assemble into defined structures such as spherical and rod-like micelles, crystalline precipitates, and lamellar bilayers, with vesicles being of chief interest. The inherent stability of these typically small unilamellar ‘equilibrium’ vesicles (SUVs) formed by cationic/anionic surfactant mixtures have established them as viable alternatives to liposomes in controlled particle synthesis,⁵⁰ encapsulation devices^{47,164} and as nano-chambers for chemical reactions.^{165,166} Cationic/anionic surfactant mixtures are classed into two groups: ‘catanionics’ are systems in which the presence of counter ions leads to salt formation; ‘ion pair amphiphiles’ (IPAs) are systems in which the counterions are replaced with hydroxide and hydronium ions.⁴⁴ Hence association of

IPA's results in water as a by-product while the catanionic mixtures produce a salt. Catanionic systems are more prevalent in studies of vesicle formation.

Electrostatically-driven coupling in cationic and anionic surfactant mixtures, with formation of a pseudo-double tailed cooperative unit that closely resembles phospholipids (Figure 2.3), is the primary driving force for aggregation in catanionic systems. Hence, long range electrostatic forces dominate inter-particle interactions in these systems at low concentrations. Catanionic surfactants mixtures exhibit a synergistic effect, in which the area of the combined headgroup (represented as a_0) is lower than the sum of the individual headgroups due to the strong electrostatic interactions. However, the tail groups experience an additive effect which increases the hydrophobic chain volume, v . This effectively increases the surfactant parameter (Eq. 2.1) to a range of $P = \frac{1}{2} - 1$, promoting vesicle formation. The synergism results in non-ideal phase behavior with large negative deviations from ideal mixing. Surface tension measurements reveal large deviations from ideal mixing behavior for catanionics, with the aggregates showing much lower critical aggregation concentrations relative to the individual surfactant's CMC.⁴⁴ Hence, mixtures of catanionic surfactants self-assemble at much lower concentrations than in the individual surfactant solutions.

In a pioneering study, Kaler et al¹⁶⁷ demonstrated spontaneous vesicle formation for mixtures of cetyl trimethylammonium tosylate and sodium dodecylbenzene sulfonate, (CTAT/SDBS) in 1989. Investigations of the phase behavior of additional catanionic aggregates focus mainly on hydrocarbon surfactant systems: cetyltrimethylammonium bromide and sodium octyl sulfate (CTAB/SOS);¹⁶⁸ didodecyldimethylammonium bromide and sodium dodecyl sulfate (DDAB/SDS);¹⁶⁹ and dodecyltrimethylammonium bromide and sodium dodecyl sulfate (DTAB/SDS).¹⁷⁰ The only catanionic systems with constituent fluorinated surfactants whose aggregation characteristics have been investigated in detail are CTAB/SPFO (sodium perfluorooctanoate)^{54,171,172} and CTAB/SPFH (sodium perfluorohexanoate).⁴⁶ The aggregates or coexistence of structures in these systems (Figure 2.5) are dependent on variables which include: molecular features of the surfactants,¹⁷³ paired surfactant asymmetry,^{46,174} total and relative cationic/anionic surfactant concentrations,^{167,175}

counterions,¹⁷⁶ ionic strength,¹⁷⁷ pH,^{51,178} temperature¹⁷⁹ and the presence of additives.^{53,180,181}

The characterization of structural aggregates and the delineation of phase boundaries of cationic aggregates are typically achieved using a combination of visual inspection, DLS (dynamic light scattering) and TEM (transmission electron microscopy).^{46,169,176,179,182,183} However other techniques applied in the study of phase behavior and vesicle bilayer characteristics include optical microscopy¹⁸⁴ fluorescence spectroscopy¹⁸⁵, DSC¹⁸⁶, ITC¹⁸⁷⁻¹⁸⁹, turbidity¹⁸⁶, rheology, NMR¹⁶⁹ and molecular modeling.¹⁷⁴

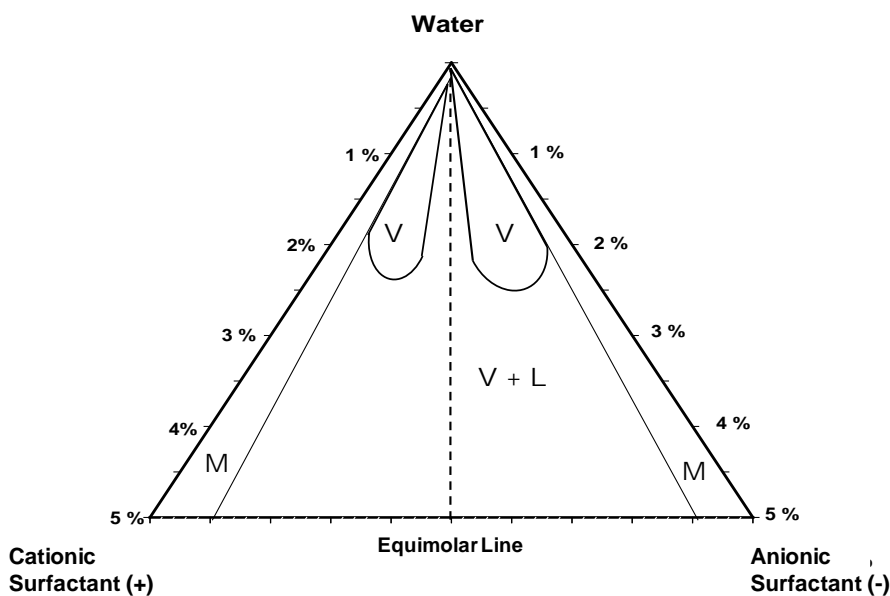


Figure 2.5. Model cationic-anionic – water pseudo-ternary phase diagram. V; vesicle lobe; M; micelle region; V+L; biphasic vesicle and multilamellar region. Adapted from Kaler et al.⁴⁴

Representations of the comprehensive phase diagrams for cationic mixtures are rather complex as the five species (quaternary system) require 4D diagram at fixed temperature and pressure. The five component species arise from dissolution of (i) Ca^+S^- (cationic surfactant) with (ii) An^-S^+ (anionic surfactant) which leads to the cationic pair (iii) Ca^+An^- , corresponding salt, (iv) S^+S^- , and (v) water. In accordance

with Gibb's phase rule that $C + 2 = F + P$ where number C is the number of components = 5, F is the number of degrees of freedom = 2 (temperature and pressure) and P , the number of phases results in 5. Phase diagrams of catanionic systems are usually simplified to 2D ternary diagrams with water, the cationic and the anionic surfactants at the different apexes (Figure 2.5).

As illustrated in Figure 2.5, in the anionic surfactant/catanionic surfactant/water phase diagram, large isotropic vesicle lobes exist on either side of the line representing catanionic surfactant equimolarity. Typically, this vesicle region is initially identified macroscopically by the clear blue Rayleigh light scattering tint. Although the equilibrium nature of these vesicles are disputed by a few,^{190,191} the prevailing rationale of vesicle stabilization in these systems is that the presence of excess surfactant, usually the shorter chained or more soluble surfactant (lower Krafft temperatures) provides stabilization. As such, precipitate is almost always observed in these systems at equimolar concentrations of cationic and anionic surfactants, with stable vesicle regions identified on either side of equimolarity in the phase diagrams.

2.3.1 Thermodynamics of Aggregation, Phase Behavior, Stability

The interplay of long range electrostatic forces, short range van der Waals forces, and mixed bilayer properties lend complexity to the study of aggregate formation in catanionic mixtures and preclude the same generalizations that apply to phospholipid surfactants. However, the thermodynamics of the spontaneous formation of vesicles in catanionic systems dictate that the total free energy be minimized for a given set of conditions and that the vesicle morphology represents the lowest energy state of the aggregates. Thermodynamic interpretations of the contribution of chain asymmetry of the catanionic surfactant mixture to vesicle formation and the stabilization mechanism of vesicle formation (enthalpic or entropic) are described below.

Spontaneous Curvature – Bilayer Chain Asymmetry. Spontaneous curvature is a function of system conditions and is determined by headgroup interactions and chain van der Waals interactions, where it describes the preference for the oil or aqueous phase (Figure 2.6). Conditions that result in deviation from the spontaneous curvature result in energetic penalty for vesicle formation. Thermodynamic descriptions of spontaneous

catanionic vesicle formation employ the membrane elasticity model developed by Helfrich,¹⁹² which is based on the properties of the bilayer film as given in the equation below:

$$\frac{E_b}{A} = 0.5 * k_e (c_1 + c_2 - 2c_o)^2 + k_s c_1 c_2 \quad \text{Equation (2.8)}$$

where E_b is the bilayer elastic free energy, A the surface area, k_e , the bending modulus or bilayer constant, (given in thermal units $k_B T$ ($k_B =$ Boltzmann constant)), k_s the Gaussian modulus, c_1 and c_2 are the local curvatures and c_o the spontaneous bilayer curvature. k_e is a mechanical description of the stress of stretching of the surfactant chains in the monolayers into spherical conformation, while k_s describes deformations in vesicle shape and topology; both are functions of molecular properties of the surfactant film.¹⁹³ For symmetrical bilayers composed of single surfactants, c_o is zero, leading to planar bilayers as the thermodynamically stable aggregates while asymmetric bilayers generate spontaneous curvature that promote vesicle morphology. The chain asymmetry and mixed bilayer composition concept is the underlying physical principle of facile vesicle formation in catanionics.

Safran et al^{193,194} investigated the framework of surfactant chain packing in catanionic bilayers using mean field theory. The bending constant, k_e was assessed as a function of surfactant chain length, the composition of mixed surfactant film, and cross-sectional area of the hydrophobic group. Bending energy, which is a function of chain stiffness, increases with surfactant chain length and decreases with cross-sectional area of the surfactant. More importantly, chain asymmetry of mixed surfactant films considerably reduced the bending energy in specific stoichiometric ranges. In catanionic bilayer films, surfactants can partition between the individual monolayers by ‘flip-flop’ or lateral diffusion and this uneven distribution reduces the tensional stress associated with bending the monolayers.

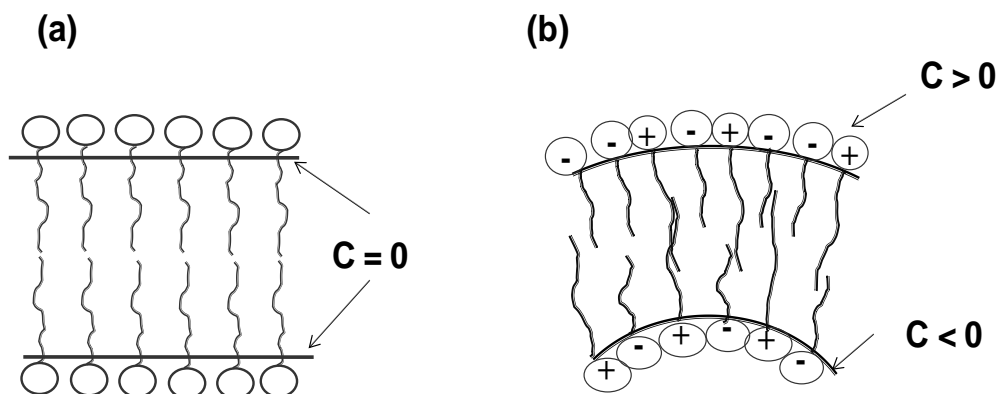


Figure 2.6. Bilayer model for (a) single surfactant film (b) Catanionic surfactant mixed film.(adapted from surfactant films in Szleifer et al's.¹⁹³

As illustrated in the two dimensional bilayer representation^{193,194} in Figure 2.6, if headgroup interactions produce cross-sectional areas that are larger than chain interactions the monolayer film will curve towards the hydrophobic region (positive curvature, $C > 0$). Conversely, if the headgroup interactions are stronger than chain interactions, the mismatch will result in a monolayer film that curves towards the aqueous phase (negative curvature, $C < 0$). These opposing effects produce monolayers of opposite curvature and generate spontaneous curvature. The mixed surfactant bilayers in catanionics can generate spontaneous curvature by having more of the complexed, smaller headgroup area in the inner monolayer and more of the uncomplexed or excess surfactant in the outer monolayer. This results in monolayers of opposite curvature, the outer convex monolayer possessing more molecules or bigger headgroup areas than the inner concave monolayer. The effect is also enhanced by the asymmetry of the bilayer chains, where faster diffusion or molecular exchange between the monolayer leaflets generates the curved film.

Enthalpic and Entropic Vesicle Stabilization

In catanionic systems, where conditions and structural features facilitate the spontaneous curvature phenomena described in the previous section, vesicle formation is enthalpically stabilized. This mechanics ensures that the vesicle morphology is the lowest energy state of the system as there is an energetic cost for deviating from this specific curvature. For enthalpically stabilized vesicles, the large membrane rigidity means that

once composition-dependent spontaneous curvature is generated, other aggregates are energetically precluded.¹⁹⁴ In the absence of the prerequisite spontaneous curvature for energy minimization, the system can be stabilized by the entropy gain of having small vesicle structures as opposed to large planar lamellar sheets. In this case, the vesicle formation is also promoted by mixing of the oppositely charged surfactants in the bilayer, which reduces the bilayer rigidity (bending modulus or constant in Eq. 2.8) to a much lower value than that observed in single surfactant systems. Thus, the vesicular structure is of higher free energy in relation to the lamellar state in entropically-stabilized systems but the favorable non-ideal surfactant mixing promotes vesicle formation. Conversely, the enthalpically-stabilized vesicles are of lowest energy state in the whole system. Hence, the vesicle size and size distribution are determined by the mechanism of vesicle stabilization (balance of entropy and energetic forces).¹⁹⁴ Enthalpically stabilized vesicles are characterized by a small size and narrow size distribution, while entropically stabilized vesicles are larger and polydisperse.

The mechanism of vesicle stabilization for a catanionic system is dictated by the interplay of headgroup and chain interactions effects on bending energy and the entropy of surfactant mixing.^{174,194,195} The effect of chain packing is evident in several studies which report larger vesicle lobes in the phase map (Figure 2.5) with increasing asymmetry of the catanionic surfactants.⁴⁴ Catanionic bilayers which possess close to symmetric chains resemble single surfactant systems, hence are subject to entropic stabilization in the absence of spontaneous curvature. However, the vesicle curvature has to be minimized to compensate for the bending penalty so large vesicles (close to planar aggregates) are associated with these systems. Marques et al¹⁹⁶ utilized polarized light microscopy (PLM), NMR and cryo-TEM to study the phase behavior of amino-derived catanionic surfactant pairs: symmetric (C12/C12) and asymmetric (C16/C8). They revealed a larger vesicle phase region in the latter, where the presence of the shorter chained surfactant increased bilayer flexibility to facilitate bending.

Theoretical models suggest that increasing chain asymmetry can shift the mechanism of stabilization of catanionic vesicles from entropic to enthalpic. Utilizing a comprehensive thermodynamic model, Yuet et al¹⁷⁴ characterized the changes in free energy contributions (entropy and enthalpic) for vesicle stabilization, as a function of

chain asymmetry for the following catanionic pairs: CTAB/SPDS (C16/C15), CTAB/SOS (C16/C8) and CTAB/SPS (C16/C5).^{174,195} Accordingly, the free energy terms that favored vesiculation were the hydrophobic effect (transfer from monomer to aggregate) and favorable entropy of the mixed surfactant bilayer. Conversely, the opposing terms were the creation of an interface (interfacial energy) and the electrostatic interface. Their study showed that the minimization of free energy of vesicle formation is a competition between the penalty costs of having an electrostatic interface and the favorable chain packing free energies. The predicted vesicle composition of the least asymmetrical catanionic pair, CTAB/SPDS, closely resembled that of the bulk solution (consistent with entropic stabilization). In contrast, the composition of vesicles for the highly asymmetric system of CTAB/SPS reflected incorporation of more of the shorter chained SPS to facilitate spontaneous curvature (consistent with enthalpically stabilized). The strain of reduced conformational freedom of similar chain lengths (i.e., CTAB/SPDS system) (effectively mimicking the phospholipid surfactants) in the individual monolayers led to the free energy of a planar bilayer being lower than that of curved vesicle structure but the favorable chain mixing promotes vesicle formation. Hence, the vesicles are larger with lower curvature to relieve the pressure on chain conformation. In the more asymmetric catanionic pair, the much shorter chained surfactant considerably reduces this pressure by incorporation into the outer monolayer, ensuring that vesicle formation is the minimized energy state.

Phase Behavior and Vesicle Characteristics

An example of an entropically stabilized system is CTAB/SOS, whose phase behavior has been studied extensively by Kaler's group.^{168,177} The vesicle lobe (refer to model in Figure 2.5) of this system is significantly larger in the SOS-rich phase than in the CTAB-rich phase, largely due to the high solubility and short chain nature of SOS. This is a common feature of most catanionic systems, where the vesicle lobe is larger in compositions with excess of the shorter chained or more soluble surfactant.^{170,197} The phases in CTAB/SOS were distinguished first by visual inspection; the vesicular structure was then detected by DLS and clearly confirmed by cryo-TEM. The size of the large, polydisperse vesicles were established after 90 days to ensure stable vesicle formation.

This study, along with several others, emphasizes the time frame needed to delineate vesicle regions; several samples initially suggested to be vesicles gradually stabilized to lamellar phases. Micellar structures were observed close to the boundaries of the vesicle lobe, with rod-like micelles observed in the CTAB-rich region and spherical micelles in the SOS-rich region of the phase diagram. Often the aggregates within the micellar phase regions assume the structure of the individual surfactants.¹⁹⁸ At equimolar and very low concentrations in the CTAB/SOS, < 0.2 wt%, a crystal precipitate was observed, as observed in other mixed surfactant systems.^{184,198}

Several studies are in agreement that within the stable vesicle region and for fixed cationic/anionic surfactant mixing ratio, the vesicle size is independent of total surfactant concentration.¹⁸² In effect, the number of vesicles increases with surfactant concentration. In the dilute region (close to water apex in Figure 2.5), the vesicles are stabilized by long range electrostatic forces. At high concentrations, the close packing constraints of the vesicles leads to aggregation and the formation of multi-lamellar bilayers.¹⁸³ Coldren et al¹⁸² employed cryo-TEM and FFTEM (freeze fracture – TEM) in the study of vesicle characteristics in the cationic and anionic-rich phase of CTAT/SDBS. Using the experimental analysis of vesicle sizes and size distributions, the membrane elasticity parameters in Eq. (2.8) were determined and found to be different for the cationic and anionic-rich phases. The effective bilayer constant, k_b of the CTAT-rich vesicles was ≈ 3.5 times lower than that of the SDBS -rich vesicles, which was ascribed to the hydrophobic tosylate counter-ion of CTAT. The entropic penalty associated with large, hydrophobic counter-ions in water (i.e. water restructuring) results in its stronger binding to the bilayer-aqueous interface, which in turn affects the strength of the cationic headgroup interactions. The closely bound counter-ion inserted into the bilayer membrane increases the effective headgroup area but reduces bilayer rigidity. The CTAT/SDBS vesicles are entropically stabilized, therefore characterized by low bending constants, resulting in large vesicles with wider size distributions.¹⁷² Consistent with the bending energies, SDBS-rich vesicles were smaller with narrower size distributions than CTAT-rich vesicles. However, for CTAB/SOS systems, the bending constant of the CTAB-rich vesicles was also determined to be 3.5-fold lower than that of the SOS-rich vesicles. However, there was no molecular property to account for this bending constant,

as the bromide ion is not hydrophobic. In essence, no single set of rules applies to all cationic surfactant mixtures; the thermodynamic driving force for vesicle formation has to be assessed on a case by case basis.

One of the requisites of thermodynamically stable vesicle formation is that the vesicle characteristics be independent of the mixing method. It has been suggested that kinetic factors associated with shear of mixing influences the energy state, vesicle characteristics and the rate at which it attains the low energy vesicle conformation. For example, the mixing method strongly affects vesicle equilibration in CTAT/SDBS mixtures.¹⁹⁷ With five different methods of surfactant mixture homogenization, the equilibration time (one month) was monitored using DLS to establish the most efficient mixing path. The method which applied hydration of the dry powder mixtures with simultaneous heating and stirring produced the lowest initial diameter at a low polydispersity, as measured by DLS. The least efficient mixing path; combining the micelle solutions with delay in stirring, initially results in aggregates of twice the size and a corresponding larger PDI. All mixing methods converged to similar size and PDI after the equilibration for a month. In a similar study, the formation path affected size, structure and polydispersity of DDAB/SDS aggregates.¹⁹⁹ Optical microscopy captured very large aggregates (vesicle tubules and clusters) for samples that had been diluted from multiphase regions while cryo-TEM images proved that well stirred micellar mixtures and mixed powder hydration produced stable, monodisperse SUVs (20 – 100 nm) that varied little with dilution.

The mixing pathway also affects the vesicle size equilibration structural transition of the aggregates. Fragmented vesicles and bilayer disks have been detected in equilibrating samples of CTAB/SOS¹⁸³ and have been hypothesized to form via bilayer-bilayer fusion.²⁰⁰ The disks and open bilayers represent non-equilibrium, transitory structures in the pathway to stable vesicles²⁰¹ and account for the long equilibration times required for defining a stable vesicle sizes.²⁰² It was proposed that the more soluble monomeric SOS is incorporated into CTAB micelles to form mixed micelles. These mixed micelles may merge to form wavelike undulated bilayers with unfavorable edge energies due to exposure of end chains to aqueous environment. The growth of the planar bilayers proceeds until a length is reached where the edge energy overcomes curvature

bending energy. This leads to formation of the non-equilibrium vesicles. Growth of vesicles occurs by fusion of smaller vesicles which is a slow process to the final stable vesicle size.

Catanionic Bilayers with Fluorinated Surfactants

In contrast to hydrocarbon/hydrocarbon surfactant systems, there are limited studies of catanionic systems with fluorinated surfactants. Kaler et al provide the very few examples with their detailed study of mixed hydrocarbon/fluorocarbon mixtures, CTAB/SPFO and CTAB/SPFH. CTAB/SPFO vesicles have been shown to adhere to enthalpic stabilization mechanisms. Van Zanten and Zasadzinski's¹⁷² cryo-TEM study were used to determine a bilayer constant (Eq. 2.8) that was more than 10-fold greater than that established for hydrocarbon, CTAT/SDBS. The high bending rigidity was attributed to the enhanced rigidity and bulkiness of the fluorinated chains in the monolayer films. In hydrocarbon surfactants, the low membrane rigidity is a feature of the packing of the more flexible hydrocarbon chains present in gauche conformations; favorable chain mixing in asymmetric catanionic bilayers promotes this phenomenon. As discussed in section 2.1, mixtures of hydrocarbon and fluorocarbon surfactants often segregate into aggregate domains due to mutual phobicity of the F-H chains and exhibit positive deviations from ideal mixing.²⁰³ However, in CTAB/SPFO monolayers, the surfactants are anchored to the bilayer surface by the electrostatic attraction. This overcomes the unfavorable hydrocarbon/fluorocarbon chain interaction. The different flexibilities of the C-H and C-F chains along with the lipophobicity and hydrophobicity of the fluorinated chains suggests much more complex chain interaction in the bilayer. The very large bending constant in CTAB/SPFO dictates that vesicle formation is energetically stabilized. Due to the very high membrane rigidity, the natural adoption of a spontaneous curvature of the CTAB/SPFO bilayer film within certain surfactant compositions facilitates the spherical morphology. This ensures that the vesicles are the lowest energy state. This spontaneous curvature ensures small vesicle sizes with Gaussian size distribution due to the energetic penalty associated with other sizes. As such, small monodisperse vesicles \approx (45 nm, diameter) have been captured by cryo-TEM in mixtures of CTAB/SPFO.⁵⁴

Interesting morphologies such as bilayer disks, cylindrical vesicles were also observed in equilibrium with the spherical bilayers in the CTAB/SPFO system and their relative proportion was dependent on the CTAB/SPFO ratios.¹⁷¹ Jung et al's¹⁷¹ cryo-TEM analysis revealed increasing numbers of cylindrical vesicles and less disks as the amount of SPFO increased for a given concentration. Similarly, the presence of disks decreased with increasing concentration of the fluorocarbon surfactant for mixtures of n-dodecyl betaine (zwitterionic surfactant) and the ammonium salt of perfluoropolyether (PFPE).²⁰⁴ Coexisting vesicle populations (25 nm and 90 nm) were also detected and attributed to inter-vesicle surfactant segregation: the hydrocarbon and fluorinated surfactants mutually separated to vesicles of very different curvature with the flexible hydroalkyl chains in the smaller, highly curved vesicles.

Others have observed polyhedral vesicles in ion-pair amphiphile (IPA) mixtures of octyltrimethylammonium perfluorooctanoate $C_7F_{15}COO^-C_8H_{17}N^+(CH_3)_3$. The faceted structure of the vesicles (300 nm) was ascribed to fluorocarbon and hydrocarbon chain segregation in the bilayer. The faceted vesicle structure is associated with low miscibility of stiff chains in the bilayer.^{205,206} At high temperatures, favorable chain mixing is promoted by increased chain motion, while cooling results in bilayer crystallization due to accumulation of the excess surfactant (typically the shorter chain) at vertices to compensate for the bending energy. These structures are often associated with very highly rigid membranes and represent energetically minimized structure between planar bilayers and curved spherical bilayers.²⁰⁶

The effect of fluorinated chain length is evident in comparing vesicles of CTAB/SPFH (sodium perfluorohexanoate; $C_5F_{11}COO^-Na^+$) to CTAB/SPFO. The bending constant or membrane elasticity of CTAB/SPFH has been estimated to be several orders of magnitude lower than that of CTAB/SPFO, and is similar to those determined for entropically-stabilized hydrocarbon surfactant mixtures.¹⁷² Iampietro and Kaler established the phase regions in this system by visual, DLS and SANS analysis⁴⁶ with vesicle formation in a narrow concentration range (2 – 4 wt%, CTAB/SPFO \geq 20:80). The resulting vesicles were larger with wider size distributions compared with CTAB/SPFO, consistent with entropically-driven vesicle formation. This change in mechanism was ascribed to the shorter chained fluorinated surfactant SPFH (FC5)

compared with SPFO (FC7). SPFH, with its higher solubility, promotes favorable chain mixing, similar to that observed for most hydrocarbon surfactants. The short chain surfactant is most probably distributed in the inner and outer bilayer leaflets, effectively reducing membrane rigidity (entropic stabilization). Also, the greater chain asymmetry (C16/C5 versus C16/C7) provides flexibility in chain conformation in the mixed bilayers. The CTAB/SPFH system had a larger isotropic vesicle phase region than CTAB/SPFO.⁴⁴

Others have reported large polydisperse vesicles (> 100 nm) in systems of double-tailed cationic fluorosurfactants^{205,207} and catanionic mixtures of fluorinated surfactants with trimethylammonium carboxylate headgroups.²⁰⁸ These studies also highlight the limitations of light scattering in determination of fluorinated aggregate size distributions due to the low refractive index of fluorinated chains.²⁰⁹ Often, the study of aggregate formation in fluorinated systems require more complex scattering techniques such as static or multi-angle scattering (SLS)^{210,211} and small-angle X-ray scattering (SAXS).²¹² The particular advantage of SAXS is due to the high electron density of fluorine atoms compared with hydrogen atoms, which means more efficient scattering. However, direct imaging by electron microscopy (TEM) remains one of the most used methods for accurate size determination.^{44,54,182}

Vesicle Aggregation and Destabilization

Fundamental to any colloidal system, are the forces which maintain inter-vesicle equilibrium. Due to ionic nature of catanionics, the electrostatic forces play a dominant role in maintaining aggregate stability. The electrostatic repulsion generated by the charged forces stabilizes the vesicles against the attractive van der Waals forces. The balance of these two opposing forces is described by the DLVO theory (Derjaguin, Landau, Verwey and Overbeek),²¹³ which describes particle interaction as a function of separation in solution. The electrostatic repulsion arises from the arrangement of ions and counter-ions (electric double layer). The electric double layer consists of an adjacent layer of tightly bound counter ions (Stern layer) at the particle interface, with a more diffuse distribution of counter-ions (diffuse layer). The charge density is concentrated in the Stern layer due to strong electrostatic attraction while in the diffuse layer, the less loosely bound counter-ions are subject to a balance of the weaker electrostatic pull and

the Brownian motion. The nature of these forces, determine their motion under an applied electric field and are the basis for zeta potential measurements. Often the Poisson-Boltzmann (P-B) equation is used to calculate the electrostatic potential of the particle surface in this diffuse layer, which is directly related to the surface charge density. The prominent parameter used is the Debye screening length, which describes the length from the vesicle surface over which the electric field is effective. In effect, the shorter the Debye length, the more effectively the vesicle surface is screened by other colloids with subsequent coalescence/aggregation.

Apart from electrostatic repulsion, the vesicles are also stabilized by repulsive forces, hydration and undulation. The hydration, a short range force, is related to the energy required to remove bound water from the vesicle surface. The undulation forces, which are described within the context of Helfrich's model²¹⁴ are oscillatory forces due to forcefield of the undulating bilayers as given below:

$$F \approx \frac{(k_B * T)^2}{k * d^3} \quad \text{Equation (2.9)}$$

where k_B is the Boltzmann constant, k the bending modulus and d , the inter-bilayer distance or water separation.¹⁹² The undulating repulsive force is of entropic origin due to steric and excluded volume effects of interacting bilayers.

Electrostatic double layer forces dominate at low surfactant concentrations and minimal vesicle aggregation occurs, but the addition of salt lowers the interaction energy barrier of the colloidal system and induces aggregation by screening the charge of the vesicles. Brasher et al¹⁷⁷ utilized a thermodynamic cell model to examine the change in free energy of CTAB/SOS aggregates with addition of salt (Na^+Br^-). The model incorporated Poisson-Boltzmann equations to determine the electrostatic free energy contributions to the system's free energy minimization as a function of salt. With added salt, the SOS-rich vesicle phase was destabilized to a micellar phase, while the CTAB-rich vesicle phase tended towards the lamellar phase. Similar effects were detected for CTAT/SDBS vesicles, where the addition of 0.5 M NaCl was estimated to reduce the Debye length by 80% and accelerate aggregation of the vesicles.²¹⁵ In a study by Jiang et al,¹⁸⁹ the addition of a hydrophobic, bulky bile salt, sodium cholate, promoted the destabilization of DEAB (dodecyltriethylammonium)/SDS vesicles to micelles. This was

attributed to an increase in effective headgroup area, thus reducing the surfactant parameter.¹⁸⁹ In general, vesicle breakdown is readily achieved by addition of excess surfactant or third surfactant to promote destabilization to micellar or multiphase region of the phase diagram.²¹⁶

Charged polyelectrolytes also affect inter-vesicle interactions in a manner dependent on their charge, molecular structure and hydrophobicity. For example, Antunes and coworkers²¹⁷ captured complex phase behavior with the addition of two cationic hydroxyethyl cellulose derivatives (one hydrophilic and one hydrophobic) to negatively charged SDS/DDAB vesicles. Increasing amounts of the polyelectrolytes produced changes in the aggregate structures. A biphasic solution of precipitate was observed, which transformed into a macroscopic gel network with increased concentration. Polygonal faceted vesicles and disks-like bilayer fragments preceded complete system destabilization in the presence of the hydrophilic and more highly charged polyelectrolyte. In contrast, vesicle clusters were observed with the hydrophobic polyelectrolyte, suggesting the hydrophilic polymer had a more perturbative effect on membrane packing. The surface adsorption of the more highly charged polyion effectively reduces the surface charge density of the vesicles by charge neutralization, and reduces the bilayer flexibility. The more hydrophobic polyelectrolyte anchors in the bilayer and generates increased vesicle-vesicle interaction by changing vesicle charge and molecular packing in the bilayer.

Nonionic organic additives, such as toluene, have also been shown to induce changes in cationic vesicle morphology^{53,181} by reducing interfacial tension of the surfactant film. FFTEM revealed transformation of positively charged DTAB/SDBS SUVs as the ratio of toluene/surfactant concentration, γ , increased. The small unilamellar vesicles increased drastically in size, evolving to MLVs and planar lamellar structure with increase in γ from 0.4 to ≈ 4 . However, the addition of similar amounts of octane generated no changes in vesicle structure. This was attributed to the preferential solubilization site. Due to its lower surface activity, toluene is located at the interface where interactions of its aromatic ring reduce headgroup interactions and surface charge density. This reduces the surface curvature of the vesicle morphology. However, the

less surface active octane was located deeper in the bilayer, where it had less effect on headgroup interactions.

Temperature also affects phase stability¹⁷⁹ and vesicle aggregation.²¹⁸ In CTAB/SOS system, the isotropic vesicle phase domain expanded for a temperature increase from 20 – 40 °C, but contracted at 50 °C.¹⁷⁹ Interestingly, the equimolar precipitate formation region was sharply reduced. With the temperature increase, it was (transformed to a mixture of micelle and lamellar phase) most likely due to melting of the chains in the fluid phase. As often observed with cationic vesicles²¹⁸, DSC analysis of the CTAB/SOS revealed no phase transition, T_m , that is typically detected in lipid surfactant organizations. This phenomenon is ascribed to chain asymmetry (reduced packing density) and the looser membrane packing requisites of spontaneous curvature.

2.3.2 Applications of Cationic Vesicles

Vesicles are compartmentalized into domains which can be utilized for reaction processes; the inner and outer bilayer leaflets, the bilayer²¹⁹ and the aqueous core.¹⁶⁶ The success of intended applications is dependent on vesicle stability and solution conditions. Cationic vesicles have been explored for use as encapsulation agents⁴⁷, carriers of biological compounds,²²⁰ controlled nano-compartment reactors^{49,165,166} and templates for material synthesis.⁵⁰ The ability to tune the properties of cationic surfactant systems to the desired application provides extra degree of freedom that is advantageous in this respect. Danoff et al demonstrated by SEC, DLS, UV and SANS analysis much higher effective encapsulation in cationic vesicles (CTAT/SDBS) relative to those comprised of egg-PC lipid vesicles.^{47,164} The superior entrapment efficiency was due to the ionic adsorption of the oppositely charged solutes and bilayer surface. Similar observations have been reported for sodium undecanoate/decyltrimethylammonium bromide vesicles, where the trapping efficiency of the anionic bromophenol blue increased with the ratio of cationic surfactant.

Mckelvey et al²²¹ showed that hydrocarbon based cationic vesicles, CTAT/SDBS and CTAB/SOS were viable templates for polymer synthesis from styrene and divinyl benzene. The vesicle bilayer integrity was retained even with the polymeric shell network with thickness < 10 nm and the polymer hollow spheres were of similar

dimensions to the vesicles. The same group also demonstrated cationic vesicles as templates for the synthesis of silica spheres,⁵⁰ discussed in further detail in the subsequent section.

2.4 Templating of Silica Hollow Spheres

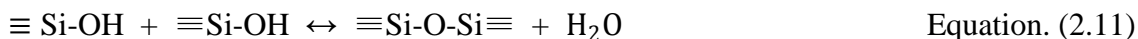
The extensive body of research in nano-sized materials stems from the broad possibilities of application in biomedical, cosmetic, catalytic and separation technologies. Silica or silicon dioxide (SiO_2) exists naturally in both crystalline and amorphous forms and is one of the most abundant natural materials. Available as sand, quartz, cristobalite, fujasite and coesite, the most distinguishing property is its hardness which makes it a fundamental component of glass and ceramics. It is also prevalent in household items, microelectronics, biomedical and industrial applications. The synthesis of nano-scaled silica materials is motivated by these and other potential uses. In particular, colloidal systems of silica materials (sol-gel chemistry) provide immense possibilities as drug delivery agents, controlled release devices²²² and controlled reaction environments.^{223,224}

The characteristics of the resulting silica material depend on variables which include choice of silica precursor, temperature, pH, organic solvents, additives (polymers, surfactants), stirring time and solution ionic strength.²²⁵ Silicon alkoxides such as the series: tetramethoxysilane (TMOS), tetraethoxysilane (TEOS) and tetra(n-propoxy) silane (TPOS) are often used as precursors in synthesis of silica. The alkoxides/alkoxysilanes ($\equiv\text{Si-OR}$) where R is the alkyl chain, $\text{C}_m\text{H}_{2m+1}$, are insoluble in water. Good mixing, and the presence of surfactants or solvents are required to achieve the necessary solubilization for the onset of hydrolysis (Eq. 2.10). The synthesis proceeds through hydrolysis, condensation and polymerization with the rate of each reaction determined primarily by the pH.

Hydrolysis



Water Condensation



Alcohol Condensation



Hydrolysis of the silicon alkoxides (Eq. 2.10) produces silanol (-Si-OH), which condenses to form the siloxane bonds (Si-O-Si) with release of water (Eq. 2.11) and alcohol (Eq. 2.12). A silica network is then produced by polymerization of the siloxane groups. The reactions are also influenced by steric effects of the alkoxide groups, water/precursor ratio, temperature, solvent polarity and the nature of the catalysts used. In both base and acid catalyzed reactions, the hydrolysis is faster with less bulky alkoxides (steric effect). For example, the rate of hydrolysis for TMOS ($\text{Si}(\text{OCH}_3)_4$) is greater than for TEOS ($\text{Si}(\text{OC}_2\text{H}_5)_4$). The rate of hydrolysis proceeds faster than condensation in acid catalyzed medium, while the rate of condensation is faster in basic medium. The stability of the polymerized silica particles is subject to DLVO forces; van der Waals and electric double layer forces, which are present in colloidal systems. Under highly acidic $\text{pH} < 1$, the silica network is positively charged and interacts preferably with negatively charged species, while silica is negatively charged in neutral and basic medium. At the isoelectric point ($\text{pH} 2$), the silica particles are unstable with the tendency to coagulate into a gel network.²²⁵

There are several approaches to the synthesis of hollow silica materials described in literature.²²⁶⁻²³⁰ In transcriptive templating, the synthesis of silica hollow spheres is fabricated by a mechanism where surface of the template serves as the reaction site. In this process, the organized silica matrix takes the form of the template morphology and assumes a nano-cast of the entrapped supramolecular aggregate. However, the success of this technique is dictated by the thermodynamic stability of the template.

Templates used include water in oil emulsions,²³¹ CO₂/water emulsions with ionic block polymers,²³² liposomes¹¹⁶ cationic vesicles,²²⁶ ion-pair amphiphiles²³³ and catanionic vesicles.⁵⁰ Song et al²³¹ utilized surfactant stabilized water/oil (kerosene) emulsion interfaces for the amine catalyzed silica synthesis with tetraethoxysilane (TEOS) as the precursor and positively charged CTAB acting as binder of negatively charged silicate species at the interface. Hollow spheres (\approx 50 - 150 nm) whose thickness increased with the length or hydrophobicity of the amine (triethylamine – dodecylamine) were produced in a controlled basic medium (pH 8-9). Within this pH range, the rate of condensation was higher than hydrolysis and depolymerization while at higher pH, the reverse case resulted in irregular shaped and solid silica particles.

The very few examples of vesicle templating are limited to mostly hydrocarbon-based vesicles. Meta-stable liposomes, such as those comprising DPPC, have been applied in fabrication of silica hollow spheres (\approx 100 nm).^{116,234} Begu et al's²³⁴ FTIR analysis suggested the zwitterionic DPPC headgroup interaction with the polymerized silica network, with the transcriptive synthesis (TEOS/acidic pH) promoted by quarternary ammonium surface of DPPC. The thin non-porous silica network (6-9 nm) was assessed with nitrogen adsorption and desorption. TEM analysis of the size and size distribution of the silica spheres was consistent with the original liposome template. The effect of the silica network on the trapped liposome template was tested by monitoring bilayer anisotropy with embedded DPH. DPH anisotropy measurements in the DPPC bilayer revealed wider phase transitions (reduced cooperativity) due to interaction of the outer bilayer leaflet with the transcribed silica network.¹¹⁶ Studies of kinetically stabilized vesicles, such as dioctadecyldimethylammonium bromide (DODAB) and didodecyldimethylammonium bromide (DDAB),²²⁶ suggest the importance of bilayer matrix organization in successful transcriptive template synthesis. Synthesis in basic medium (pH 8) with TEOS or TMOS resulted in silica hollow spheres in DODAB, while DDAB liposomes produced small solid particles. This effect was ascribed to the higher stability of DODAB vesicles ($T_m = 43$ °C) compared with DDAB ($T_m = 16$ °C). Cryo-TEM images revealed irregular shaped hollow spheres with DODAB, most probably caused by alcohol production during synthesis or pressure of the polymerized silica

network on vesicle morphology. Also, excess precursor resulted in the formation of small solid silica particles.

Yeh et al ²³⁵ produced meso-structured hollow silica (100-500 nm/TEM) from negatively charged SDS/CTAB vesicles from sodium silicate at neutral pH with neutral polyethylene, Pluronic P123 (EO₂₀PO₇₀EO₂₀). The P123 anchored on the bilayer/aqueous interface and served as a steric stabilizer of the vesicles. The P123 which was hydrogen bonded to the silica network, influenced the size of the silica pores. Kepczynski's and coworkers²³⁶ demonstrated that the bilayer of cationic vesicles (DTAB/SDBS) presents a contained environment for base catalyzed polymerization of silicone from 1,3,5,7-tetramethylcyclotetrasiloxane precursor (TMCS). Interfacial measurements suggested that TCMS monomers, situated close to the interface and solubilized in the bilayer, lowered the aggregate curvature. This was due to reduced surfactant headgroup interactions, which lowered the surface charge density. However, molar ratios of TCMS to surfactant greater than 0.5 resulted in destabilization of vesicles to planar lamellar structures or mixed micelles. Faceted hollow silica particles, which were replica of the ion-pair amphiphile template were prepared in mixtures of cetyltrimethylammonium hydroxide and myristic acid mixtures, (CTAOH/C₁₃COOH).²³³ Above a critical concentration of TEOS, the vesicular structure was disrupted due to production of ethanol.

Although fluorinated surfactant templating has been demonstrated by Rankin's group with formation of mesoporous silica with ordered pore structure,^{237,238} these do not represent vesicle templating as the silica was prepared by from micellar solutions of HFDePC. Hentze et al ⁵⁰ provide the sole example of cationic vesicle templating from a system containing a fluorinated surfactant (CTAB/SPFO). Synthesis in acidic medium (pH 3) to facilitate quick hydrolysis of TMOS produced silica of similar size to the CTAB/SPFO vesicles (60 – 100 nm), a hallmark of true transcriptive templating. SANS analysis verified the integrity of the vesicle morphology under the polymerized silica network. In the same study, synthesis with hydrocarbon-based cationic vesicles, CTAT/SDBS, resulted in bilayer destabilization, which was ascribed to the presence of methanol produced during TMOS hydrolysis. This suggests reduced stability of the fully hydrocarbon-based vesicles compared with the mixed hydrocarbon/fluorocarbon system

CTAB/SPFO. In essence, modulation of the cationic vesicle bilayers with fluorinated chains influenced their stability as stable templates and suggests the tunable properties of these systems.

CHAPTER 3

PARTITIONING OF HYDROCARBON AND FLUORINATED NICOTINIC ACID ESTERS (NICOTINATES)

This Chapter is based on work submitted to *Journal of Fluorine Chemistry* for Publication

3.1 Summary

The fluorophilicity of a series of hydrocarbon and fluorocarbon-functionalized nicotinic acid esters (nicotines) is measured from their partitioning behavior ($\log K_p$) in the biphasic solvent system of perfluoro(methylcyclohexane) (PFMCH)/toluene. Also measured are the partitioning between a fluorocarbon/aqueous system; perfluorooctyl bromide (PFOB)/water. The chain length of the hydrocarbon or fluorocarbon alkyl group of the ester ranges from one to twelve carbon atoms. Knowledge of the fluorophilicity of these solutes is relevant to the design of these prodrugs for fluorocarbon-based drug delivery. The experimental PFMCH/toluene $\log K_p$ values range from -1.72 to -3.40 for the perhydrocarbon nicotines and -1.64 to 0.13 for the fluorinated nicotines, where only the prodrug with the longest fluorinated chain (2,2,3,3,4,4,5,5,6,6,7,7,8,8,8-pentadecafluorooctyl nicotinic acid ester) partitions preferentially into the fluorinated phase ($\log K_p = 0.13$). Predictions of the PFMCH/Toluene partition coefficients using solubility parameters calculated from group contribution techniques or molecular dynamics simulation are in reasonable agreement for the perhydrocarbon nicotines and short chained perfluorinated nicotines ($\approx 0.3\%$ -38% deviation). Significant deviations from experimental PFMCH/Toluene partition coefficients (greater than 100%) are observed for the longest chain perfluoroalkyl nicotines.

Only the short chained perhydrocarbon nicotines, C1F0 ($\log K_p = -0.78$) and C2F0 ($\log K_p = -0.16$) display affinity for the aqueous phase in the PFOB/water partition measurements. All perfluorinated nicotines exhibit preference for the PFOB phase relative to water ($\log K_p = 0.48 - 0.75$). The surface activity of the longer chained

nicotines, which demonstrate poor affinity for the aqueous phase, limits analysis of the PFOB/water partition coefficients.

3.2 Introduction

Fluorocarbons have demonstrated potential for a variety of novel pharmaceutical applications, including liquid ventilation therapy, diagnostic ultrasound imaging and as blood contrast agents.^{57,160,239-242} The potential to extend fluorinated solvent applications to drug delivery is limited by the poor solubility of typical hydrocarbon-based polar and non-polar pharmaceuticals in these solvents.^{243,244} The use of a prodrug, in which cleavable functional groups facilitate solubility of the drug in the fluorocarbon solvent (perfluorooctyl bromide; PFOB), is a viable approach for the delivery of pharmaceuticals.^{35,241} The putative prodrug or functionalized drug molecule is clinically inactive and conversion to the parent drug compound, typically through enzymatic cleavage, is necessary to induce the desired pharmacological effects.²⁴¹ Also, the nicotinic acid esters or prodrugs possess surface activity. The fluorocarbon solvent system must provide sufficient solubility of the prodrug, while promoting its subsequent extraction from solution and delivery to the tissues. In addition, the prodrug/fluorocarbon solvent systems are selected to minimize the biological toxicity and maximize the prodrug efficacy. Knowledge of partition coefficients provides a thermodynamic interpretation of drug delivery and cytotoxicity. Limited studies address the partitioning behavior of homologous series of fluorinated solutes and provide direct comparisons to their hydrocarbon analogues. The ability to predict partitioning behavior has the potential to improve drug design for delivery by fluorinated solvents.

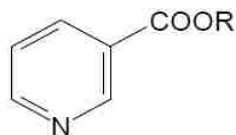
This work examines the partitioning behavior in perfluoro(methylcyclohexane (PFMCH)/toluene and the PFOB/water of a series of hydrocarbon and fluorocarbon-functionalized nicotinic acid esters (Figure 3.1). These nicotines are classified according to the alkyl chain of the ester as perhydrocarbon (C1F0 – C12F0); perfluorinated, each linked by one methylene chain to the carboxyl group (C2F3 – C8F15); and partially fluorinated, with either a terminal ω -hydrogen atom (C3F4 and C5F8) or two methylene group (C8F13) linkages in the fluorinated chain of the ester. Nicotinic acid, the parent drug compound of the nicotinic acid esters (nicotines), has

clinical benefit in the treatment of cancer. Furthermore, it is a precursor of cofactors, nicotinamide adenine dinucleotide (NAD) and NADP, that could alleviate injury to lungs caused by poisons and natural toxic compounds.^{85,241} The PFMCH-toluene partition coefficient ($\log K_p$) is an established measure of fluorophilicity^{56,97-99,245} and is calculated from the concentration ratio of prodrug in fluorocarbon phase (PFMC) to hydrocarbon phase (toluene). The PFOB-water partition coefficients are relevant to the description of PFOB-mediated prodrug delivery. Similar to the octanol/water partition coefficient for the measurement of lipophilicity and the interpretation of drug pharmacokinetics,^{90,246} fluorocarbon/hydrocarbon and fluorocarbon/water partition coefficients have the potential to be a predictive tool to describe the ability to deliver drugs from a fluorinated solvent to target cell tissues. This study compares the experimental partition values of prodrugs in PFMCH-toluene with liquid-liquid partitioning predicted from regular solution theory (RST). Two methods of solubility parameter estimations are compared: Fedors Group Contribution^{93,101} and molecular dynamic simulations using (Materials Studio (Accelrys Inc. (California), Version 4.0). Predictive methods provide a screening tool to assess the effect of functional group chain length and structure on partitioning behavior, allowing the design of prodrug candidates for fluorocarbon drug delivery.

3.3 Experimental Section

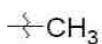
3.3.1 Materials

Perfluorooctyl bromide (PFOB; $C_8F_{17}Br \geq 98\%$) and perfluoro(methylcyclohexane) (PFMCH; $C_7F_{14} \geq 95\%$) was purchased from Sigma Aldrich. Toluene (of $\approx 100\%$ purity) was purchased from Mallinckrodt Baker Inc. (Paris, Kentucky). Synthesis of the nicotinate acid ester prodrugs (nicotines) was described previously^{241,247} and involves the addition of anhydrous dicyclohexylcarbodiimide (DCC) and dimethylaminopyridine (DMAP) to a mixture of nicotinic acid and the corresponding alcohol in anhydrous dichloromethane. The nicotinic acid esters or nicotinate prodrugs were synthesized with greater than 98% purity as determined by gas chromatography/mass spectrometry (GC/MS) analysis.

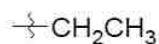


(Fluoro-)alkyl nicotinate

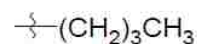
A. Perhydrocarbon Nicotinates



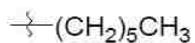
C1F0
(Methyl nicotinate)



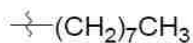
C2F0
(Ethyl nicotinate)



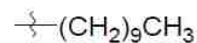
C4F0
(Butyl nicotinate)



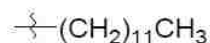
C6F0
(Hexyl nicotinate)



C8F0
(Octyl nicotinate)

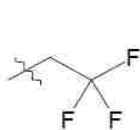


C10F0
(Decyl nicotinate)

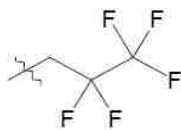


C12F0
(Dodecyl nicotinate)

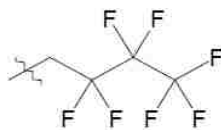
B. Fully fluorinated carbon chain length – 1H, 1H-Perfluoroalkyl nicotinates



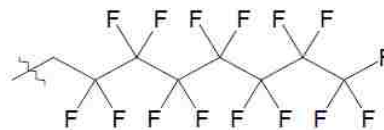
C2F3
(2,2,2-trifluoroethyl nicotinate)



C3F5
(2,2,3,3,3-pentafluoropropyl nicotinate)

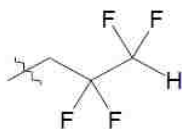


C4F7
(2,2,3,3,4,4,4-heptafluorobutyl nicotinate)

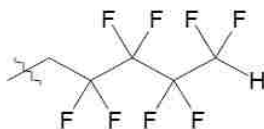


C8F15
(2,2,3,3,4,4,5,5,6,6,7,7,8,8,8-pentadecafluorooctyl nicotinate)

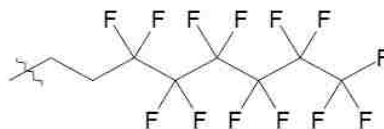
C. Partial fluorinated carbon chain length – 1H,1H, nH-Perfluoroalkyl nicotinates (n = 3 or 5)



C3F4
(2,2,3,3-tetrafluoropropyl nicotinate)

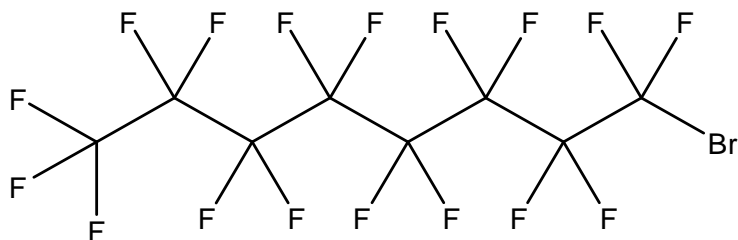


C5F8
(2,2,3,3,4,4,5,5-octafluoropentyl nicotinate)

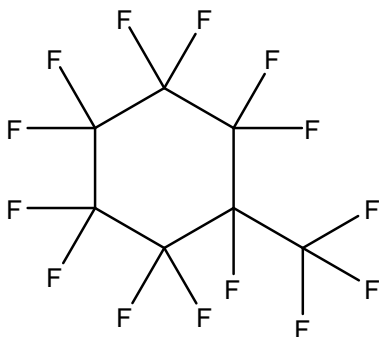


C8F13
(3,3,4,4,5,5,6,6,7,7,8,8,8-tridecafluorooctyl nicotinate)

Figure 3.1. Chemical Structures of Nicotinic Acid Esters (Nicotinates)



Perfluorooctyl bromide (PFOB)



Perfluoro(methylcyclohexane) (PFMCH)

Figure 3.2. Chemical structures of PFOB and PFMCH

3.3.2 Apparatus and Procedure

The partition coefficients for the nicotine prodrugs in perfluoro(methylcyclohexane)-toluene system were determined from the depletion of the prodrug in the fluorocarbon phase into a known volume of toluene (as measured by FID gas chromatography (Varian CP-3800 FID)). The nicotinic acid esters were initially dissolved in 3 ml or 5.5 ml volumes of fluorinated solvent (PFMCH), resulting in a known prodrug concentration in the range of 1 mM to 4 mM. Volume ratios of 1:1 and 5:1 in PFMCH-toluene systems were used to achieve measurable equilibrium concentration differences in the fluorocarbon phase after contacting with the hydrocarbon phase. For the PFOB/water system, the prodrugs were initially dissolved in PFOB in volume ratios that ranged from 1:1 to 1:30. The stir flask method⁹⁰ was employed, where only the denser fluorocarbon phase was gently stirred to facilitate equilibration, with a goal of avoiding emulsion formation. All experiments were performed at 25 °C. More than one

hour was allowed for equilibration before the fluorocarbon phase samples were drawn with a Hamilton syringe into vials lined with PTFE septums.

Duplicate initial and equilibrium samples (0.5 ml) of the fluorocarbon phase were injected onto a 15 m capillary column of 95% dimethylpolysiloxane stationary phase (Varian fused silica column/CP-SIL8 CB) with internal diameter of 0.25 mm. A high purity helium flow of 2 ml/min and FID temperature of 300°C were employed in the analysis. All the samples were spiked with 5 µl of custom internal standard (naphthalene-d8) in methylene chloride. The equilibrium nicotine concentration in the fluorocarbon phase was determined from a calibration curve while the organic phase concentration was quantified by material balance. The partition coefficients, $\log K_p$ were then calculated as given in Eqs. (3.1) and (3.2).^{56,97-99,245}

$$\log K_p = \left[\frac{\text{Concentration in PFMC (mM)}}{\text{Concentration in toluene (mM)}} \right] \quad \text{Equation (3.1)}$$

$$\log K_p = \left[\frac{\text{Concentration in PFOB (mM)}}{\text{Concentration in water (mM)}} \right] \quad \text{Equation (3.2)}$$

3.3.3 Prediction of Prodrug Partitioning in Liquid-Liquid Systems

The following expression describes the activity coefficient of the prodrug solute in solution using regular solution theory (RST):^{98,248}

$$RT \ln \gamma_i^j = V_i \left(\delta_i - \delta_j \right)^2 \quad \text{Equation (3.3)}$$

where γ_i is the activity coefficient of the solute i in solvent j (PFMC-rich phase (a) or toluene-rich phase (b)), δ is the Hildebrand solubility parameter, V_i is the molar volume of the solute, and T is the PFMCH-toluene biphasic system temperature, maintained at 298 K. Equating the activity of the solute in each phase and applying the RST expression for the activity coefficient of the solute results in the following expression:

$$\log K_P = \log \left(\frac{\gamma_i^b}{\gamma_i^a} \right) = \frac{\exp \left(\frac{V_i (\delta_i - \delta_b)^2}{RT} \right)}{\exp \left(\frac{V_i (\delta_i - \delta_a)^2}{RT} \right)} = \log \left(\exp \left(\left(-\frac{V_i}{RT} \right) (\delta_a - \delta_b) (\delta_a + \delta_b - 2\delta_i) \right) \right) + \log \left(\frac{V_b}{V_a} \right) \quad \text{Eq. (3.4)}$$

$$\delta = \sqrt{\frac{\Delta U_{\text{vap}}}{V_m}} = \sqrt{\frac{\Delta H_{\text{vap}} - RT}{V_m}} \quad \text{Equation (3.5)}$$

where ΔU_{vap} and ΔH_{vap} are the energy and enthalpy of vaporization of the solvent to a gas of zero pressure, V_m is the molar volume, R the molar gas constant and T , the temperature.

The solubility parameter (δ) or cohesive energy density (c , where $\delta = c^{1/2}$) defines the cohesive forces between solute and solvent molecules in solution (e.g., fluorine solute molecules in either PFMCH or toluene).⁹³ In the partitioning of solutes between two immiscible liquid phases, preference will be given to the phase with comparable cohesive forces to the solute. For systems of regular solutions, maximum solubility is achieved when the solute and solvent solubility parameters are similar.

Regular solution theory strictly applies to molecules that interact via only dispersion forces.^{93,248} However, the application of RST has been extended to numerous systems, such as partially fluorinated organic compounds.⁹⁸ In the case of the solvents in this investigation (PFMCH (β) and toluene (α)), the molecules are nonpolar with no hydrogen bonding capacity, fulfilling some of the criteria of regular solution theory.

3.4 Computational

3.4.1 Group Contribution Methods for the Estimation of the Nicotinate Solubility Parameters

Group contribution methods have been successfully applied to the partitioning of a broad range of fluorinated organic compounds including those which bear structural similarities with the nicotinic acid esters.^{98,99} The Hildebrand solubility parameter and molar volume of the solutes were estimated by Fedors group incremental method.⁹³ The Hildebrand solubility parameters were calculated by summing the contributions of distinct molecular units to the molar vaporization energies and molar volumes (Eq. 3.5).⁹³

3.4.2 Molecular Dynamics Simulations for the Estimation of the Nicotinate Solubility Parameters

The solubility parameters of the nicotinic acid esters were predicted using molecular dynamics simulations (Materials Studio (Accelrys Inc. (California), Version 4.0). Representative 3D models of the solutes were constructed in the Amorphous Cell module using the software's standard protocol. Cubic unit cells (21 – 30 Å) of the pure nicotinate were built in the amorphous state, under periodic boundary conditions.²⁴⁹ The densities of the nicotinate were calculated by dividing the molecular weight by the molar volume, with the latter estimated from the Group Contribution method discussed in the previous section. Before performing the molecular dynamics simulations to calculate the Hildebrand solubility parameters or cohesive energy density, δ , the cells were subjected to energy minimizations or geometry optimization steps to reduce the structural conformation from the initial high energy state to a state more representative of experimental conditions. The Smart Minimizer, which combines the three iterative procedures, Steepest descent, Conjugate gradient and Newton methods, with a medium convergence level (0.1 kcal/mol/ Å) was applied. The Steepest descent method is most applicable to systems high above thermodynamic equilibrium, that is structures far from their optimum potential energy surface and the conjugate gradient procedure for those close to equilibrium.^{250,251} The Smart Minimizer selects the appropriate energy minimization method depending on the initial configuration of the structure drawn in the amorphous cell.

Molecular dynamics simulations were performed on the Discover program using the COMPASS force field. COMPASS (condensed-phase optimized molecular potentials for atomistic simulation studies) is an ab initio forcefield.^{252,253} COMPASS is a class II forcefield, which has been demonstrated to make accurate predictions of thermodynamic properties such as cohesive energy density.²⁵⁴ The force fields for the potential energy calculations are automatically assigned by the COMPASS program to the atoms prior to the energy calculations. In COMPASS, the total energy of the system is described as the sum of bonding/valence interactions and non-bonding terms (VdW and coulombic).

$$E_{\text{total}} = E_{\text{valence}} + E_{\text{non-bond}} \quad \text{Equation (3.6)}$$

The valence or bonding terms accounted for bond bending, bond angle bending, dihedral angle torsion, inversion out of plane interactions and a Urey-Bradley (UB) term used to account for interactions between atom pairs involved in 1-3 configurations. In COMPASS, the van der Waals interactions or dispersive forces are modeled by a Lennard-Jones potential using an atom based cutoff (8-10 Å), which reflects the short-range nature of these interactions. The Ewald summation method was used to evaluate the long-range electrostatic interactions.^{249,251} The van der Waals off-diagonal parameters were calculated using geometric mean rule in the Ewald method.

Equations of motion for this NVT (number of molecules, volume and temperature) ensemble were calculated using the Velocity Verlet numerical algorithm to determine the interaction energy of the pure nicotinate molecules in the amorphous cell. The simulations were allowed sufficient number of integration steps with a 1.0 femtosecond timestep to reach equilibrium or the minimum potential energy surface. Direct velocity scaling was used to control the temperature and bring the system to equilibrium at 298 K. Full trajectory files from the molecular dynamics simulations, with information on energy, pressure, velocities and coordinates, were stored in dynamic frames and used by the Dynamics program to compute the cohesive energy density. The cohesive energy densities and solubility parameters were calculated from an ensemble average of the trajectory frames and standard deviation values deduced from the frames. Standard deviation values reported for the molecular dynamics values in Table 3.1 correspond to the solubility parameters estimated in the final frames (50 – 100) of the simulation. Studies have demonstrated the ability of class II forcefields such as COMPASS to predict cohesive energy densities that compare favorably with experimental values.²⁵⁴ The COMPASS program assigns the appropriate force field parameters based on the structure and type of atoms present. Of particular concern was the parameterization of the force fields for fluorinated groups. Our procedure was validated by using this simulation procedure to estimate the solubility parameter of our fluorinated solvent, perfluoromethylcyclohexane, which has a reported solubility parameter value of $\delta = 12.5 \text{ (J/cm}^3\text{)}^{1/2}$.⁹³ The solubility parameter estimate from this dynamics simulation approach is 12.51 ± 0.13 .

3.5 Results and discussion

3.5.1 Partitioning behavior of nicotinate prodrugs (PFMCH/Toluene)

The perhydrocarbon nicotinate demonstrated two orders of magnitude increase in fluorophilicity with increasing chain length of the functional group (from 1 carbon atom (C1F0) to 10 carbon atoms (C10F0)) (Figure 3.3). The increasingly negative $\log K_p$ values (from -1.72 for the C1F0 to -3.40 for C10F0) reflect the increasing preference for the hydrocarbon phase.

The partitioning behavior of the fluorinated nicotinate, categorized as fully fluorinated and partially fluorinated (Figure 3.1), also spans three orders of magnitude (Figures 3.4 and 3.5), although the carbon chain length of the fluorinated nicotinate (two to eight carbon atoms) varies less than the perhydrocarbon nicotinate (one to twelve carbon atoms) investigated. This demonstrates the significant effect of substituting fluorine for hydrogen atoms on a compound's chemical properties. For the fully fluorinated nicotinate, increasing the carbon chain length by four atoms (C4F7 to C8F15) results in a pronounced increase in fluorophilicity. The nicotinate with the longest fluorinated tail length is slightly fluorophilic, as indicated by its positive $\log K_p$ value ($\log K_p = 0.13$ for C8F15). These trends follow the empirical rules suggested by Kiss et al.,⁹⁸ where greater than 60 wt% fluorine content is needed to impart "fluorophilic" behavior to a molecule. In our investigation, C8F15 is the only molecule which approaches this criterion (57 wt% fluorine).

Similarly, the partitioning of the partially fluorinated molecules (C3F4 to C8F13) into the fluorinated phase increases with length of the fluorinated chain. However, all the partially fluorinated nicotinate have negative partition coefficients. The one order magnitude difference in partition coefficients between the fully fluorinated C8F15 and the partially fluorinated C8F13 (which differ by a single CH₂ linkage replacing a CF₂ group) highlights the drastic effect of fluorine substitution on the physicochemical properties of the nicotinate. The distribution and position of fluorine atoms in the molecule, as well as the amount of fluorination, are known to affect the fluorophilic behavior of perfluorinated compounds.⁹⁸ The demonstrated effect of a terminal H-atom in the fluorinated chain on the physicochemical properties of fluorinated compounds^{77,105} is apparent in the different partition values for the fully fluorinated nicotinate, C3F5, and its

partially fluorinated analogue, C3F4, which have $\log K_p$ values of -1.50 and -1.62, respectively. The presence of the terminal H-atom in perfluorinated compounds introduces a large permanent dipole in the carbon chain, significantly increasing the hydrophilicity of the solute. In surfactant systems, this effect is observed as an increased critical micelle concentration (CMC). The CMC of both ionic¹⁰⁵ and non-ionic⁷⁷ perfluorinated surfactants with terminal hydrogen atoms have been reported to be 300% greater than the fully fluorinated analogues.

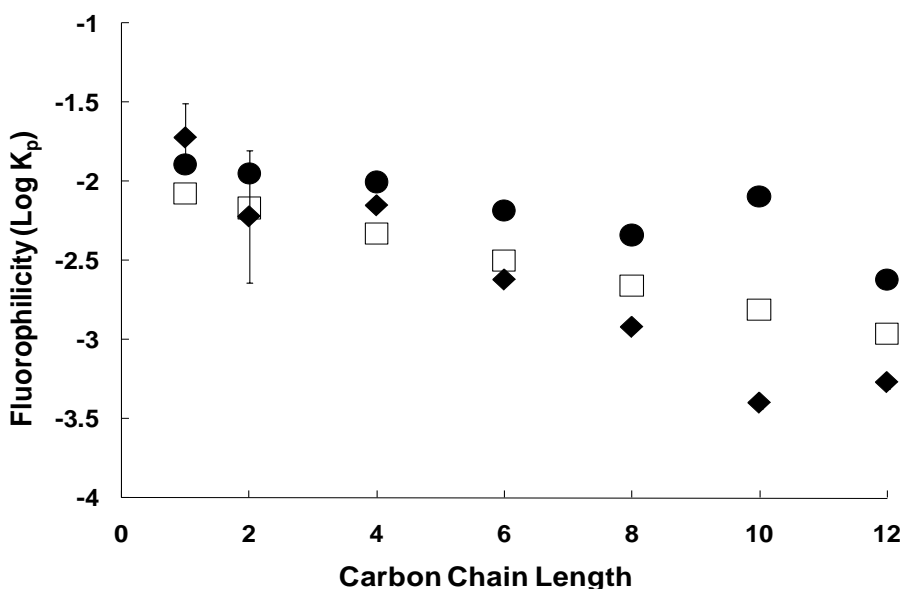


Figure 3.3. Partition coefficients for perhydrocarbon nicotines in PFMCH-Toluene as determined experimentally (◆) or from the application of regular solution theory based on solubility parameters estimated by group contribution (□) or molecular dynamics simulation (●). The experimental values are an average of two runs.

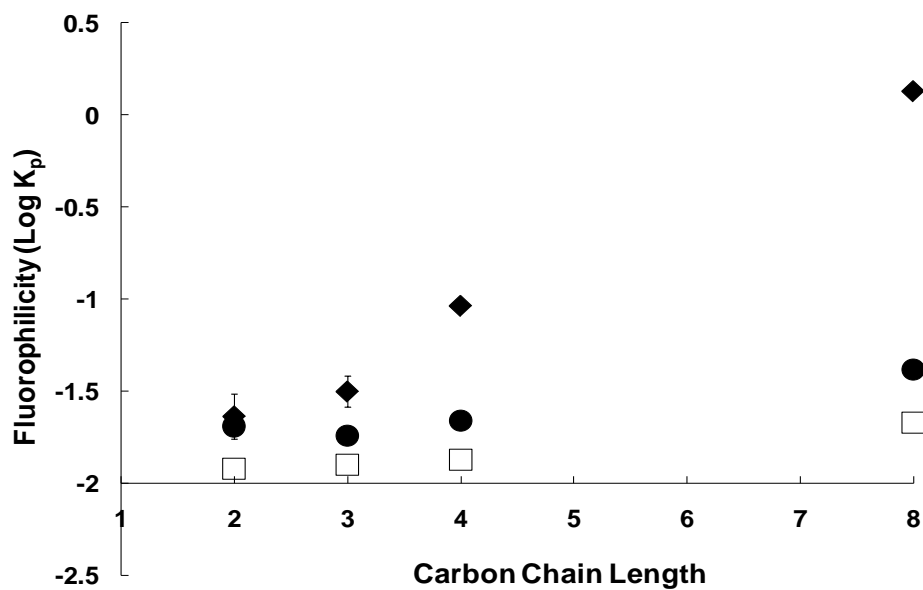


Figure 3.4. Partition coefficients for fully fluorinated functional chain length nicotines in PFMCH-Toluene as determined experimentally (◆) or from the application of regular solution theory based on solubility parameters estimated by group contribution (□) or molecular dynamics simulation (●). The experimental values are an average of two runs.

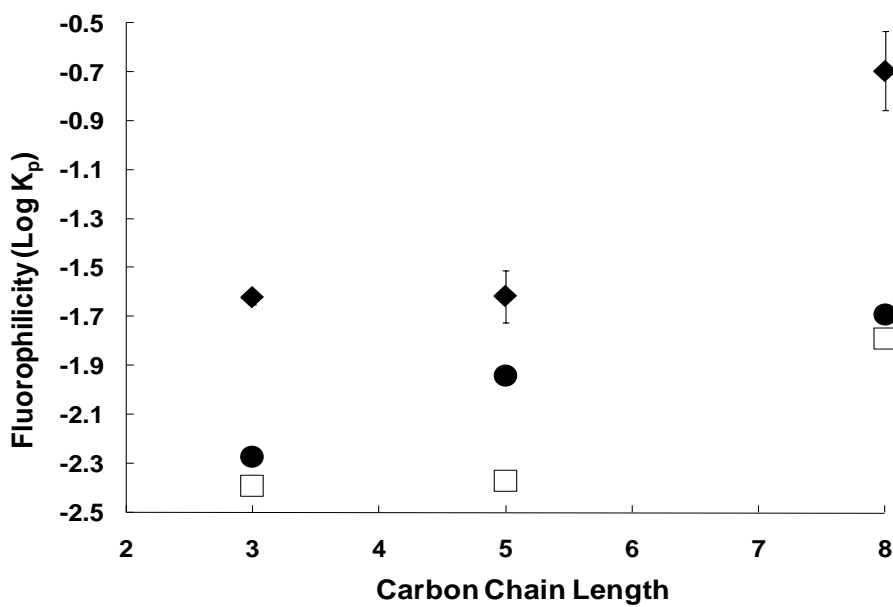


Figure 3.5. Partition coefficients for partial fluorinated functional chain length nicotines in PFMCH-Toluene as determined experimentally (◆) or from the application of regular solution theory based on solubility parameters estimated by group contribution (□) or molecular dynamics simulation (●). The experimental values are an average of two runs.

3.5.2 Prediction of Nicotinate Fluorophilicity from Molecular Structure

Predictive models of relative solubilities in biphasic solvents utilize solubility parameters, molar volumes, molecular surface area, van der Waals volume, molar refraction, solvent extended surface and solvatochromic parameters (β , α , π^*).^{97,99,100,246,255} Although recent studies have demonstrated successful correlation of molecular surface area with partitioning behavior of fluorinated molecules,^{97,245} the solubility parameter remains one of the most widely accepted parameters for predicting or interpreting physicochemical properties such as partitioning.^{98,99} We calculated the solubility parameter of the functionalized nicotines from their molecular structure using Fedors structural group contribution method⁹³ and Accelrys computational molecular dynamics (Table 3.1). The estimated solubility parameters decrease with chain length in each group of nicotines (perhydrocarbon, fluorinated, and partially fluorinated). Solubility parameter estimates by group contribution methods and molecular dynamics simulations (Table 3.1) differ by less than 10%. The solubility parameters calculated by

simulation are consistently lower than those estimated by the group contribution method. For equal carbon chain length, the solubility parameter of the perhydrocarbon compounds is greater than the corresponding fluorinated compounds, an expected trend. Substituting a hydrogen atom on the terminal carbon of a fluorinated chain results in an increase in the solubility parameter (C3F5 vs. C3F4).

The partition values ($\log K_p$) predicted using the estimated solubility parameters (Eqs. 3.4 and 3.5) are compared with the experimental values in Figures (3.3)-(3.5). Published values of solubility parameter were used for the organic solvents: toluene ($\delta = 18.2 \text{ (J/cm}^3)^{1/2}$) and perfluoromethylcyclohexane ($\delta = 12.5 \text{ (J/cm}^3)^{1/2}$).⁹³

The group contribution estimates of partition coefficients for the perhydrocarbon nicotines are closer to experimental values than the predictive estimates from simulation (Figure 3.3). Both predictive methods for the solubility parameter of the longer chain perhydrocarbon nicotines (C6 and greater) result in partition coefficient estimates which overestimate the preference of the nicotine for the fluorocarbon phase (i.e., higher $\log K_p$). Excluding the simulated estimate for C10F0 (38% difference), all the predicted values in this group of nicotines are in reasonable agreement with experimentally determined $\log K_p$ (i.e. < 20%).

Conversely, the predicted values for the fully fluorinated nicotine prodrugs are lower than the experimental values (Figure 3.4), suggesting that the predictive tools underestimated the fluorophilicity of the compounds. The molecular dynamics estimates of partitioning behavior for the fluorinated nicotines are closer to the experimental values than the estimates determined by group contribution methods. The predictive tools capture the experimental partition coefficients less accurately for fully fluorinated nicotines than for perhydrocarbon nicotines. For the fully fluorinated nicotines, only the shortest chain functional groups (C2F3 and C3F5), have predicted values that are in reasonable agreement with experiment (< 30% difference).

Partially fluorinated nicotines demonstrate similar partitioning trend to the fully fluorinated nicotines. The predicted partition coefficients of partially fluorinated nicotines (Figure 3.4) deviate considerably from experiment (> 20%), although the partition values predicted by the simulation method are slightly more accurate than the group contribution method. Also, the predictive methods do not accurately capture the

effect of a terminal hydrogen atom (C3F4 and C5F8), underestimating the fluorophilicity of the molecules. Partitioning is primarily governed by the balance between the energy required to create a cavity for the solute in the solvent and the intermolecular interactions.²⁵⁵ However other factors such as the change in shape, symmetry and moment of the molecule due to the exact position of the hydrogen in the molecule and the effects on partitioning⁹⁸ are excluded from partition estimates based on the group contribution estimation method.

The greatest differences between experimental and predicted partition coefficients are observed with the longest chained nicotines (C8F15 and C8F13), where the fluorophilicity is underestimated. Both predictive methods show several orders magnitude deviation (group contribution and model simulation values are $\log K_p$'s = -1.67, -1.38 for C8F15 and -1.79 and -1.69 for C8F13) from the experimental values for C8F15 ($\log K_p = 0.13$) and C8F13 ($\log K_p = -0.7$). Applying regular solution theory to large chain nicotines requires a significant extrapolation of RST assumptions, namely the dispersion of solute molecules in similarly sized solvents with ideal entropy as a result of random mixing.²⁴⁸ While the predictive techniques provide a reasonable estimate of partitioning behavior for the long chain perhydrocarbon nicotines, they fail to capture the fluorophilic contribution of long fluorinated carbon chains. This is attributable to several factors associated with the application of Regular Solution Theory in this work. The additive nature of the group contribution method results in propagation of error in the final estimate of the solubility parameter, which influences the predicted partition values. The Fedors^{93,101} group incremental values utilized in this work, which provides an estimate of molar vaporization energies and molar volumes (Equation 3.5) for structurally diverse molecular sub-units utilized allows for calculation of solubility parameter values of a wide variety of molecular compounds. However, the errors associated with this approximation results in cumulative error in the partition coefficient predictions.

Fluorophilicity was predicted to within 30% of the experimental $\log K_p$ for structurally similar compounds (i.e. eight fluorinated chains attached to pyridine headgroups) within Huque et al.'s¹⁰³ correlation of 90 organic compounds (both fluorinated and non-fluorinated) based on linear free energy relationships. Similarly,

Kiss et al.'s⁹⁸ demonstrated the applicability of a neural network model to correlate and predict fluorophilicities using 59 fluorinated compounds. However, these techniques also employed the physicochemical properties of the compounds of interest in the statistical parameterization of their models. Similar to our results, De Wolf and coworkers⁹⁹ report experimental and predicted differences in partitioning that range from 0% to >50% for over 50 fluorinated organic molecules based on Mobile Order and Disorder theory, which utilizes modified solubility parameters calculated by group contribution methods.

3.5.3 PFOB/Water partition coefficients of nicotines

The partition coefficients reported in Table 3.2, increase (two orders of magnitude) in the partition value with carbon chain length of the perfluorocarbon nicotines (C1 – C6). Only the short chained perhydrocarbon nicotines (CF₀; Log K_p = -0.78) and (C₂F₀; Log K_p = -0.16) demonstrated preference for the aqueous phase. Partition measurements for the longer chained perhydrocarbon and perfluorinated nicotines proved challenging and the limit in Table 3.2 (> 2.2) represents the limit of detection of the GC-FID analysis due to their surface activity and poor solubility in the aqueous phase. The values reported suggest the overall fluorine content and the length of the carbon chain has a strong effect on the partitioning behavior from PFOB to the aqueous phase. Partitioning of higher chained perfluorinated nicotines (> C₃F₅) into the aqueous phase is limited by their poor solubilization in water. Another factor to consider would be the self-association of the perhydrocarbon nicotines (methyl nicotine) in aqueous systems.²⁵⁶ The dimerization and higher order aggregates of nicotinic acid and esters in water is a general feature of pyridine groups whose aromatic nature provides for the vertical stacking in solution.²⁵⁶ However, the hydrophobicity of the higher chained nicotines might counteract the solubility facilitated by the self-association of the aromatic groups.

Application of RST produced significant deviations from experimental values for all the nicotines, indicating the limitations of RST in predicting partitioning in aqueous systems. The accuracy of our predictive models is limited by the estimation of the solubility parameter as well as the application of the regular solution theory (Eq. 3.4). The derivation of regular solution theory assumes small solute molecules dispersed

among like size solvents. Regular solution theory does not take into account the amphiphilic nature of the molecules involved or their tendency to accumulate at the surface or their self aggregation properties. Regular solution theory describes the dispersive van der Waals interactions in solute solvent systems and does not take into account the strong hydrogen bonding effects of water molecules. Water, with its high polarity, presents an extreme with solubility parameter ($\delta = 48 \text{ (J/cm}^3)^{1/2}$).⁹³ With the strong cohesive forces, the addition of nonpolar solutes such as the nicotines, causes a decrease in entropy of the self associated molecules. This results in the hydrophobic effect or rejection of the solute molecule. For this reason, the PFOB-water partition coefficients were poorly predicted from the solubility parameter of the solutes (results not shown).

3.6 Conclusion

Regular solution theory using the Hildebrand solubility parameter, determined by Fedors group contribution method and molecular dynamics simulations was applied to estimate the fluorinated/organic partition coefficient of a series of functionalized nicotinic acid esters/nicotines. This approach worked reasonably well with the series of perhydrocarbon nicotines and the shorter chained perfluorinated nicotines (C2F3 and C3F5). Significant deviation from experimental values with the higher chained perfluorinated nicotines, for which the fluorophilicity is underestimated. Knowledge of PFMCH/Toluene partition values, estimated by these predictive tools, would help in design of optimal experimental conditions for measurements and can act as the criterion for selecting drugs for synthesis and further study

The experimental PFOB-water partition coefficients increased with chain length in each group of nicotines measured. Only the shortest chained perhydrocarbon nicotines (CH3 and C2H5) demonstrated slight affinity for the aqueous phase. Due to their surface activity, measurements of the PFOB-water partition values proved challenging for the higher chained nicotines. The predictive ability of the methods failed in the case of PFOB-water partitioning because regular solution theory does not incorporate the effects of hydrogen bonding in water.

Table 3.1. Hildebrand solubility parameters of nicotinate acid ester prodrugs

Nicotinate	Molar Volume (by Group Contribution) (cm ³ /mol)	δ (by Group Contribution) ⁹³ (J/cm ³) ^{1/2}	δ (by Simulation) (J/cm ³) ^{1/2}
Perhydrocarbon nicotinate			
C1F0	114.4	23.28	22.47 ± 0.33
C2F0	130.5	22.65	21.82 ± 0.10
C4F0	162.7	21.73	20.70 ± 0.10
C6F0	194.9	21.09	20.28 ± 0.06
C8F0	227.1	20.62	19.93 ± 0.05
C10F0	259.3	20.26	18.88 ± 0.10
C12F0	291.5	19.98	19.40 ± 0.08
Perfluoroalkyl nicotinate			
C2F3	154.5	20.75	19.97 ± 0.08
C3F5	177.5	19.97	19.51 ± 0.10
C4F7	200.5	19.35	18.82 ± 0.08
C8F15	292.5	17.75	17.26 ± 0.09
Perfluoroalkyl nicotinate			
C3F4	142	22.84	22.43 ± 0.13
C5F8	188	20.96	19.82 ± 0.18
C8F13	285.6	18.03	17.85 ± 0.09

Table 3.2. PFOB/Water Partition Coefficients of nicotine acid ester prodrugs

Nicotine	PFOB/Water Volume Ratio	Log K _p
Perhydrocarbon Nicotinates		
C1F0	1:1	-0.78 ± 0.04
C2F0	1:1	-0.16 ± 0.03
C4F0	1:10	0.96
C6F0	1:5	1.24 ± 0.18
1H, 1H-Perfluoroalkyl Nicotinates		
C2F3	1:10	0.48 ± 0.02
C3F5	1:10	0.78 ± 0.1
C4F7	1:10	> 2.2
C8F15	-	> 2.2
1H, 1H-nH-Perfluoroalkyl Nicotinates (n = 3 or 5)		
C3F4	1:10	0.55 ± 0.01
C5F8	-	> 2.2
1H, 1H,2H, 2H-Perfluoroalkyl Nicotinates		
C8F13	-	> 2.2

CHAPTER 4

PARTITIONING OF HOMOLOGOUS NICOTINIC ACID ESTER PRODRUGS (NICOTINATES) INTO DIPALMITOYLPHOSPHATIDYLCHOLINE (DPPC) MEMBRANE BILAYERS

4.1 Summary

The partitioning behavior of a series of perhydrocarbon nicotinic acid esters (nicotines) between aqueous solution and DPPC membrane bilayers has been investigated as a function of increasing alkyl chain length. The hydrocarbon nicotines represent putative prodrugs, derivatives of the polar drug nicotinic acid, whose functionalization provides the hydrophobic character necessary for pulmonary delivery in a hydrophobic, fluorocarbon solvent, such as perfluorooctyl bromide (PFOB). Independent techniques of differential scanning calorimetry (DSC) and 1,6-diphenyl-1,3,5 hexatriene (DPH) fluorescence anisotropy measurements were used to analyze the thermotropic phase behavior and lipid bilayer fluidity as a function of nicotinate concentration. At increasing concentrations of nicotines over the DPPC mole fraction range examined ($X_{\text{DPPC}} = 0.6 - 1.0$), all the nicotines (ethyl (C₂H₅); butyl (C₄H₉); hexyl (C₆H₁₃); and octyl (C₈H₁₇)) partition into the lipid bilayer at sufficient levels to eliminate the pretransition, decrease the gel to fluid phase transition in the bilayer and broaden the main phase transition. The concentrations at which these effects occur appear to be chain length-dependent; the shortest chain nicotinate, C₂H₅, elicited the least dramatic effects. Similarly, the DPH anisotropy results suggest an alteration of the bilayer organization in the liposomes as a consequence of the chain length-dependent partitioning of the nicotines into DPPC bilayers. From the depressed melting temperature of the bilayers, the calculated membrane partition coefficients (logarithm values) increase from 2.18 for C₂H₅ to 5.25 for C₈H₁₇, spanning several orders of magnitude.

4.2 Introduction

Nicotinic acid is a polar drug molecule widely recognized for its many pharmaceutical benefits. Used as a food supplement, it is a precursor to nicotinamide adenine dinucleotide (NAD) and NADP;²⁵⁷ coenzymes which are important in metabolic cellular function. As a result it has potential in the treatment of lung injury associated with anticancer agent therapies,²⁵⁸ and reduction of the inhibitory respiratory effects caused by bacterial toxins.⁸⁶ Extensive clinical studies have established nicotinic acid as a critical agent in preventing or lowering the risk of cardiovascular or coronary heart disease.^{83,84,259,260} Nicotinic acid raises the level of high density lipoproteins (“good fats”) while reducing low density lipoproteins levels and triglycerides, which are critical factors in the fight against coronary heart disease.⁸⁴ Other studies suggest the therapeutic potential of nicotinic acid in the treatment of HIV²⁶¹ and the treatment of skin carcinogenesis.⁸⁵ The numerous clinical benefits provide incentive to develop a range of administration techniques for this pharmaceutical agent. The need for alternative delivery methods is highlighted by potential dose related side effects; negative pharmaceutical effects of nicotinic acid such as hepatic toxicity have been attributed to the administration formulations such as those with slow release mechanisms.²⁶²

To this end, the delivery of nicotinic acid directly to the lung in the form of prodrugs using a fluorocarbon fluid is of interest as an alternative administration technique.³⁵ Fluorocarbons, characterized by biological inertness and chemical stability, low surface tension, high fluidity with high gas dissolution capacity (CO₂ and O₂) have found potential use in a variety of biomedical applications.^{160,239} Previously, our group, established the viability of pulmonary drug transport of nicotinic acid in cell culture studies using the prominent fluorocarbon fluid, perfluorooctyl bromide (PFOB)³⁵ as the drug delivery vehicle. To achieve this novel drug delivery method,^{15,244} the polar nicotinic acid was functionalized with hydrocarbon and fluorinated side chains to facilitate solubility in the non-polar, lipophobic and hydrophobic PFOB.^{15,35,241} Application of this liquid ventilation technique for drug delivery has several advantages over conventional drug delivery therapies, which include higher doses to the targeted site and less systemic distribution.¹⁵ The chemically modified compounds/prodrugs or nicotinic acid esters (nicotinate)s which are surface active, lack clinical activity and are

enzymatically converted to the parent nicotinic acid drug at the intended lung site, after passive diffusion through several solvent layers. Homologous series of the prodrugs or nicotines were synthesized with functional carbon chain lengths from C1 – C8 for both hydrocarbon and fluorinated nicotines to establish the relationship between chain length and effective delivery.³⁵ Delivery of the prodrugs to human lung cells in culture was demonstrated through the elevated levels of NAD and NADP that were achieved following exposure to the nicotines. The nicotines, especially the hydrocarbon analogues (perhydrocarbon nicotines) could be delivered at sufficient levels to register the desired pharmaceutical response without significant inhibitory effects on cell viability, as measured by corresponding cytotoxicity studies. A chain length-related trend in cytotoxicity was evident for the perhydrocarbon nicotines when delivered from an aqueous buffer to the cells, with the shortest chain being the least toxic.

The systemic uptake of the prodrugs through a cellular matrix can also be described by models which utilize parameters of thermodynamic partitioning. Partitioning trends through isotropic solvent layers that represent the barrier domains in the passive diffusion of the nicotines to the targeted site serve as useful indicators of the transport limitations of this system. To this end, the partitioning of the solute prodrugs between immiscible liquid phases was measured experimentally: PFOB/water and perfluoromethylcyclohexane (PFMCH)/toluene (an accepted measure of the fluorophilicity of the solute, or its preference for the fluorocarbon phase).⁵⁶ The octanol/water partition coefficients, a traditional index of the nicotines' lipophilicities and propensity to distribute into membrane bilayers, were also determined using the Advanced Chemistry Development software package (Ontario, Canada).³⁵ As expected, the lipophilicity of the nicotines increased with alkyl chain length of the nicotines. Also, with increasing chain length of the nicotines (C1 – C6), the tendency to partition to the fluorocarbon phase from the corresponding immiscible aqueous (PFOB/water) also increases.³⁵ The converse trend was observed for fluorophilicity, which decreased with the chain length of the perhydrocarbon nicotines.

This work examines the effect of increasing chain length of the perhydrocarbon nicotines (ethyl nicotinate, (C₂H₅), butyl nicotinate (C₄H₉), hexyl nicotinate (C₆H₁₃) and octyl nicotinate (C₈H₁₇), Figure 4.1) on dissolution in DPPC lipid bilayers and lipid

bilayer organization using independent calorimetric (DSC) and fluorescence probe techniques. As constituents of pulmonary surfactant found in lung alveoli, 1,2-Dipalmitoyl-sn-glycerol-3-phosphatidylcholine (DPPC) lipid bilayers were the prime choice as the model membranes in this study and are frequently investigated in membrane partitioning studies of toxins and pharmaceutical agents.^{129,130} Differential scanning calorimetry informs on changes in pretransition and main transition of DPPC bilayers as a function of nicotinate concentration. Alternatively, the membrane fluidity or microviscosity, is assessed by DPH fluorescence anisotropy in liposome bilayers, where changes in the characteristic gel-fluid phase transition and the corresponding transition width are measures of the solute incorporation in the membrane matrix.^{135,136,145} The effects of the incorporation of prodrugs in the membrane bilayers as a function of alkyl chain length and concentration are discussed relative to their previously established physicochemical properties (partitioning behavior in immiscible solvent systems) and observed cytotoxicity trends.³⁵

4.3 Experimental Section

4.3.1. Materials

The chemical structures of the nicotinate acid ester prodrugs used in this study are provided in Figure 4.1. C2H5 (Across Chemicals, NJ), C4H9 (Sigma Chemicals Co, MO) and C6H13 (Sigma Chemicals Co, MO) were purified by Kugelrohr distillation to yield the respective nicotinate as colorless liquid. The purity of the nicotinate (> 98%) was confirmed by chromatographic and spectrometric techniques. C8H17 was synthesized by the addition of anhydrous dicyclohexylcarbodiimide and dimethylaminopyridine to a mixture of nicotinic acid and 1-octanol in anhydrous dichloromethane as described previously.^{241,247} The product was purified by column chromatography on silica gel using hexane as eluent to give C8H17 as a colorless liquid in 87% yield (> 98% purity). ¹H (300 MHz, CDCl₃) : 0.85 (bs, -CH₃, 3H), 1.24 (bs, 5 × -(CH₂)₂-, 10H), 1.76 (bs, -OCH₂CH₂-, 2H), 4.31 (t, -OCH₂-, 2H, J = 6.6Hz), 7.30 (d, ArH, J = 4.8Hz, 1H), 8.27 (bs, ArH, 1H), 8.74 (bs, ArH, 1H), 9.20 (bs, ArH, 1H). ¹³C (100 MHz, CDCl₃): 14.25, 22.82, 26.17, 28.81, 29.4 (2 × -CH₂-), 31.76, 31.95, 65.74, 123.40, 137.14, 151.08, 153.47, 165.47. GC-MS, m/z (relative intensity, %): 234 (C₁₄H₂₁NO₂⁺,

8), 220 (4), 206 (11), 192 (29), 178 (24), 164 (37), 151 (16), 137 (19), 124 (100), 106 (90), 78 (80), 51 (38). Dipalmitoylphosphatidylcholine (DPPC) (purity \geq 99%) was purchased from Sigma Aldrich and the fluorescent probe, 1,6-diphenyl-1,3,5-hexatriene (DPH), was purchased from Molecular Probes (Eugene, OR). Fisher Scientific supplied ACS grade chloroform, tetrahydrofuran and the deionized, ultra-filtrated water.

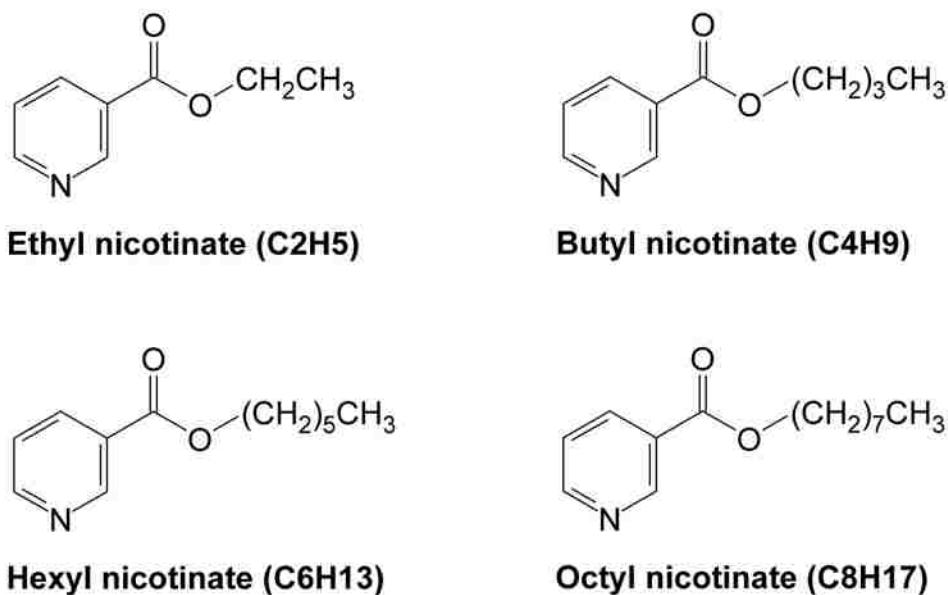


Figure. 4.1. Chemical structure of the perhydrocarbon nicotinic acid esters (nicotinate)s

4.3.2. Differential Scanning Calorimetry (DSC)

Mixtures of DPPC (450 mM DPPC) and nicotinate, prepared in a mole fraction range of 0.6 – 1.0 (X_{DPPC}), were initially dissolved in chloroform. The solvent was gently evaporated under a low pressure nitrogen stream to form an even dry film. The film was further dried under vacuum to remove any trace solvents. The samples were subsequently hydrated with deionized ultrafiltrated (DIUF) water (thrice the weight of the sample). Samples were then subjected to eight cycles of heating (\approx 50 – 55 °C) above the DPPC phase transition temperature of 41 °C,²⁶³ for 5 minutes and vortexing for 2 minutes. To minimize evaporative effects when preparing mixtures containing the lowest molecular weight nicotinate (C₂H₅), the procedure was altered slightly: aqueous solutions of the ethyl nicotinate were added in the appropriate proportion to dried lipid films of pure DPPC prior to the heating and vortexing cycles. The resulting

DPPC/nicotinate samples were weighed into aluminum hermetic pans and analyzed on a Thermal Analysis 2920 differential scanning calorimeter. Dry nitrogen was supplied at 60 mL/min when purging the DSC cell and at 120 mL/min when cooling the DSC cell using the refrigerated cooling system. All experiments were carried out in triplicate. Samples were cooled to 10 °C and heated from 10 – 80 °C at 10 °C/min. The maximum, onset, offset and peak widths of the main phase transition and pretransition were determined using the Universal Analysis software.

4.3.3. Fluorescence Anisotropy Measurements

Following the method of Bangham et al,²⁶⁴ evenly dried lipid films of DPPC and DPH in 500:1 molar ratios were prepared by initially dissolving 36.7 mg (1 mM) of DPPC in chloroform (2 ml) with addition of 1 ml of a 0.1 mM DPH/tetrahydrofuran solution in a round bottom flask. The mixed solution was then evaporated under a gentle stream of nitrogen or a rotary evaporator and further dried under vacuum for at least 4 hours to remove any residual solvents. The dried lipid films were subsequently hydrated with 45 ml DIUF and heated (55-60°C) above the lipid's phase transition temperature (DPPC $T_m = 41^\circ\text{C}$ ²⁶³) for an hour. Vigorous shaking was carried out at the same temperature range for one hour to form liposomes, followed by repeated extrusion (19 cycles) through 200 nm polycarbonate membranes (Aventis mini extruder, Ottawa, Canada) at a temperature greater than the phase transition temperature to generate small unilamellar liposomes.¹¹⁸ The resulting liposomes were diluted 10-fold for fluorescence analysis in a custom made stainless steel variable volume view cell (10 - 25 ml) designed by Thar Technologies (Pittsburgh, PA). The cell was temperature controlled with an Omega unit (model CN9000A) fitted with heating tape and the liposome suspension was stirred continuously with a magnetic stirrer to maintain uniform temperature. The DPH probe was excited at $\lambda_{\text{ex}} = 350$ nm and $\lambda_{\text{em}} = 452$ nm and steady state measurements of the manually polarized light (both excitation and emission) were recorded using a Varian Cary Eclipse fluorescence spectrophotometer (Walnut Creek, CA).²⁶⁵ An excitation slit width of 5 nm and emission slit width of 10 nm was used with 1 s average sampling time. An average of five anisotropy measurements was recorded at 1 K intervals on the cooling

cycle (50 °C to 25 °C) at approximately 0.17K/min. The fluorescence anisotropy is given in equation (4.1):

$$\langle r \rangle = \frac{I_{VV} - I_{VH}}{I_{VV} - G \cdot I_{VH}} \quad \text{Equation (4.1)}$$

where I represents the fluorescence intensity, and the subscripts, V and H refer to polarized light in the vertical and horizontal direction. G (grating factor) is the ratio of the vertical to horizontal polarized light and accounts for the sensitivity of the instrument to polarized light.²⁶⁶ The temperatures scans were carried out twice to ensure reproducibility and verify integrity of the liposomal structure.

4.3.4 Partition Coefficient Calculation

The apparent partition coefficient of the nicotines between the bulk aqueous phase and the DPPC membrane bilayer, $K_{m/w}$ was calculated as shown in Equation (4.2).²⁶⁷

$$-\Delta T_m = \frac{R \cdot T_m^2}{\Delta H_{DPPC}} \times \frac{K_{m/w}}{55.5 + C_{DPPC} \cdot K_{m/w}} C_s \quad \text{Equation (4.2)}$$

where ΔT_m is the change in melting temperature with the addition of nicotines relative to the pure DPPC liposome solution, T_m is the melting temperature of pure DPPC (315 K), ΔH_{DPPC} is the phase transition enthalpy (31.4 kJ/mol),²⁶⁸ R is the gas constant, $K_{m/w}$, the membrane-water partitioning, C_{DPPC} is the lipid concentration and C_s is the concentration of the nicotines in the bulk solution. The equation is based on the assumption of the depression in T_m (or ΔT_m) being in direct proportion to the amount of nicotine partitioned into the membrane bilayer at equilibrium. The membrane partition coefficient is determined from Eq. (4.2) using a linear regression of ΔT_m versus nicotine concentration, C_s .

4.4 Results

4.4.1 Differential Scanning Calorimetric Measurements

Calorimetric scans were performed for the nicotine/DPPC mixtures over the range of $X_{DPPC} = 0.6 - 1.0$ for the following nicotines: C2H5, C4H9, C6H13 and C8H17. Representative calorimetric scans/thermograms, associated partial phase diagrams and

changes in DPPC transition peak width are provided in Figures 4.2 – 4.4. Figure 4.2 provides the calorimetric scans of the DPPC/nicotinate mixtures; Figure 4.3 reports the DPPC pretransition and main transition property changes with increasing nicotinate concentration and Figure (4.4) shows expansion of pretransition and main transition width with concentration. The pure DPPC melting temperature or main phase transition temperature (T_m) is characterized by an endothermic peak at 42.55 ± 0.15 °C. The corresponding onset (T_o), offset (T_f) and transition width (ΔT_m) are recorded at 41.57 ± 0.07 °C, 50.25 ± 0.1 °C and 1.96 ± 0.07 °C, respectively. The pure DPPC pretransition exists in the temperature range of 35.41 ± 0.09 °C (onset temperature ($T_{p,o}$)) to 40.53 ± 0.10 °C at the offset ($T_{p,f}$); the enthalpic peak or endotherm maximum of the pretransition temperature ($T_{p,}$) occurs at 37.77 ± 0.07 °C, with a corresponding pretransition temperature width (ΔT_p) of 2.49 ± 0.14 °C. The measurements are in agreement with published values for DPPC bilayers.^{135,136}

Overall, the presence of the nicotinate decreased or eliminated the pretransition, decreased the melting temperature and increased the width of the main phase transition. The shortest chained nicotinate, C2H5, has the least disruptive effect on the bilayer lipid chain organization, as the pretransition is evident at DPPC mole fractions as low as $X_{DPPC} = 0.8$ (Figure 4.2a), below which it is eliminated. The decrease in the pretransition temperature (Figure 4.3a) and the corresponding increase in the width of the pretransition (Figure 4.4a) is not appreciable until the mole fraction of DPPC falls below 0.97 ($X_{DPPC} \leq 0.97$) (Figure 4.3a). Similarly, the main transition properties remain fairly constant in the same concentration range of $X_{DPPC} \geq 0.97$, after which a linear decrease in the enthalpy peak/DPPC melting temperature, T_m , and onset, T_o , of the transition is observed with increasing mole fractions of the nicotinate (or decreasing X_{DPPC}). The width of the main phase transition, ΔT_m , in Figure 4.4(b) appears constant for $X_{DPPC} \geq 0.9$, at which point it increases continually with incremental amounts of nicotinate. Aside from the broadening, there is no deviation or anomaly in peak shape (Figure 4.2a) from that of pure DPPC, which implies absence of complex phase behavior with the DPPC-C2H5 mixture.

The pretransition is more sensitive to the presence of C4H9 relative to C2H5, and is eliminated at a lower concentration of C4H9 (or a corresponding higher concentration

of DPPC ($X_{\text{DPPC}} < 0.9$) in the DPPC-C4H9 mixtures (Figures 4.2a and 4.3b). There was minimal variance in pretransition properties (onset, offset, peak maximum) in the concentration range over which a pretransition was observed ($X_{\text{DPPC}} = 1 - 0.9$; Figures 4.3b and 4.4a). The main transition onset, T_o and melting temperature, T_m also appear fairly constant in this composition range. However, a steep decline is evident in T_o values for $X_{\text{DPPC}} < 0.9$, while a less pronounced decrease is observed in T_m for the same mole fraction range (Figure 4.3b). The sigmoidal shape of the width of the main transition, ΔT_m , as a function of C4H9 concentration (with a rapid broadening of the peak at $X_{\text{DPPC}} < 0.9$) (Figure 4.4b), suggests that the solubilization of the C4H9 drastically influences acyl chain order. At the lowest DPPC mole fraction measured ($X_{\text{DPPC}} = 0.6$), the thermogram peak shape (Figure 4.2b) is clearly distorted and two shoulders are observed in the main phase transition endotherm (at 24.1 and 32.5 °C), indicating phase changes or complex phase behavior.

C6H13 has the most destabilizing effect on the pretransition of the nicotines studied, completely eliminating this transition at DPPC mole fractions below 0.95 (Figure 4.2c). A continual decrease in pretransition temperature (Figure 4.3c) (onset, offset and peak maximum) and corresponding increase in its width (Figure 4.4a) is observed with increasing C6H13 concentration, until the pretransition is eliminated at $X_{\text{DPPC}} = 0.95$. The main phase transition temperature decreases for the entire mole fraction range investigated ($X_{\text{DPPC}} = 1 - 0.6$) (Figure 4.3c) and the phase change broadens significantly at $X_{\text{DPPC}} < 0.8$ (Figure 4.2c). In addition, a shoulder at 18 °C is observed in the thermogram for the mixture at $X_{\text{DPPC}} = 0.7$. The main transition onset, T_o , and offset, T_p , both decrease with increase in nicotinate concentration ($X_{\text{DPPC}} = 1 - 0.6$) with the decrease more pronounced in the former.

In the case of C8H17, the longest chain nicotinate investigated, the pretransition endotherm is distinctly visible from $X_{\text{DPPC}} = 0.9 - 1.0$, after which it disappears with increasing nicotinate concentration (Figure 4.2d). The pretransition onset, offset and temperature demonstrate a similar trend to that of C6H13 for the range over which it is observed ($X_{\text{DPPC}} = 0.9 - 1.0$). Surprisingly, however, the pretransition width, ΔT_p , displays a similar trend to C4H9 in Figure 4.4(a), that is, it varies little with concentration for the range observed. The onset of the main phase transition, T_o , exhibits a steeper

decrease than T_m for $X_{DPPC} \leq 0.8$ (i.e., with increasing nicotinate concentration) (Figure 4.3d). The peak width of the main phase transition increases from 1.96 °C at pure DPPC to 10.6 °C at the highest mole fraction of nicotinate, $X_{DPPC} = 0.6$, the highest increase observed for all the nicotines. A shoulder in the main transition endotherm was recorded at 30 °C for the lowest mole fraction of DPPC. The offset of the main transition endotherm exhibits the least variation for the whole concentration range of all the nicotines in this study.

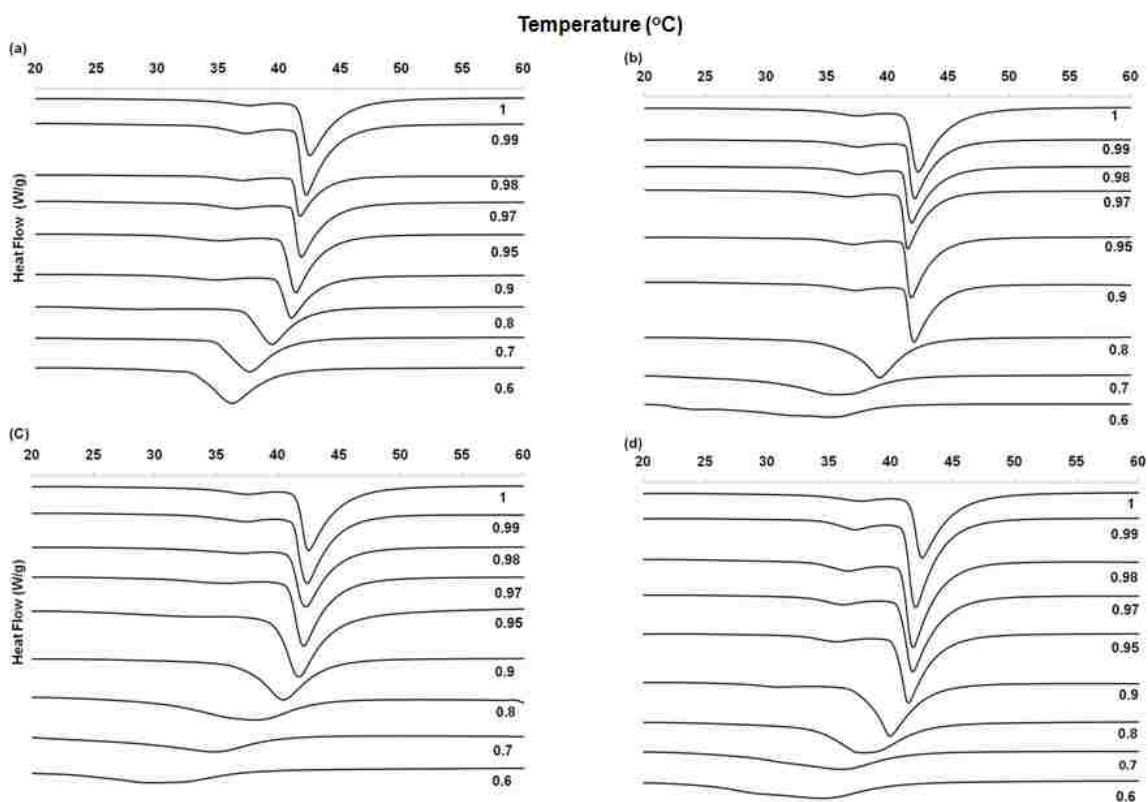


Figure 4.2. Typical calorimetric scans for mixtures of DPPC with (a) Ethyl nicotinate - C₂H₅, (b) Butyl nicotinate - C₄H₉, (c) Hexyl nicotinate - C₆H₁₃ and (d) Octyl nicotinate - C₈H₁₇ in excess water. The mole fraction of DPPC is indicated beside each scan. The heating rate was 10°C/min from 10 °C to 80 °C (selected sections of the scan with the phase transitions are displayed)

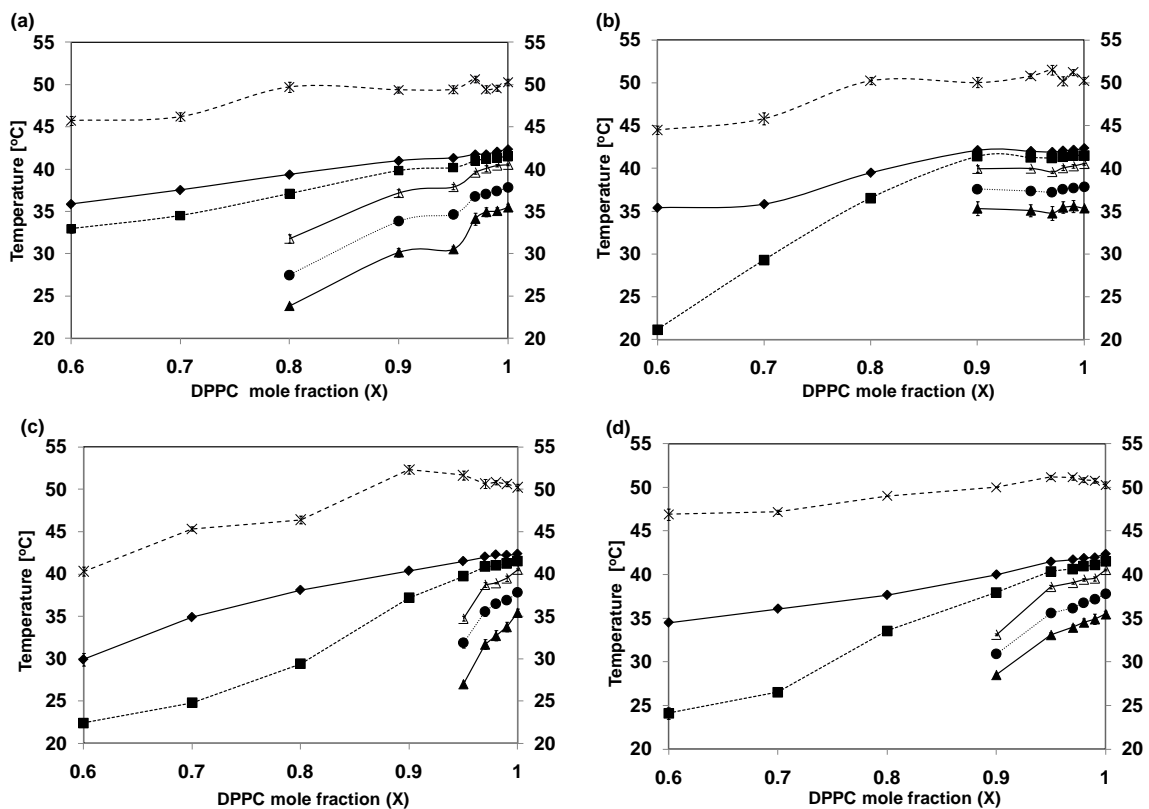


Figure 4.3. Partial phase diagrams of mixtures of DPPC with (a) C₂H₅, (b) C₄H₉, (c) C₆H₁₃ and (d) C₈H₁₇ in excess water. All data points are average of three experiments \pm SD. (□) Onset temperature of main transition, (♦) DPPC melting temperature, T_m, (×) offset temperature of main transition (▲) onset temperature of pretransition, (●) DPPC pretransition temperature, T_{op}, and (△) offset temperature of pretransition.

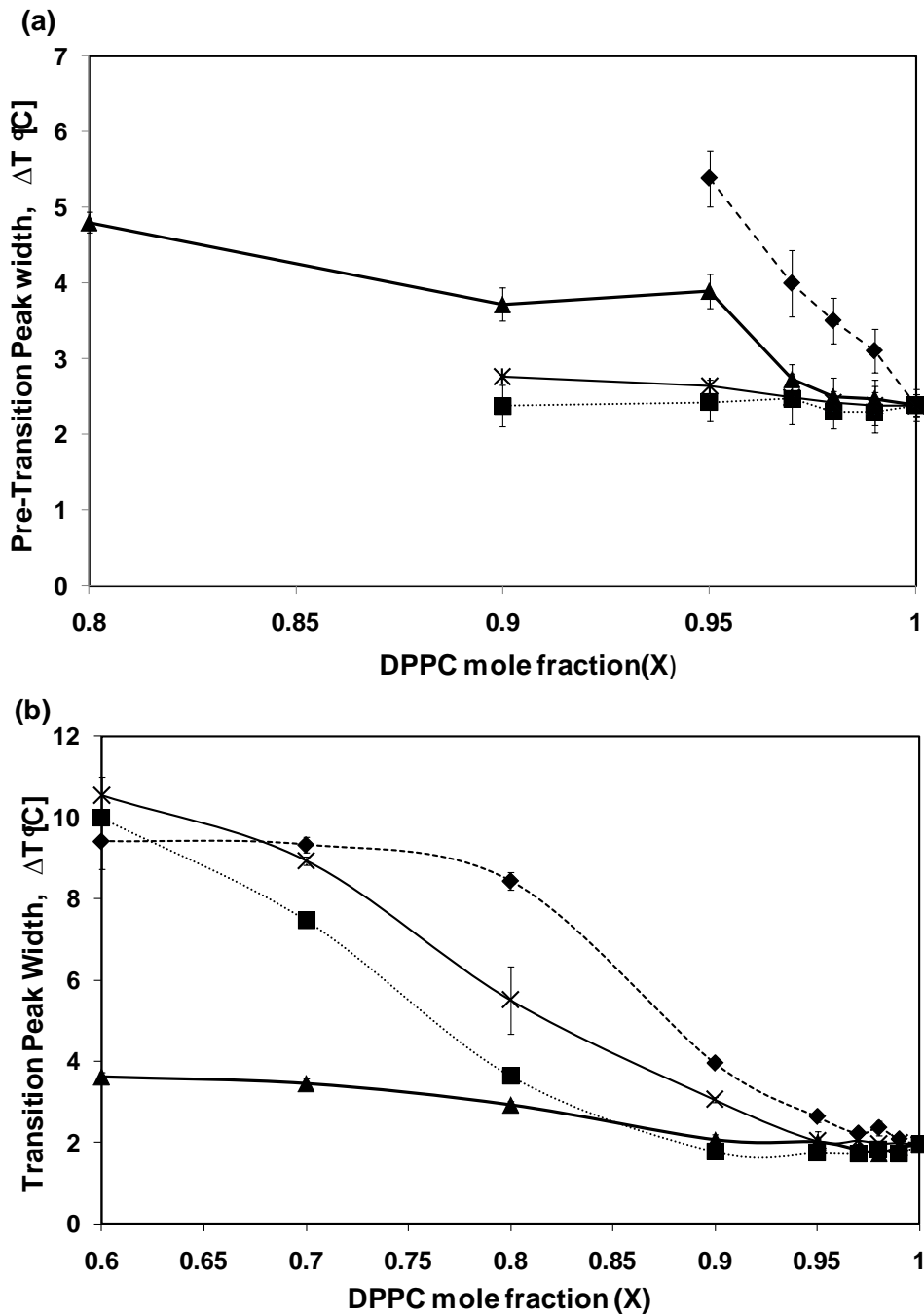


Figure 4.4. Half width of the (a) pretransition and (b) main phase transition of DPPC with (▲) C2H5, (■) C4H9, (◆) C6H13 and (×) C8H17. All data points represent average of three experiment \pm SD.

4.4.2 Fluorescence Anisotropy Measurements (DPH)

The anisotropy of the probe molecule in the bilayers of DPPC liposomes (0.1 mM) was monitored from 50 – 25°C for all the four perhydrocarbon nicotinate/DPPC mixtures at various molar concentration ranges. The melting point or phase transition temperatures, T_m , were determined from the inflection point of the anisotropy curves in Figures 4.5(a) – (d). DPH anisotropy is a measure of the membrane fluidity and decreases with temperature as the bilayer becomes more disordered. In pure DPPC liposomal systems, the bilayer gel-fluid phase change or chain melting is marked by a sharp transition at $T_m = 40.8$ °C over a 1.4 °C temperature range (width of the phase transition, ΔT_r). Here, ΔT_m in Eq. (4.2) is distinguished from ΔT_r ; the former represents the decrease in the melting temperature while the latter is the change in the gel–fluid phase transition width, both measured by DPH anisotropy. The phase transition width, ΔT_r is a measure of the cooperativity of the melting process. The anisotropy data are graphically presented for all the nicotines in Figures 4.5(a) – (d) while Figures 4.6(a) - (d) provides a trend of the changes in T_m and transition width ΔT_m with nicotinate concentration.

The effect of solubilization of ethyl nicotinate, C₂H₅, on gel to fluid phase transition, T_m of DPPC bilayers was investigated up to concentrations of 200 mM C₂H₅ (Figure 4.5a). A significant reduction of T_m , (to 37.1°C) and increase in the phase transition width, ΔT_r (to 3.8 °C) is observed at 50 mM (Figure 4.6a). At the highest concentration, 200 mM, there is a significant drop in T_m (to 30.6 °C) but the gel – fluid phase width, ΔT_r only increases to 4 °C from the pure DPPC width of 1.4 °C. The anisotropy curves also demonstrate significant deviation from that of pure DPPC at concentrations ≥ 100 mM. Although the curves for the intermediate concentrations, 50 and 100 mM are similar in shape in Figure 4.5(a), i.e. the gel and fluid anisotropy values are similar, there is a distinct shift in the transition temperature which is shown in Figure 4.6(a).

A more dramatic effect on the phase transition properties is observed for C₄H₉–DPPC systems, investigated over the concentration range of 0 - 10 mM (Figure 4.5b and 4.6b), than for the shorter chain nicotinate, C₂H₅. At 10 mM C₄H₉, the phase transition temperature/melting temperature, T_m of the DPPC bilayers decreases to 33.3 °C, ≈ 8 K

depression in T_m , relative to the 100 mM (33.3 °C, 7K) required with C2H5. The width of the gel to fluid phase transition, ΔT_r increases to 5 °C with C4H9 concentration of 10 mM. To produce a 2.5 °C increase in gel-fluid phase transition width, ΔT_r , 0.5 mM of C4H9 was needed compared with 10 mM for C2H5.

Lower nicotinate concentrations were sufficient to elicit perturbative effects on the gel to fluid phase transition as the chain length of the nicotinate was increased. The effect of C6H13 on the properties of the DPPC liposomes was examined over a range of (0 - 1mM; Figure 4.5c). There was a 9.2 °C reduction in the melting temperature of the pure DPPC liposomes in the presence of 1 mM C6H13 (Figure 4.6c). Conversely, the phase transition width, ΔT_r , increased five-fold to 7 °C over the nicotinate concentration range of 0 to 1 mM C6H13. The shape of the anisotropy curve at 1 mM C6H13 was significantly altered relative to the pure DPPC curve as there is a much broader gel-fluid phase transition; the onset of the phase transition experienced a dramatic shift at this concentration.

The C8H17/DPPC system was investigated at 0 – 0.1 mM (Figure 4.5d) and at highest concentration of C8H17, 0.1 mM, ΔT_r increased by 7.6 °C and the T_m decreased to 34.8 °C (Figure 4.6d). The anisotropy curves start to deviate from the pure DPPC curves in the presence of 50 μ M C8H17, where the steepness of the gel-fluid phase transition is lost with increasing nicotinate concentration. A concentration of 1 μ M of the longest chain nicotinate was enough to decrease T_m to 39.8 °C and increase the width by 2 °C.

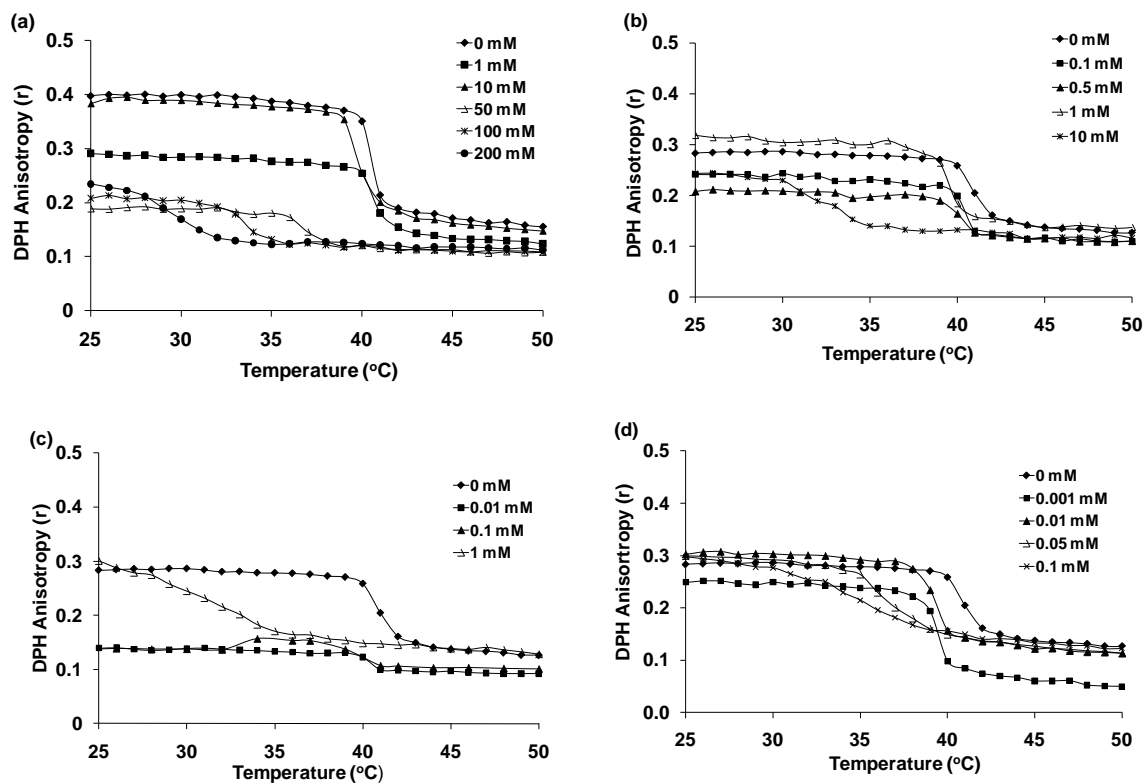


Figure 4.5. Anisotropy of DPH fluorescent probe in DPPC bilayers as a function of temperature and varying nicotinate concentrations. (a) C2H5 (b) C4H9 (c) C6H13 and (d) C8H17.

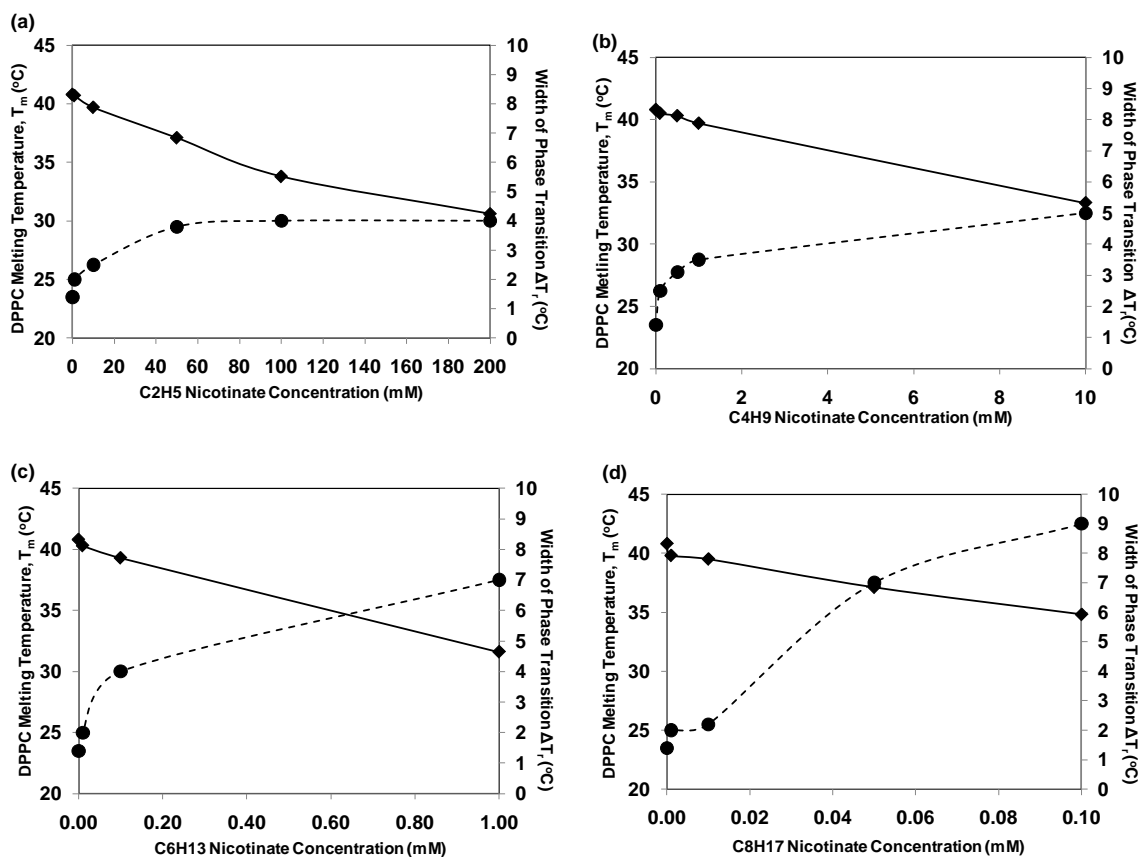


Figure 4.6. Changes in melting temperature, T_m (◆) and phase transition width, ΔT_r (●) of the DPPC phase transition as function of concentrations of (a) C2H5, (b) C4H9, (c) C6H13 and (d) C8H17 measured by DPH fluorescence anisotropy.

4.4.3 Partition Coefficients of Nicotinates

The partition coefficients of the nicotinates between the DPPC bilayers and the aqueous solution ($\log K_{m/w}$) were determined by applying Eq.(4.2) and using the quantities estimated from the anisotropy measurements (T_m , ΔT_m , C_s). Slopes of the depression of the melting temperature (ΔT_m) as a function of bulk nicotinate concentration (graphs not provided) were used in Eq. (4.2) to calculate the membrane/water partition coefficients. For C2H5, the highest concentration of 200 mM was deleted from the plot of ΔT_m against the concentration (not shown), as its presence resulted in a significant deviation from linear trend line ($R^2 = 0.99$ was reduced to 0.95 with inclusion of 200 mM). The following partition coefficients were measured: C2H5 ($\log K_{m/w} = 2.18$), C4H9 ($\log K_{m/w} = 3.21$), C6H13 ($\log K_{m/w} = 4.31$) and C8H17 (\log

$K_{m/w} = 5.25$). Figure 4.7 provides a plot of the experimental membrane/aqueous partition values relative to their octanol/water partition values, as available in literature^{35,269} and previously determined cytotoxicity levels.³⁵ Cytotoxicity levels are expressed as EC20 values in figure 4.7, which represent the nicotine concentration that generated 20% inhibitory effect on cellular activity. As with the $K_{m/w}$, the octanol/water partition values ($\text{Log } K_{o/w}$) for C2H5 to C8H17 span several orders of magnitude as determined by predictive modeling ($\log K_p = 1.4 - 4.6$) and experimentally ($\log K_{o/w} = 1.34 - 4.71$). Also, the trend in Fig. 4.7 shows an increase in cytotoxicity with increase in membrane partitioning. The shortest nicotine, C2H5 expresses the least cytotoxic effect in vitro studies while C6H13, displayed the highest cytotoxicity (C8H17 cytotoxicity not provided).

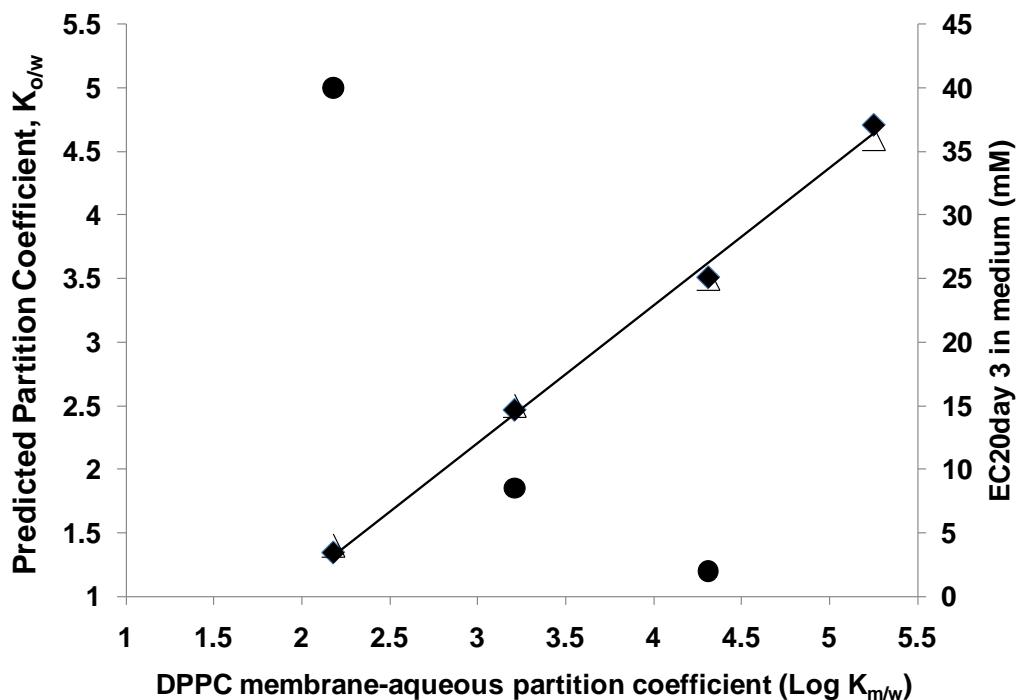


Fig. 4.7. Correlation of experimental DPPC bilayer-aqueous partition coefficients with predicted $K_{o/w}$ partitioning values³⁵ (Δ) and published octanol-water values²⁶⁹ (\blacklozenge). (\bullet)Trend with cytotoxic data.³⁵

4.5 Discussion

Calorimetric and fluorescence spectroscopy techniques provide complementary information on the interaction of perhydrocarbon nicotines with model lipid bilayers. Differential scanning calorimetry (DSC) probes subtle changes in chain order, such as the pretransition, and affords thermal assessment of changes in lipid chain organization at high lipid concentrations without the use of an external agent. Fluorescence anisotropy measurements can also be used to examine the phase transition of the bilayer and membrane fluidity as a function of temperature by changes in rotational diffusion of an embedded probe, DPH. In DSC, concentrated lipid bilayers (450 mM) are examined using significant concentrations of solute in order to generate sufficient thermal response. In contrast, perturbations of the bilayer are assessed by fluorescence anisotropy using dilute systems of liposomes (0.1 mM) to prevent light scattering effects. The four select nicotines, C₂H₅, C₄H₉, C₆H₁₃ and C₈H₁₇ are a subgroup of a homologous series of derivatized nicotinic acid esters which possess functional groups to facilitate solubility in a fluorocarbon medium for drug delivery through the pulmonary route. Physicochemical properties such as octanol-water, fluorocarbon-toluene, fluorocarbon-water partition coefficients and cytotoxicity levels, pertaining to their relevance in the uptake of the prodrugs through a cellular matrix have been previously determined.³⁵ This study of the interaction of the perhydrocarbon nicotines with model DPPC membrane bilayers provides for a fundamental interpretation of the mechanism and efficacy of the delivery of these prodrugs.

4.5.1 Differential Scanning Calorimetry

DSC is a well established technique utilized in the study of thermotropic phase behavior of lipid bilayers and used to interpret the nature of molecular interactions with lipid bilayers without the aid of any external agents. Changes in the main transition and pretransition as a function of nicotinate concentration (Figures 4.2 - 4.4) indicate the incorporation of the nicotines into the bilayer and the subsequent effects on acyl chain organization or assembly. The DPPC pretransition is a quasi-phase transition that involves the temperature induced realignment of the acyl chains from tilted gel to a rippled gel conformation.^{108,270} Due to the differences in cross-sectional area of the

DPPC head group and lipid chain, there is a tilt at the interfacial regions to accommodate van der Waals interactions within the lipid chains and maintain the repulsive interaction between the head groups.¹⁰⁸ The pretransition in pure DPPC lipid bilayers at 37.8 °C is distinguished from the main phase transition at 42.3 °C, which is concomitant with the melting of the lipid chains. All the nicotines, which are surface active, possess the same pyridine head group so differences in perturbative effects of incorporation in the bilayer can be attributed to chain length. Also, the experiments were performed at close to neutral pH, which is greater than the pKa of the nicotines, ensuring they are mostly in an unprotonated form.^{269,271} The same mole fractions of DPPC/nicotine ($X_{\text{DPPC}} = 0.6 - 1.0$) were used for all the perhydrocarbon mixtures. The trends in Figures 4.2 – 4.4, clearly demonstrate the ability of all the nicotines to partition into the DPPC bilayer and effect concentration-dependent alterations in membrane structure/organization as a result of this insertion. In addition, all the nicotines are miscible with the DPPC lipid chains as all the partial phase diagrams in figure 4.3 demonstrate a continual decrease in the thermal properties (melting temperature, onset, offset and width of transitions) with increasing solute concentration. Substantial changes in pretransition, including its elimination at higher nicotine concentrations, suggest significant perturbation of the lipid chain order with nicotine incorporation.

The pretransition was eliminated at mole fractions of $X_{\text{DPPC}} < 0.8, 0.9, 0.95, 0.9$, for C2H5, C4H9, C6H13 and C8H17, respectively. With the exception of C6H13 and C8H17, changes in the onset, melting temperature and offset of the pretransition are minimal at low concentrations (i.e. $X_{\text{DPPC}} \geq 0.97$) of the nicotines. Above this concentration, the impact of solute incorporation of the shorter chain nicotines (C2H5 and C4H9) on lipid organization is more apparent. Overall, C2H5 has the least disruptive effect on membrane organization; the solution concentrations required to elicit similar changes in the pretransition are higher for C2H5 than for the longer chain nicotines.

The endothermic peak shape of the main phase transition of C2H5-DPPC mixtures is preserved even at the highest concentration of the nicotine studies ($X_{\text{DPPC}} = 0.6$), as depicted in Figure 4.2(a). Although there are no anomalies in peak shape, the main transition peak broadening at $X_{\text{DPPC}} = 0.8$ suggests reduced cooperativity of the bilayer phase transition in the presence of the solubilized nicotines. Bilayer

cooperativity describes changes to the uniform lipid arrangement during the bilayer phase transition and is affected by incorporation of solutes. During the phase transition the sequenced rotation of the individual acyl chains of DPPC to avoid unfavorable end-chain intermolecular interactions registers as a sharp transition profile in DSC and fluorescence anisotropy measurements (see below), suggesting a highly cooperative event.¹⁰⁸ Hence, the substantial increase in transition width at $X_{\text{DPPC}} \leq 0.8$ for C2H5 (Figure 4.4a) indicates that incorporation of the nicotinate into DPPC bilayers significantly reduces the structural organization of the lipid chains. This effect is also evident in changes in pretransition width (Figure 4.4b) which are minimal at $X_{\text{DPPC}} \geq 0.97$ but increases considerably above this concentration for C2H5, till elimination at $X_{\text{DPPC}} < 0.8$. With increasing short chain nicotinate concentrations, an abrupt change in the pretransition properties and, as discussed above, concomitant changes in the main phase transition are observed (Figure 4.3a). For C2H5, the main transition width, melting temperature and onset show appreciable decrease simultaneously with dramatic changes in pretransition at $X_{\text{DPPC}} < 0.97$, until it is eliminated at $X_{\text{DPPC}} < 0.8$.

In C4H9-DPPC mixtures, the pretransition and main transition properties show little variance above $X_{\text{DPPC}} \geq 0.9$. However, an abrupt change in main transition properties is observed at $X_{\text{DPPC}} < 0.9$, at the same concentration as the pretransition is eliminated. Below $X_{\text{DPPC}} = 0.9$, the onset of the main phase transition decreases rapidly with increasing C4H9 concentration. While the effect on onset temperature was more pronounced for C4H9 than C2H5, both short chain nicotinates had the same effect on the offset of the main phase transition. This corresponds to a much greater increase in main transition width (Figure 4.4a) for $X_{\text{DPPC}} < 0.9$ for C4H9 than C2H5. The trends with the short chain nicotinates can be interpreted from their physicochemical properties. With relatively short chain lengths and hydrophilicities, C2H5 ($\log K_{\text{o/w}} = 1.4$) and C4H9 ($\log K_{\text{o/w}} = 2.5$) are expected to be solubilized in the polar interfacial regions of the DPPC bilayers, which is a preferred location for similar short chain molecules.^{128,138} The interfacial molecular area of DPPC is reported to be 49 \AA^2 , which is almost twice the area of the unprotonated nicotinate head group (25.2 \AA^2) in monolayer studies (air-water interface).²⁷¹ Xiang and Anderson's¹³⁸ molecular dynamics (MD) simulations of DPPC liposomes suggest the bilayer can be stratified into regions with the headgroup area being

the least dense with the highest hydration. Hence, the free volume created by the mismatch of DPPC headgroup and lipid chains should facilitate solubilization of relatively hydrophilic short chain nicotines (C2H5 and C4H9) with even distribution at low concentrations. Due to their small volumes, the solubilization of the short chain nicotines in dilute systems should cause minimal perturbation to the head-group/chain tilt alignment. However with increasing concentration, the insertion of nicotines in this region results in reorientation of the lipid chains, affects the headgroup/chain tilt and increases trans-gauche conformation of the lipid chains. These changes are consistent with distribution of the nicotines to the acyl chain regions of the bilayer following saturation of the interfacial region with increasing nicotinate concentration. The resulting entropically unfavorable changes to the inner bilayer region or creation of the free volume would require adaptation of the bilayer matrix to accommodate solute incorporation and reduced free volume.

The perturbative effects on the bilayer are further enhanced with the more hydrophobic, longer chain nicotines, C6H13 (Log $K_{o/w}$ = 3.5) and C8H17 (Log $K_{o/w}$ = 4.71), where possibly their longer chain lengths are able to penetrate the acyl region of the bilayers, with the nicotinate headgroup located close to the DPPC headgroup region. The reduction of pretransition properties is slightly more pronounced for C6H13 and C8H17 at lower concentrations ($X_{DPPC} \geq 0.95$) than for the shorter chained nicotines in this series. The disappearance of the pretransition peaks below these concentrations is marked by more exaggerated decrease in main transition onset and melting temperature (Figures 4.3c and d). The sigmoidal shape of the phase transition width for C6H13 suggests saturation of the bilayer at $X_{DPPC} = 0.7$ while C8H17 continues to reduce the cooperativity till the highest concentration of nicotinate measured, $X_{DPPC} = 0.6$ (Figure 4.4a). Favorable van der Waals interactions between the nicotinate alkyl chains and lipid chains are expected to promote partitioning of the longer chain nicotines (C6H13 and C8H17) into the bilayer, with the pyridine head group positioned close to the interfacial region. As both DPPC and nicotines possess larger cross-sectional headgroup areas than tail group areas (i.e., increased mismatch), the orientation or position of the latter has been suggested to adopt a similar tilt to that of DPPC for longer chained nicotines

(C15H31 – C18H37).²⁷¹ Similarly, the alkyl chains in C6H13 and C8H17 are expected to be aligned with the acyl chains of DPPC.

Complex phase behavior, characterized by asymmetrical broad peaks of the main phase transition, is observed for all nicotines at high concentrations, with the exception of C2H5. The shoulders observed in the main transition isotherms at $X_{\text{DPPC}} = 0.6$ (C4H9: 24.1 and 32.5 °C; for, C6H13: 18 °C for and C8H17: 30 °C) for are indicative of heterogeneous lipid assemblies. As X_{DPPC} decreases and the bilayer is increasingly enriched with nicotine, the peaks might represent localized nicotine-rich domains of a heterogeneous bilayer. The peaks appear at lower temperatures than the DPPC melting temperature and may represent melting phenomena in the pure nicotines. In a previous study of long chain nicotines (C15 – C18), secondary peaks at temperatures close to the melting temperatures of the pure nicotines were distinctly visible.²⁷¹ These long chain nicotines possessed melting temperatures that varied from $\approx 42 - 56$ °C, with values similar or greater than that of DPPC (42 °C). Future knowledge of the melting temperatures of our series of nicotines in this study would help elucidate the nature of the secondary peaks observed.

4.5.2 Fluorescence Anisotropy and Partition Coefficients

The fluorescence anisotropy of the DPH fluorophore is a measure of the local microviscosity of the central regions of the bilayer, where the probe is aligned in parallel with the acyl chains when the bilayer is in a gel state.²⁷² In the gel phase, the lipid chains are tightly packed and the DPH probe intercalated between the chains experiences little rotational motion. As temperature increases or chain organization is compromised due to solute incorporation, the bilayer fluidizes and the rotational motion increases. The anisotropy value experiences a decrease in going from a gel to a fluid phase bilayer, and can be used to determine the phase transition temperature and phase width.

The ability of the nicotine to lower the melting temperature and increase the width of the phase transition is a strong function of the nicotine chain length (Figures 4.5). In agreement with the DSC results, the ethyl nicotine has the least perturbing effect on the phase transition properties and the phase transition has distinguishable features even in the presence of 200 mM C2H5, the highest concentration of nicotine

investigated. The narrow width of gel-fluid phase transition of DPPC is preserved for C2H5 concentrations, 0 – 10 mM (Figure 4.6a). At concentrations \geq 50 mM, there is considerable increase in the phase transition width, with a concomitant reduction in the melting temperature. The shape of the anisotropy curve at 200 mM C2H5 (Fig. 4.5a) suggests extensive fluidization of the bilayer due to solubilization of C2H5; the melting temperature is considerably depressed to a value of 32 °C. The phase transition width as a function of C2H5 (Figure 4.6a) concentration is consistent with saturation of the DPPC bilayer at approximately 100 mM C2H5. Above this concentration, the phase transition width remains constant, although there is a further reduction in melting temperature. Analogous to DSC analysis, broadening of the phase transition width or increase in ΔT_r is a measure of the cooperativity of the lipid chains in the bilayers. At low concentrations (0 – 10 mM), the solubilization of C2H5 has minimal effect on bilayer cooperativity. As the concentration is increased, solute incorporation into the bilayer results in reduction of lipid chain order and cooperativity with increased fluidization of the bilayer.

Significant changes in the melting temperatures and width of the transition occur at 1 mM, 0.1 mM and 10 μ M for C4H9, C6H13 and C8H17, respectively (Figures 4.6b - d). The concentrations required to elicit the same decrease in the DPPC melting temperature span three orders of magnitude from the shortest to the longest alkyl chain for the nicotines. For example, the nicotine concentrations required to achieve a decrease in the melting temperature of 3.5°C (or reduction of DPPC T_m to 37.8 °C), is estimated as 36 mM (C2H5), 3.6 mM (C4H9), 0.25 mM (C6H13) and 32.5 μ M (C8H17). These values were extrapolated from the near linear functions of melting temperature, T_m , with nicotine concentration (Figures 4.6). In contrast, ΔT_r as a function of nicotine concentration displays strong deviations from linearity. In a study of a series of alcohols, from butanol to octanol, comparable effects on phase transition temperature and phase transition width were reported.¹²⁶

The partitioning of the nicotine solutes in the bilayer relative to the aqueous phase varies by orders of magnitude, with an increasing affinity for the bilayer with increasing chain length. The partition coefficients, as determined from the fluorescence anisotropy experiments, vary from log K_p of 2.18 (C2H5) to 5.25 (C8H17). The order of membrane partitioning is in direct proportion to octanol/water partitioning (Figure 4.7),

which suggests that the partitioning into the bilayer correlates with hydrophobicity/lipophilicity of the nicotines, which increases from C2H5 to C8H17. Similar trends have been reported for series of halogenated aromatic hydrocarbons,²⁷³ where the $\text{Log } K_{o/w}$ was in linear proportion to $\text{Log } K_{m/w}$ in the range of 1 – 5.5.

Partition coefficients for the nicotines, as previously determined in our laboratory³⁵ showed increased propensity for the organic phase (toluene) in immiscible perfluoromethylcyclohexane/toluene system, with nicotine hydrocarbon chain length. The partition coefficients, which range from $\log K_{\text{PMCH/Toluene}} = -2.22$ (C2H5) to -2.92 (C8H17), indicate reduced fluorophilicity with chain length. In contrast, fluorocarbon (PFOB)/water partition coefficients increased from $\log K_p = -0.16$ (C2H5) to 1.24 (C6H13), indicating reduced preference for the aqueous phase with nicotine chain length. However, these changes in partition coefficient are minimal relative to the membrane/water, $\log K_{m/w} = 2.18$ (C2H5) – 5.25 (C8H17); with the orders of magnitude variance mirrored by octanol/water partitioning ($\log K_{o/w} = 1.4 - 4.7$).

The trend in partitioning and the consequent perturbing effects on the liposome bilayer arrangement with nicotine chain length is also reflected in their cytotoxic effect on human lung cells³⁵ when delivered from medium (Figure 4.7). The concentrations of nicotine required to generate a marked cytotoxic effect when delivered from buffered medium to the cells was in inverse relation to the chain lengths of the nicotines (C2H5 – C6H13) and are in proportion to the bilayer partition coefficients, as determined in this study. With the cytotoxicity (medium) mirroring the partition trends in this study, this confirms the ability of this subgroup of perhydrocarbon nicotines to act as effective prodrug delivery agents.

4.6 Conclusion

The perhydrocarbon nicotines investigated in this study (C2H5, C4H9, C6H13 and C8H17) all partition into DPPC bilayers, although their affinity for the bilayer and the effect of their incorporation in the bilayer is a function of the length of their alkyl chain length. The combination of DSC and fluorescence anisotropy techniques allows for a better interpretation of the interaction of the nicotines with DPPC bilayers, which has significance for pulmonary targeted drug delivery. The quantitative results of DSC

and DPH fluorescence anisotropy are largely in agreement, in that bilayer disruption increases with the chain length of the nicotines. The apparent partition coefficients of the solutes in the bilayer span four orders of magnitude, from $\text{Log } K_{m/w} = 2.18 - 5.25$. The direct correlation of membrane partition coefficients with $\text{Log } K_{o/w}$, is consistent with previous findings that hydrophobicity is the primary driving force in lipid bilayer partitioning. The shortest chain nicotine, C2H5 has the lowest $\text{Log } K_{m/w}$ and the least disruptive effect on the bilayer in the series. This supports *in vitro* cytotoxicity studies which show that C2H5 has the least inhibitory effect on cellular function.³⁵ Furthermore, DSC suggests that all nicotines are solubilized in close proximity to the DPPC headgroup region at low concentrations, which affects the pretransition. At higher concentrations, more disruptive effects of the nicotines on the lipid acyl packing are evident from the reduced cooperativity of the main phase transition. Complex phase behavior with C6H13 and C8H17 suggests considerable structural disorganization with incorporation of these longer chained nicotines at high concentrations. Effective prodrug delivery through the pulmonary route requires the balance of bioavailability and minimized cytotoxicity. Insight into the interactions and uptake of solutes in a cellular matrix, as provided by the partitioning behavior in model membranes, aids the systematic design of prodrugs.

CHAPTER 5

CATIONIC-ANIONIC VESICLE TEMPLATING FROM FLUOROCARBON/FLUOROCARBON AND HYDROCARBON/FLUOROCARBON SURFACTANTS

This Chapter is based on work published as:

Ojogun, V.A.; Lehmler, H.-J.; Knutson, B.L.; *JCIS* 338 (2009) 82

5.1 Summary

Spontaneous catanionic vesicle formation is studied in systems comprising fluorinated surfactants, the cationic/anionic fluorinated surfactant system of 1,1,2,2-tetrahydroperfluorododecylpyridinium chloride (HFDPC)/sodium perfluorooctanoate (SPFO) and the analogous mixed hydrocarbon/fluorocarbon surfactant system of cetylpyridinium bromide (CPB)/SPFO. Aggregate formation is explored in the anionic-rich surfactant system (weight fraction of anionic surfactant, $\gamma = 0.66 - 0.85$) and a total surfactant concentration range of 0.1 – 2% wt/wt for the fluorinated system and 0.4 – 2.2% wt/wt for the mixed hydrocarbon/fluorocarbon system. Vesicle sizes range from approximately 40 - 200 nm for CPB/SPFO, as determined by negative staining transmission electron microscopy (TEM) and confirmed by dynamic light scattering. The primary vesicle diameter observed by TEM in the catanionic fluorinated/fluorinated surfactant system is smaller (20 – 50 nm). However, the relatively few larger vesicles (≥ 100 nm) in the HFDPC/SPFO system dominate the dynamic light scattering measurements. Successful templating of silica hollow spheres is demonstrated in both HFDPC/SPFO and CPB/SPFO vesicle systems, using tetramethoxysilane (TMOS) as the silica precursor for the acid catalyzed synthesis. The size of the resulting hollow silica particles is consistent with the templating of vesicles of the size range observed by TEM. Changes in zeta potential are used to monitor colloidal stability. At the conditions

investigated (TMOS/surfactant weight ratios of 0.25 – 1.0, pH 3), the colloidal silica particles templated from fluorinated HFDPC/SPFO vesicles are more stable than the particles templated from the corresponding mixed fluorinated CPB/SPFO system. Further improvement of the stability of the colloidal particles is achieved in the CPB/SPFO systems by titrating the acid synthesis solution with base over the course of the particle synthesis.

5.2 Introduction

In dilute aqueous solutions, mixtures of cationic and anionic surfactants self-assemble into a variety of aggregates, ranging from spherical micelles to vesicles and lamellar structures.^{44,177,274-276} Factors influencing the type of aggregates in these solutions include ionic strength,^{46,51} pH,⁵¹ temperature,^{218,277} counter ions⁵² and structure of the surfactant. In mixtures of cationic and anionic surfactants (catanionic systems), an aggregate structure of considerable interest is spontaneously formed vesicles. Spontaneous vesicle formation, driven primarily by the electrostatic interactions of the oppositely charged head groups, is dependent on the molecular geometry of the surfactants and hydrocarbon chain asymmetry of the surfactant pair used in the catanionic mixture.⁴⁴ Thermodynamically stable, unilamellar vesicles are typically observed in solutions where one of the surfactants, usually the shorter chain surfactant, is in excess.¹⁷⁷ The vesicles are stabilized by the excess charge while chain asymmetry favors spontaneous curvature through favorable packing distribution of the individual surfactants in the monolayers.^{194,278-280}

These equilibrium vesicles have emerged as attractive candidates for a broad range of applications such as encapsulation and as potential vectors for biological compounds^{47,281,282} and material synthesis.^{50,227,233} One motivation for exploring silica hollow sphere formation is their potential as reservoirs for storing and transporting solutes.^{116,222,283,284} In addition, the encapsulated aqueous core of silica hollow spheres could serve as a micro reactor or separator.²²³ The outer monolayer, bilayer and aqueous core of vesicles represent distinct environments for nano-scale applications. In the synthesis of silica hollow spheres, the surface/outer monolayer of the vesicle can serve as a viable templating site. This transcriptive templating mechanism²²⁷ is dependent on the

stability of the colloidal system.^{50,226,227,233,235} and proceeds via the hydrolysis, condensation and polymerization of silicon alkoxides.²²⁵ With the vesicle surface acting as a “nucleation site”²²⁷ for the synthesis reactions, the polymerized silica network assumes the morphology and dimensions of the vesicles while encapsulating the aqueous core. The site of the sol-gel chemistry is directed by the electrostatic interactions between the charged head groups of the vesicles and the charged silica network.

In vesicle templating, the size of the silica spheres is determined by the size of the vesicles; hence the surfactant properties and system conditions (pH, type and relative ratio of precursor to surfactant) can be tuned to control the properties of silica particles. Catanionic vesicles have been employed as templates for synthesis of silica hollow spheres.⁵⁰ However, the focus is often on vesicles with hydrocarbon bilayers (e.g., dioctadecyldimethylammonium bromide (DODAB) vesicles²²⁶ and cetyltrimethylammonium hydroxide/myristic acid vesicle solutions²³³). With the exception of mixed fluorinated/hydrocarbon system investigated by Hentze et al,⁵⁰ templating from aggregates of hydrocarbon/fluorinated and, more specifically, fluorinated/fluorinated catanionic surfactants has not been reported.

The properties of surfactants with a fluorinated carbon chain which distinguish them from traditional hydrocarbon surfactants include a greater driving force to self-aggregate.^{70,204,205,208,285-288} Fluorinated surfactants have lower critical micelle concentrations and are both hydrophobic and lipophobic in nature, with a tendency to form structures with lower curvature (i.e., rod like micelles, vesicles and lamellar phases) than analogous hydrocarbon surfactants.^{1,70,204,211} The properties of fluorinated surfactants are ascribed to the weaker intermolecular interactions versus intramolecular forces in fluorinated molecules, resulting in thermal and chemical stability.²⁸⁸ In addition, the bulkiness and stiffness of the fluorinated carbon chains restricts random motion of the chains resulting in trans-conformation as opposed to gauche chain type packing in the bilayer.^{70,205} The tightly packed chains of fluorinated bilayers reduce permeability and provide greater membrane rigidity,²⁸⁹ factors that may impact their performance in potential storage, transport and material synthesis applications.

Demixing of fluorocarbon and hydrocarbon chains in mixed micelles is well documented.⁴³ In catanionic surfactant systems, this potential effect is offset by

favorable electrostatic interactions of the head groups in cationic surfactant systems.^{44,46} The reduced permeability and increased stability of vesicle bilayers with the incorporation of fluorinated chains highlights the hydrophobic and lipophobic nature of the fluorinated chain.²⁹⁰ For example, dimyristoylphosphatidylcholine (DMPC) liposome bilayers with incorporated perfluoroalkyl chains exhibited significantly less permeability to a hydrophilic fluorescent marker, carboxyfluorescein, encapsulated in the aqueous core of the liposomes.²⁸⁹ Similarly, an increased ratio of fluorinated to hydrocarbon segments in a liposome bilayer reduces the partitioning of 2, 2, 6, 6 tetramethyl -1-piperidyl-1-oxyl (TEMPO), a probe molecule which is both hydrophilic and lipophilic, from the aqueous core of phosphatidylcholine liposomes through the lipidic bilayer to the external aqueous phase.²⁹¹ The observation was attributed to both rigid packing conformation of the hydrocarbon/fluorocarbon bilayer and immiscibility of the probe in the hydrophobic and lipophobic fluorinated chains.

Fluorination of bilayers in cationic vesicles should influence their colloidal stability and potential applications, including vesicle templating. A comparison of the templating of vesicles formed by cationic surfactants (dioctadecyldimethylammonium bromide (DODAB) and didodecyldimethylammonium bromide (DDAB)) suggests that the ability of vesicles to act as templates is directly influenced by the fluidity of the bilayer; the DDAB vesicles, with more fluid like bilayers (i.e., a lower phase transition temperature), proved unstable under their synthesis conditions.²²⁶ Alcohol production during the hydrolysis and condensation of the silica precursor could destabilize the vesicles by incorporating into the bilayer.⁵⁰ The vesicle is also susceptible to disruption under the strain of the polymerized silica network.²²⁶ Hentze et al⁵⁰ have previously established a vesicle region (approx. 1 wt% – 4 wt% total surfactant concentration) for a mixed hydrocarbon/fluorinated cationic surfactant system, cetyltrimethylammonium bromide (CTAB) and SPFO,^{44,50} and demonstrated successful templating of silica hollow spheres within this region.⁵⁰ The higher rigidity and reduced permeability of a fully fluorinated vesicle bilayer are anticipated to provide better stability to these adverse templating effects.

In the present work, aggregate formation by fluorinated/fluorinated cationic-anionic surfactants (1,1,2,2, tetrahydroperfluorododecylpyridinium chloride

HFDPC(+)/sodium perfluorooctanoate SPFO(-)) is compared with the hydrocarbon-fluorocarbon surfactant pair, cetylpyridinium bromide CPB(+)/SPFO(-), where CPB represents the hydrocarbon analogue of HFDPC (Figure 5.1). In self assembled systems, the hydrophobic effect of a CF_2 unit is equivalent to 1.5 times that of a CH_2 group.⁷⁰ Therefore, the choice of cationic surfactants HFDPC (comprising 10 CF_2 groups connected by two methylene groups (CH_2) to the pyridinium head group) and CPB (comprising 16 CH_2 groups) allows for an appropriate comparison between a mixed hydrocarbon/fluorocarbon bilayer with that of a fully fluorinated bilayer. Vesicle formation in the domain of excess anionic surfactant is explored for both the fluorocarbon/fluorocarbon and hydrocarbon/fluorocarbon surfactant systems over total surfactant concentrations of 0.4% wt/wt - 2.2% wt/wt and weight fractions of $\gamma = 0.75 - 0.85$ for CPB/SPFO and concentrations of 0.1% wt/wt - 2% wt/wt ($\gamma = 0.66 - 0.85$) for HFDPC/SPFO, where γ is defined as the weight fraction of the anionic surfactant relative to the total mass of surfactant. Conditions for successful silica templating of the vesicles using the silica precursor, tetramethoxysilane (TMOS), are established as a function of precursor to surfactant ratio and pH.

5.3. Experimental Section

5.3.1. Materials

The fluorinated anionic surfactant, sodium perfluorooctanoate (SPFO; $\text{C}_7\text{F}_{15}\text{COO}^- \text{Na}^+$; 97% purity) and the hydrocarbon cationic surfactant, cetyl pyridinium bromide (CPB; $\text{C}_{21}\text{H}_{38}\text{N}^+\text{Br}^-$; $\geq 97\%$) were purchased from Sigma Aldrich and Alfa Aesar, respectively and used without further purification. The fluorinated cationic surfactant, 1,1,2,2-tetrahydroperfluorododecylpyridinium chloride (HFDPC; $\text{C}_{10}\text{F}_{21}\text{CH}_2\text{CH}_2\text{NC}_5\text{H}_5^+\text{Cl}^- \cdot \text{H}_2\text{O}$), was synthesized with greater than 98% purity, as previously described.⁴¹ In short, alkylation of pyridine with 1H,1H,2H,2H-perfluorododecyl iodide, followed by anion exchange produces the desired HFDPC. The purity of HFDPC was assessed by spectrometric and melting point measurements and was in agreement with published values.⁴¹ Tetramethoxysilane (TMOS; $\text{CH}_3\text{OSi}(\text{OCH}_3)_3$; 99% purity) was purchased from Fisher Scientific. The hydrochloric acid solution (0.1 N) was obtained from Alfa Aesar.

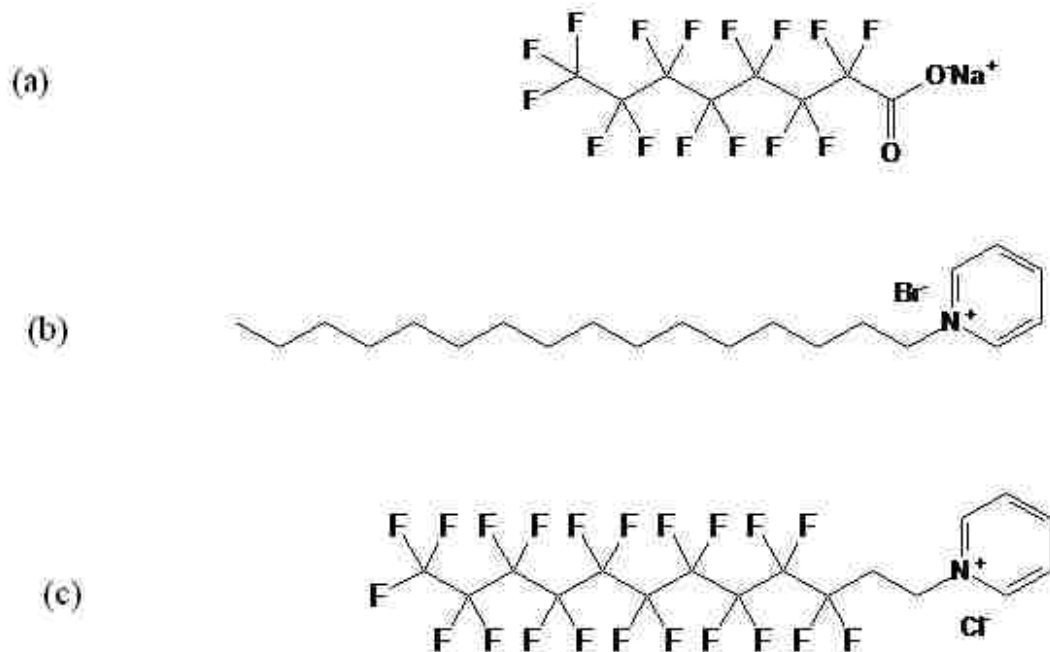


Figure 5.1. Chemical Structures of anionic surfactant (a) sodium perfluorooctanoate (SPFO; $C_7F_{15}COO^-Na^+$) and cationic surfactants (b) cetylpyridinium bromide (CPB; $C_{21}H_{38}N^+Br^-$) and (c) 1,1,2,2-tetrahydroperfluorododecylpyridinium chloride (HFDPC; $C_{10}F_{21}CH_2CH_2NC_5H_5^+Cl^- \cdot H_2O$).

5.3.2 Cationic/Anionic Surfactant Solution Preparation

Stock solutions of the individual surfactants were prepared using deionized ultra filtered water from Fisher Scientific. The solutions were prepared in acidic medium using hydrochloric acid solutions of pH 3. Vesicle formation in the phase region of excess anionic surfactant was explored for both systems. For CPB/SPFO, surfactant solutions in the total concentration range of 0.4% wt/wt - 2.2% wt/wt were prepared. The weight percentage of anionic surfactant in this solution was varied from $\gamma = 0.75 - 0.85$, which approximates a mole fraction range of 0.73 - 0.83. HFDPC/SPFO solutions were prepared with a total concentration of 0.1% wt/wt - 2% wt/wt, where γ was varied from 0.66 - 0.85 (corresponding mole fraction of anionic surfactant of 0.75 - 0.93). The pure CPB and HFDPC solutions were heated to 50 °C to ensure complete dissolution before

mixing with the anionic surfactant solutions. Prior to mixing, the stock solutions were filtered using 200 nm syringe filters (Microliter Analysis). The cationic surfactant mixtures were stirred for several hours, then stored in clear glass vials with PTFE caps and monitored visually for signs of turbidity and the bluish tint attributed to Rayleigh light scattering of vesicles.

5.3.3 Dynamic Light Scattering (DLS)

The hydrodynamic size and polydispersity of the cationic surfactant aggregates at 25°C were monitored periodically using a Malvern Zetasizer Nanoseries (Malvern Instruments, United Kingdom). The instrument was equipped with a He-Ne laser lamp (4 mW) source at 633 nm and measurements were taken at 90° scattering angle. The data were analyzed with the Cumulants Method,²⁹² which employs a single exponential fit of the intensity of the autocorrelation function to derive an average translational diffusion coefficient. An intensity weighted size average (Z-average) was then calculated using the Stokes-Einstein equation. The Z-average and polydispersity index (PDI) were taken as representative of the hydrodynamic diameter and size distribution in the samples. The PDI is given on a scale of 0 – 1.0, where 0 represents the highest level of monodispersity. The zeta potential of the vesicle solutions and the solutions during vesicle templating were measured with the same equipment at 25 °C using cuvettes with gold-plated electrodes. Zeta potential provides a quantitative measure of the interparticle electrostatic interactions and is used to assess the relative colloidal stability of the vesicle templates and the subsequent silica particles.

5.3.4 Transmission Electron Microscopy (TEM)

A Philips Tecnai BioTwin unit (Edax detector) with a Gatan Digital Micrograph 1000 operating at 100kV was used to image the surfactant aggregates. A negative staining procedure with uranyl acetate solution (2 w/v%) was used to image vesicle solutions without silica. 5 µL drops of vesicle solutions were gently placed on copper coated formvar grids and blotted after 1.5 minutes. Identical volumes of stain solution were immediately added and one minute was allowed before blotting the grids with filter

paper and air drying. No stain was required when examining the particles formed by silica synthesis.

5.3.5 Hollow Silica Particles Synthesis

The vesicle solutions were allowed to equilibrate for several weeks before the addition of the silica precursor, TMOS, in the desired proportion. TMOS to total surfactant mass ratios in the range 0.25 -1.0 were investigated, following the method of Hentze et al.⁵⁰ After the addition of the precursor, the solutions were initially stirred vigorously to ensure proper mixing of the hydrophobic TMOS in the aqueous systems. Analysis by DLS was conducted after 24 hours and monitored for a minimum of two days before TEM analysis. Maintaining similar dimensions to pre-synthesis vesicle system is an indication of successful transcriptive templating. Zeta potential measurements were used pre- and post-synthesis to monitor colloidal stability.

5.4. Results and Discussion

5.4.1 Vesicle Formation

Investigations of the self-assembly of catanionic surfactants involving fluorinated surfactants are often limited to mixed fluorinated/hydrocarbon surfactants systems.^{44,46,207,278} These mixed surfactant aggregates have been characterized by a variety of techniques, including freeze-fracture electron microscopy,^{205,207} SANS,⁴⁶ cryo-TEM^{44,278} and DLS.^{46,207} Utilizing negatively stained TEM imaging, NMR and DLS characterization techniques, Szonyi et al²⁰⁸ investigated the formation of vesicles with fully fluorinated bilayers comprising mixtures of short chain fluorinated cationic surfactants with trimethyl headgroups and fluorinated anionic surfactants with carboxylic headgroups (i.e., ammonium perfluorooctanoate). The resulting perfluorinated aggregates were polydisperse with monomodal-sized unilamellar vesicles detected in the shorter chained anionic-rich compositions and bimodal sizes in the longer chained cationic-rich mixtures. In this study, DLS, TEM and visual observations of phase behavior are used to characterize catanionic vesicle systems with fully fluorinated bilayers, HFDPC/SPFO and compared with an analogous, mixed hydrocarbon/fluorocarbon bilayer system, CPB/SPFO.

5.4.2 CPB/SPFO Vesicles

The CPB/SPFO aggregate solutions (0.4% wt/wt - 2.2% wt/wt $\gamma = 0.75 - 0.80$) were monitored by visual observation and dynamic light scattering to establish a stable vesicle phase in the anionic rich region. The aggregate diameter increases for the CPB/SPFO systems after preparation (by approximately 60%) followed by very little variance in size after two months. Conversely, the PDI of the CPB/SPFO vesicles (2.2% wt/wt, $\gamma = 0.85$) decrease with time (PDI = 0.337 (initial) to PDI = 0.226 (month 5)) suggesting the transition to a more homogeneous aggregate system. An average aggregate diameter of 103 nm is determined by DLS for the CPB/SPFO vesicles (2.2 % wt/wt, $\gamma = 0.85$). Similar sizes and PDIs are found for other CPB/SPFO samples within that concentration range (1.8% wt/wt, $\gamma = 0.75$ and 2% wt/wt, $\gamma = 0.8$), as listed in Table 5.1. Hydrodynamic diameters are reported in Table 1 only for stable vesicle solutions. Lower concentrations of the CPB/SPFO surfactant mixtures (0.4% wt/wt and 1.0% wt/wt, $\gamma = 0.8$) at pH 3 were also prepared. Initially, these solutions appeared homogeneously blue (a Rayleigh scattering effect indicative of particles within the typical vesicle size range). The hydrodynamic diameters were also in the typical vesicle range, (114 nm and 135 nm, respectively). However, a visible phase separation with particle sedimentation is observed with time, indicating a multiphase region at lower surfactant compositions.

TEM images of negatively stained CPB/SPFO vesicles (2.2% wt/wt, $\gamma = 0.85$, pH 3) are presented in Figures 5.2(a) and (b). The micrographs reveal a densely packed dispersion of aggregates, consisting primarily of small, spherical, unilamellar vesicles, with diameters ranging from below 40 nm to over 200 nm. The bilayer is discerned from the darker rim of the hollow vesicle structures. Slight deviations from the expected spherical shape of the vesicles and the visible aggregation observed on the TEM grids might be attributed to the combined effect of staining and drying. Also visible on the grids are a few vesicles with rod-like bilayer structures in the 125 – 200 nm size range, similar to those observed by Jung et al in their CTAB/SPFO cryo-TEM study.¹⁷¹ The hydrodynamic sizes of vesicles determined by DLS (Table 5.1) are consistent with TEM images for the CPB/SPFO system.

The average hydrodynamic size of CPB/SPFO vesicles (103 nm) is larger than those reported for a similar hydrocarbon/fluorocarbon surfactant pair (CTAB/SPFO; 60

nm).⁴⁴ However, some vesicles within the same size range are observed in the TEM images (Figure 5.2b). While CTAB/SPFO systems are known to form monodisperse vesicles due to enthalpic stabilization,^{171,293} the TEM images of the stained CPB/SPFO system clearly suggest some polydispersity, indicative of an entropic stabilization mechanism.⁴⁴

Table 5.1. Characterization of cationic system aggregates (at pH 3) by dynamic light scattering.

Surfactant Mixture	CPB/SPFO			HFDPC/SPFO			
	1.8	2	2.2	0.73	0.75	1.18	2
Concentration (total % wt/wt)	1.8	2	2.2	0.73	0.75	1.18	2
Weight fraction of anionic surfactant (SPFO) in mixture (γ)	0.75	0.8	0.85	0.72	0.66	0.78	0.8
Hydrodynamic Diameter (nm)	108.4	106.6	102.6	209.9	207.2	204.2	241
Polydispersity Index	0.20	0.21	0.23	0.138	0.155	0.1	0.308

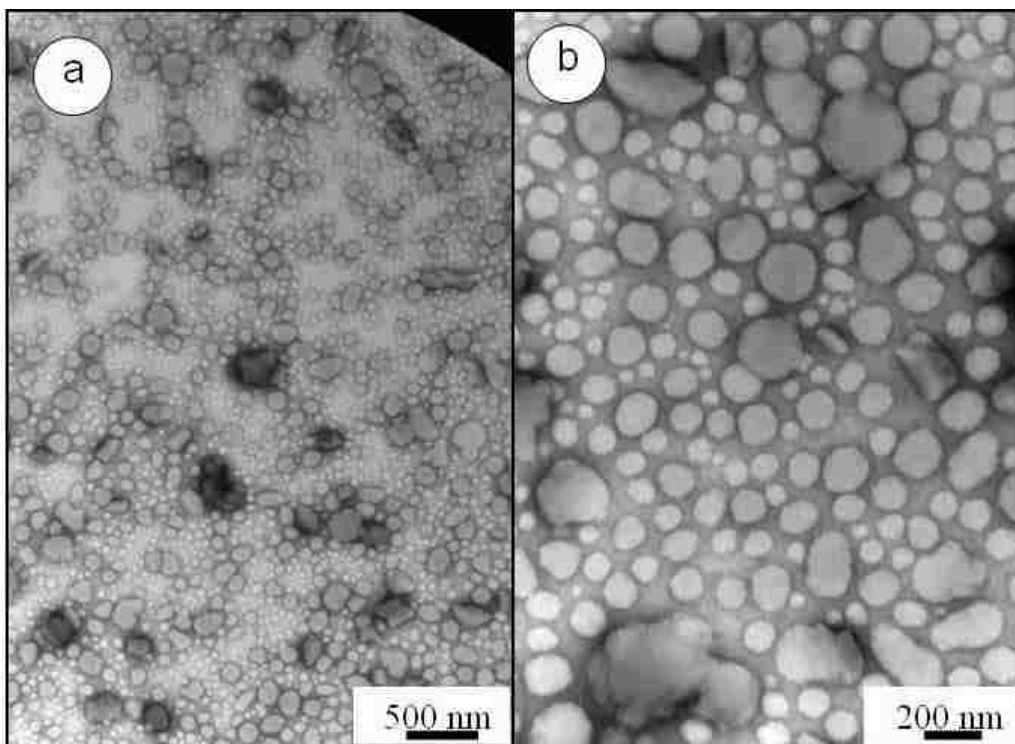


Figure 5.2. Images of negatively stained CPB/SPFO (2.2% wt/wt, $\gamma = 0.85$, pH=3) vesicles (a) TEM image at 18.5 K magnification, (b) TEM image at 49 K magnification

In entropically stabilized systems, a primary driving force for transforming infinitely long planar bilayers to curved vesicle conformation is the favorable entropy of mixing and the energy compensation for having finite-sized structures.^{174,194} In contrast, enthalpic stabilization of vesicles is possible for mixed composition bilayers, in which non-ideal mixing leads to spontaneous curvature of the bilayer and dictates the resulting vesicle structure and size. The stabilization mechanism of vesicle formation can be interpreted from the vesicle size distribution. Enthalpically driven vesicle formation, associated with asymmetric surfactant chains, is characterized by smaller and more monodisperse vesicles relative to entropic stabilization.⁴⁴ The chain lengths and counterions in cationic surfactants, CTAB and CPB, are identical. Thus, the increase of the polydispersity of the CPB-containing vesicles is attributed to differences in the steric and electronic properties of the surfactant head groups. The structural differences between the planar pyridinium headgroup in CPB and the bulky tetrahedral trimethylammonium group in CTAB results in lower charge density and reduced steric hindrance in the

former.^{294,295} Another consideration is the difference in pH of the systems; the size of the CTAB/SPFO vesicles were reported at neutral pH⁴⁴ while the CPB/SPFO were prepared in acidic medium (pH 3). However, Hentze et al⁵⁰ determined that the pH had minimal effect on the size of CTAB/SPFO vesicle systems. This observation is confirmed for the CPB/SPFO system. The average CPB/SPFO vesicle diameter and polydispersity are 131 nm and 0.23, respectively, for the same composition (2.2% wt/wt, $\gamma = 0.85$) at neutral pH.

5.4.3 HFDPC/SPFO Vesicles

Vesicle formation in the domain of excess anionic surfactant was explored for the fluorocarbon/fluorocarbon surfactant system (HFDPC/SPFO) using overall surfactant concentrations of 0.1% wt/wt - 2% wt/wt ($\gamma = 0.66 - 0.85$). The Z-average diameter and PDI of the stable HFDPC/SPFO aggregates (Table 1) approach relatively constant values (± 10.6 nm) within a few days of preparation. Samples of HFDPC/SPFO above 0.5% wt/wt ($\gamma = 0.66 - 0.85$) are clear solutions while those at or below 0.5% wt/wt total surfactant contained visible precipitates, suggesting deviation from a stable vesicle region, and are excluded from Table 5.1. The weaker light scattering intensity of the clear HFDPC/SPFO solutions relative to CPB/SPFO systems suggests a smaller concentration of aggregates. Spontaneous vesicle formation is demonstrated at lower concentrations for fluorinated surfactants (HFDPC/SPFO) than the CPB/SPFO systems. This observation is consistent with the greater aggregation tendency and lower CMCs of fluorinated surfactants relative to analogous hydrocarbon surfactants. In the case of the cationic surfactants employed in this investigation, HFDPC has a CMC of 0.33 mM (or 0.022 wt%),⁷⁰ which is slightly lower than that of CPB (0.64 mM or 0.025 wt%).²⁹⁶ The CMC of the anionic surfactant, SPFO, is 31 mM (1.33 wt%)²⁸⁷.

In contrast to the CPB/SPFO system, TEM micrographs of HFDPC/SPFO solutions (0.75% wt/wt, $\gamma = 0.72$, pH=3) reveal vesicles with a less heterogeneous vesicle population (Figure 5.3a). The aggregate diameters, 20 – 100 nm, are comparable to those reported for vesicles with fully fluorinated bilayers (50 – 180 nm).^{205,208} Larger vesicles (≈ 100 nm) are interspersed with smaller, uniform vesicles (≈ 20 nm). More uniform distributions of stained vesicles are also observed (images not shown), where the majority of fluorinated bilayer vesicles are in the 20 - 50 nm range. HFDPC/SPFO vesicles are

unilamellar and most appear spherical. Interestingly, rod-like bilayer structures (20 nm in length) similar to those observed by cryo-TEM for CTAB/SPFO¹⁷¹ are also detected (images not shown). Vesicles of two distinct size ranges, previously observed in cationic hydrocarbon surfactant systems,¹⁶⁹ have been attributed to the entropic stabilization commonly associated with hydrocarbon chains which have low bending energy⁴⁴. Bimodal aggregate distributions have been observed in a mixture of a zwitterionic hydrocarbon and an anionic fluorocarbon surfactant (n-dodecylbetaine and perfluoropolyether, respectively).²⁰⁴ The bimodal distribution was attributed to the demixing that occurs in the hydrocarbon/fluorocarbon surfactant systems. In our case, both surfactant tails are fluorinated chains of comparable length and surfactant demixing is not expected. However, geometric factors, such as stiffness of the fluorinated chains and asymmetry of HFDPC (10 x (CF₂) in the surfactant tail) and SPFO (7 x (CF₂) in the surfactant tail) may contribute to the same phenomenon in the HFDPC/SPFO systems. Polydisperse vesicles have been reported for other fully fluorinated surfactant bilayer systems.²⁰⁵

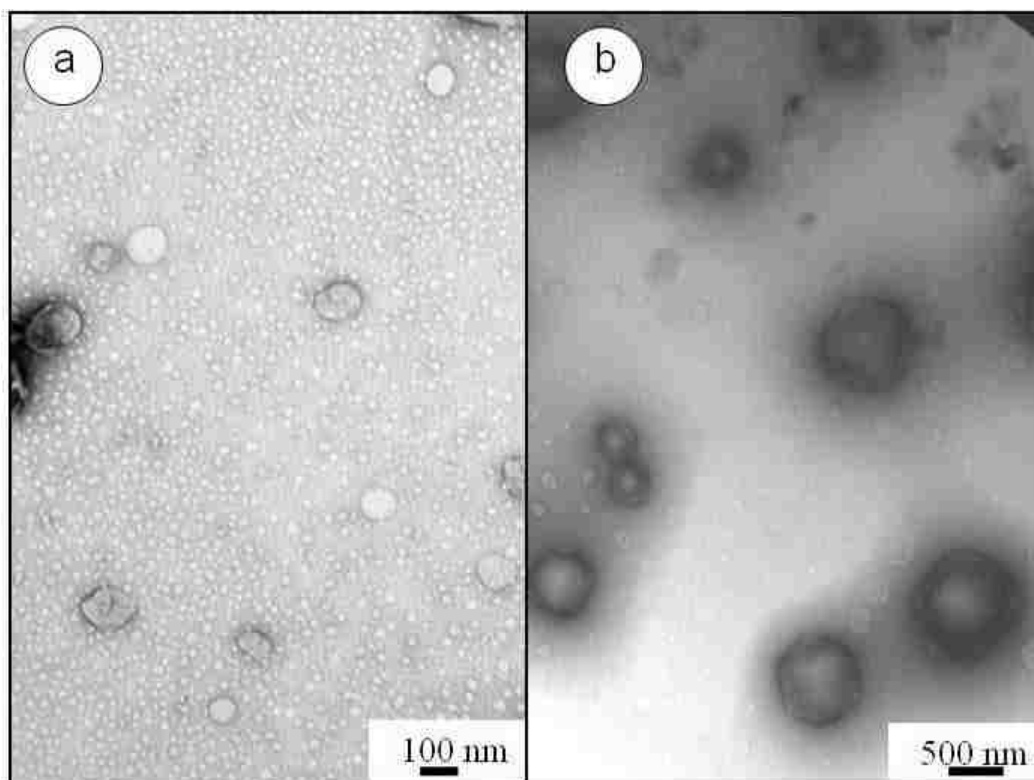


Figure 5.3. Stained images of HFDPC/SPFO vesicles (a) 0.73% wt/wt, $\gamma=0.72$, pH 3, (b) 2% wt/wt, $\gamma = 0.8$, pH 3.

Structural changes in the HFDPC/SPFO system at higher concentration (2% wt/wt, $\gamma = 0.8$) are revealed as multi-lamellar polygonal vesicles (≈ 500 nm) (Figure 5.3b), matching the higher polydispersity observed in DLS (PDI = 0.308). A deviation from spherical structure has been observed in both mixed perfluoroalkyl/ hydrocarbon²⁷⁸ and fully fluorinated bilayers²⁰⁵. This phenomenon has been attributed to intra-vesicle segregation of the immiscible chains in the former case, and gel-state packing in the latter system. The increase in vesicle sizes and multi-lamellarity of the HFDPC/SPFO system at higher concentrations suggests a transition from a planar lamellar structure. The faceted structure represents a balance between thermodynamically unfavorable aqueous exposure of the end chains in planar aggregates and the high bending energy required for the stiff fluorinated chains to form a closed structure.²⁷⁸ These structures are absent from the CPB/SPFO systems at a similar surfactant composition (2.2% wt/wt, $\gamma = 0.85$), suggesting a change in the driving force for aggregation between the mixed fluorinated/hydrocarbon vesicles and fluorinated/fluorinated vesicles.

The narrower size distribution observed for HFDPC/SPFO vesicles (Figure 5.3a) compared to CPB/SPFO aggregates is reflected by their lower PDI values (0.1 – 0.155 relative to 0.2 – 0.23, as reported in Table 5.1). However, the Z-average diameter (≈ 200 nm) does not capture the population distribution of vesicles observed by TEM (primarily 20 nm); the latter aggregate population was undetected even as a peak by DLS analysis. The disparity between DLS and TEM analysis might be a result of the resolution limitations of dynamic light scattering. DLS provides a scattered intensity-based size of a colloidal particle, thus the Z-average is biased towards larger sized vesicles even though they may occupy a much smaller fraction of the vesicle population.¹⁸² This problem is accentuated by the low refractive index of fluorinated molecules.^{209,212,297} These combined factors may result in the 20 nm vesicles being largely masked by the much larger vesicles, which have higher scattering intensity. More sensitive techniques such as SAXS or cryo-TEM could be employed in the future to address this ambiguity.

In summary, stable unilamellar spherical vesicle formation is demonstrated at lower concentrations for the HFDPC/SPFO than in the CPB/SPFO systems. This is probably a reflection of the greater propensity of fluorinated aggregates to adopt morphologies such as closed vesicle bilayers, which limits surfactant-water chain contact. For similar surfactant compositions (2% wt/wt, $\gamma = 0.85$), the CPB/SPFO system consists primarily of spherical vesicles, while HFDPC/SPFO vesicles (2% wt/wt, $\gamma = 0.8$) are multilamellar polygonal shaped. This suggests a concentration-dependent structural transition of the fully fluorinated bilayer aggregates (i.e., the vesicle conformation deviates from the spherical shape as the surfactant concentration increases to a more faceted structure).

5.4.4 Synthesis of Silica Hollow Spheres

A prerequisite for the transcriptive synthesis of silica hollow spheres in cationic surfactants systems is templating in a predominantly vesicle phase region. Presence of multiphase, micellar or other structural variations of these aggregates is not conducive to synthesis of silica hollow particles of controlled size.⁵⁰ Success of the transcriptive synthesis mechanism is also dependent on the stability of the vesicle templates, as determined by the surfactant type and the synthesis conditions. In template synthesis, the

denser silica material provides for the direct imaging of the hollow particles in TEM, precluding the need for staining techniques. As bare vesicles are not visible without external agents in conventional TEM, template synthesis serves as a complementary method to negative staining and labor intensive cryo-TEM techniques in the study of self-aggregating structures.⁵⁰

The stability of cationic vesicles is sensitive to changes in ionic strength¹⁷⁷, pH, temperature¹⁷⁹ and additives such as the TMOS precursor.⁵⁰ The optimal TMOS/surfactant ratio provides sufficient precursor for the formation of a complete hollow cast without disruption of the vesicle structure, while minimizing the side reactions due to excess precursor that lead to phase separation. Vesicle solutions of CPB/SPFO and HFDPC/SPFO of pH 3 were equilibrated over several weeks before initiating the synthesis of silica hollow particles by the addition of the silica precursor, TMOS. TMOS is hydrophobic and its addition to the predominantly aqueous system leads to emulsion formation. Hence, vigorous mixing of the vesicle solution is required upon the addition of the precursor. The hydrophobic precursor may potentially partition into the vesicle bilayers and disrupt the vesicle structure⁵⁰. Therefore, templating in acidic pH, which promotes rapid hydrolysis of the precursor to the soluble silicic acid monomer, is favored.²²⁵ The reaction then proceeds through the condensation and polymerization of the silicic acid to form a silica network on the vesicle surface.

Vesicle templating is examined as a function of the weight ratio of silica precursor to surfactant, α . Results of silica synthesis are summarized in Tables 5.2 and 5.3 (CPB/SPFO and HFDPC/SPFO, respectively) for precursor to surfactant ratios of $\alpha = 0.25 - 1$ (corresponding to molar ratios of 0.70 - 2.79 for CPB/SPFO and 0.78 - 3.10 for HFDPC/SPFO). Particle size, dispersity, and zeta potential were monitored pre and post synthesis. The templating processing is marked by an increase in zeta potential. The stable vesicle templates are negatively charged and have low zeta potentials while the relatively unstable silica particle systems have close to zero surface charge (at pH 3). Thus, increases in zeta can be used to monitor the synthesis reaction and serve as an index of the colloidal stability of the resulting silica particles.

Table 5.2: Synthesis of silica particles from CPB/SPFO vesicle solutions (2% wt/wt, $\gamma = 0.8$, pH = 3) as a function of TMOS:surfactant ratio (α)

	Hydrodynamic Diameter (nm) (PDI)		Zeta Potential (mV)	
	Day 1	Day 14	Day 1	Day 14
Pre-Synthesis	105.5 (0.19)		-101 \pm 15.4	
$\alpha = 0.25$	109.6 (0.23)	157.4 (0.21)	-	-68 \pm 13.5
$\alpha = 0.35$	114.2 (0.23)	151.5 (0.24)	-61.9 \pm 8.4	-55.7 \pm 11.0
$\alpha = 0.5$	123.1 (0.24)	140.6 (0.23)	-42.8 \pm 11.4	-
$\alpha = 0.7$	122.7 (0.24)	323.3 (0.284)	-32.3 \pm 13.9	-
$\alpha = 0.85$	127.1 (0.26)	309.4 (0.475)	-	-

5.4.5 CPB/SPFO Vesicle Templated Silica Hollow Particles

For CPB/SPFO system (2% wt/wt, $\gamma = 0.8$, pH 3), with original average vesicle hydrodynamic diameter of 105.5 nm, the particle size increases range from 109.6 nm (4% increase) to 127.6 nm (20% increase) with increasing TMOS to surfactant ratio ($\alpha = 0.25$ to 0.85), as measured 24 hours after the addition of the precursor (Table 5.2). An increase in turbidity, and a corresponding increase in light scattering intensity, is observed with the addition of the precursor to the vesicle solution. Flocculation is evident after several days of synthesis at the intermediate TMOS/surfactant ratios investigated ($\alpha = 0.7$ and 0.85). Systems with lower silica precursor/surfactant ratios (e.g., $\alpha = 0.25 - 0.5$) flocculate after several weeks, resulting in an appreciable increase in particle dimensions from the initial vesicle template size (14% - 44%). Within several days of templating, particle aggregation precedes gel formation at high TMOS/surfactant ratios, ($\alpha = 1$), indicating that the threshold for ideal templating conditions had been exceeded. The sample at this composition ($\alpha = 1$) was sufficiently turbid prior to gelation that size analysis by DLS was not possible.

Visible flocculation and aggregation during synthesis is marked by an increase in the zeta potential (Table 5.2). The highly negative zeta potential of the vesicle solution

prior to TMOS addition (-101 mV) increases to -42.8 mV ($\alpha = 0.5$) and -32.3 mV ($\alpha = 0.7$). The unstable region of sols or aqueous colloidal systems is in the range of 30 ± 5 mV.²¹³ Thus, the zeta potential values imply increasing aggregation of the silica particles with increasing ratio of precursor to surfactant. Aggregation of the silica particles is also a function of the pH chosen for synthesis.²²⁷ While pH 3 facilitates rapid hydrolysis of the TMOS, the polymerized silica network experiences close to zero surface charge in this pH range.²²⁵ The resulting sol-gel systems are meta-stable with a greater tendency to aggregate.

Evidence of successful transcriptive templating in CPB/SPFO mixtures is provided by the retention of the dimensions and spherical structure of the vesicle templates (40 – 100 nm) by the hollow silica particles (Fig. 5.4a). Uniform deposition of a silica coating is achieved at $\alpha = 0.5$. At a higher precursor to surfactant ratio ($\alpha = 0.7$; Fig. 5.4b), the resulting ellipsoidal structures observed by TEM have dimensions almost identical to the original vesicles (40 – 100 nm), suggesting morphological changes due to the strain of templating.²²⁶ The vesicular structure might also be altered by the increasing amount of methanol produced by the excess precursor.²²⁶ The solid or darkened regions in the templated vesicles (Figure 5.4b and 5.4c) may be due to localized regions of silica precursor in the vesicle bilayer, which result in higher concentration of the polymerized silica along certain axes of the vesicle. However, it is difficult to determine from the images if these concentrated regions of polymerized silica are on the vesicle surface or projecting from the bilayer. The latter case would suggest that the hydrophobic precursor, TMOS, partitioned into the bilayers at sufficient levels to generate discrete regions of silica via the normal synthesis route. Interestingly, these images were observed at higher TMOS to surfactant ratios ($\alpha > 0.5$). Similar parachute-like and folded structures have been captured by cryo-TEM²⁹⁸ for synthesized polymers and conventional TEM²²⁶ for TEOS (tetraethoxysilane) synthesized silica hollow particles in vesicle systems of the cationic surfactant, dioctadecyldimethylammonium bromide DODAB. Jung and coworkers,²⁹⁸ who studied styrene polymerization in DODAB vesicle bilayers, attributed these structures to localization of the monomer or aggregation of the synthesized polymer in the bilayer. They provide two possible routes for the localized regions of the styrene polymer in DODAB vesicle bilayer: monomer diffusion to a region

within the bilayer with subsequent polymerization or the aggregation of synthesized polymer due to steric restrictions in the bilayer following an initial even distribution of monomer. The additional solid particles (10 nm) visible on the grid are most likely products of condensation reactions in aqueous solution, independent of the vesicle templates suggesting phase separation of excess precursor from the vesicles. At high relative amounts of precursor ($\alpha = 1$), fused silica hollow particles with dimensions consistent with vesicle templating are observed (image not provided), suggesting aggregation of vesicle templated silica particles.

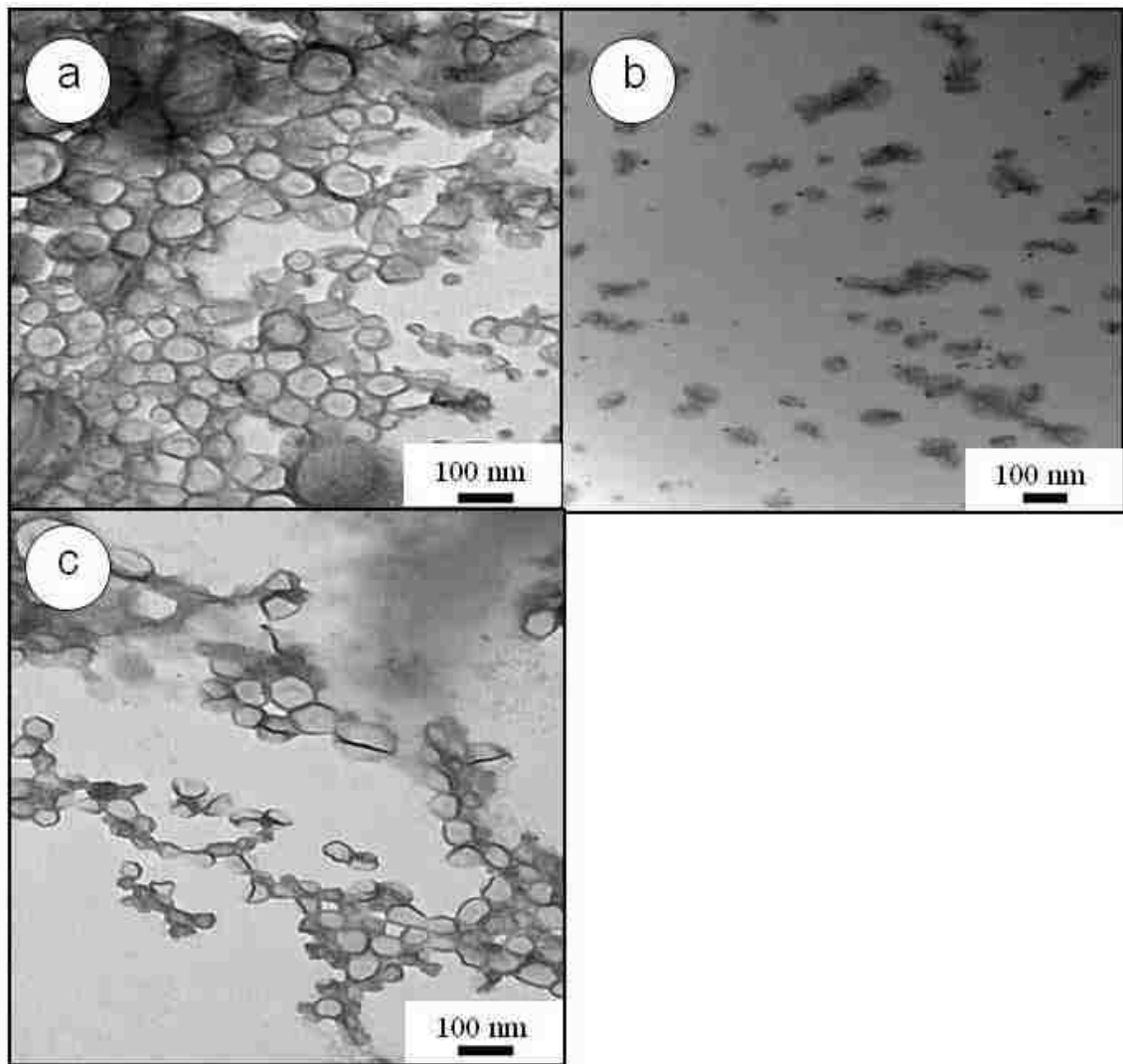


Figure 5.4. TEM images of silica particles templated in CPB/SPFO vesicle solutions (2% wt/wt, $\gamma = 0.8$, pH 3), and a TMOS/surfactant ratio of (a) $\alpha = 0.5$ and (b) $\alpha = 0.7$. (c) Silica particles templated at 2% wt/wt, $\gamma = 0.85$, $\alpha = 1$ (titration from an initial pH 6 to final pH 8 with NaOH).

5.4.6 Stable Silica Hollow Spheres in CPB/SPFO

The production of a stable solution of aqueous hollow silica spheres suggests applications of these materials in catalysis^{223,224}, coating technology, transport and controlled release of drug compounds.²²² Techniques to improve the stability of the silica hollow spheres were investigated for the system of CPB/SPFO templated silica spheres, which are less stable than the HFDPC/SPFO system using the acid-catalyzed synthesis procedure described in sections 3.5 and 3.6. In silica particle synthesis, stable sols are

known to exist in basic solution, while metastable particle formation and gelation is associated with acidic pH.²²⁵ Following the technique of Hah et al,²²⁹ in which changing the pH of the synthesis was used to modify the driving force of the condensation reactions and produce silica hollow spheres in the absence of templates, strongly basic solution was added several minutes after the addition of the silica precursor. Starting with a CPB/SPFO vesicle solution (2% wt/wt, $\gamma=0.85$) at pH 6, a precursor amount equivalent to $\alpha = 1$ was added to the solution and stirred for 15 minutes. A drop in pH to 4.5, recorded at the onset of the titration, is interpreted as conversion of the precursor to the silicic acid in the synthesis hydrolysis reaction. Drops of a 0.5 M NaOH solution were added over a two hour period in a microtitrator to a final pH of 8.

Stable sols in CPB/SPFO systems were produced by changing the pH using this synthesis procedure. The resulting hydrodynamic size and polydispersity index of the particles remain within the same range as the original vesicle solution. Two weeks after synthesis, the average hydrodynamic size (Z-average) has changed 112.9 nm (pre-synthesis) to 119 nm and the PDI increases slightly from 0.188 to 0.224. The increase in pH from 3 to 6 before addition of precursor had negligible effect on the hydrodynamic vesicle size and polydispersity. The vesicle size in pH 3 medium is 110.2 nm and increases to 112.9 nm at pH 6. The zeta potential measured after two weeks was -62.2 ± 9.59 mV and the solution was transparent without any visible aggregation or gelation. Figure 5.4c provides evidence of successful CPB/SPFO vesicle templating, with the resulting particle sizes in good agreement with DLS analysis. The pH adjustment during the synthesis reactions permitted templating at a higher TMOS/[S] ratio without gelation. As a result, a thicker coating, consistent in several micrographs is observed for the silica hollow particles, although with the spherical shape of the particles slightly deformed. The appearance of flocculated silica spheres in the pH adjusted systems may be an artifact of TEM sample preparation. The unadjusted pH samples in Figure 5.4(b) were more diluted (20 fold dilution) than in the pH adjusted samples of Figure 5.4(c) (10 fold dilution) prior to drying and TEM imaging. The lower zeta potential and visual appearance, even after a two-week period, provides strong evidence of improved colloidal stability in the latter system.

5.4.7 HFDPC/SPFO Vesicle Templated Silica Hollow Particles

In contrast to the CPB/SPFO systems (pH = 3), the initial diameter of the particles increases only slightly with the TMOS/surfactant ratio (from 204.1 nm pre-synthesis to 209.1 nm at the highest TMOS concentration, $\alpha = 1$) one day after the addition of silica precursor (Table 5.3). Overall, the zeta potential of each solution increases with the precursor to surfactant ratio over the range of $\alpha = 0.25$ -1.

Table 5.3: Synthesis of silica particles from HFDPC/SPFO vesicle solutions (1.18% wt/wt, $\gamma = 0.78$, pH = 3) as a function of TMOS:surfactant ratio (α)

	Hydrodynamic Diameter (nm) (PDI)		Zeta Potential (mV)	
	Day 1	Day 14	Day 1	Day 14
Pre-Synthesis	204.1 (0.15)		-93.6 \pm 12.3	
$\alpha = 0.25$	208.7 (0.12)	216 (0.15)	-84.3 \pm 12.0	-69.9 \pm 17.0
$\alpha = 0.35$	207.2 (0.12)	214.8 (0.14)	-77 \pm 8.3	-48.2 \pm 9.4
$\alpha = 0.5$	207.2 (0.18)	204.4 (0.1)	-53 \pm 9.2	-31.8 \pm 10.7
$\alpha = 0.7$	205.7 (0.12)	218.8 (0.14)	-35.1 \pm 8.7	-22.7 \pm 9.2
$\alpha = 0.85$	205.2 (0.1)	251.5 (0.15)	-31.7 \pm 10.0	-15.8 \pm 4.8
$\alpha = 1$	209.1 (0.1)	277.3 (0.22)	-32.3 \pm 6.0	-13.2 \pm 4.5

The hydrodynamic diameter increases significantly after the 14 days (to 251.5 nm at $\alpha = 0.85$ and 277.1 nm at $\alpha = 1.0$), although flocculation is not observed visually. This increase in hydrodynamic diameter at 14 days is interpreted as particle aggregation; the corresponding increase in the zeta potentials at 14 days relative to day one is consistent with less stable colloidal systems. However, CPB/SPFO templated silica spheres synthesized at the same TMOS/surfactant ratios flocculated to an extent that DLS analysis was not possible 14 days after synthesis (Table 5.2). Increasing the overall surfactant concentration of HFDPC/SPFO (2% wt/wt, $\gamma = 0.8$) results in the formation of gels at $\alpha = 1.0$, similar to CPB/SPFO. The ability to form fluorinated vesicles at lower overall surfactant concentrations may be beneficial to vesicle templating. The presence of

salts may accelerate gelation in acidic medium;²²⁵ lowering the concentration of ionic surfactants (and corresponding counter ions) may reduce the formation of non-templated particles.

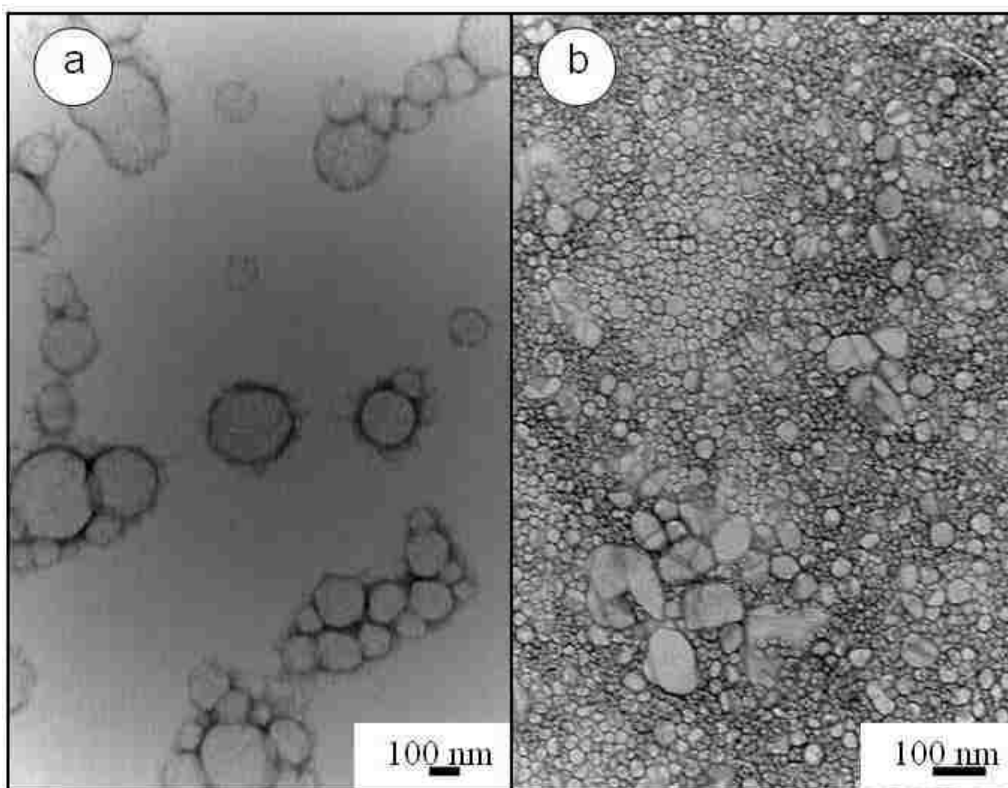


Figure 5.5. TEM images of silica particles templated from HFDPC/SPFO solutions at pH 3 (a) 1.18% wt/wt and $\gamma = 0.78$ vesicle solution with TMOS:surfactant $\alpha = 1$, and (b) 0.73% wt/wt and $\gamma = 0.72$ vesicle solution with TMOS:surfactant $\alpha = 2$.

TEM images of the HFDPC/SPFO (1.18% wt/wt, $\gamma = 0.78$, $\alpha = 1$) templated systems from TEM reveal particles with a diameter range from 100 – 300 nm (Figure 5.5a), in agreement with the hydrodynamic sizes (200 nm) of the vesicle templates (Table 5.3). Also, fewer ellipsoidal particles are observed in the fully fluorinated system than in the CPB/SPFO templated systems (Figures 5.5). The resulting hollow silica particles are spherical, suggesting that the fully fluorinated vesicles are less affected by the strain of the silica network or the incorporation of alcohol and precursor during the templating process in acidic pH. The structural differences between silica-templated in CPB/SPFO and HFDPC/SPFO vesicles may be the result of the uniform fluorinated

bilayer in the latter. Lipophobicity coupled with increased hydrophobicity and rigidity in HFDPC/SPFO bilayers would confer enhanced barrier effects to organic compounds, such as the TMOS precursor or side products of synthesis, and restrict silica synthesis to the surface of the vesicles. This rationale is supported by the ability to template at much higher TMOS/surfactant ratios ($\alpha = 2$) from the HFDPC/SPFO vesicle solution (0.73% wt/wt, $\gamma = 0.72$, pH 3). The size of the resulting silica hollow spheres templated from the HFDPC/SPFO vesicles at $\alpha = 2$ are bimodal, primarily 20 – 50 nm, with 100 nm particles present (Figure 5.5b). These particles sizes are consistent with the negatively stained vesicle images for the same composition in Figure (5.3). The same aggregate population that was undetected via DLS analysis was captured in both TEM and in vesicle templating. Thus, templating is a viable method of capturing the structural morphologies in these fully fluorinated aggregates.

Overall, the results of both CPB/SPFO and HFDPC/SPFO vesicle templating complement the negatively stained vesicle images. The improved colloidal stability exhibited by HFDPC/SPFO over CPB/SPFO systems demonstrates the tuning of surfactant properties to achieve the desired particle characteristics in template synthesis.

5.5 Conclusion

Regions of spontaneous vesicle formation have been established in fluorinated and mixed hydrocarbon /fluorinated catanionic surfactant systems of HFDPC/SPFO and CPB/SPFO using DLS and negative staining imaging (TEM) techniques. The average hydrodynamic size is 200 nm for HFDPC/SPFO systems and 100 nm for the CPB/SPFO vesicles. Stable unilamellar vesicle formation was observed at lower surfactant concentrations for the fully fluorinated catanionic vesicle bilayers, HFDPC/SPFO (0.72% wt/wt) than in the mixed hydrocarbon/fluorinated bilayers, CPB/SPFO (1.8 % wt/wt). The mixed hydrocarbon/fluorinated surfactant CPB/SPFO aggregates are more polydisperse than the fluorinated bilayer vesicles based on the PDI measured from DLS. However, apart from the vesicles in the range of 100 nm , negatively stained TEM images also reveal a separate population of ≈ 20 nm vesicles, undetected in DLS, for the fully fluorinated bilayer system of HFDPC/SPFO. The low refractive index of fluorinated chains may obscure smaller aggregates (i.e., 20 nm vesicles) in the presence

of much larger, 100 nm aggregates. A change in morphology is also observed for the fluorinated/fluorinated, HFDPC/SPFO vesicles with increasing surfactant concentration, from mostly spherical (0.73% wt/wt, $\gamma = 0.72$) to faceted multi-lamellar structures (2% wt/wt, $\gamma = 0.8$).

Successful transcriptive templating was demonstrated in the fluorinated/hydrocarbon and fluorocarbon/fluorocarbon vesicle systems. Optimal templating conditions were found to exist at lower TMOS to surfactant ratios for CPB/SPFO than for HFDPC/SPFO. Zeta potential measurements suggested that the HFDPC/SPFO vesicle templated silica spheres demonstrated better colloidal stability than the CPB/SPFO. The titration of the acidic synthesis solution with base during the synthesis reactions produced stable sols of CPB/SPFO templated particles.

The advantage of lower surfactant concentration requirements for stable spontaneous vesicle formation was clearly demonstrated in silica synthesis applications. The presence of more counter ions due to higher concentration in CPB/SPFO may have promoted aggregation in the silica systems. Most HFDPC/SPFO-templated silica particles maintain the original vesicle morphology (spherical shape) even at elevated precursor concentrations, in contrast with CPB/SPFO-templated particles, whose TEM images reveal strong deviation from the initial vesicle sphericity. The structures in the latter suggest partitioning of precursor into localized regions of the bilayer. An enhanced barrier effect of the homogeneous fluorinated bilayer matrix in HFDPC/SPFO compared with the more heterogeneous hydrocarbon/fluorocarbon bilayer of CPB/SPFO would facilitate less permeation of any organic or synthesis-related compounds, a potential effect which is being examined in future work. Additionally, the smaller 20 nm HFDPC/SPFO vesicles undetected by DLS are also captured by template synthesis of silica hollow spheres of similar size when imaged via TEM, which confirms the limitation of light scattering in capturing the true size dispersions in fluorinated aggregates. The robustness of fluorinated/fluorinated bilayers for transcriptive templating is suggested by the ability to template at higher precursor to surfactant ratios than in catanionic fluorinated/hydrocarbon vesicles with retention of the original aggregate shape.

CHAPTER 6

PHASE INVESTIGATION OF CATIONIC-ANIONIC VESICLE FORMATION IN MIXTURES OF HYDROCARBON/FLUOROCARBON AND FLUOROCARBON/FLUOROCARBON SURFACTANTS

6.1 Summary

The phase behavior of combinations of cationic and anionic surfactant mixtures of cetylpyridinium bromide (CPB), 1,1,2,2-tetrahydroperfluorododecylpyridinium chloride (HFDPC), sodium perfluorooctanoate (SPFO) and sodium perfluorohexanoate (SPFH) are investigated in aqueous solution using a combination of dynamic light scattering (DLS), visual inspection and transmission electron imaging (TEM). The selection of mixed hydrocarbon/fluorocarbon catanionic pairs; CPB/SPFO, CPB/SPFH and fully fluorinated bilayers, HFDPC/SPFO and HFDPC/SPFH provides a framework in which the impact of homogeneous and heterogeneous bilayer matrices of varying asymmetry on phase behavior can be assessed. Larger stable vesicle regions were identified in the more asymmetric CPB/SPFH and HFDPC/SPFH systems, while the narrowest vesicle region was established in the fully fluorinated least asymmetrical (HFDPC/SPFO). TEM revealed the most polydisperse vesicles in the mixed hydrocarbon/fluorocarbon system of CPB/SPFO (40 – 200 nm), while HFDPC/SPFO vesicles possessed narrower size distribution (20 – 50nm). The size and phase behavior of HFDPC/SPFO vesicles suggest enthalpic stabilization, which is attributed to the stiffness of the combined fluorinated chains, generating high membrane rigidity in the curved vesicles. In the more asymmetrical systems, TEM revealed vesicle sizes in the range 30 – 70 nm for the mixed CPB/SPFH and average vesicle size of 20 nm for HFDPC/SPFH. However, populations of large polydisperse vesicles (≥ 100 nm) were also captured in these systems, suggesting an entropic stabilization mechanism. Further characterization of the bilayer matrix of CPB/SPFO and HFDPC/SPFO with pyrene and pyrene derivatized fluorescent probes provides insight into the chain organization of the bilayers. The solvatochromic behavior of pyrene was used to determine aggregation events, such as vesicle formation. The local

intra-aggregate position of pyrene in the bilayer was inferred from fluorescence quenching and excimer formation. Pyrene derivatized probes, 1-pyrene hexadecanoic acid/ pyrene (CH₂)₁₅COOH (Py-C16), 1-pyrene decanoic acid/ pyrene (CH₂)₉COOH (Py-C10) and 1-pyrene butanoic acid/ pyrene (CH₂)₃COOH (Py-C4), allowed probing of various depths of the bilayer. Fluorescent results suggest higher chain order or better packing in the homogeneous HFDPC/SPFO than in mixed CPB/SPFO.

6.2 Introduction

The non-ideal mixing of cationic and anionic surfactants in aqueous solution yields interesting phase behavior, with formation of structures that range from mixed micelles to planar bilayers. Of particular interest are spontaneously formed vesicles, which are characterized by thermodynamic stability. This is in contrast to meta-stable phospholipid based vesicles (liposomes), which relapse to their equilibrium planar lamellar form after short periods of time. The strong electrostatic attraction of the oppositely charged headgroups results in a synergistic effect, where the effective headgroup area is less than the sum of the individual cationic-anionic headgroup areas. This, combined with the additive volume of the hydrocarbon chains of the two surfactants, effectively increases Israechavili's⁶⁰ packing parameter favoring formation of lamellar bilayers, which close to form vesicles. Factors critical to cationic vesicle formation include surfactant molecular structure,¹⁷³ cationic tail asymmetry,¹⁷⁴ temperature,¹⁷⁹ ionic strength¹⁷⁷ and the presence of organic additives.¹⁸⁰ Knowledge of homogeneous vesicle phase regions is essential for tailored applications of self-assembled aggregates. With stable vesicle domains established in pseudo-ternary phase maps, the system properties can be effectively tuned to facilitate favorable conditions for materials synthesis of nano-spheres⁵⁰ or encapsulation of model compounds.⁴⁷

Various aspects of phase behavior, mechanism of vesicle formation,^{176,200} destabilization,^{177,215} size and size distribution^{169,182,183} and bilayer characteristics have been well explored for hydrocarbon cationic surfactant mixtures.^{168,169,173,174,176,177,182,184,191,197,199,200,299} The comprehensive analysis of phase behavior in these systems frequently involves a combination of several techniques including visual observations, dynamic light scattering (DLS),^{182,278} transmission electron

microscopy imaging (TEM),^{172,300} small angle neutron scattering (SANS),⁴⁶ polarized light microscopy (POM)¹⁸⁴ and fluorescence characterization.¹⁸⁵ The composition-dependent aggregate morphology can be interpreted in terms of physicochemical properties of the individual surfactants (CMC, solubility) and is dictated by the interplay of electrostatics and geometric packing effects.⁴⁴ Key features of catanionic surfactant mixtures include precipitate formation in equimolar mixtures, with isotropic vesicle regions observed in either the anionic and cationic-rich compositions. At low concentrations, inter-vesicle interactions are governed primarily by repulsive electrostatic forces; with increased surfactant concentration, the higher number density of vesicles leads to packing constraints that induce aggregation and phase separation into multilamellar systems.¹⁹⁷ In compositions with large excess of either surfactant, the aggregate morphology and phase behavior is similar to that in the single surfactant solution.⁴⁴ The size of the vesicle region is strongly influenced by bilayer composition and can be expanded by increasing asymmetry of the catanionic pair, as observed with CTAB/SOS(C16/C8) and DTAB/SDS (C12/C12).^{44,174} Conversely, the addition of sodium bromide (NaBr) salt to CTAB/SOS vesicles produces a strong contraction of the stable vesicle region in favor of the adjacent micellar phase, through electrostatic screening of the vesicle surface.

There are limited studies exploring aggregate formation where one or both tails of the catanionic surfactants are fluorinated. Kaler and coworkers⁴⁴ provide the exception with their detailed investigations into the phase behavior of hydrocarbon/fluorocarbon surfactant mixtures of cetyltrimethylammonium bromide/sodium perfluorooctanoate (CTAB/SPFO)⁴⁴ and CTAB/sodium perfluorohexanoate (SPFH)⁴⁶ with subsequent demonstration of the former as suitable templates in synthesis of silica hollow spheres.⁵⁰ Fluorinated surfactants, which are both lipophobic and hydrophobic, possess bulkier chains than hydrocarbon surfactants. With chains in *trans-gauche* conformation, fluorinated surfactants tend to adopt lower curvature aggregate structures such as rod-like micelles and lamellar bilayers.⁷⁰ Surfactant mixtures of hydrocarbons and fluorocarbons are typically characterized by demixing into separate phase regions or aggregates.⁴³ However, the ionic attraction of oppositely charged headgroups in catanionic surfactant mixtures overrides the mutual dislike of the hydrocarbon/fluorocarbon surfactant chains.

Phase delineations using visual inspection, DLS, small angle neutron scattering (SANS) and cryo-TEM revealed isotropic vesicle domains in the anionic-rich side (SPFO and SPFH) of the phase diagrams. Interestingly, small difference in fluorinated chain length (SPFO(FC7)) and (SPFH(FC5)) alters the mechanism of vesicle formation in the two systems. CTAB/SPFO is characterized by small monodisperse vesicles, which are enthalpically stabilized⁵⁴ while CTAB/SPFH is subject to entropic-stabilization with larger, polydisperse vesicles.⁴⁶ The difference in system properties as a result of changes in surfactant chain length merits further study into the impact of fluorinated surfactants in cationic vesicle bilayers.

In previous work,³⁰¹ regions of stable vesicle formation in anionic-rich mixtures of mixed hydrocarbon/fluorocarbon and fluorocarbon/fluorocarbon cationic surfactant: cetylpyridinium bromide/sodium perfluorooctanoate (CPB/SPFO) and 1,1,2,2-tetrahydroperfluorododecylpyridinium chloride (HFDPC/SPFO) were established in acidic medium (pH 3), with the goal of using the aggregates as templates for materials synthesis. Stable vesicle dispersions were identified at lower overall surfactant concentrations for the homogeneous fluorinated bilayer, HFDPC/SPFO, than for the heterogeneous, CPB/SPFO system, which had implications in synthesis of silica hollow spheres. Hollow silica spheres synthesized from the fully fluorinated bilayer system, HFDPC/SPFO, demonstrated improved colloidal stability relative to the mixed hydrocarbon/fluorinated system, CPB/SPFO. The lower concentrations of surfactants in HFDPC/SPFO cationic vesicle systems resulted in lower concentration of counter-ions for electrostatic screening of the silica particles, which may contribute to more stable colloidal systems. An additional effect of the increased hydrophobicity and lipophobicity of fully fluorinated bilayers may be the exclusion of the reactants and by-products of the silica synthesis reactions, resulting in a more robust synthesis process.

Here, the phase investigation in acidic medium (pH 3) is expanded to include the more asymmetric cationic pairs with the shorter chained anionic surfactant, SPFH (FC5); CPB/SPFH and HFDPC/SPFH. Phase behavior is examined in acidic medium in the anionic-rich phase for CPB/SPFO, HFDPC/SPFO, CPB/SPFH and HFDPC/SPFH (chemical structures provided in Figure. 6.1). This combination of fluorinated and hydrocarbon surfactant pairs provides for the investigation of both mixed

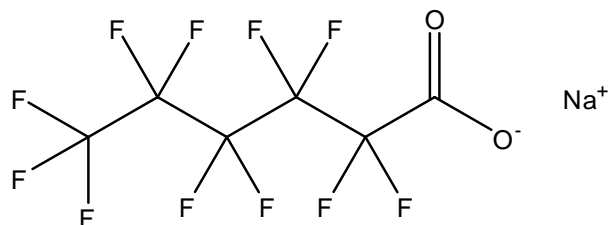
hydrocarbon/fluorinated surfactants and chain asymmetry on aggregate phase behavior. Isotropic vesicle regions are identified by visual inspection, dynamic light scattering and transmission electron microscopy. Further characterization of vesicle bilayers matrix is provided by fluorescence spectroscopic measurements of pyrene and pyrene-derivatized carboxylic acid probes. Fluorescence is a useful tool in the study of inter and intra-aggregate structural transitions and is widely applied in study of self assembled systems such as micelles,⁴² vesicles¹⁸⁵ and monolayer films.³⁰² Here, the solvatochromic character of pyrene is used to traverse micelle to vesicle transition with the photophysical processes of excimer formation and quenching providing information on intra-aggregate organization. Pyrene derivatives with increasing alkane chains length: (1-pyrenebutanoic acid (PBA/Py-C4)), 1-pyrenedecanoic acid (PDA/Py-C10) and 1-pyrenehexadecanoic acid (PHA/Py-C16)) whose chemical structures are provided in figure 6.2, are used to probe the chain packing at various depths of the vesicle bilayer.

6.3 Experimental Section

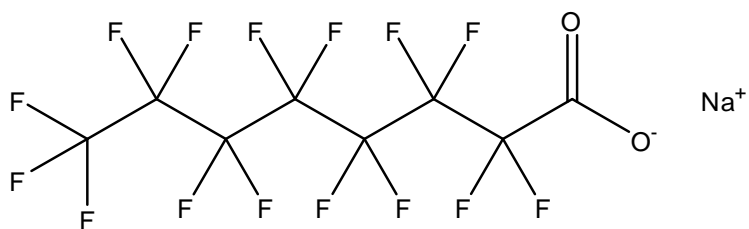
6.3.1 Materials

The fluorinated anionic surfactant, sodium perfluorooctanoate (SPFO; $C_7F_{15}COO^- Na^+$; 97% purity) and the hydrocarbon cationic surfactant, cetylpyridinium bromide (CPB; $C_{21}H_{38}N^+Br^-$; $\geq 97\%$) were purchased from Sigma Aldrich and Alfa Aesar, respectively and used without further purification. The short chained fluorinated anionic surfactant, sodium perfluorohexanoate (SPFO; $C_4F_9COO^- Na^+$) was synthesized by neutralization of perfluorohexanoic acid with NaOH and the purity tested by ^{19}F NMR spectroscopy (98% purity). The fluorinated cationic surfactant, 1,1,2,2-tetrahydroperfluorododecylpyridinium chloride (HFDPC; $C_{10}F_{21}CH_2CH_2NC_5H_5^+Cl^- \cdot H_2O$), was synthesized with greater than 98% purity, as previously described.⁴¹ In short, alkylation of pyridine with 1H,1H,2H,2H-perfluorododecyl iodide, followed by anion exchange produces the desired HFDPC. The purity of HFDPC was assessed by spectrometric and melting point measurements and was in agreement with published values.⁴¹ Reagent grade hydrochloric acid solution (0.1 N) was obtained from Alfa Aesar. The fluorescent probes, pyrene and pyrene derivatives: 1-pyrene hexadecanoic acid/ pyrene $(CH_2)_{15}COOH$ (PHA/Py-C16), 1-pyrene decanoic acid/ pyrene $(CH_2)_9COOH$

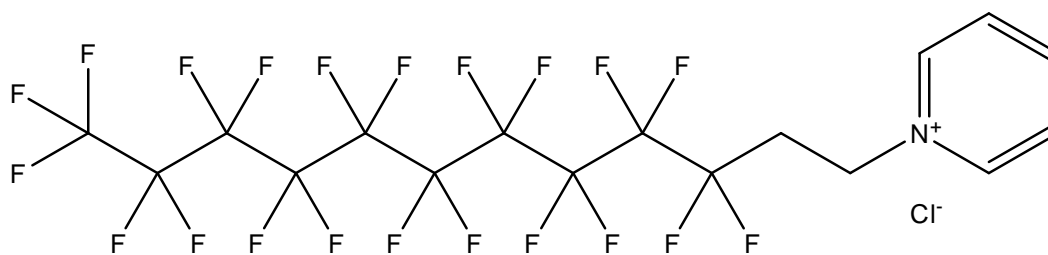
(PDA/Py-C10) and 1-pyrene butanoic acid/ pyrene (CH₂)₃COOH(PBA/Py-C4) were all purchased from Molecular Probes with greater than 99% purity and used without further purification.



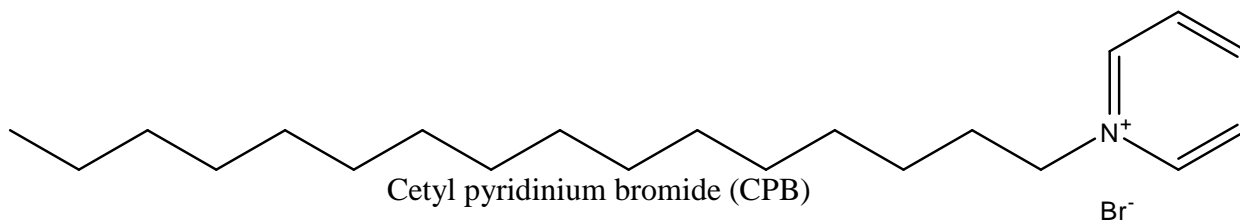
Sodium perfluorohexanoate (SPFH)



Sodium perfluorooctanoate (SPFO)



1H,1H, 2H, 2H-tetrahydroperfluorododecylpyridinium chloride (HFDPC)



Cetyl pyridinium bromide (CPB)

Figure 6.1. Chemical structures of anionic and cationic surfactants

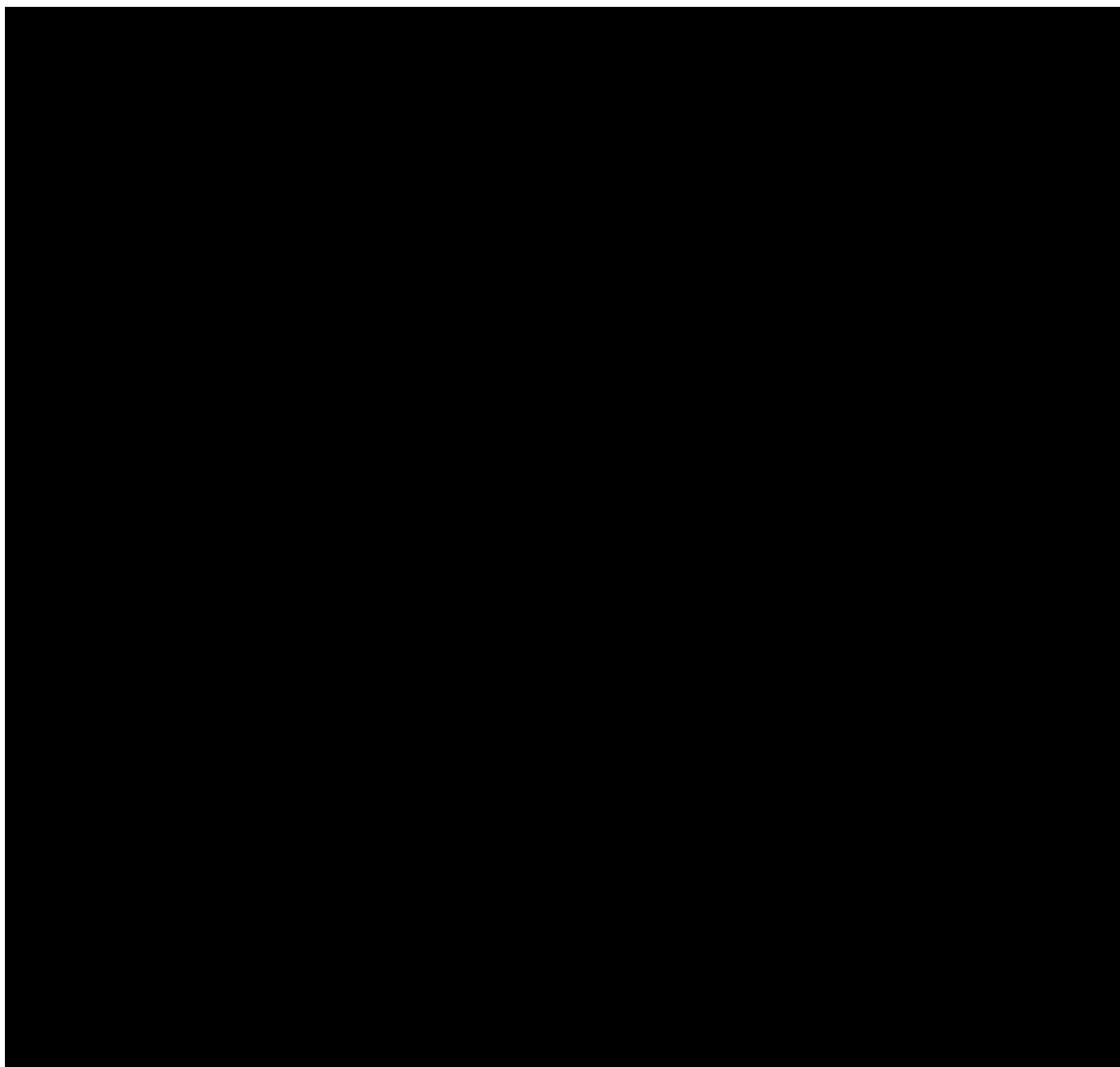


Figure 6.2. Chemical structures of pyrene and pyrene derivatized probes.

6.3.2 Sample Preparation

Cationic samples for the phase studies were prepared by mixing aqueous stock solutions of hydrochloric acid (pH 3) of the anionic and cationic surfactants in the required proportions to the desired concentrations (% wt/wt). The sample was then stirred vigorously before serial dilutions to lower concentrations. This procedure was repeated for several mixing fractions i.e. fraction of anionic surfactant, SPFO in overall surfactant mixture (γ). For mixtures containing cationic surfactants, CPB and HFDPC, the individual surfactant solutions were heated to 50°C for a few minutes prior to mixing with the anionic surfactant solutions.

6.3.3 Phase Assignment

The different aggregate phases typically observed in cationic surfactant mixtures were designated using visual observation and dynamic light scattering (DLS). Vesicle characteristics were subsequently characterized by negatively stained transmission electron microscopy imaging (TEM).

Dynamic Light Scattering (DLS) and TEM Analysis

The hydrodynamic size and polydispersity of the cationic surfactant aggregates at 25°C were monitored periodically using a Malvern Zetasizer Nanoseries (Malvern Instruments, United Kingdom). The instrument was equipped with a He-Ne laser lamp (4 mW) source at 633 nm and measurements were taken at 90° scattering angle. The data were analyzed with the Cumulants Method,²⁹² which employs a single exponential fit of the intensity of the autocorrelation function to derive an average translational diffusion coefficient. An intensity weighted size average (Z-average) was then calculated using the Stokes-Einstein equation. The Z-average (intensity weighted average) and polydispersity index (PDI) were taken as representative of the size and size distribution in the samples. The PDI is given on a scale of 0 – 1.0, where 0 represents the highest level of monodispersity.

A Philips Tecnai BioTwin unit (Edax detector) with a Gatan Digital Micrograph 1000 operating at 100kV was used to image the surfactant aggregates. A negative staining procedure with uranyl acetate solution (2 w/v%) was used to image vesicle

solutions without silica. 5 μL drops of vesicle solutions were gently placed on copper coated formvar grids and blotted after 1.5 minutes. Identical volumes of stain solution were immediately added and one minute was allowed before blotting the grids with filter paper and air drying.

6.3.4 Probing Surfactant Aggregates using Fluorescence Spectroscopy

For measurements in vesicle systems, ethanol solutions of the probes and cationic surfactants (CPB, CTAB, HFDPC) in the required proportions were dried under an inert low pressure nitrogen stream for 4-6 hrs to form a dry film. The film was further dried under vacuum to remove any residual solvents. Aqueous solutions of the anionic surfactant, SPFO, was then added to the film and heated at 50 $^{\circ}\text{C}$ for 40 minutes. The vesicle solutions were mixed further at 25 $^{\circ}\text{C}$ for another five hours. The surfactant mixtures were filtered using 0.45 micron filters. The hydrodynamic sizes of the vesicles were determined by DLS. One vesicle composition in the anionic-rich region was investigated for each surfactant pair: CPB/SPFO (2 wt/wt%; $\gamma = 0.85$), CTAB/SPFO (2 wt/wt%; $\gamma = 0.85$) and HFDPC/SPFO (1.18 wt/wt%; $\gamma = 0.78$). All samples were prepared in neutral pH solutions. To induce micellization of the cationic vesicles, NaCl salt in dry crystal form was added to the systems, heated and mixed thoroughly. For studies with individual surfactant solutions (i.e. SPFO micelles, CPB micelles, HFDPC micelles), ethanol solutions of the probes (without surfactant) were dried as described above and aqueous solutions of the surfactant added. The same fixed concentration (5 μM) of pyrene and its derivatives was used in all the experiments. For the steady state fluorescence analysis, the excitation wavelength was set at 334 nm with respective excitation and emission widths of 5 nm and 1.5 nm.

6.4 Results and Discussion – Phase Behavior

The partial phase diagrams for cationic surfactant pairs: CPB/SPFO, HFDPC/SPFO, CPB/SPFH and HFDPC/SPFO are presented in Figures 6.3(a) – (d), respectively at 25 $^{\circ}\text{C}$. Phase behavior study was limited to the anionic phase region and assessed in acidic medium (pH 3) with implications for template synthesis applications. The phase boundaries were estimated from visual inspections and DLS analysis after

several months (≥ 2 months) and the morphology of the cationic vesicles were confirmed with TEM imaging. Preliminary assessment of the CPB/SPFO and HFDPC/SPFO systems is provided in an earlier work, where compositions of stable vesicle formation were identified.³⁰¹ Here, the systems in the anionic-rich vesicle phase boundaries are clearly defined. Also, determination of the phase behavior is presented for the more asymmetric mixed and fully fluorinated counterparts, CPB/SPFH and HFDPC/SPFH, chain asymmetry on phase behavior in vesicles.

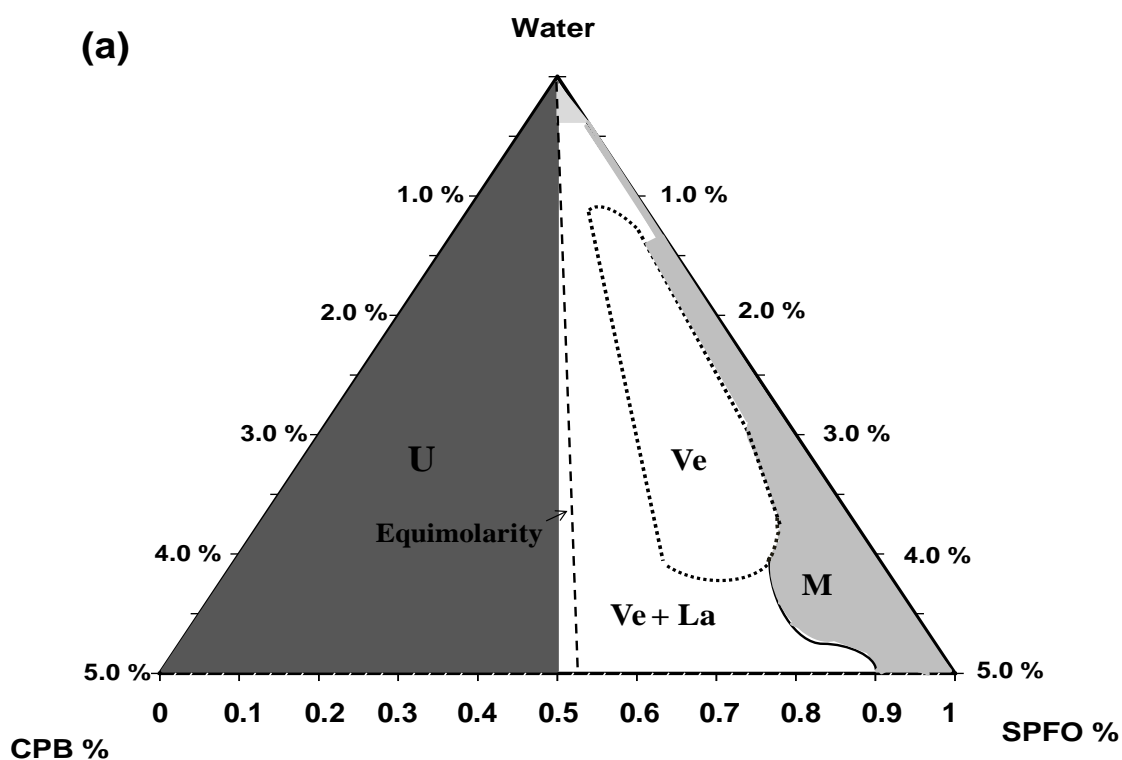


Figure 6.3: Partial Phase Diagrams of (a) CPB/SPFO, (b) HFDPC/SPFO, (c) CPB/SPFH and (d) HFDPC/SPFH in acidic solution (pH 3). Ve denotes the vesicle region, Ve + La, the vesicle and lamellar phase region, M, micelles, M-P, multiphase regions, B-G, bluish gel phase and U, the experimentally undetermined phase. The total surfactant concentrations are in wt/wt% units while the bottom axes of the phase diagrams represent the mass fraction of the anionic surfactants, γ .

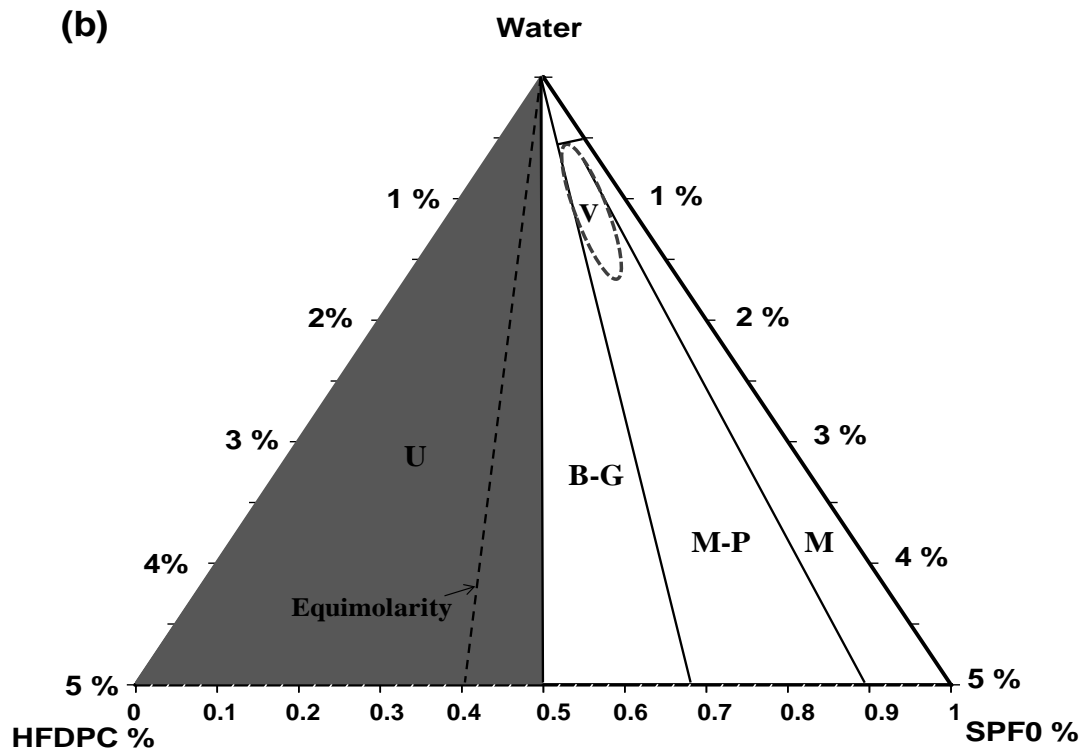


Figure 6.3 Continued

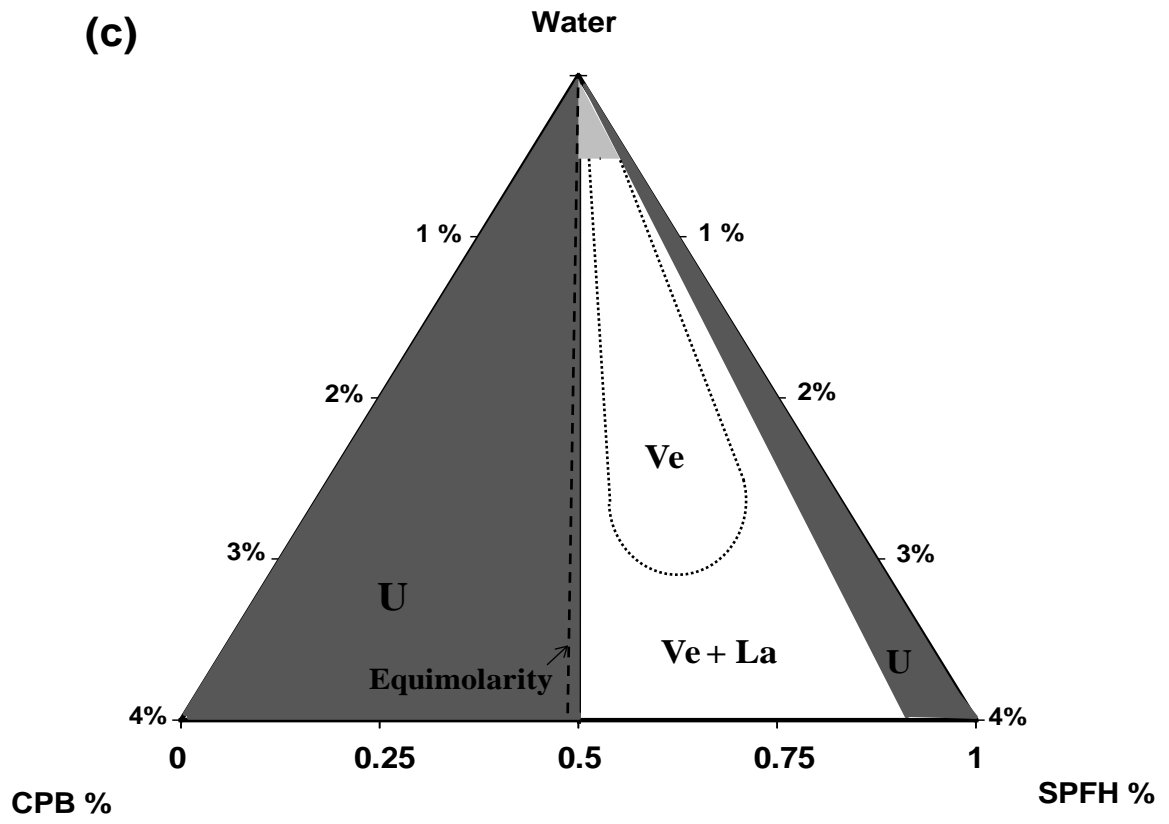


Figure 6.3 Continued

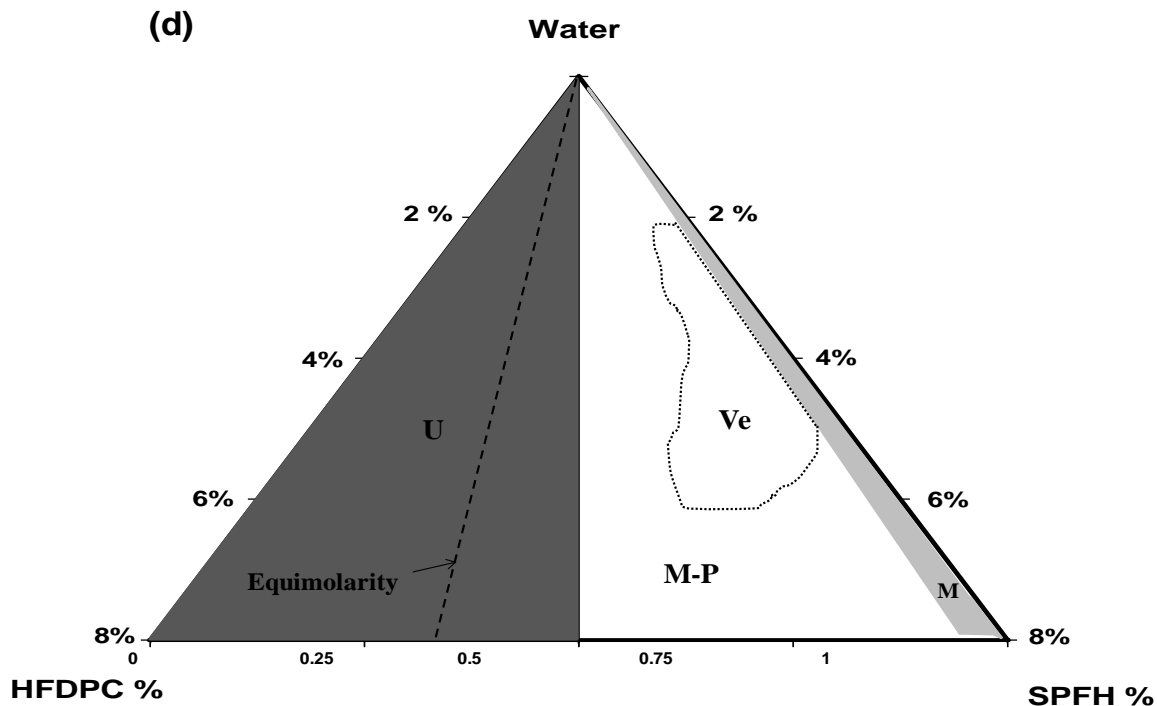


Figure 6.3 Continued

6.4.1 CPB/SPFO Aggregates

The phase behavior CPB/SPFO is assessed in an overall surfactant range of 0 – 5% wt/wt with $\gamma = 0.5 - 1$, where equimolar composition was at $\gamma = 0.53$. Phase boundaries were assigned based on over 100 samples monitored for a minimum of 2.5 months. The isotropic vesicle domain depicted in figure 6.3(a) was established after a five month observation period. For the pure SPFO solutions (0.1 - 4% wt/wt; $\gamma = 1$), a clear liquid was observed, where the CMC of SPFO is (1.35% wt/wt/31 mM).²⁸⁷ As depicted in the phase diagram, the micellar solution is still present for compositions up to $\gamma = 0.9$. The low refractive index of fluorinated chains limited accurate assessment of micellar size by DLS. However, rod-like micelles have been assigned to this region in the structurally similar CTAB/SPFO (> 2wt%) system and are the expected structural transition for fluorinated surfactants such as SPFO.⁴⁴ At low total surfactant concentrations (i.e. < 0.5% wt/wt) over all the mixing ratios ($\gamma = 0.5 - 1$), two phase systems comprising a clear upper fluid phase, which exhibited minimal light scattering with flocs and settled precipitate was observed. Similar observations are reported for

CTAB/SOS, where crystalline precipitates were detected in all mixing ratios for low surfactant concentrations ($< 0.1\text{wt}\%$).¹⁶⁸ Dilution to the region below the CMC of SPFO would expectedly generate surfactant monomers. However the presence of minute amounts of the cationic CPB ($0.025\% \text{ wt/wt}/0.64 \text{ mM}$)²⁹⁶ would result in complexation with SPFO and small amounts of crystalline precipitate, explaining the crystals observed in this region. The non-ideal mixing behavior of catanionic surfactant mixtures means their critical aggregate concentrations are significantly lower than that of the individual surfactant CMCS.⁴⁴ Hence, even in this very dilute composition region, aggregates of CPB/SPFO are expected. Future characterization of these samples with polarized optical microscopy would clarify the nature of the structures that constitute the precipitates.

Adjacent to the SPFO-rich micellar region, with increasing amounts of CPB (decrease in γ) in the surfactant mixtures, is the isotropic vesicle lobe. In the vesicle region (approx. $1 - 4\% \text{ wt/wt}$; $\gamma = 0.7 - 0.9$), the samples possess the bluish tint ascribed to Rayleigh light scattering and DLS sizes consistent with vesicle morphology. Within the vesicle lobe, the hydrodynamic sizes (diameters) ranged from 98.91 nm ($\text{PDI} = 0.1$) to 149.8 nm ($\text{PDI} = 0.3$). No consistent trend of vesicle size with overall surfactant concentration was determined from DLS measurements. Several studies have shown that within the isotropic vesicle region, dilution along a fixed surfactant composition γ (vertical slice across phase diagram), does not affect the size of vesicles but that the number density or volume fraction of vesicles increases with surfactant concentration.^{169,197} However, for a fixed surfactant concentration (horizontal slice across the phase diagram), vesicle size increased slightly as ratio of CPB increased (γ decreased). In effect, as the surfactant composition approached equimolarity, DLS reported slightly larger vesicle sizes. This effect might be ascribed to the alteration of bilayer interfacial curvature with increasing incorporation of CPB (γ decrease) in the aggregate systems.¹⁶⁹

Bordering the isotropic vesicle domain is a two-phase region speculated to consist mainly of vesicles and condensed lamellar structures in equilibrium.^{44,168} In this region, for surfactant concentrations $\geq 0.5\% \text{ wt/wt}$, the samples display a bluish tint which gets deeper as the concentration increases. At higher total surfactant concentrations ($> 3\% \text{ wt/wt}$), the bluish phase becomes much more turbid with an almost milky-blue color,

which is indicative of multi-bilayer aggregates. However, all samples within this region also possess a cloudy phase settled at the bottom of the vessels, which has been reported to be a condensed lamellar phase.¹⁶⁹ The thickness of the cloudy layer increased with increase in total concentration and at concentrations below 1.5% wt/wt, only cloud-like wisps were observed. Gentle shaking produced a homogenous turbid dispersion with reversion to the separated phase after a few days. This suggests that these systems consist of vesicle aggregates in equilibrium with a condensed lamellar phase.⁴⁴ DLS analysis of the upper bluish phase of the biphasic solutions revealed aggregate diameters that ranged from 118.6 – 250 nm with PDIs that varied from 0.1 - 0.55. In effect, this observation supports the view that dense packing of vesicles leads to aggregation and destabilization to multi-lamellar bilayers. Overall, the phase diagram is strikingly similar to that of CTAB/SPFO (neutral pH) described by Kaler and coworkers⁴⁴ which has a stable vesicle region in approx. 0.5 – 4 wt%; $\gamma = 0.75 - 0.9$. Indeed a full phase map (0 – 8wt%; $\gamma = 0 - 1$) was established for CTAB/SPFO and revealed a predominantly biphasic region of vesicles and lamellar structures, which spanned a wide surfactant composition range; $\gamma = 0.2 - 0.75$. With the CPB/SPFO system, in this study, TEM analysis of samples bordering the biphasic region (1% wt/wt; $\gamma = 0.85$) revealed large vesicles of size range 300 – 500 nm (Figure 6.4a). Also captured in Figure 6.4(b) are regions of dense packing with vesicle aggregation. For samples within the vesicle lobe, our previous TEM analysis³⁰¹ captured a polydisperse distribution, ($\approx 40 - 200$ nm) of spherical unilamellar vesicles with a small population of cylindrical bilayer vesicles (125 – 200 nm), similar to those detected by cryo-TEM in CTAB/SPFO system by Jung et al.¹⁷¹ However, where the CTAB/SPFO systems were shown to be enthalpically stabilized monodisperse vesicles (30 – 60 nm), our CPB/SPFO vesicles are polydisperse, indicative of entropic stabilization. With similar chain lengths (C16/FC7), the difference in stabilization mechanism must be influenced by the headgroups. Compared with the tetrahedral trimethylammonium in CTAB, the planar pyridinium headgroup in CPB would result in different headgroup attraction with SPFO, which affects the bilayer rigidity (or flexibility). Enthalpically stabilized vesicles are formed from bilayers with high bending rigidity compared with the low bending rigidity in entropic systems and the exchange of CPB for CTAB might have caused the change in mechanism.

6.4.2 HFDPC/SPFO Aggregates

The phase behavior of HFDPC/SPFO is assessed in an overall composition range of 0 – 5% wt/wt; $\gamma = 0.5 - 1$, which was beyond the equimolar composition ($\gamma = 0.39$), as depicted in Figure 6.3 (b). The samples were monitored for a minimum of 2.5 months before assignment of phase boundaries. Similar to CPB/SPFO, the phase boundary of predominantly SPFO surfactant mixtures ($\gamma > 0.9$), is characterized by clear liquid solutions. Also, as seen with CPB/SPFO, for weight ratios of SPFO/CPB greater than 0.8 and in dilute surfactant systems ($\leq 0.5\%$ wt/wt), settled precipitate was observed.

The catanionic surfactant mixture of two fluorocarbon surfactants possesses a much smaller isotropic vesicle region than with the mixed hydrocarbon/fluorocarbon, CPB/SPFO. In the vesicle region (0.6 – 1.5% wt/wt; $\gamma = 0.7 - 0.9$), the diameter from DLS analysis is 120 – 272 nm, with corresponding PDIs of 0.09 – 0.24. No size dependence was found with concentration or stoichiometry within the vesicle lobe for HFDPC/SPFO. Previous TEM results suggested that the HFDPC/SPFO system in this region was mainly populated by small unilamellar vesicles, much smaller (20 – 50 nm) than determined by DLS, although there was a small population of larger vesicles (≈ 100 nm).³⁰¹ The discrepancy between DLS and TEM diameters is a common feature of colloidal size assessment, as DLS is an intensity based size measurement weighted toward the detection of larger colloids. The measurement of fluorinated vesicle size is further hindered by the low refractive index of the fluorinated chains in HFDPC/SPFO,³⁰³ which further limits the detection of small sized vesicles in presence of larger ones. Even with mixtures of hydrocarbon surfactants such as CTAT/SDBS, whose chains have higher refractive indices, Coldren et al¹⁸² report size discrepancies as high as 33% between DLS and their cryo-TEM measurements of vesicle size.

Previously, we assessed HFDPC/SPFO vesicle to possess narrower size distribution than CPB/SPFO³⁰¹ and this is clearly evident in Figure 6.4(c). The TEM image shows HFDPC/SPFO vesicles, which range from 20 – 40 nm, coexisting with cylindrical bilayer aggregates (≤ 50 nm), (not previously characterized) that are also observed in CPB/SPFO system. Interestingly, the sizes of the HFDPC/SPFO vesicles appear to be more narrowly distributed than the CPB/SPFO.

The HFDPC/SPFO phase map possesses a sizeable unresolved multi-phase region adjacent to the micellar region and at concentrations above the vesicle region. In this region, ($>1.5\%$ wt/wt; $\gamma = 0.7 - 0.9$), samples were clear fluid. The increased viscosity of these solutions relative to the micellar region suggests the presence of rod-like micelles, but other aggregates might be present. DLS measurements in this region indicate very large aggregates (400 to > 600 nm) with very high polydispersities ($PDI > 0.54$).

Adjacent to the multi-phase region is a phase state denoted as the blue-gel (B-G) phase region; at these compositions, the system is turbid and assumes gel-like qualities with high viscosity (macroscopic flow retardation). The viscosity of the samples increases as the compositions become increasingly enriched in HFDPC. For pure HFDPC surfactant solutions (pH 3) within this composition range, the viscosity also increased with increasing surfactant concentration. DLS sizes in this region of the blue-gel region of the phase diagram were exceedingly large (> 500 nm) with PDIs greater than 0.6.

Previously, large faceted multilayered vesicles (300 – 500 nm) were captured by negatively stained TEM in HFDPC/SPFO system in the multiphase region (2% wt/wt; $\gamma = 0.8$, pH 3), which suggests transition to a planar bilayer morphology.³⁰¹ This faceted vesicle morphology has been observed in mixed hydrocarbon/fluorocarbon bilayer,²⁷⁸ and ascribed to molecular segregation in the bilayer with crystallization of chains.²⁰⁶ TEM images revealed V- shaped rolled-up bilayer structures (Figure 6.4(d)) with sizes ≈ 100 nm mixed with unilamellar spherical vesicles for HFDPC/SPFO compositions close to the boundary of the turbid-gel boundary phase (0.7% wt/wt; $\gamma = 0.68$). These rolled up bilayer aggregates bear similarities to tubules or rolled up bilayers detected by freeze fracture TEM and phase contrast optical microscopy in aqueous dispersions of single chained fluorinated (FC8 – FC10) dimorpholinophosphate surfactant.³⁰⁴ Similar rolled up membranes have also been captured by negative stained TEM images in equimolar mixtures of catanionic hydrocarbon/fluorocarbon sugar-based surfactants (perfluorodecyl derivatives).²⁷⁴ The proposed mechanism of formation of these aggregates is the aggregation and fusion of vesicles to flat or loosely coiled membrane sheets, which roll from opposite edges to form U or V-shaped tubules.³⁰⁴ Giulieri and Krafft¹⁶³ suggest that

fluorinated chains crystallize in sections of the bilayer due to rigidity, reduced mobility and conformation of FC chains, effectively inducing this morphological transition.

A narrower concentration region for vesicle formation is observed for HFDPC/SPFO (Figure 6.3(b)) relative to CPB/SPFO (Figure 6.3(a)). This can be attributed to the homogeneous fluorinated bilayer in the former compared with the heterogeneous bilayer in the latter, although the chain asymmetry might play a role, (C12/C7) versus (C16/C7). The combined fluorinated chains in HFDPC/SPFO would result in more efficient packing than in the mixed CPB/SPFO bilayer, which is expected to impact the bilayer rigidity. Fluorinated chains are stiff and bulky and the curvature energy required to form vesicles would likely be higher with HFDPC/SPFO than CPB/SPFO. Spontaneous vesicle formation in cationic surfactant mixtures is a compromise between the entropy of mixing and membrane curvature elasticity.¹⁸² Studies^{54,172} have shown that the CTAB/SPFO bilayers possess high membrane rigidity, \approx 12 times higher than that determined for hydrocarbon pair, CTAT/SDBS,¹⁸² due to the bulkiness and stiffness of fluorinated chains. The high membrane rigidity resulted in enthalpically stabilized vesicles in CTAB/SPFO with narrow size distribution. The narrow size distribution is a criterion for the enthalpic stabilization mechanism due to the penalty associated with deviation from the spontaneous curvature.⁵⁴ Factors that reduce membrane rigidity, such as branched chains,¹⁸² chain asymmetry⁴⁶ and counter-ion association¹⁷² typically produce entropically stabilized vesicles and expand the vesicle phase region. Indeed, the addition of small amounts of polymer induced dramatic changes in the stabilization mechanism of CTAB/SPFO by strong reduction in bilayer rigidity.⁵³ The smaller vesicle region in HFDPC/SPFO suggests that higher bending rigidity (anticipated to be higher than the mixed CPB/SPFO) and smaller chain asymmetry, imposes restrictions on vesicle formation outside a small composition range due to the high energy required to bend the chains for vesicle curvature.

6.4.3 CPB/SPFH Aggregates

The phase behavior of CPB/SPFH is assessed in an overall surfactant range of 0 - 5% wt/wt with $\gamma = 0.5 - 0.9$, with equimolarity beyond the scope of this work at $\gamma = 0.47$. Phase boundaries were assigned based on over 70 samples, which were observed for over

six months. The region adjacent to the binary axis, SPFH-water ($\gamma = 0.95 - 1$), was not experimentally determined and marked U in Figure 6.3(c). SPFH aqueous solutions have been reported to consist of rod-like micelles above the CMC (172 mM/5.7% wt/wt), which is approximately 6-fold higher than that of SPFO. In the dilute surfactant region ($< 0.5\%$ wt/wt) for almost all mixing ratios, clear solutions were identified with white precipitates, which is similar to observations made for CPB/SPFO and HFDPC/SPFO. As with the CTAB/SPFH⁴⁶ the CPB/SPFH phase map is dominated by the biphasic vesicle/lamellar region. DLS analysis of the homogeneous upper phase suggested sizes in the biphasic region which were consistent with the presence of vesicles (115 – 181 nm) with moderate polydispersity < 0.4 .

The isotropic vesicle lobe for CPB/SPFH exists in the approximate range of 0.5 – 3% wt/wt, $\gamma = 0.6 - 0.85$, as delineated in the phase map in Figure 6.3 (c). DLS provides vesicle sizes which range from 121 nm - 157 nm with low polydispersities (PDI = 0.05 - 0.18). TEM revealed spherical vesicles mostly in the range of 30 – 70 nm for this system (Figure 6.4e), although some larger more polydisperse vesicle populations (≈ 100 nm) were also observed. The anionic-rich vesicle region exists for a slightly wider composition range in CPB/SPFH than in CPB/SPFO (1 – 4% wt/wt; $\gamma = 0.7 - 0.9$), with stable vesicle formation observed at lower surfactant concentrations for the less asymmetric pair (C16/FC7). This parallels the CTAB/SPFH and CTAB/SPFO system, where slightly larger vesicle phase regions were determined for the more asymmetric pair. The structurally similar system of CTAB/SPFH⁴⁶ revealed a vesicle phase region in a composition range of 1.8 – 4.2 wt% ($\gamma = 0.8 - 0.99$). The CTAB/SPFH vesicles were reported to be polydisperse, suggesting entropic stabilization, in contrast to the less asymmetric CTAB/SPFO system, which is enthalpically stabilized.⁴⁶ The expansion of the vesicle region was ascribed to the increased chain asymmetric effect and the higher solubility of the SPFH surfactant which contributed to the different stabilization mechanisms reported.

6.4.4 HFDPC/SPFH Aggregates

The phase behavior of HFDPC/SPFH is assessed in a wide concentration range of approximately 0 - 8% wt/wt with $\gamma = 0.5 - 1$ (equimolarity at $\gamma = 0.33$). Samples were

examined for at least 2 months before phase boundaries were designated. At high concentrations ($\geq 5\%$ wt/wt) in the multi-phase region (M-P) in Figure 6.3(d), the samples were biphasic, with bluish upper phase and sedimented cloudy lower phase, suspected to be condensed lamellar phase observed in previous systems. Some of the samples in this region closer to equimolarity, ($\geq 4\%$ wt/wt/ $\gamma < 0.55$), exhibited slight macroscopic viscosity, suggesting the coexistence of rod-like micelles with vesicles and lamellar aggregates. Aggregates in these multiphase region range from 121 – 370 nm in diameter (PDIs = 0.13 – 0.55).

As illustrated in Figure 6.3(d), the anionic-rich vesicle lobe of HFDPC/SPFH mixtures exists close to the binary phase axis and spans a large composition range (from approx. 2 – 5% wt/wt; $\gamma = 0.65 - 0.95$.) Vesicle sizes in the range of 94.9 - 160.8 nm with PDIs = 0.02 – 0.39, as measured by DLS. TEM images revealed relatively monodisperse populations of small unilamellar spherical vesicles ≈ 20 nm in the vesicle lobe (3.7% wt/wt; $\gamma=0.9$) in Figure 6.4(f). This is similar to the size distribution of HFDPC/SPFO vesicles. However, in other sections of the TEM grid much larger polydisperse vesicles (30 – 150 nm) are detected. Compared with the similar homogeneous fluorinated but less asymmetric HFDPC/SPFO bilayer, (FC10/FC7 vs FC10/FC5) the vesicle region is established at higher surfactant concentrations over a much larger composition range. This effect might be a combined function of the CMC of SPFH, which is four-fold greater than that of SPFO and the increased asymmetry.

6.4.5 Summary of Phase Behavior

The structural transition of aggregate morphology through the different phase states is a combined effect of surfactant geometry and electrostatic interactions. A clear demonstration has been made of the ability to modulate complex phase behavior in catanionic surfactants by changes in fluorinated surfactant geometry. The largest isotropic phase region was established in the fully fluorinated bilayer, HFDPC/SPFH (2 – 5% wt/wt; $\gamma = 0.65 - 0.95$), which also possesses the largest asymmetry. The smallest vesicle region was observed in the least asymmetric fluorinated pair, HFDPC/SPFO (0.6 – 1.5% wt/wt; $\gamma = 0.7 - 0.9$). This was ascribed to the stiffness of the combined fluorinated chains generating very rigid bilayer membranes. TEM analysis reveals

smaller size vesicles with narrower size distributions in HFDPC/SPFO (20 – 50 nm), HFDPC/SPFH (≥ 20 nm) and CPB/SPFH (30 – 70nm) than in CPB/SPFO (40 – 200 nm) systems. However, a small population of large vesicles were also captured in the fully fluorinated system, HFDPC/SPFO (100 nm), which skewed the DLS measurements towards large average sizes. The size distributions suggest that all the systems with the exception of HFDPC/SPFO are dictated by entropic stabilization mechanism. Taking into account, the expected high membrane rigidity of combined fluorinated chains, enthalpically stabilized vesicles are expected for the HFDPC/SPFO system and the smaller size distribution does support this rationale. However, the presence of a few large vesicles (≈ 100 nm) does not currently allow for effective resolution of the stabilization mechanism. Further detailed characterization of this system with cryo-TEM analysis of the various compositions within the vesicle region, would help clarify the stabilization mechanism. HFDPC/SPFO vesicle region with cryo-TEM analysis would improve understanding of the mechanism of this system.

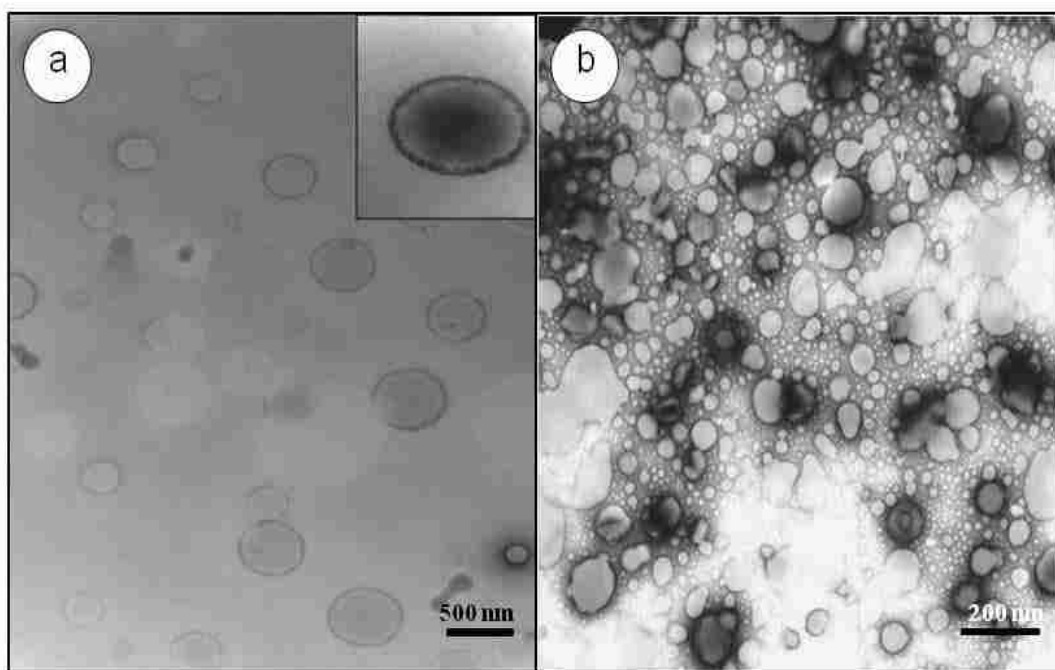


Figure 6.4: Images of negatively stained aggregates in (a) CPB/SPFO in 1 % wt/wt; $\gamma = 0.85$ and (b) 3% wt/wt; $\gamma = 0.65$ (c) HFDPC/SPFO in 0.92 % wt/wt; $\gamma = 0.85$ and (d) 0.7 % wt/wt/ $\gamma = 0.7$. (e) CPB/SPFH 1% wt/wt; $\gamma = 0.65$. (f) HFDPC/SPFH 3.7% wt/wt; $\gamma = 0.9$.

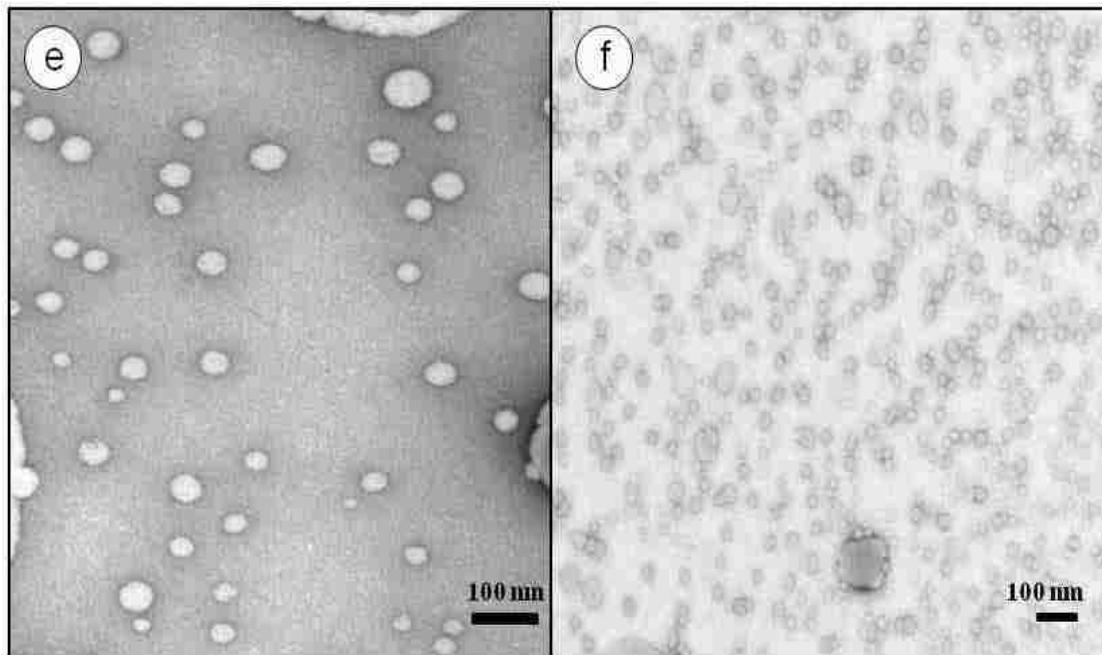
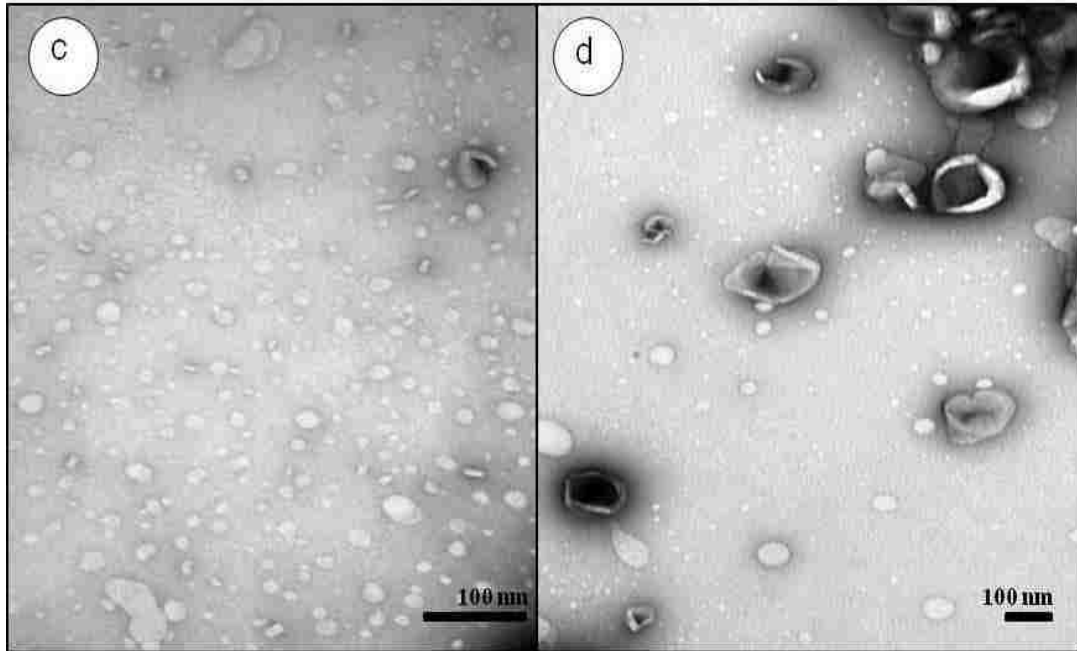


Figure 6.4 Continued

6.5 Results and Discussion – Fluorescence Study

Vesicle formation and bilayer organization in the cationic surfactant systems, CPB/SPFO, HFDPC/SPFO, is characterized with fluorescence spectroscopic probes, pyrene and 1-pyrene carboxylic acid derivatives, in neutral pH conditions. Interpretation of the fluorescence results was first verified for the well characterized CTAB/SPFO vesicle system.⁴⁴ The surfactant compositions chosen are within the vesicle phase lobes for the three systems used in the investigation. The fluorescent probes were also utilized in study of micellar systems of the single surfactant solutions prior to study of vesicle formation. Disintegration of the vesicles to mixed micelles with the addition of NaCl is detected by visual observation and DLS measurements. Probing these mixed micelle systems, provides information on the nature of the surfactant aggregates.

The solvatochromic behavior of pyrene, excimer formation and fluorescent quenching in different solvents or aggregate systems serve as useful indicators of perturbations to the local environments for the mixed and single surfactant systems. The pyrene solvatochromic parameter, which is a ratio of the first to third vibronic peak (I_1/I_3) of the fluorescence spectra is an index of solvent polarity,³⁰⁵ that is widely applied in the analysis of aggregate structures in surfactant solutions³⁰⁶⁻³⁰⁸ and has been used to identify regions of micelle formation. I_1/I_3 values decrease from polar aqueous environments (1.8) to apolar hydrocarbon solvents such as hexane (0.6), with solvents of intermediate polarity (methanol = 1.38, ethanol = 1.15, isopropanol = 1.05)³⁰⁹ between these end points.³⁰⁶ The formation of excimers, which are transient dimer complexes of an excited pyrene moiety and unexcited pyrene (ground state pyrene) moiety, is often interpreted as a diffusion controlled process.³¹⁰ The frequency of excimer formation (as measured by the intensity of the excimer fluorescence peak) is directly related to the proximity of the pyrene molecules and is a measure of microfluidity of their environment. Pyrene excimer formation is often employed in the study of membrane viscosity of liposomes,³¹¹ and biological membranes,³¹² the structural organization of monolayer films³¹³ and the microfluidity of surfactant aggregates. Quenching of the monomer fluorescence intensity results from several processes, which include dynamic interactions (dynamic collisions) with the quenching moiety, ground state complex of pyrene with the quencher (static quenching), excited state reactions, molecular rearrangements and energy transfer

mechanisms.²⁶⁶ Pyrene quenching is used to determine the location of the fluorophore in the aggregate systems, hence used to qualify the probe localization in the aggregates. Interactions between the quencher and fluorophore are typically defined by the distance of closest approach which is the combined radii of the fluorophore and quencher. This is based on the Smoluchowski model³¹⁴ further defined by Collins and Kimball's³¹⁵ radiation boundary condition (RBC), where direct contact is required for quenching and is interpreted as a diffusion controlled process. Complete quenching is taken as a short ranged molecular interaction between the fluorophore and quencher (over a small space of $< 2\text{\AA}$ ²⁶⁶) taking into consideration the van der Waals interactions. However, distance dependent quenching model has been defined for certain fluorophore-quencher interactions.³¹⁶ Typically these involve molecules where long range energy transfer contributes to quenching but the spatial interactions are still defined by short distances in angstroms.³¹⁷ Additionally this complex quenching effect is assessed using time resolved fluorescence techniques^{316,317} beyond the scope of steady state fluorescence applied here.

The pyrene carboxylic acids used in this investigation are derivatives of the pyrene fluorophore (structures in Figure 6.2). They differ in the alkane chain lengths between the pyrene moiety and terminal carboxylic group (COOH): 1-pyrenebutanoic acid/Py-C4 (PBA), 1-pyrenedecanoic acid/Py-C10 (PDA) and 1-pyrenehexadecanoic acid/Py-C16 (PHA), which provides flexibility to probe various depths of the bilayer matrix and provide insight into the bilayer chain order or organization. All fluorescence experiments were replicated thrice and the values presented represent the average of these experiments (the single surfactant micelle systems, represent the average of two experiments).

Fluorescence Analysis Assumptions

The following section constitutes mainly a qualitative analysis of the fluorescence results and assumptions made about the pyrene and derivatized probe behavior are briefly discussed here. The recognized quenchers in this study are the pyridinium headgroups in cationic surfactants, CPB and HFDPC and the bromide counterion. Pyrene quenching with the pyridinium headgroup is known to occur via an excited charge transfer complex.³¹⁸ With the bromide ion, there is an intersystem crossing to an excited

triplet state with a long life time which leads to quenching by other processes.²⁶⁶ As a result, quenching by the pyridinium headgroups is expected to be much more pronounced than by the bromide counterions. Considering the space requirements of quenching, a reasonable assumption has been made that the pyrene is sequestered in the micellar or bilayer aggregates and the phenomena of quenching and excimer formation is a direct result of this localization which brings the pyrene in close proximity with CPB or HFDPC. The possibility that the sequestered pyrene or pyrene derivatives might be affecting intra-aggregate or bilayer dynamics, which in turn influences the fluorescence spectra has not been taken into account as the surfactant to probe ratios used here are sufficiently high. Also exciplex formation of the surfactants and pyrene molecules and their contribution to the fluorescence spectra might be another effect to take into consideration. Excimer formation is treated as a diffusion controlled process although it might also be formed by ground state complexes. Homogeneous distribution of the pyrene has been assumed where pyrene monomers or excimers might be distributed in both hydrophilic and hydrophobic microenvironments with the I_1/I_3 attributed to both. Also, the effects might be also attributed to the non-homogeneity of the surfactant aggregates and the partitioning and random occupancy of the pyrene molecules between these aggregates.

6.5.1 Probing CPB/SPFO Aggregates with pyrene, Py-C4, Py-C10 and Py-C16

For study of the CPB/SPFO vesicles, a fixed surfactant composition in the anionic-rich region of the vesicle lobe was investigated: 2% wt/wt; $\gamma = 0.85$ (SPFO = 1.7% wt/wt, CPB = 0.3% wt/wt). This is equivalent to a molar concentration of 47.5 mM with the anionic surfactant mole fraction of $X_{\text{SPFO}} = 0.83$. Prior to study in the vesicle system, pyrene fluorescence was examined in micelle solutions of SPFO and CPB.

Pyrene Study of SPFO micelles

To study SPFO micelle formation, increasing amounts of the dry surfactant powder (0 – 1.7% wt/wt) were added to the pyrene probe dissolved in water and mixed thoroughly. The fluorescence spectrum was recorded at each interval of surfactant addition. The surfactant to pyrene ratios varied from 458 to 7800. As depicted in Figure

6.5(a), the pyrene fluorescence peaks were well resolved at even the highest SPFO concentration, with the five peaks observed at 373, 379, 384, 389 and 393 nm. The emission intensity (measured from the solvent-sensitive peak at 373 nm) decreased with increasing concentrations of SPFO (54% decrease at 1.7% wt/wt), with a simultaneous increase in the intensity of the pyrene excimer at 475 nm (20-fold increase). There was a gradual decrease in I_1/I_3 with increasing amounts of SPFO. The I_1/I_3 of pyrene decreased from 1.89 in pure water to 1.32 at the CMC of SPFO (1.3% wt/wt). I_1/I_3 further decreased to 1.25 at 1.5% wt/wt, after which it was constant.

Studies suggest that pyrene is often located close to the micelle interface of most micellar aggregate systems due to its exclusion from the aggregate packing^{319,320} with the I_1/I_3 utilized as a measure of the surface density or headgroup compactness.³¹⁹ However, others have shown pyrene penetration into the micellar core of some hydrocarbon surfactants.³²¹ Our trends in I_1/I_3 and excimer formation with increasing SPFO concentration suggest that pyrene is located in close proximity to the headgroup region in SPFO, with the excimer formation attributed to the antipathy of hydrocarbon and fluorinated chains. SPFO is composed of uniform fluorinated chains with no hydrocarbon spacer. Hence, there is no lipophilic region for the solubilization of the hydrocarbon pyrene in its micellar or pre-micellar aggregates. Previous analysis of both SANS³²² and F NMR³²³ indicate minimal penetration of the fluorinated micellar core of SPFO by water, but considerable water contact for the CF₂ group adjacent to the carboxylic headgroup.³²⁴ As such, the pyrene fluorophores might be restricted to the more solvated micelle interface of SPFO, confined to pseudo-domains, where frequent self-collision increases the probability of excimer formation. The concentration-dependent quenching is probably due to the self exclusion and localization of the pyrene probes in the solvated interfacial region of the fluorinated SPFO micelles and is a reflection of the mutual dislike of the hydrocarbon probe and fluorinated chains. The trend is in accord with several studies which assert that the lipophobic nature of fluorinated chains limits solubilization of pyrene either in mixtures of hydrocarbons and fluorocarbons^{42,43,325} or in fluorocarbons alone.³²⁶⁻³²⁸

Pyrene in CPB micelles

A concentration range of 0 – 0.3% wt/wt was used in the study CPB micelle formation. The concentration gave surfactant to pyrene ratios of 260 – 1600, which were lower than in the SPFO micelles. In contrast to SPFO system, excimer formation is not detected in CPB, as shown in Figure 6.5(b). However, a much larger reduction in monomer intensity (a 97% decrease at the CPB CMC (0.025% wt/wt) relative to pure pyrene) is observed with increasing CPB concentration. The pyrene fluorescence was effectively quenched by the aromatic pyridinium headgroup of CPB, which is a well known quencher.³²⁹ The I_1/I_3 displayed no consistent trend above the CMC, varying around an average of 1.70 but exhibited a sharp decrease to 1.3 below the CMC. This behavior is very similar to that observed for cetylpyridinium chloride (CPC), whose I_1/I_3 values decreased from 1.83 – 1.2. at the CMC.⁴² In CPB solution, the pyrene quenching mechanism changes from predominantly dynamic collision in pre-micellar aggregates to both static and dynamic in fully formed micelles.³³⁰ In effect below the CMC of CPB, the quenching of pyrene is propagated via diffusional collision with the pyridinium headgroup quencher (dynamic quenching) while above the CMC, the quenching occurs mainly by molecular binding with headgroup quencher. The significant quenching effect in CPB compared with SPFO reflects the low solubilization of the fluorinated system towards lipophilic pyrene.

Pyrene in CPB/SPFO Vesicles

Figure 6.5 (c) presents changes in fluorescence of pyrene as incremental amounts of CPB (up to 0.3% wt/wt) were added to SPFO micelles (1.7% wt/wt) to form vesicles. Vesicle formation was visualized by the appearance of the homogeneous bluish tint ascribed to vesicles and DLS sizes (107.5 nm/PDI = 0.2) comparable with values observed in pH 3 medium (98.9 nm/PDI = 0.1).

Increasing incorporation of CPB (decreasing mass fraction of SPFO; $\gamma = 1 - 0.85$) into SPFO micelles caused a dramatic decrease in both monomer intensity (93%) and excimer formation (97%). This suggests a change in the microenvironment from SPFO micelles to the mixed bilayer aggregate of CPB/SPFO. The strong reduction in monomer intensity (or increased quenching) is much greater than that observed in the SPFO

micelles but similar to that observed in CPB micelles. These trends in quenching suggest that pyrene is situated in close proximity to the aromatic CPB headgroup in the mixed bilayer system. With increasing CPB incorporation, the pyrene fluorophore is better solubilized into the lipophilic environment provided by the hydrocarbon chains of the CPB micelles, with correspondingly less excimer formation. Indeed, this phenomenon parallels several observations of pyrene in mixed hydrocarbon/fluorocarbon surfactant systems and has been used to delineate demixing of the mutually phobic chains.^{42,43,325} An alternative interpretation of the trends in emission intensity and excimer formation is based on the heterogeneous nature of the vesicle fluid bilayer as a result of the chain asymmetry of CPB (C16) and SPFO (FC7). Asymmetry would result in large free volume in the bilayer, promoting frequent collision with the CPB headgroup quencher due to increased intra-membrane mobility of the pyrene fluorophore.

Rapid destabilization of the SPFO/CPB vesicles to mixed micelles with addition of NaCl salt (0.34M; 2% wt/wt) leads to only a very slight recovery of the fine vibronic structure of pyrene (Figure 6.5(a)). Demicellization was evident in the appearance of clear, colorless solutions and substantiated by large departure in DLS, from vesicle sizes (510 nm/PDI = 0.86). In accordance with the CPB/SPFO phase map in figure 6.3 (a), destabilization of vesicles should yield SPFO-rich micelles due to excess of the anionic surfactant ($\gamma = 0.85$). This is consistent with Brasher et al's¹⁷⁷ study where addition of sodium bromide salt (NaBr) to anionic-rich CTAB/SOS vesicles promoted transition to the adjacent SOS-rich micellar phase. The equally diminished pyrene intensities in both vesicles and mixed micelles Figure 6.6(a) suggests the fluorophore experiences similar intra-aggregate environments, in close proximity to the CPB headgroup quencher.

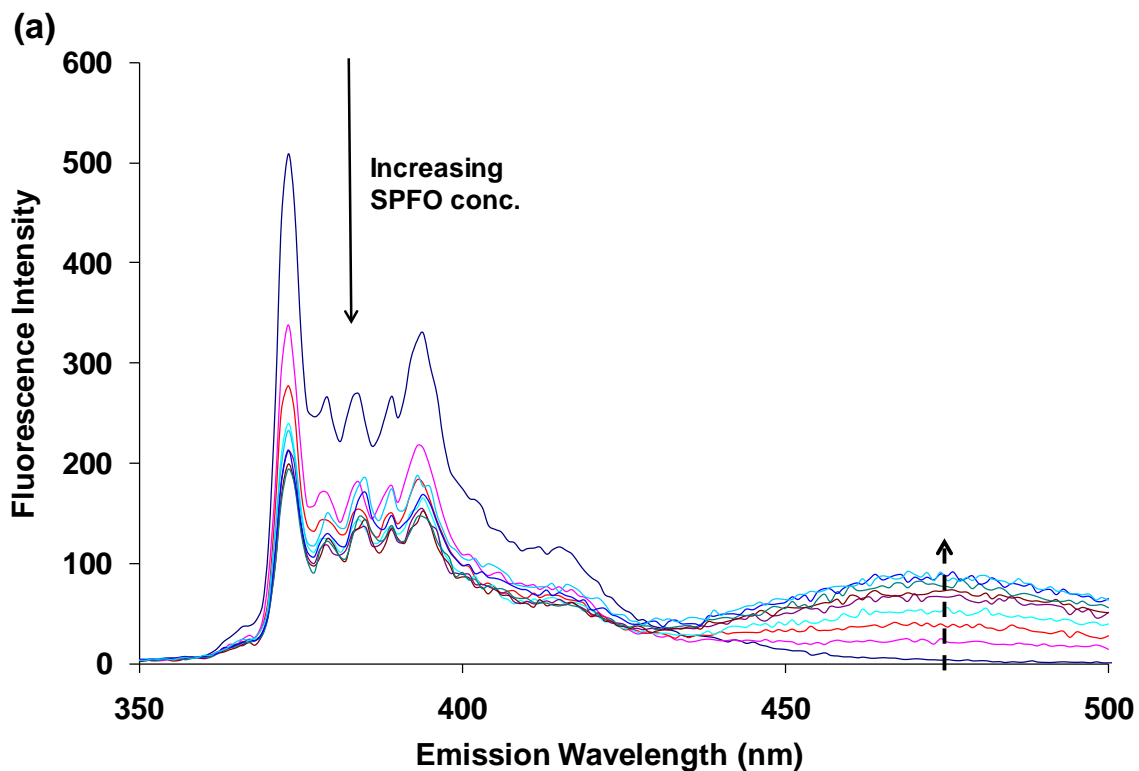


Figure 6.5: (a) Pyrene in SPFO solution; 0 – 1.7% wt/wt (b) Pyrene in aqueous solutions of CPB; 0 – 0.3% wt/wt (c) Increasing amounts of CPB (0 – 0.3% wt/wt) added to aqueous solution of SPFO/pyrene (1.7 % wt/wt). (broken arrow indicates excimer formation)

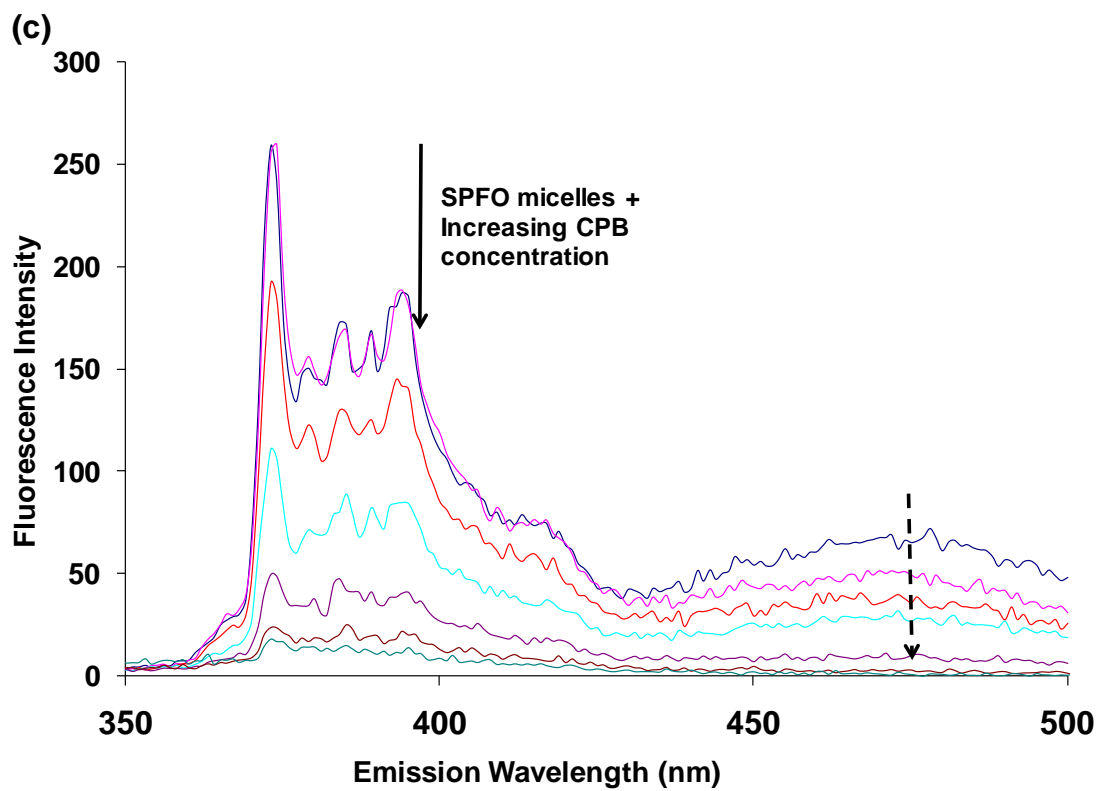
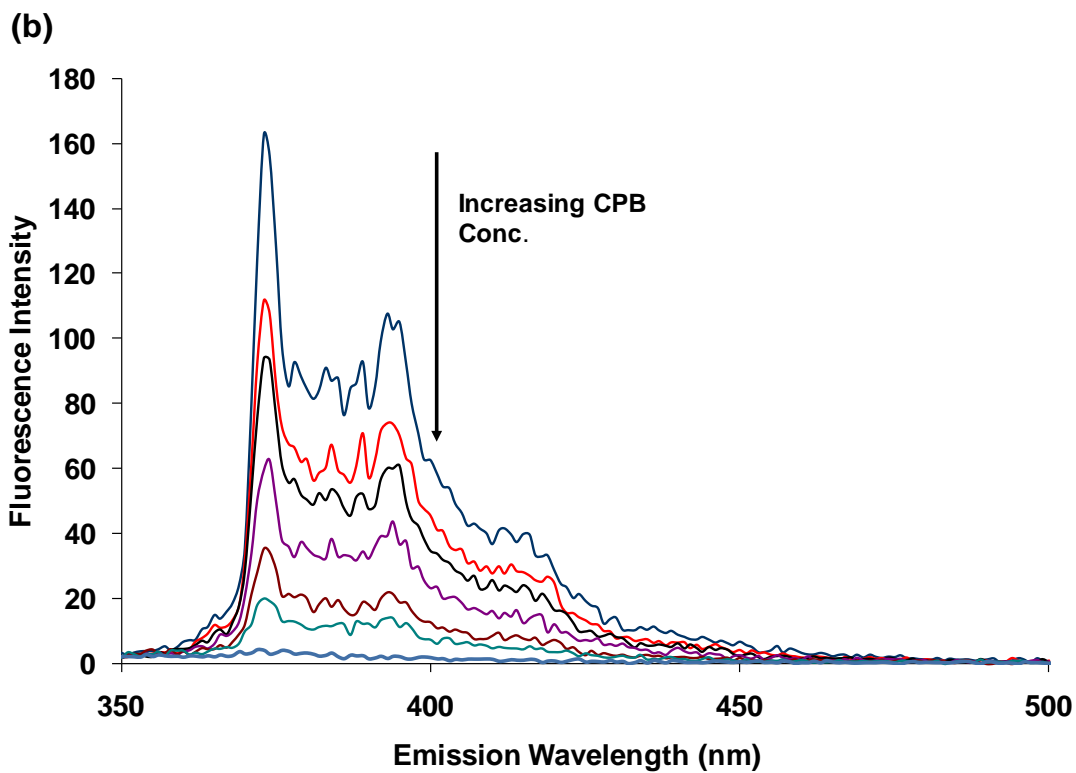


Figure 6.5 Continued

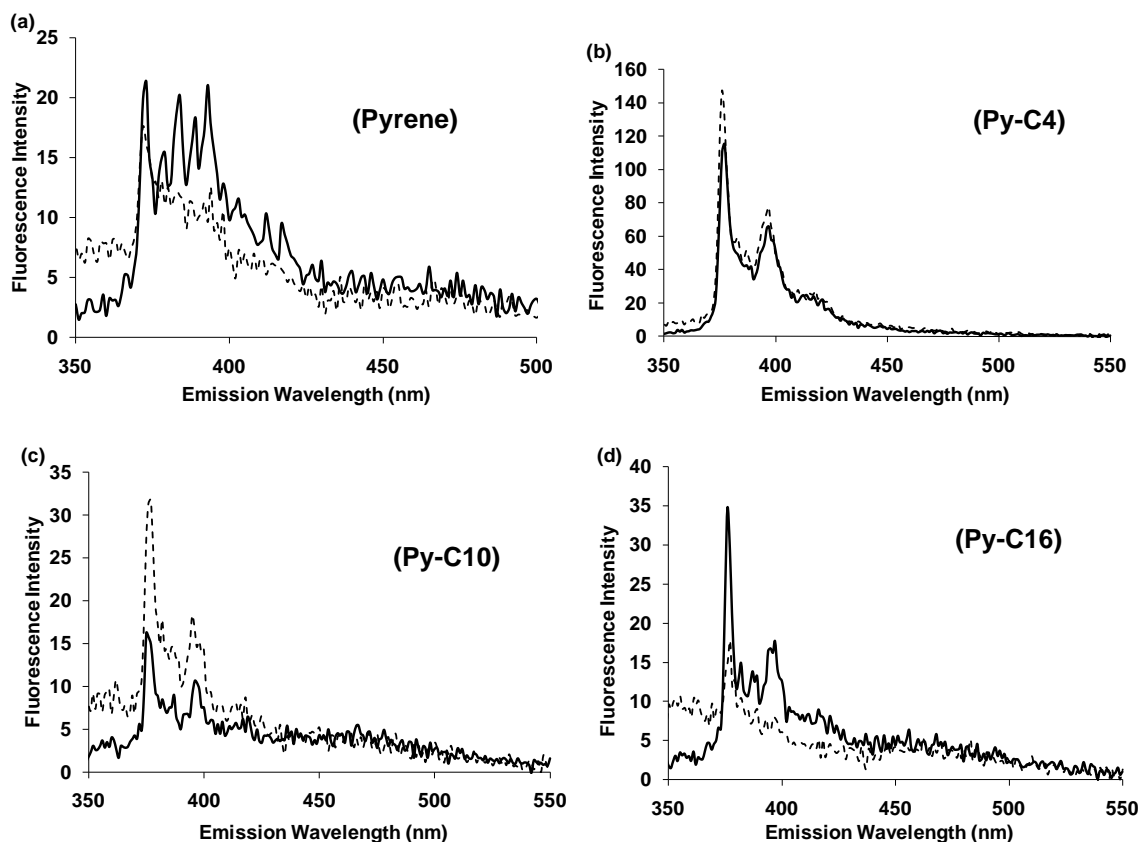


Figure 6.6: Fluorescence spectra of (a) pyrene (b) PBA/Py-C4 (c) PDA/Py-C10 (d) PHA/Py-C16 fluorescent probes in CPB/SPFO vesicles (---) and mixed micelle systems (—); destabilization of vesicles to micelles as a result of salt addition, NaCl (2% wt/wt/0.34M).

Probing CPB/SPFO Aggregates with Py-C4, Py-C10 and Py-C16

The fluorescence spectra of the pyrene derivatized probes in CPB/SPFO vesicles and micelles systems are presented in Figures 6.6(b) – (d) for Py-C4, Py-C10, and Py-C16, respectively. Dried films of CPB/probe were hydrated with SPFO solutions, heated and stirred before fluorescence analysis. Identical compositions to that of pyrene studies were employed (2% wt/wt; $\gamma = 0.85$). Although the probes share identical chromophores with pyrene, the alkane appendage with carboxylic end group diminishes the sensitive vibronic structure due to loss of molecular symmetry.³³¹ However, fluorescence studies of the derivatized probes in different solvents reveal that the I_1/I_3 of the pyrene moiety in PBA, still demonstrates some sensitivity to the local solvent environment, with values ranging from 1.9 – 3.4 from apolar to polar media.³⁰² The carboxylic end group of the

derivatized probes provides for association with the surfactant head groups. In neutral and basic pH, the carboxylic acid group is expected to be largely deprotonated,³³² hence negatively charged ionic association with the positively charged CPB headgroup occurs. This ionic association can be used to anchor the carboxylic terminal group at the aggregate surface, with the pyrene moiety intercalated in the intra-bilayer chain environment.

For the shortest probe Py-C4 (Figure 6.6 (b)), the I_1/I_3 ratio displayed an average change from 2.76 in vesicles to 2.95 in the mixed micelles, suggesting similar local environments of the fluorophore in vesicles and micelles. For the longer chained Py-C10 and Py-C16, (Figure 6.6(c and d)), the resolution and emission intensity of the fluorescence spectrum are diminished in the system, suggesting quenching of the pyrene moiety. The Py-C4 is geometrically constrained by its short chain, restricting the bending back conformation, so the fluorophore is located at reasonable distance from the headgroup region, with quenching effect minimized. The quenching of the pyrene moiety attached to the more flexible, longer alkyl chains of Py-C10 and Py-C16 can be attributed to folded conformation (adoption of U shaped geometry), making the pyrene fluorophore accessible to the pyridinium headgroup quencher at the interface. This implies presence of disordered chain packing or free volume in the CPB/SPFO bilayers and mixed micelles. Similar inference was made from steady state fluorescence studies of self-assembled alkanolic acid monolayers using the same probes.³⁰² Decreasing asymmetry between the alkanolic acid chains (C22 – C12) and Py-C16 resulted in a decrease in I_1/I_3 ratios, with the pyrene moiety located in a more lipophobic region. The trend was reversed at a critical ratio of the acid and probe chain length (Py-C16/C16). In the longer chained monolayers, PHA was embedded in the alkanolic acid monolayer chains but decrease in chain length of the latter resulted in exposure of PHA to aqueous environment. This unfavorable exposure resulted in the probe bending back to intercalate in the hydrophobic alkyl chain regions of shorter chained monolayers (C16). The same effect is reflected here with free volume cavities³³³ created by mismatched chains (fluid bilayers) in the CPB/SPFO vesicle facilitating folding of the probes with insertion of the pyrenyl fluorophore in the headgroup region of the vesicles.

The trends in our study suggest that the pyrene fluorophore is readily accessible to the pyridinium headgroup in both the CPB/SPFO vesicle bilayers and mixed micelles. The free volume of the mismatched chains in the bilayer (C16/FC7) might provides sufficient flexibility of the folded chain conformation in Py-C10 and Py-C16 probes. The short chain of Py-C4 reduces the probability of the folded conformation and results in less quenching of the probe. Overall, this suggests some fluidity of the mixed hydrocarbon bilayer in CPB/SPFO.

6.5.2 Probing CTAB/SPFO Aggregates with pyrene, Py-C4, Py-C10 and Py-C16

CTAB/SPFO is a cationic system which has been studied in detail (cryo-TEM, DLS) by Kaler and coworkers.^{44,54} With a common anionic surfactant and similar bilayer chain environments (C16/FC7) to CPB/SPFO, the fluorescence study of CTAB/SPFO in this work serves as a standard by which the headgroup effects can be effectively assessed.

The microenvironment of pyrene probes in anionic-rich CTAB/SPFO vesicles were studied at a total surfactant concentration of 2 wt% and $\gamma = 0.85$, the same surfactant composition by weight as the CPB/SPFO system. This is equivalent to a 47 mM surfactant solution where $X_{\text{SPFO}} = 0.83$. This vesicle solution was micellized with the addition of NaCl (2% wt/wt; 0.34 M). DLS measurements confirmed the transformation of phases from vesicles (diameter = 117 nm; PDI = 0.27) to mixed micelles (diameter = 386.6 nm; PDI = 0.69) in micellar solution. The micelle solutions were clear, colorless and slightly viscous, suggesting the presence of rod-like micelles.³³⁴

The fluorescence spectra of pyrene, Py-C4, Py-C10 and Py-C16 in CTAB/SPFO vesicles and micellar systems are presented in Figures 6.7(a) – (d), respectively. All emission spectra display the well resolved five peak vibronic structures of the fluorophore. Interestingly, in contrast to CPB/SPFO aggregates, the spectra are intense and excimer formation is not evident in either the vesicle or mixed micelle systems of CTAB/SPFO. This provides strong evidence that the loss of fluorescence intensity observed in CPB/SPFO is a direct effect of quenching by the pyridinium headgroup.

Pyrene in pure CTAB micelles display high intensity (spectrum not shown) with I_1/I_3 values (1.32) similar to literature values (1.30), consistent with solubilization in the palisade region.³⁰⁶ Bromide ions are recognized as quenchers of pyrene³²¹ and used to

characterize CTAB aggregates in aqueous solution.³³⁵ However, relative to the pyridinium headgroup in CPB, the effect of the bromide counterion is insignificant. The intensity of the emission spectra of pyrene in CTAB/SPFO vesicles and mixed micelles is similar (Figure 6.7a), but the I_1/I_3 decreases from 1.15 in vesicles to 0.99 in mixed micelle systems. Pyrene experiences a slightly more hydrophobic region in the vesicles and mixed micelles than in the pure CTAB micelles based on the I_1/I_3 values.

The fine spectra of Py-C4, Py-C10 and Py-C16 in CTAB/SPFO aggregates (Figures. 6.7 (b) – (d)) provide for clear assessment of changes in micropolarity as the vesicles were micellized, although, the scale of I_1/I_3 values is higher scale for derivatized pyrene (1.9 – 3.4) relative to pyrene (0.6 – 1.8). For the shortest probe, Py-C4, I_1/I_3 changed from 2.94 (vesicles) to 2.86 (mixed micelles). The I_1/I_3 values of Py-C10 were unchanged (3.22). The I_1/I_3 values of the longest hydrocarbon chain probe, Py-C16, decreased slightly in going from vesicles (3.13) to mixed micelles (3.01). Recalling that the derivatized probes are anchored at the interface by the electrostatic interaction of the carboxylic endgroup (COO^-) and the pyridinium headgroup (CP^+), the position of the pyrene fluorophore is then attributed to the flexibility of the alkane chains and the fluidity it experiences in the aggregate. The I_1/I_3 values indicate similar, highly polar environments in the vicinity of pyrene in both vesicles and mixed micelles. As with CPB/SPFO, the pyrene moiety of Py-C4 is projected to be intercalated in the mismatched bilayer of the C16/FC7 chains while the pyrene fluorophore in the longer chained Py-C10 and Py-C16 might be in contact with the aqueous regions of the bilayer.

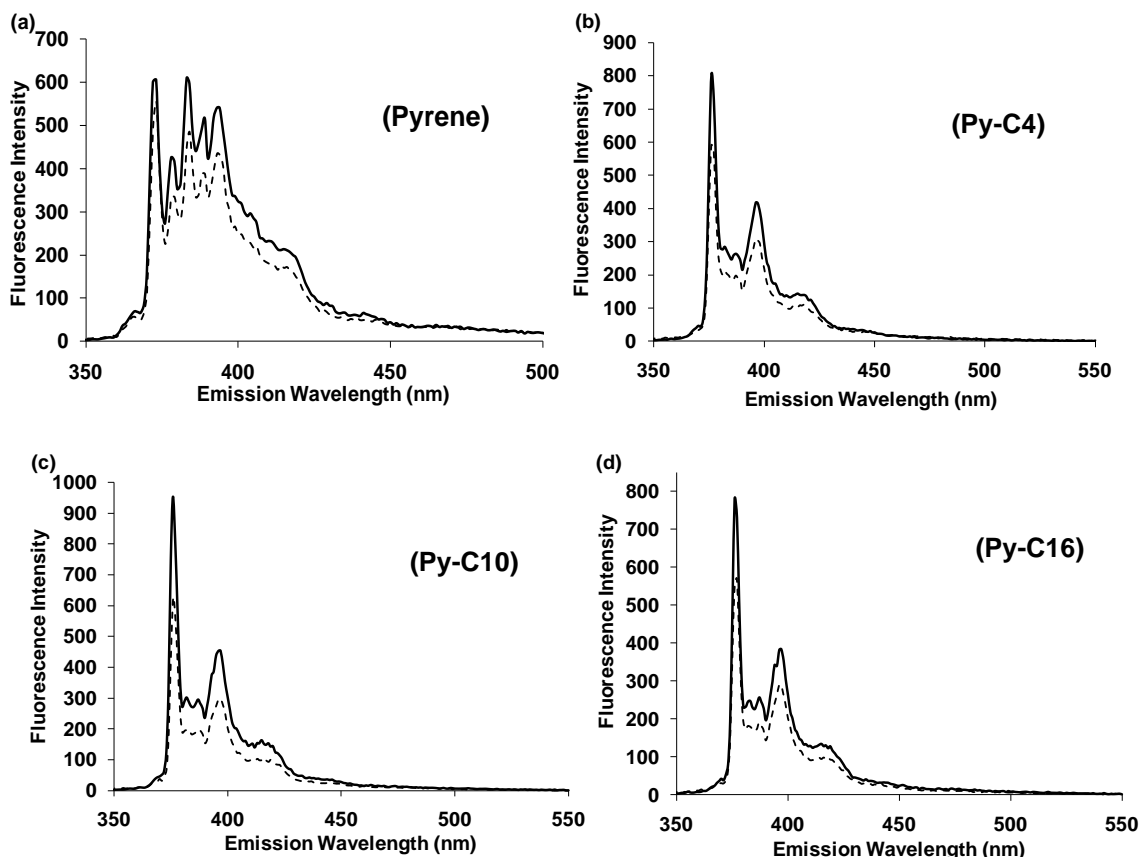


Figure 6.7: Fluorescence spectra of (a) pyrene (b) PBA/Py-C4 (c) PDA/Py-C10 (D) PHA/Py-C16 fluorescent probes in CTAB/SPFO vesicles (---) and mixed micelle systems (—); (destabilization of vesicles to micelles as a result of salt addition, NaCl, 2% wt/wt/0.34M).

Overall, the I_1/I_3 values of the longer chained Py-C10 and Py-C16 in the bilayer suggest high micropolarity, which could be interpreted in two ways: the pyrene moiety in close proximity to the headgroup region or the result of exposure of the pyrene fluorophore to aqueous microenvironment of the bilayer (chain mismatch effect). Taking into account the possibility that the probe is anchored at the interface by the carboxylic end group, the lack of quenching in CTAB/SPFO supports our analysis on the position of the fluorophore in CPB/SPFO. The pyrene fluorophore is probably adopting a U shaped conformation (Py-C10 and Py-C16) in CPB/SPFO. This geometric conformation brings the fluorophore in direct contact with the pyridinium headgroup quencher.

6.5.3. Probing HFDPC/SPFO Aggregates with pyrene, Py-C4 and Py-C16

For study of the HFDPC/SPFO system, a fixed surfactant composition in the anionic-rich region of the vesicle lobe was investigated: 1.18% wt/wt; $\gamma = 0.78$ (SPFO = 0.927% wt/wt; HFDPC = 0.026% wt/wt). This is equivalent to a molar concentration of 25 mM with the anionic surfactant mole fraction $X_{\text{SPFO}} = 0.85$. Prior to study in the vesicle system, pyrene fluorescence (5 μM) was used to characterize solutions of HFDPC.

Pyrene in HFDPC micelles

Figure 6.8(a) shows pyrene fluorescence intensity decreases as a function of HFDPC concentration (0 – 0.264% wt/wt) in aqueous solution, corresponding to a minimum surfactant/pyrene ratio of 1500. Similar to CPB (Figure 6.5(c)), the concentration dependent quenching coupled with absence of excimers suggests pyrene is closely associated with the pyridinium headgroup quencher. The I_1/I_3 value showed minimal variance around an average of 1.76 for pre-micellar to micellar concentration. Figure 6.8(b) illustrates the slightly, higher quenching effect of HFDPC than CPB, which is ascribed to the fluorophilic nature of HFDPC. Almgren et al.³⁰³ deduced from fluorescence decay curves of pyrene, quenching was propagated by dynamic collision below the CMC (dynamic quenching) for aqueous solutions of 1,1,2,2-tetrahydroperfluorodecylpyridinium chloride, HFDePC (FC8) while above the CMC, static quenching was more dominant. With cetylpyridinium chloride (CPC) considerable static quenching existed even below the CMC due to the affinity of the pyrene fluorophore for the lipophilic CPC chains. The alkane link between the headgroup and fluorinated chains in HFDPC, apart from acting as a solubilization site, affords ready accessibility to the aromatic headgroup, with the resultant quenching effect. This is supported by findings³⁰³ which report vastly different solubilization capacities between isotropic solvents and micellar aggregates. Pyrene solubility is 700 times higher in n-dodecane than in n-perfluoroheptane while it only differs by a factor of 60 in the analogous CTAC and HFDePC micelles. This disparity is ascribed to the presence of the methylene group in HFDePC, similar to HFDPC, acting as a solubilization site for the pyrene.

Probing HFDPC/SPFO Aggregates with Pyrene, Py-C4 and Py-C16

The fluorescence of pyrene in HFDPC/SPFO vesicles was studied by adding incremental amounts of HFDPC (0 – 0.264% wt/wt) to solutions of SPFO (0.927% wt/wt) which contained dissolved pyrene (5 μ M). The DLS vesicle size was 177.8 nm with PDI of 0.2. Addition of NaCl salt (1% wt/wt; 0.17M) resulted in DLS sizes (511 nm; PDI = 0.63) and a mixed micelle solution that displayed macroscopic viscosity, which suggests rod-like micelles. Analogous to the system of CPB/SPFO, both pyrene emission intensity and excimer formation decreased as the fraction of HFDPC was increased (Figure 6.8a). The intensity of the pyrene I_1 peak decreased 50%, while the corresponding excimer intensity decreased by 70% at the highest HFDPC concentration added to SPFO solution. The pyrene I_1/I_3 displayed no consistent trend with the surfactant addition and fluctuated around an average of 1.59. This reflects the position of pyrene at the aqueous interfacial region of the vesicles or preformed vesicular aggregates. HFDPC/SPFO vesicles possess a fully fluorinated bilayer core and would effectively exclude lipophilic pyrene, restricting the probe to the aqueous interfacial regions. The I_1/I_3 value for HFDPC/SPFO vesicles (1.59) is higher than that reported for CTAB/SPFO vesicles (1.15), which suggests that pyrene is located at greater depth of the bilayer in the mixed hydrocarbon/fluorocarbon bilayers. This might be attributed to the combined effect of microviscosity and solubilization. With both tails fluorinated, the bilayer in HFDPC/SPFO would consist of chains in mostly extended, trans-conformation due to stiffness and bulkiness of fluorine chains; the outcome being a well packed bilayer region with the pyrene confined to the more hydrated interfacial regions. Also, the increased lipophobicity of the fluorinated chains would result in expulsion of the lipophilic pyrene from the inner chain regions of HFDPC/SPFO to the headgroup region. In CTAB/SPFO and CPB/SPFO, the long chains of the hydrocarbon CTAB or CPB (C16) would most likely adopt gauche conformation and the presence of the fluorinated SPFO fluoroalkyl chains (FC7) might promote such geometry in the bilayer. Hence, the bilayer is expected to be less organized in CTAB/SPFO vesicles, facilitating penetration of pyrene into hydrocarbon regions, reporting a lower I_1/I_3 value. This difference in pyrene I_1/I_3 values suggests different incorporation mechanisms into CTAB/SPFO and HFDPC/SPFO vesicle bilayers.

The fluorescence spectrum of Py-C4 inserted in HFDPC/SPFO (FC10/FC7) vesicles and mixed micelles was well resolved (Figure 6.8(d)). The I_1/I_3 values were 2.98 and 3.08 in the respective vesicles and mixed micelles, indicating the pyrene moiety in Py-C4 detects similar local environments and polarity in the vesicles and micelles. With both tails fluorinated, the possibility of more uniformly mixed micelles of HFDPC/SPFO is higher than in CTAB/SPFO or CPB/SPFO. Therefore, the Py-C4 probe is projected to encounter more uniform intra-chain environments in both vesicles and mixed micelles of HFDPC/SPFO. The nature of the interaction the hydrocarbon Py-C4 in the fluorinated bilayer of HFDPC/SPFO would be different to both CTAB/SPFO and CPB/SPFO due to increased lipophobicity.

Fluorescence was completely quenched in HFDPC/SPFO vesicles and mixed micelles using the longer chained probe, Py-C16. The intermediate probe, Py-C10, was not investigated. An analysis of the Py-C16 probe in HFDPC micelles revealed complete quenching and the same effect was observed in SPFO micelles. The lack of fluorescence emission in either the pure micelles (HFDPC and SPFO), the mixed vesicle and mixed micelles, suggests the Py-C16 probe is not solubilized in the homogeneous fluorinated bilayer systems. This reflects limited solubilization of the homogeneous fluorinated bilayer core in HFDPC/SPFO towards the lipophilic long chained Py-C16 probe. This inference can be made based on comparisons with the probe in CPB/SPFO system. Considering that fluorescence emission was observed for Py-C16 in mixed CPB/SPFO (Fig. 6.6d), albeit significantly smaller than with Py-C4, the complete lack of fluorescence emission in HFDPC/SPFO supports our rationale that the Py-C16 is effectively excluded from the fluorinated bilayer. Additionally, the long chained probe (C16) would be geometrically constrained in the shorter fluorinated chains of the bilayer ((C2FC10)) that is the length of two monolayers. The longer chains in CPB/SPFO ((C16/FC7)) might facilitate insertion into the mixed hydrocarbon/fluorinated bilayer.

Overall, the inference can be made that HFDPC/SPFO possesses a bilayer that excludes the lipophilic, long chained, Py-C16 while Py-C4 is short enough to attain moderate penetration in the fluorinated/fluorinated bilayer. Considering that all probes were inserted in the CPB/SPFO, this effect demonstrates that the HFDPC/SPFO with lipophobic and hydrophobic bilayer is less fluid and better organized.

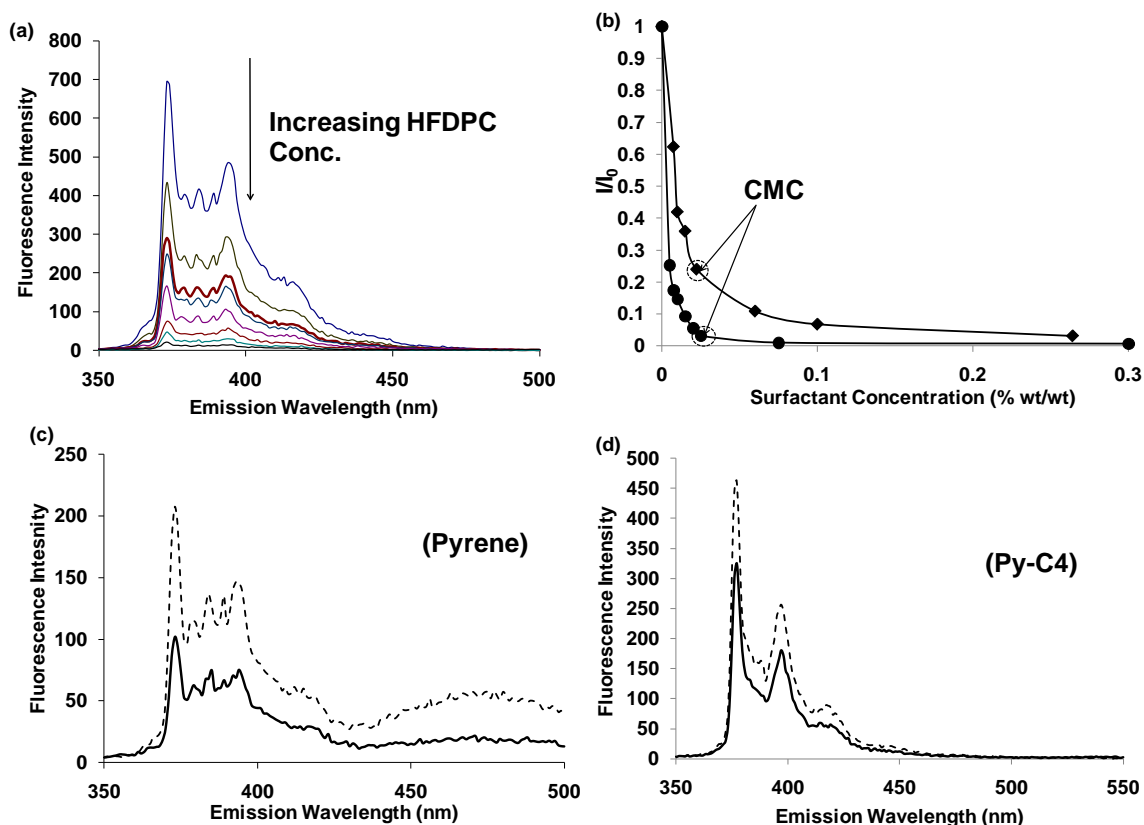


Figure 6.8: (a) Emission spectra of pyrene as a function of increasing HFDPC concentration (0 – 0.264% wt/wt) in aqueous solution. (b) Decrease in monomer intensity or quenching of pyrene with increasing concentration of CPB (○) and HFDPC (◆) in aqueous solutions. (c) Fluorescence spectra of pyrene in SPFO micelles (---) and in HFDPC/SPFO vesicles (—). (d) Fluorescence of PBA/Py-C4 in HFDPC/SPFO vesicles (---) and in HFDPC/SPFO micelles (—).

6.6. Conclusion

Phase behavior has been examined in mixed hydrocarbon/fluorocarbon bilayers, CPB/SPFO, CPB/SPFH and fluorinated/fluorinated bilayers, HFDPC/SPFO and HFDPC/SPFH, with the goal of identifying regions of stable cationic vesicle formation. Larger vesicle phase regions were identified in the more asymmetric bilayers, CPB/SPFH (C16/FC5) and HFDPC/SPFH (FC10/FC5) than in CPB/SPFO (C16/FC7) and HFDPC/SPFO (FC10/FC7). HFDPC/SPFO possessed the narrowest vesicle region of all systems studied showing that the combination of reduced asymmetry and stiff, bulky fluorinated chains results in high membrane rigidity for vesicle curvature.

However, the vesicle region is expanded in more asymmetric fluorinated bilayers of HFDPC/SPFH. The increased chain asymmetry in HFDPC/SPFH results in reduced packing density and more fluid bilayers than in HFDPC/SPFO.

Further characterization of the systems with pyrene and pyrene derivatized probes suggest greater fluidity of the mixed hydrocarbon/fluorocarbon bilayer in CPB/SPFO than in HFDPC/SPFO. The bilayer of the mixed CPB/SPFO possesses sufficient fluidity to promote bending of the longer chained probes, Py-C10 and Py-C16, with subsequent quenching of the pyrene fluorophore. The structural conformation is confirmed by comparisons with CTAB/SPFO, where no quenching is observed for any of the probes and the fluorescence emissions register high intensities. This supports the solubilization of the probe moiety in mixed hydrocarbon/fluorocarbon bilayers. With HFDPC/SPFO, the fully fluorinated bilayer prevents solubilization of the longer chained lipophilic pyrene derivatized probe, Py-C16. Future efforts will be made to assess the differences in the more asymmetric counterparts, CPB/SPFH and HFDPC/SPFH.

CHAPTER 7

ENCAPSULATION OF FLUORESCENT DYES IN HYDROCARBON/FLUORINATED AND FULLY FLUORINATED CATANIONIC VESICLES

7.1 Summary

Encapsulation of a neutral and a cationic solute dye, riboflavin and rhodamine 6G (R6G), is investigated in catanionic vesicle systems with mixed hydrocarbon/fluorocarbon bilayers (cetylpyridinium bromide (CPB)/sodium perfluorooctanoate (SPFO)), and compared with the fully fluorinated analogue (1,1,2,2-tetrahydroperfluorododecylpyridinium chloride (HFDPC)/ SPFO). Both vesicle systems were prepared with excess molar concentrations of the anionic surfactant, SPFO, resulting in negatively charged aggregate systems. Size exclusion chromatography (SEC) was used to determine the efficiency of solute encapsulation and vesicle stability. Vesicle aggregate size was monitored with dynamic light scattering. The neutral solute, riboflavin, is not effectively encapsulated in either vesicle system, while significant encapsulation is achieved with R6G. This is consistent with specific ionic association of the oppositely charged species (anionic vesicles and cationic R6G) as a principal driving force for encapsulation. Greater encapsulation of R6G is achieved with CPB/SPFO (85% and 65% for 1mM and 0.05mM) relative to HFDPC/SPFO (14% for 0.05mM). The HFDPC/SPFO vesicles demonstrated higher retention of the captured R6G (11%) while more than half the captured dye was released in CPB/SPFO vesicles. The destabilization effect on the vesicles with increasing R6G concentration was more prominent for the HFDPC/SPFO bilayers than for the CPB/SPFO system, suggesting a difference in the incorporation mechanism for the two systems.

7.2 Introduction

Vesicles, as model membrane structures, have found use in a range of applications including the synthesis of nanoparticles,^{50,116} as aqueous reservoirs for chemical reactions,^{165,336} and as encapsulation and controlled drug delivery systems.^{337,338} Vesicles are characterized by four distinct compartments for molecular association: (1) the outer vesicle surface, (2) the bilayer, (3) inner membrane surface, and (4) the inner aqueous pool. The effective encapsulation of solutes or reactants in vesicles, the stability of these encapsulated systems, and permeability of the vesicle bilayers are critical properties in designing vesicles for specific applications. The barrier properties of phospholipid-based vesicles (liposomes), which require preparation with mechanical force, have been well investigated^{129,339} even though they are constrained¹ by thermodynamic instability and may transform to their equilibrium lamellar state. By comparison, catanionic vesicles, prepared by mixing dilute aqueous solutions of oppositely charged surfactants, form spontaneously and are relatively stable for long periods of time. Vesicles are the form of the surfactant aggregate often observed in these catanionic systems. Excess surface charge is hypothesized to be a primary stabilization mechanism of these vesicles when one surfactant, particularly the shorter chain or more soluble surfactant is in excess.^{167,197,280,340} The thermodynamic stability of catanionic vesicles is also attributed to other factors, including the asymmetry of the mixed surfactant chains and the reduction of the combined cationic-anionic headgroup area. The size and polydispersity of catanionic vesicles are determined by the surfactant structure, ionic strength of the solutions and the composition of the mixture, hence allowing for manipulation of the vesicle size for specific encapsulation applications.³⁴⁰

Catanionic vesicles have been demonstrated as a vehicle for encapsulation,^{47,48,164,282,341-343} and may provide some advantages relative to conventional liposomes.^{47,164} For example, enhanced encapsulation efficiencies of a fluorescent marker, 5(6) carboxyfluorescein (CF), was demonstrated in a catanionic vesicle system, cetyltrimethylammonium tosylate/sodium dodecyl benzene sulfonate, (CTAT/SDBS; 21% encapsulation efficiency) relative to lipid based egg yolk phosphatidylcholine (EYPC) liposomes (1.6% efficiency).¹⁶⁴ Further, rapid release of the encapsulated probe was observed in the EYPC liposomes compared with CTAT/SDBS; the release

time for half the encapsulated dye was two days in the liposome systems compared with over 80 days in cationic system.

Encapsulation efficiency is highly dependent on specific ionic association of the oppositely charged vesicles and solute species.^{47,344,345} In the previous example, the encapsulation is driven by the electrostatic attraction of the oppositely charged vesicle surface (positively charged CTAT/SDBS vesicles) and the solute species (negatively charged CF). Danoff et al⁴⁷ observed significantly higher encapsulation (up to 700 fold) when their selection of UV active dyes (R6G, CF, doxorubicin hydrochloride) were matched with CTAT/SDBS vesicles of overall opposite charge than in systems where both species were of the same charge. They conclude that adsorption to the vesicle walls or bilayer (i.e. interfacial interactions) accounts for about three-quarters of the encapsulation efficiency. Zhao et al³⁴¹ support these observations in their encapsulation of the anionic bromophenol blue dye in cationic rich vesicles of sodium 10-undecanoate (anionic) and decyltrimethylammonium bromide (cationic). The amount of trapped bromophenol blue increased 30-fold from the anionic-rich to the cationic-rich vesicle phase region.

The ionic association of solutes with cationic vesicles may provide significant improvements in entrapment compared with conventional liposomes. R6G and CF encapsulation efficiencies in CTAT/SDBS vesicles were 6-fold⁴⁷ and 24-fold¹⁶⁴ higher than that reported for egg-phosphatidylcholine (EYPC)³⁴⁶ and lipid mixtures of dipalmitoylphosphatidylcholine/ dipalmitoylphosphatidylglycerol (DPPC/DPPG)³⁴⁷, respectively. Similarly, the strong affinity of DNA for positively charged cationic vesicles of cetyltrimethylammonium bromide (CTAB) and sodium octyl sulfate (SOS) (excess CTAB) as investigated by Dias et al,⁴⁸ suggests the tremendous potential of these systems in gene delivery and other biopharmaceutical applications.

However, some investigations suggest that the dynamic nature of the short chain components of cationic vesicles and the ionic character of these systems might limit their trapping capabilities.^{342,343} For example, Caillet et al.³⁴² observed minimal glucose or CF encapsulation (0.1 - 0.2% encapsulation efficiency) in negatively charged cationic CTAB/ excess SOS vesicles. Slightly higher levels of glucose were detected in vesicles in which the counter ions had been removed (1% encapsulation efficiency).

This study suggested that the negatively charged CF probe destabilized the negatively charged vesicles, although the high probe concentrations (50 mM) has been suggested to be a contributing factor.⁴⁷ Others^{167,282,340} have reported trapping of neutral molecules such as glucose and riboflavin (neutral at pH <10) with cationic vesicle, but the efficiencies are much lower than that for ionic solutes. Fischer et al.²⁸² report 2% encapsulation of glucose in CTAT/SDBS vesicles, which is low in comparison to entrapment of the anionic CF (21 %) in the same system.¹⁶⁴ Also, over 70% of the encapsulated glucose was lost from these vesicles in 8 hours. However, the glucose encapsulation efficiencies in the cationic vesicles still compare favorably with those of DPPC liposomes, which ranged from 1.9% at 25°C to 1% at 45°C.³⁴³ Although the underlying mechanism for solute encapsulation in cationic vesicles may be dominated by charge, the influence of bilayer chain order in cationic vesicles cannot be completely ignored. The bilayer is accepted as modulator of vesicle activity in traditional liposomal systems and regulates transport to and from the aqueous core to the continuous phase,¹⁵⁴ with permeability of vesicles dependent on the temperature-dependent phase of the bilayer³⁴⁸ and the hydrocarbon chain organization.^{130,134} By extension to cationic systems, reduced solute permeability is expected for better organized, structured, bilayer environments. In cationic vesicles, the chain asymmetry and distribution of surfactants in the inner and outer monolayers dictated by spontaneous curvature to form the vesicles suggests a less structured membrane chain arrangement or packing than in double chained liposome systems.^{179,278}

Incorporation of hydrophobic and lipophobic fluorinated chains in the bilayer has been demonstrated as an effective means of reducing liposome permeability.^{349,350} Fluorinated surfactants possess several distinguishing properties from traditional hydrocarbon surfactants, including a greater driving force to self-aggregate due to their high hydrophobicity as well as lipophobicity.^{70,204,205,208,285-288} The properties of fluorinated surfactants are ascribed to the weaker intermolecular interactions in fluorinated molecules.²⁸⁸ The bulky and rigid fluoroalkyl chains also tend to form structures with lower curvature (i.e., rod like micelles, vesicles and lamellar phases) than the analogous hydrocarbon surfactants.^{1,70,204,211} In addition, the bulkiness and stiffness of the fluorinated carbon chains restrict random motion of the chains, resulting in trans-

conformation as opposed to gauche chain type packing in the bilayer.^{70,205} The tightly packed chains of fluorinated bilayers reduce permeability and provide greater membrane rigidity,³⁵¹ factors that are expected to impact their performance as encapsulation agents.

This study investigates the encapsulation of the cationic UV active dye, rhodamine 6G (R6G), and nonionic riboflavin (chemical structures in Figure 7.1) by the hydrocarbon/fluorinated catanionic surfactant mixture, cetylpyridinium bromide (CPB(cationic))/sodium perfluorooctanoate(SPFO(anionic)) and its fully fluorinated equivalent, 1,1,2,2-tetrahydroperfluorododecylpyridinium chloride (HFDPC(cationic))/SPFO). Vesicle formation, as well as the ability to form stable silica hollow spheres using the vesicles as templates, has been previously demonstrated in the anionic-rich phase region of these surfactant mixtures.³⁰¹ Vesicle stability, encapsulation efficiency and subsequent solute retention were determined by combined analysis of filtration (size exclusion chromatography), dynamic light scattering, UV and fluorescence spectroscopic techniques. The interaction and encapsulation of R6G with anionic-rich partially and fully fluorinated vesicles was examined as a function of R6G concentration.

7.3 Experimental Section

7.3.1 Materials

The fluorinated anionic surfactant, sodium perfluorooctanoate (SPFO; $C_7F_{15}COO^- Na^+$; 97% purity) and the hydrocarbon cationic surfactant, cetylpyridinium bromide (CPB; $C_{21}H_{38}N^+Br^-$; $\geq 97\%$) were purchased from Sigma Aldrich and Alfa Aesar, respectively, and used without further purification. The fluorinated cationic surfactant, 1,1,2,2-tetrahydroperfluorododecylpyridinium chloride (HFDPC; $C_{10}F_{21}CH_2CH_2NC_5H_5^+Cl^- \cdot H_2O$), was synthesized with greater than 98% purity, as previously described.⁴¹ To summarize, alkylation of pyridine with 1*H*,1*H*,2*H*,2*H*-perfluorododecyl iodide, followed by anion exchange produces the desired HFDPC. The purity of HFDPC was assessed by spectrometric and melting point measurements and was in agreement with published values.⁴¹ The cationic dye, rhodamine 6G (R6G; benzoic acid, 2-[6-(ethylamino)-3-(ethylimino)-2,7-dimethyl-3*H*-xanthen-9-yl]-ethyl ester, monohydrochloride) and the nonionic dye, riboflavin, (3, 10-dihydro-7,8-dimethyl-10-[(2*S*,3*S*,4*R*)-2,3,4,5-tetrahydroxypentyl]benzo-[g]pteridine-2,4-dione;7,8-dimethyl-

10-(1'-D-ribityl)isoalloxazine) were purchased from Sigma Aldrich (99% purity) and Fisher Scientific (98% purity), respectively. The pre-packed Sephadex G25 (medium mesh) in PD10 desalting columns were used as purchased from GE healthcare (Amersham Biosciences).



Figure 7.1. Chemical structures of (a) Rhodamine 6G and (b) Riboflavin

7.3.2 Vesicle/Solute Preparation

Fixed surfactant compositions of vesicles of CPB/SPFO (7.8 mM CPB, 39.2 mM SPFO, 5-fold molar excess SPFO) and HFDPC/SPFO (2.2 mM HFDPC, 19.6 mM SPFO, 9-fold molar excess of the anionic surfactant) were prepared. Previously, we determined that the lower surfactant concentration utilized here for the HFDPC/SPFO system produced stable vesicles, while a higher surfactant concentration was required for CPB/SPFO vesicles.³⁰¹

The effect of the cationic solute on vesicle size and stability was examined by preparing vesicle solutions with different concentrations of the cationic solute, R6G: 0.05 mM, 0.5 mM, 1 mM and 5 mM. The vesicle/R6G samples were prepared by adding aqueous solutions of R6G to dry mixed surfactant powders. The solutions were heated to 50°C for 20 minutes and mixed for another hour, stored in darkness for at least 48 hours,⁴⁷ and then filtered with 0.45 micron Millipore syringe filters. Solutions were prepared at neutral pH using deionized ultra-filtrated water. The encapsulation of one

concentration of the nonionic riboflavin (0.1 mM) in the two vesicle systems was examined at neutral pH. Identical preparative procedures were adopted for the vesicle-riboflavin samples as for the R6G-loaded vesicles.

7.3.3 Dynamic Light Scattering

The hydrodynamic size and polydispersity of the cationic surfactant aggregates at 25°C were monitored by dynamic light scattering (DLS) using a Malvern Zetasizer Nanoseries (Malvern Instruments, United Kingdom). The instrument was equipped with a He-Ne laser lamp (4 mW) source at 633 nm and measurements were taken at 90° scattering angle. The data were analyzed with the Cumulants Method,²⁹² which employs a single exponential fit of the intensity of the autocorrelation function to derive an average for the diffusion coefficient. An intensity weighted size average (Z-average) was then calculated using Stokes-Einstein equation. The Z-average (intensity weighted average) and polydispersity index (PDI) were taken as representative of the size and size distribution in the samples.

7.3.4 Dye Encapsulation and Retention in Vesicles

Size Exclusion Chromatography of Vesicle Solutions. The prepacked columns of sephadex G25 (medium mesh) or PD 10 (prepacked disposable) desalting columns with bed volumes of 8.5 ml (1.5 x 6.5 cm) were used as purchased. The columns are designed for group separations, or separations involving large molecular weight differences, such as the case with vesicles and vesicle aggregates (> 30,000) and free dye solutes (< 500). In size exclusion chromatography, the smaller molecular weight compounds permeate the pores of the bed while the much larger compounds i.e. vesicles are excluded and elute in the void volume of the column. Due to this very large size difference between the vesicles and free solutes, bed volumes and column length can be minimized to achieve effective separation. Fractionation of compounds with narrower molecular weight differences requires longer columns (at least twice the length used here) for efficient resolution.³⁵² Prior to SEC, the column's void volume was determined by loading 1 ml of 2 mg/ml Blue Dextran 2000 kDa, which eluted at approximately 3 ml with DIUF water. This represents about 30% of the column volume. This confirmed that the bed had been

properly packed, as the 30% represents the void volume or the excluded volume of the column.

Samples of the vesicle/solute mixtures were loaded on Sephadex G25 column to separate the free probe (R6G or riboflavin) from the probe that was effectively encapsulated in the vesicle's aqueous core or attached to the vesicle surface or bilayer. The vesicle/R6G was subsequently eluted using the continuous phase of the vesicle systems (i.e., at the salt concentration/salinity of the surfactant mixture). For the CPB/SPFO/solute systems, 0.75 ml of the vesicle/solute sample was loaded on the column and eluted with 1.5 ml of NaCl aliquot solutions (10 mM) (i.e. series of 1.5 ml fractions were collected and analyzed by DLS and UV). For the HFDPC/SPFO/Solute systems, 1.5 ml sample was loaded on the columns and eluted with 2 ml of NaCl solution (2 mM) (i.e. 2 ml fractions were collected and analyzed). These elution volumes resulted in a 2-fold dilution for the CPB/SPFO vesicles and 1.5-fold dilution for HFDPC/SPFO vesicles. For both systems, the vesicle-entrapped dye was eluted in the second and third fractions.

In preliminary experiments, the stability of the vesicles to the SEC procedure and migration through the column was verified. Bare vesicles of CPB/SPFO and HFDPC/SPFO without any dye were prepared following the same procedure described above and processed in the SEC columns. The vesicles were eluted in the void volume of the column using the same eluant described above and the fractions analyzed by DLS to confirm the vesicle integrity. Both the CPB/SPFO and HFDPC/SPFO systems were relatively unaffected by the separation using the sephadex resin. For CPB/SPFO, the average size changed from 124 nm (PDI = 0.19) to 154 nm (PDI = 0.18) after SEC. For HFDPC/SPFO, there was an average size decrease from 218 nm (PDI = 0.21) to 187 nm (PDI = 0.18).

Analysis of Dye Encapsulation. The amounts of free and encapsulated dye (riboflavin and R6G) were quantified from the eluent using UV-vis spectroscopy (Hewlett Packard spectrophotometer, model 8453). The absorbance at the spectral peaks of 525 ± 8 nm and 443 nm for R6G and riboflavin, respectively, were used to determine the corresponding dye concentration. The encapsulation efficiency was quantified from the

ratio of the dye material in the vesicle-SEC to the original unfiltered vesicle-dye samples using Danoff et al's method⁴⁷ (Eq. 7.1):

$$\text{Encapsulation efficiency} = \frac{\text{Abs}_{\text{fraction}}}{\text{Abs}_{\text{initial}}} \times \text{SEC dilution factor} \times 100\% \quad \text{Equation (7.1)}$$

where Abs_{frac} and $\text{Abs}_{\text{initial}}$ represent the UV absorbance of the fraction containing the vesicle-entrapped dye and the absorbance of the original vesicle-dye solution, respectively. The dilution factor accounts for the difference in volume of sample loaded on the column to the volume applied in elution. The above equation effectively relates the concentration of dye (UV absorbance x volume) entrapped by vesicles to the initial amount of dye in solution.⁴⁷ This analysis method assumes that all free or external dye (dye not associated with vesicles) was effectively separated from the vesicle-entrapped dye during SEC.

Subsequent dye release from vesicles or retention of the original dye solution was determined at regular time intervals, with modifications to the above SEC procedure. Separation of any released dye from any vesicle-retained dye was achieved by two minute centrifugation \approx (2000g) on dehydrated sephadex G25 column. During centrifugation, the vesicles with captured dye were eluted and collected at the bottom of the column while any released or free dye was retained on the column.⁴⁷ This procedure precluded further dilution effects inherent with buffer elution in the first encapsulation measurements. Time dependent dye retention is reported from the absorbance of the dye-entrapped vesicle solution relative to the original dye solution using Eq. (7.1).

7.3.5 Fluorescence Spectroscopy of R6G /vesicles systems

The mechanism of dye (R6G) incorporation into the vesicle matrix was examined using the emission and polarization spectral measurements (Varian Cary Eclipse fluorescence spectrophotometer) of the R6G-loaded vesicles. The R6G probe was excited at $\lambda_{\text{ex}} = 470$ nm and emission, $\lambda_{\text{em}} = 478$ nm with an excitation slit width of 5 nm and emission slit width of 2.5 nm. Steady state measurements of the manually polarized light were recorded²⁶⁵ with 1s average sampling time. The Varian manual polarizers were applied to both emission and excitation and the average of three polarization values

was reported. Due to saturation of the photodetector and excessive formation of non-fluorescent dimerization of R6G, the vesicle samples analyzed for fluorescence were restricted to low dye concentrations (below 0.05 mM). The polarization was calculated using Eq.(7.2):

$$P = \frac{I_H - I_V}{I_H + I_V} \quad \text{Equation (7.2)}$$

where I_H and I_V represent fluorescence intensity parallel and perpendicular to the excitation plane, respectively.

7.4 Results and Discussion

The CPB/SPFO and HFDPC/SPFO catanionic vesicles in this study have recently been characterized by TEM, DLS and material templating techniques.³⁰¹ This previous investigation revealed slightly more uniform size distribution in the HFDPC/SPFO at lower surfactant concentration than in the CPB/SPFO system. Vesicle sizes ranged from approximately 40 - 200 nm for CPB/SPFO in the surfactant concentration range of 1–2 wt/wt %, (27.5 – 47 mM) as determined by negative staining transmission electron microscopy (TEM) and in agreement with dynamic light scattering. Similarly sized vesicles were observed for HFDPC/SPFO at lower concentrations \leq 1wt/wt%, 22 mM). The lower concentration required for stable vesicle formation in fully fluorinated bilayers is a consequence of the hydrophobicity and rigidity of the fluoroalkyl chains relative to hydrocarbon surfactant tails. Fluorinated surfactant systems tend towards aggregates with low curvature conformation, such as vesicle bilayers, in order to minimize fluoroalkyl chain bending.⁴⁰

This work explores the potential effects of fully fluorinated bilayers on the encapsulation and stability of model solutes in anionic rich mixed surfactant vesicles.

Although electrostatic effects dominate the encapsulation of molecules in catanionic vesicle systems, the hydrophobicity and bilayer packing of the fully fluorinated bilayers relative to the mixed hydrocarbon/fluorocarbon analogue may impact its ability to encapsulate and retain solutes. The encapsulation and solute retention in partially fluorinated (CPB/SPFO) and fully fluorinated (HFDPC/SPFO) bilayers are compared for the capture of both a cationic dye (R6G) and nonionic dye (riboflavin) (structures

provided in Figure 7.1) in vesicles formed in the anionic-rich solutions. R6G is a deeply red-hued cationic, slightly hydrophobic³⁵³ xanthene laser dye^{354,355} and has been employed in studies of cell structure, membrane fusion, protein orientation^{356,357}, biological cells³⁵⁸ and cationic vesicles.⁴⁷ In addition to the ease of measurement of dye concentration with UV absorbance, the tendency of R6G to form non-fluorescent dimers in aqueous solutions has been used to examine the mechanism of incorporation at the silica/water interface.^{359,360} Riboflavin is a yellow non-ionic (neutral pH) vitamin B-2 compound and its inclusion in this study is key in examining encapsulation in the absence of solute-vesicle electrostatic interactions.

7.4.1 Effect of R6G dye concentration on vesicles

Prior to dye encapsulation and release experiments, the effect of the cationic dye, R6G, on vesicle stability was evaluated by visually observing the solution phase behavior and monitoring the constancy of the size of the vesicles by DLS over a period of two weeks. Varying R6G concentrations at fixed surfactant compositions were examined for both CPB/SPFO and HFDPC/SPFO systems (Table 7.1). Both vesicle systems investigated here are negatively charged due to excess of the anionic surfactant, SPFO. The ratio of cationic surfactant to R6G (presented in Table 7.1) is also relevant to the interpretation of the stability, as the cationic solute could compete with the anionic surfactants in vesicle formation. Disproportionate amounts of R6G could prevent vesicle formation or result in structural destabilization of formed vesicles. Changes in morphology with disks, fragmented membranes and multilamellar structures have been captured by cryo-TEM with increasing addition of polyions to oppositely charged didodecyldimethylammonium bromide/sodium dodecyl sulfate vesicles (DDAB/SDS).³⁶¹

The electrostatic effect of the cationic R6G is reflected in size deviations from the bare vesicle systems. The addition of R6G could potentially reduce the surface charge density which might lead to enlargement of the vesicles, multi-walled vesicles and eventually destabilization to lamellar phases.⁴⁵ The maximum or critical dye concentration (Table 7.1) at which the vesicles are stable is greater for the CPB/SPFO vesicles (1 mM R6G) than for the HFDPC/SPFO vesicles (0.05 mM R6G). The HFDPC/SPFO systems were meta-stable (\approx 10 days) before sediments and flocs were

observed confirming destabilization by R6G. The critical dye concentration of 1 mM for the CPB/SPFO system is in agreement with a previous study suggesting that the concentration of R6G should be below 5 mM in order to maintain vesicle stability in their CTAT/SDBS system.⁴⁷ At 1 mM concentration of solute (R6G, CF, DX, etc), the surfactant/solute ratios employed in Danoff et al's⁴⁷ encapsulation studies were 9:1 in the anionic SDBS-rich phase regions to 7:1 for cationic, CTAT-rich vesicle phase regions, similar to our values for CPB/SPFO vesicles (CPB/R6G = 8). However, the cationic surfactant to R6G ratios which correspond to the maximum dye concentration (0.05 mM) are 4-fold lower for HFDPC/SPFO vesicles (HFDPC/R6G = 44) than for the CPB/SPFO vesicles. This suggests that the interaction and destabilization mechanism of R6G in the CPB/SPFO to the HFDPC/SPFO system may not be identical.

Table 7.1. Hydrodynamic sizes for different surfactant to R6G ratios in CPB/SPFO vesicles (47 mM total surfactant, $X(\text{SPFO}) = 0.835$) and HFDPC/SPFO vesicles (21.75 mM, $X(\text{SPFO}) = 0.9$). Sizes reported 14 days after sample preparation.

R6G Concentration (mM)	<i>CPB/SPFO Vesicles</i>		<i>HFDPC/SPFO Vesicles</i>	
	[CPB]/[R6G]	Diameter. (nm)	[HFDPC]/[R6G]	Diameter. (nm)
0	-	119	-	214
0.05	155	110 ± 2	44	207 ± 1
0.5	16	135 ± 44	4	-
1	8	100 ± 4	2	-
5	2	-	-	-

7.4.2 R6G dye encapsulation and retention in CPB/SPFO vesicles

R6G encapsulation and release was investigated at a fixed surfactant composition resulting in anionic-rich vesicles (total surfactant concentration of 47 mM, $X_{\text{SPFO}} = 0.835$) at dye concentrations of 0.05 mM and 1 mM (as described in Section 7.3.4). These concentrations of R6G (+) correspond to cationic surfactant (CPB) to dye molar ratios of 155 and 8, respectively. SEC was applied to separate free and vesicle-encapsulated dye,

and the concentration of free dye was used to quantify encapsulation efficiency and dye release over time.

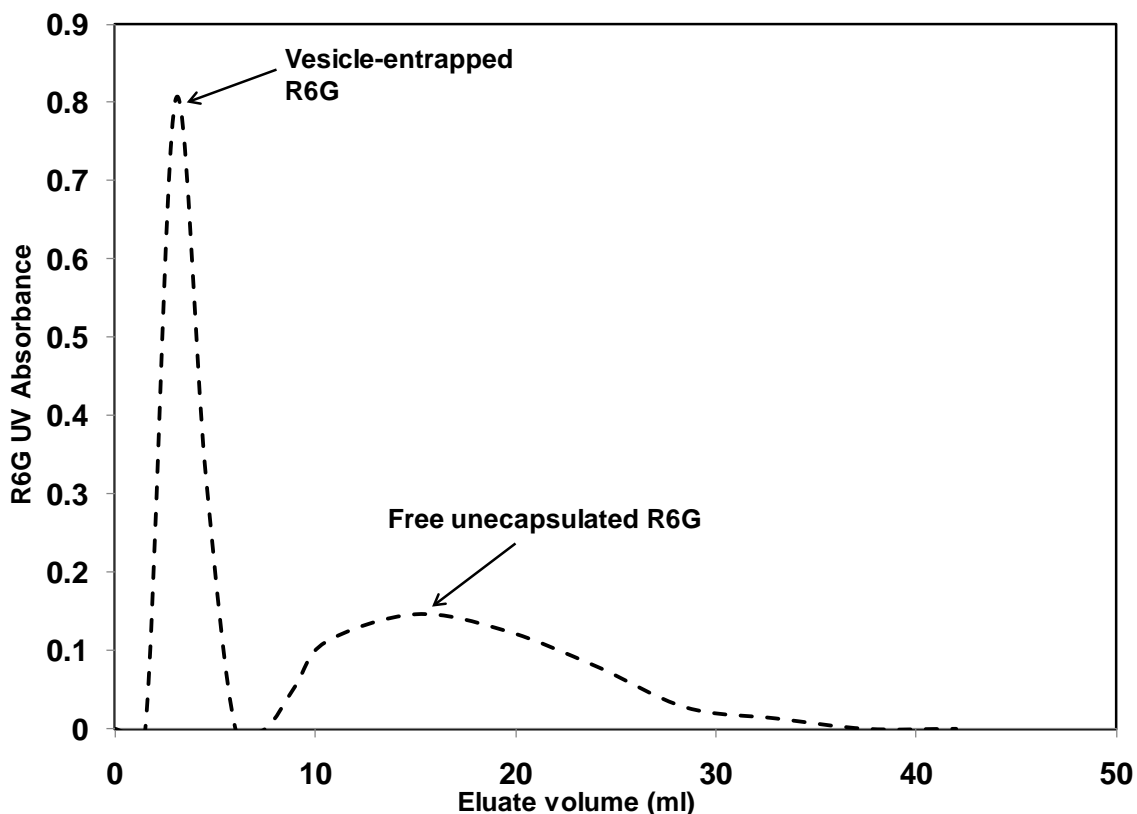


Figure 7.2. Elution profile of R6G-CPB/SPFO system at neutral pH. Surfactant composition is 47 mM, $X_{\text{SPFO}} = 0.835$ and R6G (1 mM).

During SEC, the vesicle-entrapped R6G were consistently eluted in the void volume of the column (i.e., in the second and third fractions (of 1.5 ml each), as depicted in the elution profile in Figure 7.2). The first peak corresponds to elution of the vesicle-associated dye and the second peak corresponds to the free unencapsulated dye. There was distinct separation of the vesicle-dye band from free dye. However, more than twice the column volume (35 ml of 150 mM NaCl solution) was required to completely remove the free dye from the sephadex column. Ideally, the total dye should have been eluted in the total column volume (10 ml), as the chromatographic separation is based on molecular weight differences. However, the chromatographic packing (i.e. the sephadex resin) possesses some hydroxyl end groups, which interact with the cationic R6G and

impedes the elution of the free dye. The hydrodynamic diameters of vesicles were monitored before and after SEC to demonstrate the stability of the vesicles (Table 7.2).

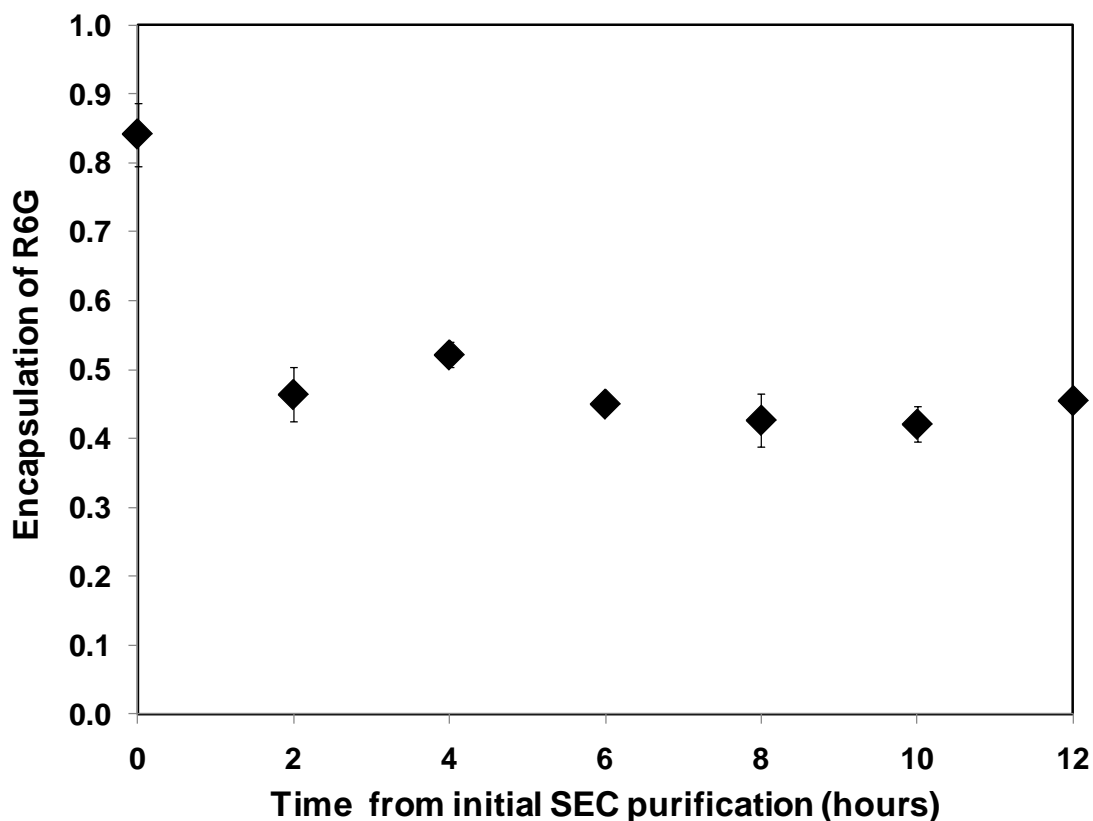


Figure 7.3. Effective encapsulation profile of R6G (1mM) in CPB/SPFO vesicles at neutral pH. Results with the data range are average of two experimental runs.

The initial encapsulation efficiency of 1 mM R6G in the CPB/SPFO vesicles is 85% of the initial dye (Figure 7.3). Subsequent dye release or the amount of R6G retained was determined at regular time intervals using the method described in section 2.4. After approximately 2 hours, dye retention is reduced by half, with the system relatively stable over the next 12 hour time period. A greater percentage of the dye is captured and subsequently retained at the higher R6G concentration of 1mM than at 0.05 mM. At 0.05 mM initial concentration of R6G, the encapsulation efficiency in CPB/SPFO vesicles was initially 65%. However, only 11% of the initial dye in solution was retained 2 hours later. Although these levels of R6G encapsulation are comparable to those reported for CTAT/SDBS (72 %) ⁴⁷ the disparity in retention at 0.05 mM and 1

mM R6G is considerable. This concentration dependence may be attributed to the adsorption of polyions on oppositely charged vesicle surfaces, which would increase the permeability of encapsulated solutes via structural disorganization of the bilayer.¹⁵⁸ The degree of the perturbative effect (formation of pores and defects in bilayer) is proportional to the amount of adsorbed compounds,³⁶² but these interpretations have been applied primarily to liposomal systems. An increase in retention with increased R6G concentration is observed here, suggesting that bilayer permeability has not been increased.

The concentration-dependence of the interaction of R6G with the vesicles was investigated using UV and fluorescence spectroscopy, and polarization measurements. The fluorescence and UV spectra of R6G are highly sensitive to local concentration, medium polarity, steric restrictions, ionic strength and ionic association.^{344,359,363} Changes in these spectral features offer insight into the mechanism of R6G incorporation in the vesicle systems.³⁶⁴ Incorporation of R6G produced UV peaks at 529 ± 1 nm (0.05 mM) and 523 ± 2 nm (1mM), with shoulders observed in both systems (spectra not shown). At concentrations greater than 1 μ M, R6G forms multiple aggregates in aqueous solution (dimers, trimers tetramers) with concomitant absorption energy shifts;³⁵³ the shoulder at 500 nm represents a dimer absorption wavelength.³⁶⁵ In the case of 0.05 mM dye, the shoulder at 500 nm is a strong indication of dimer formation while the peak at 529 nm, red shifted from that of free R6G monomer in solution (525 nm), suggests binding to the anionic-charged vesicle surface.³⁴⁵ Similar shifts have been reported for mixtures of R6G and anionic surfactants³⁶⁶ and are attributed to reduced polarity and restricted motion at the surfactant ionic surface.^{359,367} At 1 mM R6G concentration, dimers and higher order aggregates (trimers and tetramers) dominate the system and they shift the absorbance peak towards lower values.³⁶⁸

The extent of aggregation of R6G, both in the presence and absence of vesicles, can be interpreted from its fluorescence spectra. At 1 mM R6G, the emission intensity is effectively quenched due to the formation of R6G aggregates (spectrum not shown), which do not fluoresce. However, the fluorescence emission peak is clearly observed at 560 nm in the 0.05 mM R6G solution (Figure 7.4a), suggesting less aggregate formation than with 1mM. The intensity of the emission peak diminishes slightly in the following

order: R6G in aqueous solution in absence of the mixed surfactant vesicles, R6G/vesicle systems before SEC, and R6G/vesicle systems following SEC, which might be attributed to dilution in the SEC procedure.

The fluorescence polarization of R6G, which is an indicator of the relative mobility of the dye, was used to interpret the nature of the vesicle surface interactions with the dye. This analysis was limited to 0.05 mM R6G as the fluorescence quenching precluded study of the effect at 1 mM. The polarization value (Eq. 7.2) of the dye increases considerably from 0.018 in aqueous solution to 0.144 in the vesicle system with 0.05 mM R6G, reflecting the change in environment of R6G from free diffusional rotation in bulk solution to restricted mobility due to binding or adsorption at the oppositely charged vesicle surface. Similar changes in fluorescence polarization of R6G have been observed in silica-water systems.³⁵⁹ Due to specific ion interactions, R6G cations would be presumed to be bound to regions in close proximity to the anionic surfactant, SPFO (the excess surfactant in the vesicle systems). The larger, more hydrophobic cation, R6G, could readily displace the counterion (Na⁺) from the vesicles surface, affecting the strength of the cetylpyridinium (CP⁺)/perfluorooctanoate headgroup interactions (COO⁻) and introducing perturbative effect on bilayer organization. The strength of these interactions should vary with concentration as the vesicle surface becomes saturated with R6G. Steady state fluorescence lifetime measurements have also shown that adsorption mechanism of R6G changes with the dye concentration.³⁴⁴ The adsorption of R6G to anionic latex particles is electrostatically driven at R6G low concentrations (10 μ M) and hydrophobically driven at higher concentrations.

With increase in R6G concentration from 0.05 mM to 1 mM, surface overcrowding and the resulting steric hindrance of the dye might lead to increased partitioning of the dye into the bilayer, eventually saturating the bilayer. This rationale is in agreement with the higher initial encapsulation (85%) observed with 1 mM relative to 0.05 mM (65%). The different retention values, 45% for the former compared with 11%, for the latter suggests a slightly different incorporation mechanism with increased concentration. The hydrophobic xanthene moiety of the dye, which is planar,³⁶⁶ could orient in a manner to avoid contact with water and may intercalate in the bilayer, with the

charged group located at the vesicle-aqueous interface. Similarly, the hydrophobic aromatic tosylate counterion in CTAT was shown to intercalate into the bilayer of CTAT/SDBS vesicles and influence the nature of the vesicle-ionic dye interactions.¹⁹⁷ Surface saturation followed by micelle penetration has also been proposed for the xanthene moiety of R6G in anionic micelles while anchored at the surface.³⁶⁶

The strength of headgroup interactions affects the bilayer matrix order and has been known to influence the permeability of liposomes.¹²⁸ Cholesterol intercalated in liposome bilayers with the polar group anchored at the interface increases the surface density (reduces liposome headgroup spacing) and reduces the membrane's permeability to solutes.¹⁵⁵ The more fluidized bilayers of catanionic vesicles relative to conventional liposomes, an effect of chain asymmetry,¹⁷⁹ may provide more void space to accommodate the hydrophobic xanthene moiety of R6G in the CPB/SPFO vesicle bilayers.

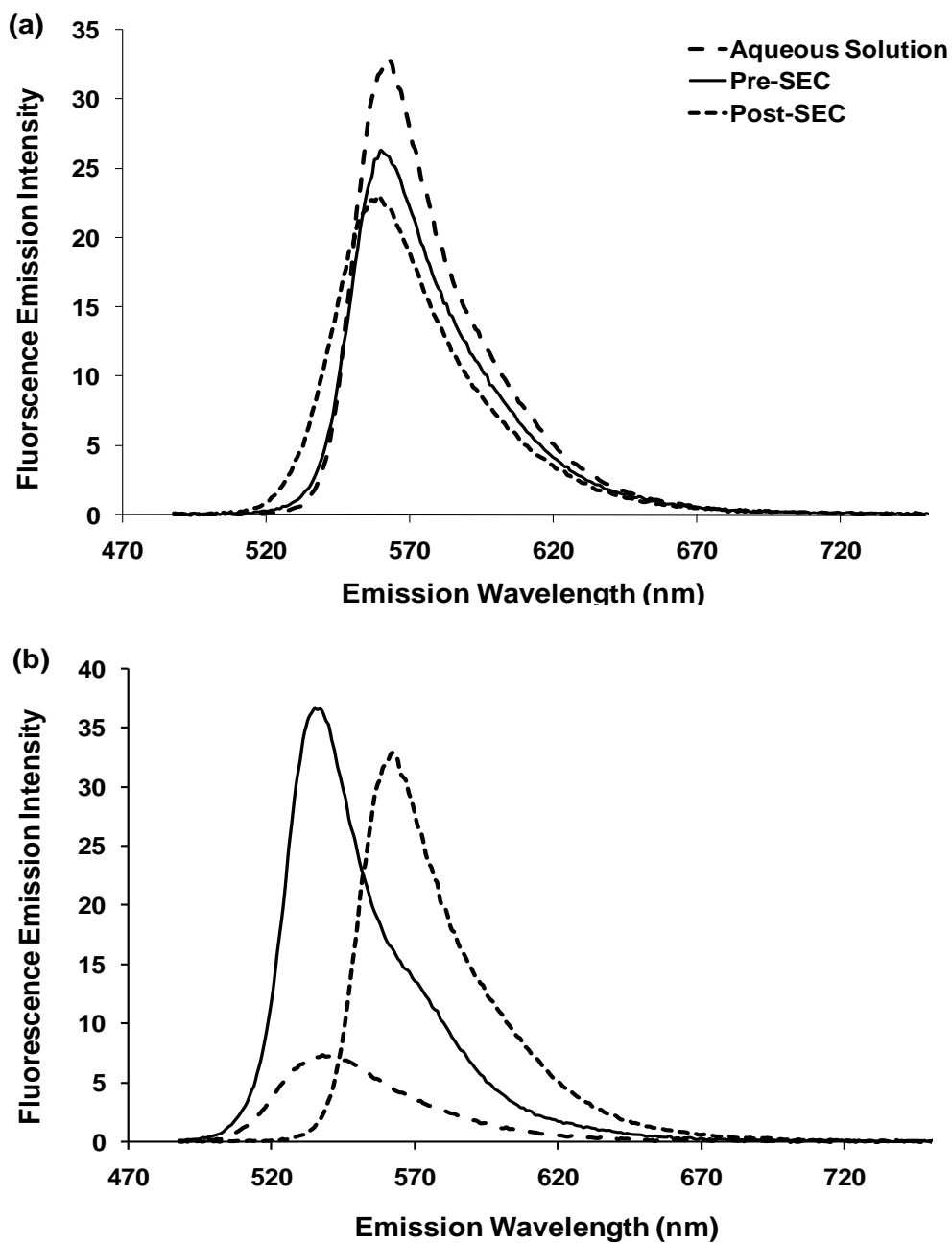


Figure 7.4. Fluorescence emission of R6G (0.05 mM) in (a) CPB/SPFO and (b) HFDPC/SPFO vesicle systems in neutral pH medium. The inset line markers indicate spectrum in water only, pre-SEC and post-SEC as listed.

Table 7.2: Vesicle diameters and polydispersities before and immediately after SEC for the initial encapsulation

Dye Conc. (mM)/pH	CPB/SPFO (47mM, X = 0.835)		HFDPC/SPFO (21.75 mM, X = 0.9)	
	Vesicle diameters (nm) and PDI			
	Pre-SEC	Post-SEC	Pre-SEC	Post-SEC
0 mM/neutral	124 0.19	154 0.18	218 0.21	187 0.18
R6G (1mM)/neutral	96 ± 1 0.23	161 ± 20 0.53	239 ± 19 0.33	237 ± 3 0.38
R6G (0.05mM)/neutral	99 ± 3 0.16	108 ± 7 0.22	194 ± 8 0.38	173 0.3
R6G (1 mM)/pH 3	87 0.1	111 ± 22 0.38	233 0.47	254 ± 6 0.79
Rb (0.1mM)/neutral	120 0.19	153 0.19	185.7 0.29	187.2 0.24

7.4.3 R6G dye encapsulation and retention in HFDPC/SPFO vesicles

Interestingly, the post-SEC vesicle sizes (Table 7.2) increases by only 10% for 0.05 mM R6G solutions, but increases significantly (67%) for 1 mM R6G, which suggests either reduced colloidal stability or enhanced vesicle screening due to predominance of R6G cation in the latter. This could also be factored into the difference in retention values observed at the different R6G concentrations.

The encapsulation efficiency of R6G was investigated at 0.05 mM for the HFDPC/SPFO (21.75 mM, X = 0.9) vesicle system. With the HFDPC/SPFO surfactant composition used in vesicle formation, the molar ratio of the cationic surfactant (HFDPC) to cationic dye (R6G) is ≈ 44 (Table 7.1), which is lower by a factor of 3.6 than the ratio in the CPB/SPFO system at the same R6G concentration (0.05 mM). Hence, the competition of R6G and HFDPC for complexation with the anionic surfactant, SPFO, is

higher in the HFDPC/SPFO systems, with more potential perturbative effects on surfactant headgroup interactions.

The encapsulation efficiency for this system, 14%, is much lower than that observed for CPB/SPFO. However, the incorporated dye system was very stable, with the retention of dye in the vesicles remaining at 14% even after a week. The hydrodynamic diameter of the HFDPC/SPFO vesicles increased 11% with the encapsulation of the dye (Table 7.2). The UV analysis of the dye/vesicle mixture shows a stronger blue shift in HFDPC/SPFO vesicles (to 513 nm) compared with that in CPB/SPFO (Figure 7.5). The shoulder at 500 nm, which signifies the presence of R6G dimers, is present before SEC, but is severely diminished after SEC (in the dye-encapsulated vesicle solution). This is consistent with the much lower encapsulation of the HFDPC/SPFO vesicles. In contrast, dimers are still evident following SEC in the CPB/SPFO systems, suggesting sufficient vesicle encapsulated dye to promote surface dimerization of R6G. Similarly, the fluorescence spectra of the dye (Figure 7.3(b)) entrapped in vesicles (post SEC) decreases in intensity relative to the original vesicle suspension to a much greater extent than the dilution factor of 1.5, indicating low encapsulation efficiency, and also experiences a blue shift. The blue shift of the R6G spectra in HFDPC/SPFO vesicle systems relative to surfactant-free aqueous solution might suggest a different localization of the dye, as there was no significant shift in the CPB/SPFO system (Figure 7.4a). As with the CPB/SPFO system, the fluorescence polarization changed from 0.018 in free aqueous solution to 0.198 in HFDPC/SPFO vesicle systems, indicating restricted motion of R6G due to fixation on the vesicle surface.

The localization of the probe and the bilayer arrangement is hypothesized to play a role in both the reduced efficiency and improved retention of R6G in HFDPC/SPFO vesicles relative to CPB/SPFO vesicles. The homogenous fluorinated bilayer in HFDPC/SPFO may constitute a better barrier to solute permeation and penetration of the R6G hydrocarbon moieties than with the heterogeneous hydrocarbon/fluorinated, CPB/SPFO. Studies have reported similar observations where the more fluid bilayers in dimyristoylphosphatidylcholine, DMPC (which has shorter alkyl chains) exhibited 15% more thymostimulin (polypeptide) encapsulation than in dipalmitoylphosphatidylcholine

(DPPC) but showed 6-times the release in the former.¹⁵³ Although surface adsorption accounts for the encapsulation of the R6G to the vesicles due to electrostatic attractions, the bound dye would experience less intercalation into the lipophobic fluorinated bilayer.

In addition, the potential for surface adsorption may be different in these systems. While the electrostatic attraction between oppositely charged headgroups of the surfactants provide pseudo-double tailed groups in these mixed surfactant systems, unequal distribution of surfactant in the inner and outer leaflet facilitates spontaneous curvature in catanionic vesicles.²⁷⁸ In terms of geometric considerations, approximate surfactant parameters suggest SPFO (1.24) would be located in the inner leaflet while both CPB (0.29) and HFDPC (0.35) would be in the outer leaflet. Differences in distribution of anionic and cationic surfactants in the inner and outer monolayers of CPB/SPFO and HFDPC/SPFO would result in different surface charge densities. These differences might not be reflected in the bulk surfactant composition, but could affect the adsorption and retention of the dye in the respective systems.

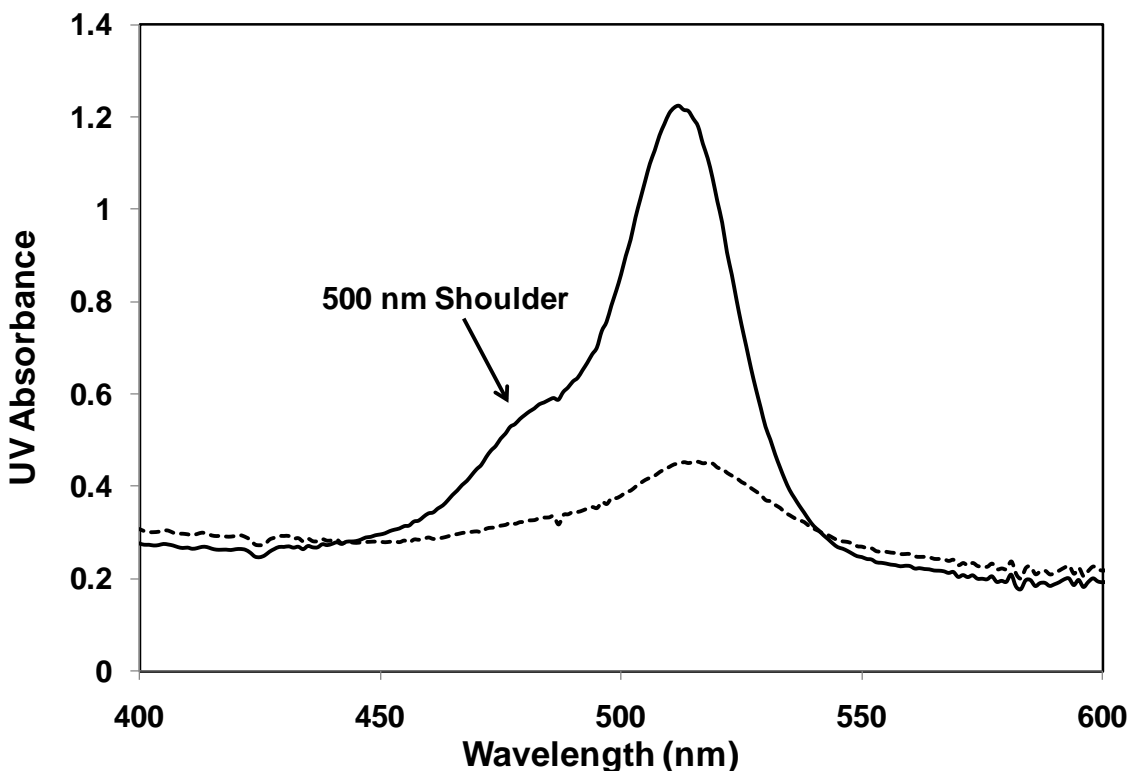


Figure 7.5: Absorbance spectra of R6G in HFDPC/SPFO vesicles pre-SEC (solid line) and post-SEC (broken line).

7.4.4 Encapsulation of Nonionic Riboflavin

Both CPB/SPFO and HFDPC/SPFO vesicle systems were prepared at neutral pH with 0.1 mM riboflavin solutions, where its aqueous solubility is 0.22 mM.³⁶⁹ The respective vesicle-solute sizes were 120.3 and 189.3 nm for CPB/SPFO and HFDPC/SPFO systems, showing little variance from the bare vesicle sizes of 124 nm and 218 nm. This suggests that the presence of the riboflavin solute had minimal effect on vesicle formation, which is expected due to lack of ionic association with the charged vesicle systems.

Encapsulation of this neutral solute was measured by performing SEC, and analyzing the fractions using DLS and UV. Less than 0.1 % encapsulation of the probe was observed for both CPB/SPFO and HFDPC/SPFO. The vesicles were eluted intact in the void volume of the column in the second and third fractions, as observed for CPB/SPFO and HFDPC/SPFO with R6G but without the riboflavin. The yellow colored riboflavin band was observed migrating through the column much later than the vesicles and was finally eluted in the total bed volume. This suggests that the riboflavin was in the continuous phase of the vesicle systems and freely permeated the pores of the column, as expected for a molecule of its molecular weight (< 500). The vesicle population was distinguished from the unencapsulated riboflavin by dynamic light scattering following visual observation of the separate bands on the SEC column. The hydrodynamic sizes of the vesicles presented in Table 7.2 indicate that the vesicles were unaffected by passage through the columns.

The inability to effectively encapsulate the neutral riboflavin in these catanionic vesicle of fluorinated/hydrocarbon and fluorinated/fluorinated systems supports previous findings¹⁶⁴ that electrostatics dominates the encapsulation process. Similar observations are reported for the encapsulation of riboflavin in CTAB/SOS vesicles, where the encapsulation was less than 0.5%.³⁴² However, in contrast to the lack of chromatographic resolution of free and encapsulated riboflavin in the aforementioned study, the CPB/SPFO and HFDPC/SPFO vesicles are well resolved from the free riboflavin molecules. In the CTAB/SOS vesicle system, the lack of resolution is interpreted as a continuous release of the probe from vesicles, while a complete dissociation of the nonionic riboflavin from the catanionic vesicles from the probe is observed in this study.

Some have attributed the inability to encapsulate riboflavin in catanionic vesicles to the leakiness of the vesicles,³⁴⁸ an effect of greater translational diffusion of the shorter chains in the systems facilitates open pores for leakage.³⁴³ Without ionic interactions with the vesicle surface, the riboflavin would be expected to be stored in the vesicle aqueous core and be susceptible to release through open pores. This is consistent with the lack of encapsulation of riboflavin in either CPB/SPFO or HFDPC/SPFO.

7.5 Conclusions

Effective encapsulation of the cationic dye, rhodamine 6G has been achieved in both CPB/SPFO and HFDPC/SPFO catanionic vesicles. Strong evidence is provided that this encapsulation is driven by the affinity of the cationic dye for the negatively charged vesicle surface, as encapsulation of the nonionic riboflavin was unsuccessful in these systems. Much higher encapsulation (65 - 85%) was detected for the mixed hydrocarbon/fluorinated bilayer vesicles (CPB/SPFO) than in the fully fluorinated bilayer vesicles (HFDPC/SPFO) (14%) at neutral pH. However, the HFDPC/SPFO vesicles exhibited better dye retention than the CPB/SPFO in the same time period of 12 hours.

This investigation further support electrostatic adsorption to the vesicle bilayer as a means for effective solute encapsulation in the catanionic vesicle systems, but also probes the role of the bilayer in solute retention. The difference in subsequent dye retention for the CPB/SPFO and HFDPC/SPFO vesicles, where the latter displayed much higher retention of the cationic R6G dye, was rationalized in terms of the homogenous fluorinated bilayer environment. The fully fluorinated bilayer matrix in HFDPC/SPFO is uniformly lipophobic and hydrophobic, precluding solubilization of the hydrophobic moiety of R6G, while the heterogeneous bilayer of CPB/SPFO would more likely accommodate R6G in its non-uniform hydrocarbon-fluorocarbon matrix. In comparison, no encapsulation of the neutral molecule, riboflavin was detected confirming that vesicle bilayer surface electrostatic adsorption is the primary mechanism of capturing ionic solutes

CHAPTER 8

CONCLUSIONS AND FUTURE WORK

8.1 Conclusions

The unique properties of fluorinated compounds have established their promise as viable candidates in applications ranging from biomedical to environmental. With biocompatible characteristics such as biological and chemical inertness, coupled with low surface tension, hydrophobicity, lipophobicity, favorable spreading and high density, fluorocarbon fluids such as the prominent PFOB have demonstrated potential in drug delivery and ventilation therapy. Essential to these applications are fluorinated surfactants, which play a key role in effective design of fluorocarbon-based formulations and colloidal aggregates. Fluorinated surfactants self-assemble more readily than their hydrocarbon analogues, forming organized structures with lower curvature such as planar bilayers and vesicles. Their enhanced hydrophobicity, coupled with immiscibility with hydrocarbon surfactants, produces interesting complex phase behavior in solution.

This work expands the knowledge of the influence of fluorination on the thermophysical properties and phase behavior of fluorinated surfactants and solutes, with particular attention paid to the impact in organized bilayer assemblies. Also, the properties of fluorinated bilayers were explored in material synthesis and encapsulation applications. The fundamental aspects of phase behavior in both isotropic and self-aggregated systems are covered, which highlight the unusual characteristics of these systems and reflect the need for understanding the parameters that allow for effective modulation of phase behavior.

Partition Behavior of Solutes

The investigation of the partitioning behavior of a functionalized series of fluorinated and hydrocarbon nicotinic acid esters or nicotines (prodrugs) in immiscible solvents and model membrane bilayers aids in the analysis of the viability of

fluorocarbon mediated prodrug delivery for administration through the pulmonary route. Thermodynamic parameters pertinent to this novel prodrug transport through solvent interfaces were assessed and provided an interpretation of the mechanism of targeted prodrug delivery. In Chapter 3, the equilibrium partitioning between a fluorocarbon/organic (PFMC/toluene) biphasic system was evaluated as a function of chain length for the perhydrocarbon and the perfluorinated nicotines. The PFMC/toluene partition coefficients, a standard index of fluorophilicity, decrease by two orders of magnitude ($\text{Log } K_p = -1.72$ to -3.4) for the perhydrocarbon nicotines ($\text{CH}_3 - \text{C}_{12}\text{H}_{25}$), suggesting increasing preference for the organic phase. Conversely, both the fully and partially perfluorinated nicotines ($\text{C}_2\text{F}_3 - \text{C}_8\text{F}_{15}$) and ($\text{C}_3\text{F}_4 - \text{C}_8\text{F}_{13}$) demonstrate increasing propensity for the fluorocarbon phase ($\text{Log } K_p = -1.64 - 0.13$) spanning three orders of magnitude. With the only positive partition coefficient value ($\text{Log } K_p = 0.13$), only C_8F_{15} qualified as truly fluorophilic. This was attributed to the relatively higher fluorine content of the nicotine (57%) and in accord with established empirical rules⁹⁸ that 60% molecular fluorination is required for fluorophilicity. The partially fluorinated series possess lower affinity for the fluorocarbon phase than the fully fluorinated nicotines. Specifically, the difference between C_8H_{17} ($\text{Log } K_p = 0.13$) and C_8H_{15} ($\text{Log } K_p = -0.7$) highlights the modification of fluorophilic character with subtle alterations of molecular structure.

In the PFOB/aqueous system, both series of perhydrocarbon and perfluorinated nicotines demonstrated increasing preference for the PFOB phase with chain length. Negative partition values for CH_3 ($\text{Log } K_p = -0.78$) and C_2H_5 ($\text{Log } K_p = -0.16$) indicate better solubilization in the aqueous phase. PFOB/water partition coefficients of the longer chained perfluorinated nicotines ($> \text{C}_3\text{F}_5$) were not determined due to the challenges associated with the surface activity of the molecules and their low aqueous solubility.

The partition behavior (fluorophilicity) was also predicted by Regular Solution Theory (RST) approach, utilizing the solubility parameters from group contribution methods and molecular dynamics simulation. Both predictive approaches provide partition coefficients that are in reasonable agreement with experimental values for the hydrocarbon and short chain fluorinated nicotines ($\leq 38\%$) but deviate significantly

with the longer chained fluorinated nicotines (> 50%). This pattern highlights the challenges associated with thermodynamic descriptions of fluorinated surfactant systems.

The findings reveal no strong correlation of the biphasic partitioning trends with biological markers/endpoints of cytotoxicity and metabolic cellular function for the PFOB mediated delivery. In effect, delivery from PFOB is not expected to be a barrier to drug transport for the nicotines. Only the longer chained fluorinated nicotines (C8F15 and C8F13) exhibit cytotoxicity that paralleled partitioning behavior, suggesting their strong affinity for PFOB limits delivery to the target pulmonary cells. This rationale was derived from cytotoxic measurements in an organic-aqueous media system that showed strong correlation with the nicotine chain length.

Further description of the prodrug uptake through a cellular matrix was provided by model membrane partitioning measurements for the select series of perhydrocarbon nicotines, C2H5, C4H9, C6H13 and C8H17 (Chapter 4). Complementary calorimetric and fluorescence anisotropy techniques identified a chain length dependent pattern in the interaction of the perhydrocarbon nicotines with the DPPC model membrane matrix (liposome). The incorporation of the nicotines was measured from the membrane water partition coefficients, which increased by several orders of magnitude from $\text{Log } K_{m/w} = 2.13$ (C2H5) to 5.17 (C8H17).

Catanionic Vesicles with Fluorinated Surfactant Bilayers

Cationic-anionic (catanionic) vesicle bilayers which show potential as candidates for material synthesis and encapsulation applications were studied. The non ideal mixtures of cationic and anionic surfactants produce a wide range of composition dependent aggregate structures, which include mixed micelles and lamellar structure. Catanionic vesicles form spontaneously in dilute aqueous solutions and serve as potential substitutes to conventional meta-stable liposome-based vesicles. Although electrostatics govern intra- and inter-aggregate interactions, the fluorinated bilayer matrix in catanionic surfactant mixtures also exerts strong influence on phase behavior.

Regions of spontaneous vesicle formation were identified for mixed hydrocarbon/fluorocarbon bilayers, CPB/SPFO (cetylpyridinium bromide/sodium perfluorooctanoate) and fluorocarbon/fluorocarbon bilayers, HFDPC(1,1,2,2-

tetrahydroperfluorododecylpyridinium chloride)/SPFO, in the anionic-rich compositions. Smaller, less polydisperse vesicles are captured by TEM, at lower surfactant concentrations for the homogeneous fluorinated bilayer, HFDPC/SPFO (20 – 50 nm) than in the heterogeneous bilayer, CPB/SPFO (40 – 200 nm). However, due to the low refractive index of fluorinated chains, the DLS measurements are biased towards a few large vesicles in the HFDPC/SPFO system, reporting much larger sizes (200 nm) than observed with TEM (Chapter 5). The study of catanionic phase behavior (in anionic-rich compositions) was expanded with inclusion of the more asymmetric counterparts, CPB/SPFH (sodium perfluorohexanoate) and HFDPC/SPFH (Chapter 6). Delineation of aggregate phase boundaries in the pseudo-ternary phase maps, reveal HFDPC/SPFO to have the narrowest composition-dependent isotropic vesicle region, while the more asymmetric counterpart, HFDPC/SPFH possessed a larger vesicle domain; comparable with that observed for the mixed bilayers, CPB/SPFO and CPB/SPFH. Vesicle formation in catanionic surfactant systems is dictated by both electrostatics and chain packing effects. The smaller vesicle region in HFDPC/SPFO is ascribed to combined effects of chain asymmetry and the large energy associated with bending stiff and bulky fluorinated chains into spherical curvature. The expanded vesicle region in the HFDPC/SPFH system was a result of increased chain asymmetry and the higher solubility of SPFH than SPFO. With uniform fluorinated bilayer, better chain packing was hypothesized in HFDPC/SPFO than in CPB/SPFO. This rationale was supported by fluorescence spectroscopic measurements of pyrene and pyrene derivatives; 1-pyrenebutanoic acid (PBA/Py-C4), 1-pyrenedecanoic acid (PDA/Py-C10) and 1-pyrenehexadecanoic acid (PHA/Py-C16).

Silica hollow spheres were successfully fabricated using the CPB/SPFO and HFDPC/SPFO vesicles as templates. The advantage of lower surfactant concentration requirements for stable vesicle formation was clearly demonstrated in the acid catalyzed synthesis, using the silica precursor, tetramethoxysilane (TMOS). Higher colloidal stability was achieved in HFDPC/SPFO templated silica system than CPB/SPFO as a consequence of the lower ionic strength of its surfactant composition. Stable silica spheres were detected at higher precursor to surfactant ratios in the HFDPC/SPFO than in CPB/SPFO. The enhanced barrier properties of the homogeneous lipophobic,

hydrophobic fluorinated bilayer environment of HFDPC/SPFO, limited incorporation of the hydrophobic precursor, with preservation of spherical morphology. Distorted vesicle structures observed in the mixed CPB/SPFO suggested the heterogeneous bilayer was more permeable to the TMOS precursor.

Relative encapsulation and retention of a model cationic dye (R6G) was determined for CPB/SPFO and HFDPC/SPFO vesicles using a combination of size exclusion chromatography, DLS and UV techniques (Chapter 7). In accord with several reports, the encapsulation was driven by surface electrostatic interactions between the dye and oppositely charged vesicles.^{47,164} Much higher encapsulation was achieved with CPB/SPFO than HFDPC/SPFO due to the higher surfactant concentration of the former. However, superior dye retention was determined for the HFDPC/SPFO. Similar to the silica synthesis conditions, due to increased hydrophobicity and lipophobicity, the fully fluorinated bilayer in HFDPC/SPFO, may provide a greater barrier effect to permeation than in the mixed CPB/SPFO vesicles. Overall, the robustness of the fluorinated//fluorinated bilayers was demonstrated in applications. The modulation of phase behavior with fluorinated chain length offers opportunities in tunable applications of fluorinated bilayers.

8.2 Future Work

Partition measurements of the nicotinic acid prodrugs show that equilibrium partitioning between the relevant binary solvents do not necessarily translate to transport barriers in the PFOB system. However, partitioning trends in model membranes for the perhydrocarbon nicotinates can be used to interpret the mechanism of incorporation in a cellular matrix. Similar knowledge of the liposome membrane partitioning of the fluorinated nicotinates would complete assessment of the incorporation mechanism as function of fluorination in the prodrug series. These measurements will advance the goal of designing fluorinated prodrugs, which balance the need for prodrug solubility in a fluorinated phase and transfer into a cellular matrix, with minimized cellular toxicity. It is anticipated that the perfluorinated nicotinates will exhibit higher membrane/water partitioning than their hydrocarbon analogues due to their higher hydrophobicity. Studies have reported membrane partition coefficient values for fluorinated salts that are twice

those of their hydrocarbon analogues.¹³⁵ The partition coefficient trends are also expected to mirror those of the perhydrocarbon nicotines, in that they increase with chain length (C₂F₃ – C₈F₁₅) of the nicotines. Additionally, the lipophobicity of the fluorinated nicotines is expected to generate more pronounced perturbative effects on the hydrocarbon liposome bilayer packing and fluorocarbon-rich domains might exist in the bilayer at higher nicotine concentrations.³⁷⁰

Predictive tools used in assessment of fluorophilicity can be extended to other prodrug compounds. Such preliminary evaluations will help assess the partitioning behavior and serve as a guide in the synthesis of prodrugs for drug delivery. Several other approaches exist to estimate solubility parameters an alternative method to Fedors group contribution method would be the application of Hansen solubility parameters which accounts for dispersion, polar and hydrogen bonding parameters.⁹¹

The incorporation of fluorinated surfactants in self-assembled catanionic bilayers has been shown to have practical implications for material synthesis and encapsulation applications. Further characterization using several techniques will help elucidate the mechanism of vesicle formation and determine the energetic constants associated with bending the fluorinated bilayers. Molecular dynamics simulation is a useful tool to determine the structural conformations of the chains in the fluorinated and mixed hydrocarbon/fluorinated bilayers. This would elucidate the minimized energy conformations of the chains in the different catanionic pairs and the relative ease of vesicle formation. Schuy et al³⁷¹ applied a variety of techniques (atomic force microscopy, ellipsometry, attenuated total reflection FTIR) to study the chain dynamics and structural conformation of perfluorinated lipid bilayers. The partially fluorinated chains were determined to adopt a conformation that minimized unfavorable hydrocarbon-fluorocarbon chain interactions. Similar methods can be applied to our catanionic surfactant pairs to determine the effect of chain interaction on bilayer properties and the influence of headgroup attractions on these.

Catanionic surfactant mixtures are defined by their non-ideal phase behavior and surface tension measurements can be used to quantify the deviation from ideal mixing.²⁷⁶ Nuclear magnetic resonance (NMR) used to study the structural transition of aggregates in hydrocarbon catanionic systems¹⁶⁹ can be extended to these systems. With F NMR,

fluorinated surfactant exchange between aggregates can be traced to determine the formation path to equilibrium vesicles. F NMR might also help determine the orientation of surface bound compounds in the catanionic vesicle systems. Cryo-TEM is another useful tool in the study of morphology of self-assembled catanionic surfactant systems, as it eliminates the artifacts intrinsic to dried TEM imaging process.^{44,169} Smaller microstructures such as the rod like micelles, globular micelles and any irregular structures can be directly viewed with this method.^{54,170,182} This combined with polarized optical microscopy (POM) images will provide a complete characterization of the multi-aggregate regions of the phase diagrams. Cryo-TEM analysis of the size and size distribution is particularly useful in discerning the method of vesicle stabilization (entropic or enthalpic). This can be accomplished by an intensive size analysis of large vesicle populations for various surfactant compositions within the vesicle lobe.¹⁸² The size distribution from the histograms can subsequently be applied to thermodynamic models to determine the effective bending constant.^{54,182}

The highly sensitive isothermal titration microcalorimetry (ITC) technique can be used to determine the enthalpies of aggregate formation as applied to sodium dodecyl sulfate and dodecyltrimethylammoniumbromide (SDS/DTAB).¹⁸⁷ Series of ITC experiments to determine the enthalpies of micellization of the single and mixed surfactant systems would provide quantitative measure of the non-ideal interactions. The enthalpies of aggregate formation at various compositions in the vesicle lobe for both CPB/SPFO and HFDPC/SPFO might inform on the mechanism of stabilization.

Other important aspects that deserve consideration are phase behavior in the cation-rich surfactant regions of the surfactant mixtures, changes in the counter-ions and pH. Systematic study of these effects will complement current observations and help explain the interplay of fluorinated chain packing and ionic interactions. Another means of modulating phase behavior is with supercritical carbon dioxide, $sc\ CO_2$, which has been established as a fluorophilic fluid.³⁷² Solvation of the fluorinated/fluorinated bilayer in HFDPC/SPFO with $sc\ CO_2$ can be anticipated to fluidize the stiff bilayers and expand the catanionic vesicle phase region of these systems. The bilayer fluidization as a function of CO_2 solvation can be monitored by fluorescence probing. However, the

formation carbonic acid (HCO_3^-) as result of CO_2 dissolution should also be taken into account, as this might influence cationic headgroup attractions.

With respect to applications, several avenues can be explored with these fluorinated vesicle bilayers. Encapsulation of solutes in the cationic vesicles can be examined as a function of surfactant composition to determine the optimal trapping efficiency conditions. The material synthesis silica spheres can also be investigated in varied templating conditions of basic pH, stirring time, organic additives and precursors which promote steric stabilization of the polymerized silica through the action of their functional groups. Applications should be explored for the asymmetric cationic pairs, HFDPC/SPFH and CPB/SPFH to assess the impact on reduced rigidity on bilayer function.

Overall, modulation of phase behavior with practical applications of fluorinated bilayer systems has been demonstrated in this work. The observations and results emerging from this study present numerous potential areas of research into fluorinated surfactant systems.

REFERENCES

- (1) Kissa, E. In *Surfactant Science Series*; Marcel Dekker: New York, 1994.
- (2) Scott, R. L. *J. Phys. Chem.* **1958**, *62*, 136-145.
- (3) Goss, K.-W., Bronner, G. *J. Phys. Chem. A* **2006**, *110*, 9518-9522.
- (4) Shinoda, K., Hato, M., Hayashi, T. *J. Phys. Chem.* **1972**, *76*, 909-914.
- (5) Tadros, T. F. *J. Colloid and Interface Science* **1980**, *74*, 196-200.
- (6) Horvath, I. T. *Acc. Chem. Res.* **1998**, *31*, 641-650.
- (7) Barthel-Rosa, L. P., Gladysz, J. A. *Coordination Chemistry Reviews* **1999**, *190-192*, 587-605.
- (8) Horvath, I. T. R., *J. Science* **1994**, *266*, 72-75.
- (9) Yoshida, J.-I., Itami, K. *Chem. Rev.* **2002**, *102*, 3693-3716.
- (10) Horvath, I. T., Rabai, J. In *Handbook of Fluorous Chemistry*; Gladysz, J. A., Curran, D. P., Horvath, I. T., Ed.; Wiley/VCH: Weinheim, 2004, p 5-10.
- (11) Clark, L. C. J., Gollan, F. *Science* **1966**, *152*, 1755-1756.
- (12) Riess, J. G., Krafft, M. P. *Biomaterials* **1998**, *19*, 1529-1539.
- (13) Riess, J. G. *Chem. Rev.* **2001**, *101*, 2797-2919.
- (14) Lattes, A., Rico-Lattes, I. *Art. Cells. Blood. Subs., and Immob. Biotech.* **1994**, *22*, 1007-1018.
- (15) Lehmler, H.-J., Bummer, P. M., Jay, M. *Chemtech* **1999**, *29*, 7-12.
- (16) Scott, M. G., Kucik, D. F., Goodnough, L. T., Monk, T. G. *Clin. Chem.* **1997**, *43*, 1724-1731.
- (17) Leach, L. C., Greenspan, J. S., Rubenstein, D. S., Shaffer, T. H., Wolfson, M. R., Jackson, J. C., Delemos, R., Fuhrman, B. P. *N. Engl. J. Med.* **1996**, *335*, 761-767.
- (18) Bull, J. L., Tredici, S., Komori, E., Brant, D. O., Grotberg, J. B., Hirschl, R. B. *J. Appl. Physiol.* **2004**, *96*, 1633-1642.
- (19) Hood, C. I., Modell, J. H. *CHEST* **2000**, *118*, 1436-1440.
- (20) van Eden, S. F., Klut, M. E., Leal, M. A., Alexander, J., Zonis, Z., Skippen, P. *Am. J. Respir. Cell. Mol. Biol.* **2000**, *22*, 441-450.
- (21) Doctor, A., Ibla, J. C., Grenier, B. M., Zurakowski, D., Ferretti, M. L., Thompson, J. E., Lillehei, C. W., Arnold, J. H. *J. Appl. Physiol.* **1998**, *84*, 1540-1550.
- (22) Clark, L. C. J., Becattini, F., Kaplan, S., Obrock, V., Cohen, D., Becker, C. *Science* **1973**, *181*, 680-682.
- (23) Weers, J. G., Liu, J., Fields, T., Resch, P., Cavin, J., Arlauskas, R. A., *Art. Cells. Blood. Subs., and Immob. Biotech.* **1994**, *22*, 1175-1182.
- (24) Yasu, T., Schmid-Schonbein, G. W., Cotter, B., DeMaria, A. N. *J. Am. Coll. Cardiol.* **1999**, *34*, 578-586.
- (25) Fritz, T. A., Unger, E. C., Sutherland, G., Sahn, D. *Invest Radiol* **1997**, *32*, 735-740.
- (26) Mulvagh, S. L., Foley, D. A., Aeschbacher, B. C., Klarich, K. K., Seward, J. B. *J. Am. Coll. Cardiol.* **1996**, *27*, 1519-1525.

- (27) Mattrey, R. F., Trambert, M. A., Brown, J. J., Young, S. W., Bruneton, J. N., Wesbey, G. E., Balsara, Z. N. *Radiology* **1994**, *191*, 841-848.
- (28) Santaella, C., Frezard, F., Vierling, P., Riess, J. G. *FEBS Letters* **1993**, *336*, 481-484.
- (29) Hoang, K. C., Mecozzi, S. *Langmuir* **2004**, *20*, 7347-7350.
- (30) Santaella, C., Vierling, P., Riess, J. G. *Agnew. Chem. Int. Ed. Engl.* **1991**, *30*, 567-568.
- (31) Guillod, F., Greiner, J., Riess, J. G. *Biochim. Biophys. Acta* **1996**, *1282*, 283-292.
- (32) Gadras, C., Santaella, C., Vierling, P. *J of Controlled Release* **1998**, *57*, 29-34.
- (33) Sadtler, V. M., Krafft, M. P., Riess, J. G. *Colloids and Surfaces A: Physicochem. Eng. Aspects* **1999**, *147*, 309-315.
- (34) Blinder, K. J., Peyman, G. A., Paris, C. L., Dailey, J. P., Alturki, W., Lui, K. -R., Gremillion, C. M. Jr., Clark, L. C. Jr. *Brit. J. Ophthalmol* **1991**, *75*, 240-244.
- (35) Lehmler, H.-J., Xu, L., Vyas, S. M., Ojogun, V. A., Knutson, B. L., Ludewig, G. *International Journal of Pharmaceutics* **2008**, *353*, 35-44.
- (36) Sato, S., Lida, J., Suzuki, K., Kawano, M., Ozeki, T., Fujita, M. *Science* **2006**, *313*, 1273-1276.
- (37) Riess, J. G., Krafft, M. P. *Chemistry and Physics of Lipids* **1995**, *75*, 1-14.
- (38) Schmutz, M., Michels, B., Marie, P., Krafft, M. P. *Langmuir* **2003**, *19*, 4889-4894.
- (39) Ferro, Y., Krafft, M. P. *Biochim. Biophys. Acta* **2002**, *1581*, 11-20.
- (40) Krafft, M. P., Giuleri, F., Riess, J. G. *Agnew. Chem. Int. Ed. Engl.* **1993**, *32*, 741-743.
- (41) Asakawa, T., Hisamatsu, H., Miyagishi, S. *Langmuir* **1995**, *11*, 478-482.
- (42) Asakawa, T., Miyagishi, S. *Langmuir* **1999**, *15*, 3464-3468.
- (43) Asakawa, T., Hisamatsu, H., Miyagishi, S. *Langmuir* **1996**, *12*, 1204-1207.
- (44) Kaler, E. W., Herrington, K.L., Iampietro, D.J., Coldren, B.A., Jung, H-T., Zasadzinski, J.A., In *Mixed Surfactant Systems*; 2nd Edition ed.; Masahiko, A., Scamehorn, J. F., Ed.; Marcel Dekker: New York, 2005; Vol. 124, p 289-337.
- (45) Bergstrom, M. *Langmuir* **1996**, *12*, 2454-2463.
- (46) Iampietro, D. J., Kaler, E.W. *Langmuir* **1999**, *15*, 8590-8601.
- (47) Danoff, E. J., Wang, X., Tung, S. -H., Sinkov, N. A., Kemme, A. M., Raghavan, S. R., English, D. S. *Langmuir* **2007**, *23*, 8965-8971.
- (48) Dias, R. S., Lindman, B., Miguel, M. G. *J. Chem. Phys. B* **2002**, *106*, 12600 - 12607.
- (49) Yang, Y., Li, L., Chen, G. *Journal of Magnetism and Magnetic Materials* **2006**, *305*, 40-46.
- (50) Hentze, H.-P., Raghavan, S.R., McKelvey, C.A., Kaler, E.W. *Langmuir* **2003**, *19*, 1069-1074.

- (51) Vautrin, C., Zemb, T., Schneider, M., Tanaka, M. *J. Phys. Chem. B* **2004**, *108*, 7986-7991.
- (52) Gradzielski, M. *J. Phys.: Condens. Matter* **2003**, *15*, R655-R697.
- (53) Kang, S.-Y., Seong, B. -S., Han, S. Y., Jung, H. -T. *Biomacromolecules* **2003**, *4*, 360-365.
- (54) Jung, H. T.; Coldren, B.; Zasadzinski, J. A.; Iampietro, D. J.; Kaler, E. W. *Proc Natl Acad Sci U S A* **2001**, *98*, 1353-7.
- (55) Reed, T. M. In *Fluorine Chemistry*; Simmons, J. H. Academic Press: New York, 1964; Vol. 5, p 133-221.
- (56) Rocaboy, C., Rutherford, D., Bennett, B. L., Gladysz, J. A. *Journal of Physical Organic Chemistry* **2000**, *13*, 596-603.
- (57) Courier, H. M., Vandamme, T. F., Krafft, M. P. *Colloids and Surfaces A: Physicochem. Eng. Aspects* **2004**, *244*, 141-148.
- (58) Courier, H. M., Pons, F., Lessinger, J. M., Frossard, N., Krafft, M. P., Vandamme, Th. F. *International Journal of Pharmaceutics* **2004**, *282*, 131-140.
- (59) Tanford, C. *The hydrophobic effect*; Wiley: New York, 1973.
- (60) Israelachvili, J. M., D. J., Ninham, B. W. *J. Chem. Soc. Faraday Trans. 2* **1976**, *72*, 1525-1568.
- (61) Nagarajan, R., Ruckenstein, E. *Langmuir* **1991**, *7*, 2934-2969.
- (62) Nakano, T.-Y., Sugihara, G., Nakashima, T., Yu, S. -C. *Langmuir* **2002**, *18*, 8777-8785.
- (63) Jarvis, N. L., Zisman, W. A. *J. Phys. Chem.* **1959**, *63*, 727.
- (64) Ravey, J. C., Stebe, M. J. *Colloids and Surfaces A: Physicochem. Eng. Aspects* **1994**, *84*, 11-31.
- (65) Damas, C., Naejus, R., Coudert, R., Frochot, C., Brembilla, A., Viriot, M. -L. *J. Phys. Chem. B* **1998**, *102*, 10917-10924.
- (66) Mukerjee, P., Handa, T. *J. Phys. Chem.* **1981**, *85*, 2298-2303.
- (67) Turberg, M. P., Brady, J. E. *J. Am. Chem. Soc.* **1988**, *110*, 7797-7801.
- (68) Lehmler, H.-J. *Chemosphere* **2005**, *58*, 1471-1496.
- (69) Hoffmann, H., Kalus, J., Thurn, H. *Colloid. Polym. Sci.* **1983**, *261*, 1043-1049.
- (70) Wang, K., Karlsson, G., Almgren, M. *J. Phys. Chem. B* **1999**, *103*, 9237-9246.
- (71) Fontell, K., Lindman, B. *J. Phys. Chem.* **1983**, *87*, 3289-3297.
- (72) Wen, W. Y., Muccitelli, J. A. *J. Solution Chem.* **1979**, *8*, 225.
- (73) Wilhelm, E., B., R., Wilcock, R. J. *Chem. Rev.* **1977**, *77*, 219-262.
- (74) Tomasic, V., Chittofrati, A., Kallay, N. *Colloids and Surfaces A: Physicochem. Eng. Aspects* **1995**, *104*, 95-99.
- (75) Gough, C. A., Pearlman, D. A., Kollman, P. *J. Chem. Phys.* **1993**, *11*, 9103-9110.
- (76) Bernett, M. K., Zisman, W. A. *J. Phys. Chem.* **1967**, *71*, 2075-2082.
- (77) Eastoe, J., Paul, A., Rankin, A., Wat, R., Penfold, J., Webster, J. R. P. *Langmuir* **2001**, *17*, 7873-7878.
- (78) Prapaitrakul, W., King, A. D. Jr. *J Colloid Interface Sci* **1986**, *112*, 387-395.

- (79) Sadtler, V. M., Guileri, F., Krafft, M. P., Riess, J. G. *Chem. Eur. J.* **1998**, *4*, 1952-1956.
- (80) Mukerjee, P., Yang, A. Y. S. *J. Phys. Chem.* **1976**, *80*, 1388-1390.
- (81) Pedone, L. M., D. C., Caponetti, E., Floriano, M. A., Triolo, R. *J. Phys. Chem. B* **1997**, *101*, 9525-9531.
- (82) Barthelemy, P., Tomao, V., Selb, J., Chaudier, Y., Pucci, B. *Langmuir* **2002**, *18*, 2557-2563.
- (83) Altschul, R., Hoffer, A., Stephen, J. D. *Arch. Biochem. Biophys.* **1955**, *54*, 558-559.
- (84) Schachter, M. *Cardiovascular Drugs and Therapy* **2005**, *19*, 415-422.
- (85) Jacobson, E. L., Shieh, W. M., Huang, A. C. *Molecular and Cellular BioChemistry* **1999**, *193*, 69-74.
- (86) Nagai, A., Yasui, S., Ozawa, Y., Uno, H., Konno, K. *Eur. Respir. J.* **1994**, *7*, 1125-1130.
- (87) Adson, A., Burton, P., Raub, T. J., Barsuhn, C.L., Audus, K. L., Ho, N. F. H. *J. Pharm. Sci.* **1995**, *84*, 1197-1203.
- (88) Zasadzinski, J. A. *Curr Opin Solid State Mater Sci* **1997**, *2*, 345-349.
- (89) Berthod, A., Carda-Broch, S. *J Chromatography A* **2004**, *1037*, 3-14.
- (90) Danielsson, L.-G., Zhang, Y. -H. *Trends in analytical chemistry* **1996**, *15*, 188-196.
- (91) Barton, A. F. M. *Handbook of Solubility Parameters and Other Cohesion Parameters*; 2nd ed.; CRC Press, 1991.
- (92) Trapani, A., Lopodota, A, Denora, N., Laquintana, V., Franco, M., Latrofa, A., Trapani, G., Liso, G. *International Journal of Pharmaceutics* **2005**, *295*, 163-175.
- (93) Fedors, R. F., Van Krevelen, D. W., Hoftyzer, P. J. In *CRC Handbook of solubility parameters and other cohesion parameters*; Barton, A. F. M., CRC Press: Boca Raton, FL, 1983, p 64-66.
- (94) Endo, S., Schmidt, T. C. *Fluid Phase Equilibria* **2006**, *246*, 143-152.
- (95) Altomare, C., Carotti, A., Trapani, G., Liso, G. *J. Pharm. Sci.* **1997**, *86*, 1417-1425.
- (96) Goss, K.-W. *Fluid Phase Equilibria* **2005**, *233*, 19-22.
- (97) Daniels, S. D., Robert, A., Saunders, R. A., Platts, J. A. *J. Fluorine Chemistry* **2004**, *125*, 1291-1298.
- (98) Kiss, L. E., Kovesdi, I., Rabai, J. *J. Fluorine Chemistry* **2000**, *108*, 95-109.
- (99) De Wolf, E., Ruelle, P., Broeke, J., Deelman, B. -J., Koten, G. J. *J. Phys. Chem. B* **2004**, *108*, 1458-1466.
- (100) Sarraf, E. G. *J. Chem. Soc., Faraday Trans.* **1997**, *93*, 2519-2525.
- (101) Fedors, R. F. *J. Polymer. Eng and Sci* **1974**, *14*, 147-154.
- (102) Chernyak, Y. *J Chemical Eng. Data* **2006**, *51*, 416-418.
- (103) Huque, F. T. T., Jones, K., Saunders, R. A., Platts, J. A. *Journal of Fluorine Chemistry* **2002**, *115*, 119-128.
- (104) Arp, H. P. H., Niederer, C., Goss, K. -U. *Environ. Sci. & Technol.* **2006**, *40*, 7298-7304.

- (105) Downer, A., Eastoe, J., Pitt A. R., Simister, E. A., Penfold, J. *Langmuir* **1999**, *15*, 7591-7599.
- (106) Szoka, F. J., Papahadjopoulos, D. *Ann. Rev. Biophys. Bioeng.* **1980**, *9*, 467-508.
- (107) Bangham, A. D., Horne, R. W. *J. Mol. Biol.* **1964**, *8*, 660-668.
- (108) Nagle, J. F. *Ann. Rev. Phys. Chem.* **1980**, *31*, 157-195.
- (109) Marcotte, L., Barbeau, J., Edwards, K., Karlsson, G., Lafleur, M. *Colloids and Surfaces A: Physicochem. Eng. Aspects* **2005**, *266*, 51-61.
- (110) Inoue, T., Muraoka, Y., Fukushima, K., Shimozawa, R. *Chemistry and Physics of Lipids* **1988**, *46*, 107-115.
- (111) Israelachvili, J. N., Wennerstrom, H. *Langmuir* **1990**, *6*, 873-876.
- (112) Kunitake, T. *Agnew. Chem. Int. Ed. Engl.* **1992**, *31*, 709-726.
- (113) Lasch, J. *Biochim. Biophys. Acta* **1995**, *1241*, 269-292.
- (114) Carrozzino, J. M., Khaledi, M.G. *Pharm. Res.* **2004**, *21*, 2327-2335.
- (115) El Maghraby, G. M., Barry, B. W., Williams, A. C. *Eur. J. Pharm. Sci.* **2008**, *34*, 203-222.
- (116) Begu, S., Pouessel, A.A., Lerner, D.A., Tourne-Peteilh, C., Devoisselle, J.-M. *J. Controlled Release* **2007**, *118*, 1-6.
- (117) Antonietti, M., Forster, S. *Adv. Mater.* **2003**, *15*, 1323-1333.
- (118) Olson, F., Hunt, C. A., Szoka, F. C., Vail, W. J., Papahadjopoulos, D. *BBA - Biomembranes* **1979**, *557*, 9-23.
- (119) Watts, A., Marsh, D., Knowles, P. F. *Biochemistry* **1978**, *17*, 1792-1801.
- (120) Huang, C. H. *Biochemistry* **1969**, *8*, 344-352.
- (121) Carafa, M., Santucci, E., Alhaique, F., Coviello, T., Murtas, E., Riccieri, F. M., Lucania, G., Torrisi, M. R. *International Journal of Pharmaceutics* **1998**, *160*, 51-59.
- (122) Huang, C. *Biochemistry* **1991**, *30*, 26-30.
- (123) Silvius, J. R., Read, B. D., McElhaney, R. N. *Biochim. Biophys. Acta* **1979**, *555*, 175-178.
- (124) Denich, T. J., Beaudette, L. A., Lee, H., Trevors, J. T. *J. Microbiological Methods* **2003**, *52*, 149-182.
- (125) Gregoriadis, G. In *Trends in Biotechnology*; Elsevier: 1995; Vol. 13, p 527-537.
- (126) Lee, A. G. *Biochemistry* **1976**, *15*, 2448-2454.
- (127) Viriyaroj, A., Kashiwagi, H., Ueno, M. *Chem. Pharm. Bull.* **2005**, *53*, 1140-1146.
- (128) De Young, L. R., Dill, K. A. *Biochemistry* **1988**, *27*, 5281-5289.
- (129) Austin, R., Barton, P., Davis, A., Fessey, R., Wenlock, M. *Pharm. Res.* **2005**, *22*, 1649-1657.
- (130) Kwon, J., -H., Liljestrand, H. M., Katz, L. E. *Environmental Toxicology & Chemistry* **2006**, *25*, 1984-1992.
- (131) Walter, A., Gutknecht, J. *J. Membrane Biol.* **1986**, *90*, 207-217.
- (132) Deo, N., Somasundaran, T., Somasundaran, P. *Colloids and Surfaces B: Biointerfaces* **2004**, *34*, 155-159.
- (133) De Castro, B., Gameiro, P., Lima, J. L. F. C., Matos, C., Reis, S. *Colloids and Surfaces A: Physicochem. Eng. Aspects* **2001**, *190*, 205-

212.

- (134) Xiang, T.-X., Anderson, B. D. *Biophysical Journal* **1998**, *75*, 2658-2671.
- (135) Xie, W., Kania-Korwel, I., Bummer, P. M., Lehmler, H. -J. *Biochim. Biophys. Acta* **2007**, *1768*, 1299-1308.
- (136) Lehmler, H.-J., Xie, W., Bothn, .G.D., Bummer, P.M., Knutson, B.L. *Colloids and Surfaces B: Biointerfaces* **2006**, *51*, 25-29.
- (137) Omran, A. A., Kitamura, K., Takegami, S., Kume, M., Yoshida, M., El-Sayed, A.A., Mohammed, M. H., Abdel-Mottaleb, M. *J. Pharmaceutical and Biomedical Anaylsis* **2002**, *30*, 1087-1092.
- (138) Xiang, T.-X., Anderson, B. D. *Advanced drug delivery reviews* **2006**, *58*, 1357-1378.
- (139) Sikkema, J., Bont, J. A. M., Poolman, B. *J. Biol. Chem.* **1994**, *269*, 8022-8028.
- (140) Escher, B. I., Schwarzenbach, R. P. *Environ Sci Technol* **1995**, *30*, 260-270.
- (141) Marqusee, J. A., Dill, K. A. *J. Chem. Phys.* **1986**, *85*, 434-444.
- (142) Tu, K., Tobias, D. J., Blasie, J. K., Klein, M. L. *Biophysical Journal* **1996**, *70*, 595-608.
- (143) Arrowsmith, M., Hadgraft, J., Kellaway, I. W. *International Journal of Pharmaceutics* **1983**, *14*, 191-208.
- (144) Rowe, E. S. *Biochemistry* **1983**, *22*, 3299-3305.
- (145) Aguilar, L. F., Sotomayor, C. P., Lissi, E. A. *Colloids and Surfaces A: Physicochem. Eng. Aspects* **1996**, *108*, 287-293.
- (146) Kamaya, H., Matubayasi, N., Ueda, I. *J. Phys. Chem.* **1984**, *88*, 797-800.
- (147) De La Maza. A., P., J. L. *Langmuir* **1996**, *12*, 3393-3398.
- (148) Lopez, O., Cocera, M., Parra, J. L., De La Maza, A. *Colloid. Polym. Sci.* **2001**, *279*, 909-915.
- (149) Deo, N., Somasundaran, P. *Langmuir* **2003**, *19*, 7271-7275.
- (150) Weakliem, C. L., Fujii, G., Chang, J. -E., Ben-Shaul, A., Gelbart, W. M., *J. Phys. Chem.* **1995**, *99*, 7694-7697.
- (151) Deo, N., Somasundaran, P. *Langmuir* **2003**, *19*, 2007-2012.
- (152) Terashima, M., Hibi, K., Katoh, S. *Biochemical Eng. J.* **1999**, *4*, 77-79.
- (153) Panico, A. M., Pignatello, R., Puglisi, G., Mazzone, G., Petrone, G. *International Journal of Pharmaceutics* **1992**, *80*, 93-100.
- (154) Kepczynski, M., Nawalany, K., Kumorek, M., Kobierska, A., Jachimska, B., Nowakowska, M. *Chemistry and Physics of Lipids* **2008**, *155*, 7-15.
- (155) De Young, L. R., Dill, K. A. *J. Phys. Chem.* **1990**, *94*, 801-809.
- (156) El-Sayed, M. Y., Guion, T. A., Fayer, M. D. *Biochemistry* **1986**, *25*, 4825-4832.
- (157) Woodle, M. C., Matthay, K. K., Newman, M. S., Hidayat, J. E., Collins, L. R., Redemann, C., Martin, F. J., Papahadjopoulos, D. *BBA* **1992**, *1105*, 193-200.
- (158) Vial, F., Rabhi, S., Tribet, C. *Langmuir* **2005**, *21*, 853-862.
- (159) Krafft, M. P., Schieldknecht, L., Marie, P., Giuleri, F., Schmutz, M., Poulain, N., Nakache, E. *Langmuir* **2001**, *17*, 2872-2877.

- (160) Krafft, M. P., Reiss, J. G. *Biochimie* **1998**, *80*, 489-514.
- (161) Ravily, V., Santaella, C., Vierling, P., Gulik, A. *Biochim. Biophys. Acta* **1997**, *1324*, 1-17.
- (162) Giulieri, F., Krafft, M. P. *Colloids and Surfaces A: Physicochem. Eng. Aspects* **1994**, *84*, 121-127.
- (163) Giulieri, F., Krafft, M. P. *Thin Solid Films* **1996**, *284-285*, 195-199.
- (164) Wang, X., Danoff, E. J., Sinkov, N. A., Lee, J., -H., Raghavan, S. R., English, D. S. *Langmuir* **2006**, *22*, 6461-6464.
- (165) Yaacob, I. I., Bhandarkar, S., Bose, A. *Journal of Materials Research* **1993**, *8*, 573-577.
- (166) Yaacob, I. I., Nunes, A. C., Bose, A., Shah, D. O. *J. Colloid and Interface Science* **1994**, *168*, 289-301.
- (167) Kaler, E. W., Murthy, A. K., Rodriguez, B.E., Zasadzinski, J. A. N. *Science* **1989**, *245*, 1371-1374.
- (168) Yacilla, M. T., Herrington, K. L., Brasher, L. L., Kaler, E. W., Chiruvolu, S., Zasadzinski, J. A. *J. Phys. Chem.* **1996**, *100*, 5874-5879.
- (169) Marques, E. F., Regev, O., Khan, A., Miguel, M. G., Lindman, B. *J. Phys. Chem. B* **1998**, *102*, 6746-6758.
- (170) Herrington, K. L., Kaler, E. W., Miller, D. D., Zasadzinski, J. A., Chiruvolu, S. *J. Physical Chemistry* **1993**, *97*, 13792-13802.
- (171) Jung, H.-T., Lee, S.Y., Kaler, E.W., Coldren, B., Zasadzinski, J.A., *PNAS* **2002**, *99*, 15318-15322
- (172) van Zanten, R., Zasadzinski, J. A. *Curr Opin Colloid & Interface Sci* **2005**, *10*, 261-268.
- (173) Salkar, R. A., Mukesh, D., Samant, S.D., Manohar, C. *Langmuir* **1998**, *14*, 3778-3782.
- (174) Yuet, P. K., Blankschtein, D. *Langmuir* **1996**, *12*, 3819-3827.
- (175) Hao, J., Hoffmann, H. *Curr Opin Solid State Mater Sci* **2004**, *9*, 279-293.
- (176) Vlachy, N., Drechsler, M., Verbavatz, J. -M., Touraud, D., Kunz, W. *J. Colloid and Interface Science* **2008**, *319*, 542-548.
- (177) Brasher, L. L., Herrington, K.L., Kaler, E.W. *Langmuir* **1995**, *11*, 4267-4277.
- (178) Huang, J.-B., Zhao, G. -X. *Colloid. Polym. Sci.* **1995**, *273*, 156-164.
- (179) Tsuchiya, K., Nakanishi, H., Sakai, H., Abe, M. *Langmuir* **2004**, *20*, 2117-2122.
- (180) Huang, J.-B., Zhu, B. -Y., Zhao, G. -X., Zhang, Z. -Y. *Langmuir* **1997**, *13*, 5759-5761.
- (181) Mao, M., Huang, J., Yin, B. Y., Fu, H. *Langmuir* **2002**, *18*, 3380-3382.
- (182) Coldren, B., van Zanten, R., Mackel, M.J., Zasadzinski, J.A., Jung, H.-T. *Langmuir* **2003**, *19*, 5632-5639.
- (183) Almgren, M., Rangelov, S. *Langmuir* **2004**, *20*, 6611-6618.
- (184) Vivares, D., Soussan, E., Blanzat, M., Rico-Lattes, I. *Langmuir* **2008**, *24*, 9260-9267.
- (185) Karukstis, K. K., McCormack, S. A., McQueen, M. T., Goto, K. F. *Langmuir* **2004**, *20*, 64-72.
- (186) Yin, H., Huang, J., Lin, Y., Zhang, Y., Qiu, S., Ye, J. *J. Phys. Chem. B*

- 2005**, *109*, 4104-4110.
- (187) Meagher, R., Hatton, T. A., Bose, A. *Langmuir* **1998**, *14*, 4081-4087.
- (188) Wang, Y., Bai, G., Marques, E. F., Yan, H. *J. Phys. Chem. B* **2006**, *110*, 5294-5300.
- (189) Jiang, L., Wang, Ke., Deng, M., Wang, Y., Huang, J. *Langmuir* **2008**, *24*, 4600-4606.
- (190) Laughlin, R. G. *Colloids and Surfaces A: Physicochem. Eng. Aspects* **1997**, *128*, 27-38.
- (191) Hao, J., Yuan, Z., Liu, W., Hoffmann, H. *J. Phys. Chem. B* **2004**, *108*, 5105-5112.
- (192) Helfrich, W. *J. Phys.* **1973**, *47*, 321-329.
- (193) Szleifer, I., Kramer, D., Ben-Shaul, A., Gelbart, W. M., Safran, S. A. *J. Chem. Phys.* **1990**, *92*, 6800-6817.
- (194) Safran, S. A., Pincus, A., Andelman, A., Mackintosh, F. C. *Phys. Rev.* **1991**, *43*, 1071-1078.
- (195) Yuet, P. K., Blankshtein, D. *Langmuir* **1996**, *12*, 3802-3818.
- (196) Marques, E. F., Brito, R. O., Silva, S. G., Rodriguez-Borges, J. E., Luisa do Vale, M., Gomes, P., Araujo, M. J., Soderman, O. *Langmuir* **2008**, *24*, 11009-11017.
- (197) Kaler, E. W., Herrington, K.L., Murthy, A. K. *J. Phys. Chem.* **1992**, *96*, 6698-6707.
- (198) Marques, E. F., Khan, A., Miguel, M. D. -G., Lindman, B. *J. Phys. Chem.* **1993**, *97*, 4729-4736.
- (199) Marques, E. F. *Langmuir* **2000**, *16*, 4798-4807.
- (200) Shioi, A., Hatton, T. A. *Langmuir* **2002**, *18*, 7341-7348.
- (201) O'Connor, A. J., Hatton, T. A., Bose, A. *Langmuir* **1997**, *13*, 6391-6940.
- (202) Xia, Y., Goldmints, I., Johnson, P. W., Hatton, T.A., Bose, A. *Langmuir* **2002**, *18*, 3822-3828.
- (203) Lopez-Fontan, J. L., Blanco, E., Ruso, J. M., Prieto, G., Schulz, P.C., Sarmiento, F. *Journal of Colloid and Interface Science* **2007**, *312*, 425-431.
- (204) Rossi, S., Karlsson, G., Ristori, S., Martini, G., Edwards, K. *Langmuir* **2001**, *17*, 2340-2345.
- (205) Trabelsi, H., Szonyi, S., Gaysinski, M., Cambon, A. *Langmuir* **1993**, *9*, 1201-1205
- (206) Dubois, M., Lizunov, V., Meister, A., Gulik-Krzywicki, T., Verbavatz, J. M., Perez, E., Zimmerberg, J., Zemb, T. *PNAS* **2004**, *101*, 15082-15087.
- (207) Trabelsi, H., Szonyi, S., Reuter, P., Wehrli, E., Geribaldi, S. *Supramolecular Chemistry* **2001**, *13*, 583-591.
- (208) Szonyi, S., Cambon., H., Watzke, H.J., Schurtenberger, P., Wehrli, E. *Springer Proceedings in Physics* **1992**, *66*, 198-201.
- (209) Yu, Z.-J., Neuman, R.D. *Langmuir* **1992**, *8*, 2074-2076.
- (210) Ristori, S., Appell, J., Porte, G. *Langmuir* **1996**, *12*, 686-690.
- (211) Oelschlaeger, C., Waton, G., Buhler, E., Candau, S. J., Cates, M.E. *Langmuir* **2002**, *18*, 3076-3085.

- (212) Wagner, J., Hartl, W., Hempelmann, R. *Langmuir* **2000**, *16*, 4080-4085.
- (213) Stokes, E. J., Evans, D. F., *Fundamentals of Interfacial Engineering*; Wiley-VCH: New York, 1997.
- (214) Helfrich, W. Z. *Naturforsch* **1978**, *33a*.
- (215) Walker, S. A., Zasadzinski, J. A. *Langmuir* **1997**, *13*, 5076-5081.
- (216) Bucak, S., Robinson, B. H., Fontana, A. *Langmuir* **2002**, *18*, 8288-8294.
- (217) Antunes, F. E., Marques, E. F., Gomes, R., Thuresson, K., Lindman, B., Miguel, M. G. *Langmuir* **2004**, *20*, 4647-4656.
- (218) Yin, H., Lin, Y., Huang, J., Ye, J. *Langmuir* **2007**, *23*, 4225-4230.
- (219) Jung, M., Den Ouden, I., Montoya-Gori, A., Hubert, D. H. W., Frederick, P. M., van Herk, A. M., German, A. L. *Langmuir* **1999**, *16*, 4185-4195.
- (220) Bonincontro, A., La Mesa, C., Proietti, C., Risuleo, G. *Biomacromolecules* **2007**, *8*, 1824-1829.
- (221) McKelvey, C. A., Kaler, E. W., Zasadzinski, J. A., Coldren, B., Jung, H. -T. *Langmuir* **2000**, *16*, 8285-8290.
- (222) Zhu, Y., Shi, J., Li, Y., Chen, H., Shen, W., Dong, X. *Microporous and Mesoporous Mater.* **2005**, *85*, 75-81.
- (223) Song, C., Wang, C., Zhu, H., Wu, X., Dong, L., Chen, Y. *Catal Lett* **2008**, *120*, 215 - 220.
- (224) Baca, M., Li, W.J., Du, P., Mul, G., Moulijn, J.A., Coppens, M. -O. *Catal Lett* **2006**, *109*, 207-210.
- (225) Brinker, C. J., Scherer, G.W. *Sol-Gel Science: The Physics and Chemistry of Sol-Gel Processing*; Academic Press: San Diego, 1990.
- (226) Hubert, D. H. W., Jung, M., Frederik, P.M., Bonnans, P.H.H., Meuldijk, J., German, A.L. *Adv. Mater.* **2000**, *12*, 1286-1290.
- (227) Hubert, D. H. W., Jung, M., German, L.A. *Adv. Mater.* **2000**, *12*, 1291-1294.
- (228) Wang, Q., Liu, Y., Yan, H. *Chem. Commun.* **2007**, 2339-2341.
- (229) Hah, H. J., Kim, J.S., Jeon, B.J., Koo, S.M., Lee, Y.E. *Chem. Commun.* **2003**, *14*, 1712-1713.
- (230) Katagiri, K., Hamasaki, R., Katsuhiko, A., Kikuchi, J. -I. *J. Sol-gel Sci. & Tech.* **2003**, *26*, 393-396.
- (231) Song, L., Ge, X., Wang, M., Zhang, Z. *J. Non-Crystalline Solids* **2006**, *352*, 2230-2235.
- (232) Wang, J., Xia, Y., Wang, W., Poliakoff, M., Mokaya, R. *J. Mater. Chem.* **2006**, *16*, 1751-1756.
- (233) Lootens, D., Vautrin, C., Van Damme, H., Zemb, T. *J. Mater. Chem.* **2003**, *13*, 2072-2074.
- (234) Begu, S., Durand, R., Lerner, D. A., Charnay, C., Tourne-Peteilh, C., Devoisselle, J. -M. *Chem. Commun.* **2003**, *5*, 640-641.
- (235) Yeh, Y.-Q., Chen, B.-C., Lin, H.-P., Tang, C.-Y. *Langmuir* **2006**, *22*, 6-9.
- (236) Kepczynski, M., Lewandowska, J., Romek, M., Zapotoczny, S., Ganachaud, F., Nowakowska, M. *Langmuir* **2007**, *23*, 7314-7320.

- (237) Tan, B., Dozier, A., Lehmler, H-J., Knutson, B.L., Rankin, S.E. *Langmuir* **2004**, *20*, 6981-6984.
- (238) Tan, B., Lehmler, H -J., Vyas, S. M., Knutson, B. L., Stephen, E. *Adv. Mater.* **2005**, *22*, 2368-2371.
- (239) Reiss, J. G., Krafft, M. P., *Biomaterials* **1998**, *19*, 1529-1539.
- (240) LoNostro, P., Choi, S. -M., Ku, C. -Y., Chen, S. -H. *J. Phys. Chem. B* **1999**, *103*, 5347-5352.
- (241) Hsu, C.-H., Jay, M., Bummer, P. M., Lehmler, H. -J. *Pharm. Res.* **2003**, *20*, 918-925.
- (242) Weers, J. G., Arlauskas, R. A., Tarara, T. E., Pelura, T. J. *Langmuir* **2004**, *20*, 7430-7435.
- (243) Lehmler, H.-J., Bummer, P. M., Jay, M., *Chemtech* **1999**, *29*, 7-12.
- (244) Lehmler, H.-J. *Expert Opinion on Drug Delivery* **2007**, *4*, 247-262.
- (245) Duchowicz, P. R., Fernandez, F. M., Castro, E. A. *J. Fluorine Chemistry* **2005**, *125*, 43-48.
- (246) Ruelle, P. *J. Chem. Inf. Comput. Sci.* **2000**, *40*, 681-700.
- (247) Morishita, S., Saito, T., Hirai, Y., Shoji, M., Mishima, Y., Kawakami, M. *J. Med. Chem.* **1988**, *31*, 1205-1209.
- (248) Praustnitz, J. M., Lichtenhaler, R. N., De Azevedo, E. G. *Molecular Thermodynamics of fluid-phase equilibria*; 2nd ed.; Prentice-Hall Inc.: Englewood Cliffs, N. J. 1986.
- (249) Allen, M. P., Tildesley, D. J. *Computer simulation of liquids*; Oxford University Press: Oxford, 1987.
- (250) Spyriouni, T., Vergelati, C. *Macromolecules* **2001**, *34*, 5306-5316.
- (251) Zhang, M., Choi, P., Sundararaj, U. *Polymer* **2003**, *44*, 1979-1986.
- (252) Sun, H. *J. Phys. Chem. B* **1998**, *102*.
- (253) Rigby, D., Sun, H., Eichinger, B. E. *Polym. Int.* **1998**, *44*, 311-330.
- (254) Eichinger, B. E., Rigby, D., Muir, M. H. *Comput. Polym. Sci.* **1995**, *5*.
- (255) Bodor, N., Buchwald. P. *J. Chem. Phys. B* **1997**, *101*, 3404-3412.
- (256) Peral, F., Gallego, E. *J Mol Structure* **1992**, *274*, 105-114.
- (257) Rongvaux, A., Andris, F., Van Gool, F., Leo, O. *Bioessays* **2003**, *25*, 683-690.
- (258) Wang, Q., Giri, D. M., Hyde, M., Nakashima, J. M., Javadi, I. *J. Biochem. Toxicol.* **1990**, *5*, 13-22.
- (259) Kamanna, V. S., Kashyab, M. L. *Curr. Atheroscl. Rep.* **2000**, *2*, 36-46.
- (260) Vogt, A., Kassner, H., Hostalek, U., Steinhagen-Thiessen, E. *Vascular Health and Risk Management* **2007**, *3*, 467-479.
- (261) Murray, M. F. *Medical Hypotheses* **1999**, *53*, 375-379.
- (262) Guyton, J. R., Bays, H. E. *American Journal of Cardiology* **2007**, *99*, 22C-31C.
- (263) Ladbrooke, B. D., Chapman, D. *Chem. Phys. Lipids* **1969**, *3*, 304-356.
- (264) Bangham, A. D., Standish, M. M., Watkins, J. C. *J. Mol. Biol.* **1965**, *13*, 238-252.
- (265) Bothun, G. D., Knutson, B. L., Strobel, H. J., Nokes, S. E. *Langmuir* **2004**, *21*, 530-536.
- (266) Lackowicz, J. R.; 2nd ed.; Kluwer Academic: New York, 1999.

- (267) Inoue, T., Miyakawa, K., Shimozawa, R. *Chem. Phys. Lipids* **1986**, *42*, 261-270.
- (268) Koynova, R., Caffrey, M. *Biochim. Biophys. Acta* **1998**, *1376*, 91-145.
- (269) Le, V. H., Lippold, B. C. *International Journal of Pharmaceutics* **1998**, *163*, 11-22.
- (270) McIntosh, T. J. *Biophys. J.* **1980**, *29*, 237-245.
- (271) Lehmler, H.-J., Fortis-Santiago, A., Nauduri, D., Bummer, P.M. *J. Lipid. Res.* **2005**, *46*, 535-546.
- (272) Sklar, L. A., Hudson, B. S., Peterson, M., Diamond, J. *Biochemistry* **1977**, *16*, 813-819.
- (273) Gobas, F. A. P. C., Mackay, D., Shiu, W. Y., Lahittete, J. M., Garofalo, G. *J. Pharm. Sci.* **1987**, *77*, 265-272.
- (274) Pasc-Banu, A., Stan, R., Blanzat, M., Perez, E., Rico-Lattes, I., Lattes, A., Labrot, T., Oda, R. *Colloids and Surfaces A: Physicochem. Eng. Aspects* **2004**, *242*, 195-201.
- (275) Del Burgo, P., Aicart, E., Llorca, O., Junquera, E. *J. Phys. Chem. B* **2006**, *110*, 23524-23539.
- (276) Bergstrom, M. *Langmuir* **2001**, *17*, 993-998.
- (277) Yin, H., Huang, J., Gao, Y., Fu, H. *Langmuir* **2005**, *21*, 2656-2659.
- (278) Gonzalez-Perez, A., Schmutz, M., Waton, G., Romero, M. J., Krafft, M.P. *J. Am. Chem. Soc.* **2007**, *129*, 756-757.
- (279) Marques, E. F., Regev, O., Khan, A., Lindman, B. *Advances in Colloid and Interface Science* **2003**, *100-102*, 83-104.
- (280) Regev, O., Khan, A. *Journal of Colloid and Interface Science* **1996**, *182*, 95-109.
- (281) Letizia, C., Andreozzi, P., Scipioni, A., La Mesa, C., Bonincontro, A., Spigone, E. *J. Phys. Chem. B* **2007**, *111*, 898-908.
- (282) Fischer, A., Hebrant, M., Tondre, C. *J. Colloid Interface Sci* **2002**, *248*, 163-168.
- (283) Botterhuis, N. E., Sun, Q., Magusin, P.C.M.M., van Santen, R.A., Sommerdijk, N.A.J.M. *Chem. Eur. J.* **2006**, *12*, 1448-1456.
- (284) Zhu, Y., Shi, J., Shen, W., Chen, H., Dong, X., Ruan, M. *Nanotechnology* **2005**, *16*, 2633-2638.
- (285) Szonyi, S., Watzke, H.J. *Progr. Colloid Polym. Sci.* **1993**, *93*, 364-365.
- (286) Lopez-Fontan, J. L., Sarmiento, F., Schulz, P.C. *Colloid. Polym. Sci.* **2005**, *283*, 862-871.
- (287) Gonzalez-Perez, A., Ruso, J.M., Prieto, G., Sarmiento, F. *J. Surfactants and Detergents* **2004**, *7*, 387-395.
- (288) Krafft, M. P., Reiss, J.G. *Biochimie* **1998**, *80*, 489-514.
- (289) Trevino, L., Frezard, F., Rolland, J. P., Postel, M., Riess, J. G. *Colloids and Surfaces A: Physicochem. Eng. Aspects* **1994**, *88*, 223-233.
- (290) Guittard, F., Geribaldi, S. *J. Fluorine Chemistry* **2001**, *107*, 363-374.
- (291) Riess, J. G. *Colloids and Surfaces A: Physicochem. Eng. Aspects* **1994**, *84*, 33-48.
- (292) Koppel, D. E. *J. Chem. Phys.* **1972**, *57*, 4814-4820.
- (293) Jung, H. T., Coldren, B., Zasadzinski, J.A., Iampietro, D.J., Kaler,

- E.W. *PNAS* **2001**, 98, 1353-1357.
- (294) Silva, B. F. B., Marques, E. F. *Journal of Colloid and Interface Science* **2005**, 290, 267-274.
- (295) Huibers, P. D. T. *Langmuir* **1999**, 15, 7546-7550.
- (296) Skerjanc, J., Kogej, K., Cerar, J. *Langmuir* **1999**, 15, 5023 - 5028.
- (297) Koenderink, G. H., Sacanna, S., Pathmamanoharan, C., Rasa, M., Philipse, A. P. *Langmuir* **2001**, 17, 6086-6093.
- (298) Jung, M., Hubert, D. H. W., Bomans, P. H. H., Frederik, P. M., Meuldijk, J., van Herk, A. M., Fischer, H., German, A. L. *Langmuir* **1997**, 13, 6877-6880.
- (299) Jokela, P., Jonsson, B., Eichmuller, B., Fontell, K. *Langmuir* **1988**, 4, 187-192.
- (300) Coldren, B. A., Warriner, A., van Zanten, R., Zasadzinski, J. A., Sirota, E. B. *Langmuir* **2006**, 22, 2474-2481.
- (301) Ojogun, V. A., Lehmler, H. -J., Knutson, B. L. *JCIS* **2009**, 338, 82-91.
- (302) Chen, S. H., Frank, C. W. *Langmuir* **1991**, 7, 1719-1726.
- (303) Almgren, M., Wang, K., Asakawa, T. *Langmuir* **1997**, 13, 4535-4544.
- (304) Giulieri, F., Krafft, M. P. *J Colloid Interface Sci* **2003**, 258, 335-344.
- (305) Glushko, V., Thaler, M. S. R., Karp, C. D. *Arch. Biochem. Biophys.* **1981**, 210, 33-42.
- (306) Kalyanasundaram, K., Thomas, J. K. *J. Am. Chem. Soc.* **1977**, 99, 2039-2044.
- (307) Damas, C., Frochot, C., Naejus, R., Brebilla, A., Viriot, M. -L., Coudert, R. *J. Colloid and Interface Science* **2001**, 241, 188-198.
- (308) Kodama, T., Ohta, A., Toda, K., Katada, T., Asakawa, T., Miyagishi, S. *Colloids and Surfaces A: Physicochem. Eng. Aspects* **2006**, 277, 20-26.
- (309) Yue, Y., Wang, J., Dia, M. *Langmuir* **2000**, 16, 6114-6117.
- (310) Pansu, R. B., Yoshihara, K., Arai, T., Tokumaru, K. *J. Phys. Chem.* **1993**, 97, 1125-1133.
- (311) Sandstrom, M. C., Ickenstein, L. M., Mayer, L. D., Edwards, K. *J Controlled Release* **2005**, 107, 131-142.
- (312) Vanderkooi, J. M., Callis, J. B. *Biochemistry* **1974**, 13, 4000-4006.
- (313) Yamazaki, I., Tamai, N., Yamazaki, T. *Chem. Phys. Lett.* **1986**, 124, 326-330.
- (314) Smoluchowski, M. V. Z. *Phys. Chem.* **1917**, 92, 129-168.
- (315) Collins, F. C., Kimball, G. E. *Journal of Colloid and Interface Science* **1949**, 4, 425-437.
- (316) Zelent, B., Kusba, J., Gryczynski, I., Johnson, M. L., Lackowicz, J. R. *J. Fluorescence* **1993**, 3, 199-207.
- (317) Vanderkooi, J. M., Englander, S.W., Papp, S., Wright, W. W., Owen, C. S. *Proc. Natl. Acad. Sci.* **1990**, 87, 5099-5103.
- (318) Wade, D.A., T., S. A. *Talanta* **2000**, 53, 571-578.
- (319) Neal, S. L., Villegas, M. M. *Anal. Chem.* **1995**, 67, 2659.
- (320) Abuin, E., Lissi, E., Aravena, D., Zanocco, A., Macuer, M. *J. Colloid and Interface Science* **1988**, 122, 201-208.
- (321) Gratzel, M., Thomas, J. K. *J. Am. Chem. Soc.* **1973**, 95, 6885-6889.

- (322) Berr, S. S., Jones, R. R. M. *J. Phys. Chem.* **1989**, *93*, 2555-2558.
- (323) Muller, N., Simsohn, H. *J. Phys. Chem.* **1971**, *75*, 942-945.
- (324) Ulmius, J., Lindman, B. *J. Phys. Chem.* **1981**, *85*, 4131-4135.
- (325) Kujawa, P., Liu, R. C. W., Winnik, F. M. *J. Phys. Chem. B* **2002**, *106*, 5578-5585.
- (326) Asakawa, T., Okada, T., Hayasaka, T., Kuwamoto, K., Ohta, A., Miyagishi, S. *Langmuir* **2006**, *22*, 6053-6055.
- (327) Kalyanasundaram, K. *Langmuir* **1988**, *4*, 942-945.
- (328) Szajdzinska-Pietek, E., Wolszczak, M. *Langmuir* **2000**, *16*, 1675-1680.
- (329) Asakawa, T., Ishikawa, K., Miyagishi, S. *JCIS* **2001**, *240*, 365-367.
- (330) Ayala, J. H., Afonso, A. M., Gonzalez-Diaz, V. *Microchemical Journal* **1998**, *60*, 101-109.
- (331) Varadaraj, R., Valint, P., Bock, J., Zushma, S., Brons, N. *J. Colloid and Interface Science* **1991**, *144*, 340-344.
- (332) Nayak, R. R., Roy, S., Dey, J. *Colloid. Polym. Sci.* **2006**, *285*, 219-224.
- (333) De Weerd, R. J. E. M., De Haan, J. W., Van de Ven, L. J. M., Achten, M., Buck, H. M. *J. Phys. Chem.* **1982**, *86*, 2523-2528.
- (334) Weican, Z., Ganzuao, L., Jianhai, M. U., Qiang, S., Liqiang, Z., Haojun, L., Chi, W. *Chinese Science Bulletin* **2000**, *45*, 1854-1857.
- (335) Cuomo, F., Palazzo, G., Ceglie, A., Lopez, F. *J. Photochemistry and Photobiology A. Chemistry* **2009**, *202*, 21-27.
- (336) Annesini, M. C., Guilio, A. D., Marzio, L. D., Finazzi-Agro, A., Mossa, G. *Journal of Liposome Research* **1992**, *2*, 455-467.
- (337) Rose, P. G. B., J. A.; Lele, S.; Abulafia, O. *Gynecol. Oncol.* **2006**, *102*, 210-213.
- (338) Ostro, M. J., Cullis, P. R. *Am. J. Health-System. Pharm.* **1989**, *46*, 1576-1587.
- (339) Khalil, S. A., Martin, A. N. *J. Pharm. Sci.* **1967**, *56*, 1225-1233.
- (340) Kondo, Y., Uchiyama, H., Yoshino, N., Nishiyama, K., Abe, M. *Langmuir* **1995**, *11*, 2380-2384.
- (341) Zhao, G., -X., Yu, W -L. *J. Colloid and Interface Science* **1995**, *173*, 159-164.
- (342) Caillet, C., Hebrant, M., Tondre, C. *Langmuir* **2000**, *16*, 9099 - 9102.
- (343) Oliger, P., Fischer, A., Hebrant, M., Tondre, C. *Progr. Colloid Polym Sci* **2004**, *123*, 48-51.
- (344) Mubarekyan, E., Santore, M. *Langmuir* **1998**, *14*, 1597-1603.
- (345) Hayakawa, K., Satake, I., Kwak, J.C.T., Gao, Z. *Colloids and Surfaces* **1990**, *50*, 309-320.
- (346) Arien, A., Dupuy, B. *J. MicroEncapsulation* **1997**, *14*, 753-760.
- (347) Volodkin, D., Mohwald, H., Voegel, J. -C., Ball, V. *J. Controlled Release* **2007**, *117*, 111-120.
- (348) Bhattacharya, S., De, S., Subramanian, M. *J. Org. Chem.* **1998**, *63*, 7640-7651.
- (349) Frezard, F., Santaella, C., Vierling, P., Riess, J. G. *Biochim. Biophys. Acta* **1994**, *1192*, 61-70.

- (350) Santaella, C., Vierling, P., Riess, J. G., Gulik-Krzywicki, T., Gulik, A., Monasse, B. *Biochim. Biophys. Acta* **1994**, *1190*, 25-39.
- (351) Trevino, L., Frezard, F., Rolland, J. P., Postel, M., Riess, J. G., *Colloids Surf* **1994**, *88*, 223-233.
- (352) Mori, S., Barth, H. G. *Size Exclusion Chromatography*; Springer-Verlag: New York, 1999.
- (353) Lin, C. T., Mahloudji, A. M., Li, L., Hsiao, M. W. *Chemical Physics Letters* **1992**, *193*, 8-16.
- (354) Peterson, O. G., Tuccio, S. A., Snaveley, B. B. *Appl. Phys. Lett.* **1970**, *17*, 245.
- (355) Sorokin, P. P., Lankard, J. R., Moruzzi, V. L., Hammond, E. C. *J. Chem. Phys.* **1968**, *48*.
- (356) van Zandvoort, M. A. M. J., Vossen, D. L. J., van Ginkel, G., Torre, R., Bartolini, P., Ricci, M., Thomas-Oates, J., Zuilhot, H. *Phys. Chem. Chem. Phys.* **1999**, *1*, 4571-4582.
- (357) Visser, A. J. W. G., Vos, K., van Hoek, A., Santema, J. S. *J. Phys. Chem.* **1988**, *92*, 759-765.
- (358) Mandala, M., Serck-Hansseen, G., Martino, G., Helle K. B. *Analytical Chemistry* **1999**, *274*, 1-6.
- (359) Chen, Z., Tang, Y., -J., Xie, T., -T., Chen, Y., Li, Y., -Q. *J. Fluoresc* **2008**, *18*, 93-100.
- (360) Bujdak, J., Iyi, N., Sasai, R. *J. Phys. Chem. B* **2004**, *108*, 4470-4477.
- (361) Marques, E. F., Regev, O., Khan, A., Miguel, M. D., Lindman, B. *Macromolecules* **1999**, *32*, 6626-6637.
- (362) Thomas, L. J., Tirrell, D. A. *J Controlled Release* **2000**, *67*, 203-209.
- (363) Zheng, X., -Y., Wachi, M., Harata, A., Hatano, Y. *Spectrochimica Acta Part A* **2004**, *60*, 1085-1090.
- (364) Huang, Y., Yuwono, V., Sevick-Muraca, E. *Langmuir* **2002**, *18*, 9192-9197.
- (365) Geroges, J. *Spectrochimica Acta* **1995**, *51A*, 985-9944.
- (366) Tajalli, H., Gilani, A. G., Zakerhamidi, M. S., Moghadam, M. *Spectrochimica Acta Part A* **2009**, *72*, 697-702.
- (367) Li, Y., Ding, L. -J., Gong, Y. -K., Nakashima, K. *J. Photochemistry and Photobiology A. Chemistry* **2004**, *161*, 125-129.
- (368) Toptygin, D., Packard, B. Z., Brand, L. *Chemical Physics Letters* **1997**, *277*, 430-435.
- (369) Coffman, R. E., Kildsig, D. O. *J. Pharm. Sci.* **1996**, *85*.
- (370) Lehmler, H.-J., Bummer, P. M. *BBA* **2004**, *1664*, 141-149.
- (371) Schuy, S., Faiss, S., Yoder, N.C., Kalsani, V., Kumar, K., Janshoff, A., Vogel, R. *J Phys. Chem. B* **2008**, *112*, 8250-8256.
- (372) Ghosh, K., Vyas, S. M., Lehmler, H. -J., Rankin, S. E., Knutson, B. L. *J. Phys. Chem. B* **2007**, *111*, 363-370.

VITA

Date of Birth: November 30, 1978

Place of Birth: Lagos, Nigeria

EDUCATION

Joint BEng-MEng. Chemical Engineering with Industrial Placement,
University of Manchester, Institute of Science and Technology (UMIST)
Manchester, England (July 2002)

PROFESSIONAL POSITIONS

Process Engineering Intern, Shell Exploration and Production, Scotland, UK (2000 -2001)
Technical Assistant, University of Kentucky – Environmental Research Teaching Laboratory
(ERTL), (2006 – 2008)

PUBLICATIONS

Ojogun, V.A., Lehmler, H.-J., Knutson, B.L., ‘Cationic-Anionic Vesicle Templating from Fluorocarbon/Fluorocarbon and Hydrocarbon/Fluorocarbon Surfactants’. *Journal of Colloid and Interface Science.* 338 (2009) 82-91

Lehmler, H.-J., Ling X., Sandhya, S.M., Ojogun, V.A., Knutson, B.L., Ludewig, G., ‘Synthesis, Physicochemical Properties and *In Vitro* Cytotoxicity of Nicotinic Acid Ester Prodrugs Intended for Pulmonary Delivery Using Perfluorooctyl Bromide as Vehicle’. *International Journal of Pharmaceutics* 353 (2008) 35-44

PRESENTATIONS

Ojogun, V.A., Lehmler, H.-J., Knutson, B.L., ‘Nano-structured cationic-anionic vesicle templating from fluorocarbon/fluorocarbon and hydrocarbon/fluorocarbon surfactants,’ Kentucky Nanomaterials Convention, Louisville, KY (March 2008).

Ojogun, V.A., Knutson, B.L., Lehmler, H.-J., ‘Characterization of Fluorinated and Hydrocarbon Mixed Cationic-Anionic Surfactant Vesicles,’ AIChE annual meeting, Salt Lake City, UT (November 2007).

Ojogun, V.A., Knutson, B.L., Ling X., Sandhya, S.M., Ludewig, G., Lehmler, H.-J., ‘Thermodynamics of fluorinated prodrugs and surfactants for drug delivery in a fluorocarbon medium,’ AIChE annual meeting, San Francisco, CA (2006).

Ojogun, V.A., Knutson, B.L., Ling X., Sandhya, S.M., Ludewig, G., Lehmler, H.-J., 'Thermodynamics of fluorinated prodrugs and surfactants for drug delivery in a fluorocarbon medium,' Chemical Engineering Graduate Student Symposium, Lexington, KY (2006).

Ojogun, V.A., Knutson, B.L., Ling X., Sandhya, S.M., Ludewig, G., Lehmler, H.-J., 'Thermodynamics of fluorinated prodrugs and surfactants for drug delivery in a fluorocarbon medium,' Chemical Engineering Graduate Student Symposium, Morgantown, WV (2006).